ABSTRACT

Title of dissertation: TRANSMON QUBITS COUPLED TO SUPERCONDUCTING LUMPED ELEMENT RESONATORS
Baladitya Suri, Doctor of Philosophy, 2015

Dissertation directed by: Professor Frederick C. Wellstood
Department of Physics

Dr. Benjamin S. Palmer
Laboratory for Physical Sciences

I discuss the design, fabrication and measurement at millikelvin-temperatures of $Al/AlO_x/Al$ Josephson junction-based transmon qubits coupled to superconducting thin-film lumped element microwave resonators made of aluminum on sapphire. The resonators had a center frequency of around 6 GHz, and a total quality factor ranging from 15,000 to 70,000 for the various devices. The area of the transmon junctions was about $150\,\text{nm} \times 150\,\text{nm}$ and with Josephson energy E_J such that $10\,\text{GHz} \leq E_J/h \leq 30\,\text{GHz}$. The charging energy of the transmons arising mostly from the large interdigital shunt capacitance, was $E_c/h \approx 300\,\text{MHz}$.

I present microwave spectroscopy of the devices in the strongly dispersive regime of circuit quantum electrodynamics. In this limit the ac Stark shift due to a single photon in the resonator is greater than the linewidth of the qubit transition. When the resonator is driven coherently using a coupler tone, the transmon spectrum reveals individual "photon number" peaks, each corresponding to a single additional photon

in the resonator. Using a weighted average of the peak heights in the qubit spectrum, I calculated the average number of photons $\bar{n}$ in the resonator. I also observed a nonlinear variation of $\bar{n}$ with the applied power of the coupler tone P_{rf}. I studied this nonlinearity using numerical simulations and found good qualitative agreement with data.

In the absence of a coherent drive on the resonator, a thermal population of 5.474 GHz photons in the resonator, at an effective temperature of 120 mK resulted in a weak $n = 1$ thermal photon peak in the qubit spectrum. In the presence of independent coupler and probe tones, the $n = 1$ thermal photon peak revealed an Autler-Townes splitting. The observed effect was explained accurately using the four lowest levels of the dispersively dressed Jaynes-Cummings transmon-resonator system, and numerical simulations of the steady-state master equation for the coupled system.

I also present time-domain measurements on transmons coupled to lumped-element resonators. From T_1 and Rabi oscillation measurements, I found that my early transmon devices (called design LEv5) had lifetimes ($T_1 \sim 1\,\mu$s) limited by strong coupling to the 50 Ω transmission line. This coupling was characterized by the the rate of change of the Rabi oscillation frequency with the change in the drive voltage ($\mathrm{d}f_{Rabi}/\mathrm{d}V$) – also termed the Rabi coupling to the drive. I studied the design of the transmon-resonator system using circuit analysis and microwave simulations with the aim being to reduce the Rabi coupling to the drive. By increasing the resonance frequency of the resonator $\omega_r/2\pi$ from 5.4 GHz to 7.2 GHz, lowering the coupling of the resonator to the transmission line and thereby increasing the external quality

factor Q_e from 20,000 to 70,000, and reducing the transmon-resonator coupling $g/2\pi$ from 70 MHz to 40 MHz, I reduced the Rabi coupling to the drive by an order of magnitude ($\sim$ factor of 20). The $T_1 \sim 4\,\mu$s of devices in the new design (LEv6) was longer than that of the early devices, but still much shorter than the lifetimes predicted from Rabi coupling, suggesting the presence of alternative sources of noise causing qubit relaxation. Microwave simulations and circuit analysis in the presence of a dielectric loss tangent $\tan\delta \simeq 5\times10^{-6}$ agree reasonably well with the measured T_1 values, suggesting that surface dielectric loss may be causing relaxation of transmons in the new designs.

TRANSMON QUBITS COUPLED TO SUPERCONDUCTING LUMPED ELEMENT RESONATORS

by

Baladitya Suri

Dissertation submitted to the Faculty of the Graduate School of the
University of Maryland, College Park in partial fulfillment
of the requirements for the degree of
Doctor of Philosophy
2015

Advisory Committee:
Prof. Frederick C. Wellstood, Chair
Dr. Benjamin S. Palmer
Prof. Chris Lobb
Dr. Kevin D. Osborn
Prof. John Cumings

Dedication

To the Grand Illusion.

The Seer, Seeing and The Seen.

Acknowledgments

It is not very often that one gets the opportunity and this much room to express gratitude. So here is the long list of people that I feel compelled from within to thank. My limitations as a human being sadly make this list not entirely exhaustive. I want to begin by thanking my advisors, Ben Palmer and Fred Wellstood, for their guidance throughout my work. Their guidance and encouragement sustained and nurtured my enthusiasm for physics. I consider myself lucky to have worked under a brilliant scientist and a wonderful advisor in Fred. Our weekly group-meetings with him sometimes left us awed at his intuition for experiment. He has also been utmost friendly to talk to at all times. Working with Ben has been a huge learning experience for me, both professionally and personally. He taught me a whole lot about the minute details of experiment. His work-ethic is often humbling, and he is never busy to help his students out if they get stuck with something. I look forward to future collaborations with both of them.

My research would not have been possible without the cooperation of my colleagues. I thank all my labmates – Sergey, Vitaley, Zaeill, Zach, Jenn, Shavi, Jen-Hao and Jay – for a friendly and stimulating environment at work. I learned a lot through my discussions with each one of them. Their contribution to my work has been invaluable. I wish them all the very best in their future endeavours. I also thank my entire class of Physics at Maryland, particularly Rashmish, Anita, Prateek, Yigit, Bhupal, Dinko, Pavel, Megan, Joyce, Remington, Jennifer, Kanupriya for enriching my time in the Department. I also want to thank my colleagues, Kevin Osborn,

Moe, Micah, Bahman, Aruna, Yaniv, Chris Richardson, Nathan Siwak, Lev Bishop, Rusko Ruskov, Charlie Tahan, Vanita Srinivasa, Rangga Budoyo, Ben Cooper, Kristen Voigt, Jared Hertzberg, Toby Olver, Sean Flannery, Steve Brown, Warren Berk, Scott Horst, Dan Hinkel, Curt Walsh, Russel, Dong Park, Dr. Leng, Rob Galemba, Mark Thornton, Althia, Cynthia, and several others at LPS for helping me through my stay. I thank Dr. Rabindra Mohapatra for his guidance during the two years I worked with him. I want to thank all my professors at Maryland, Dr. Hassam, Dr. Drake, Dr. Cohen, Dr. Antonsen, Dr. Wallace, Dr. Buonanno, Dr. Yakovenko, Dr. Einstein, Dr. Bhagat, Dr. Chacko, Dr. Kulin and Dr. Coplan, in whose classes I gained tremendous insight into physics.

Among my family, I want to first thank my parents Sri Kumaraswamy and Smt. Vedavati and my brother Balachandra for all the love and constant support they have given me and, more importantly, for the atmosphere of intellectual and spiritual growth they nurtured around me. Music in particular, and arts in general, are a gift I received from my parents and I sometimes wonder what I would be without them. They gave me freedom to question and explore from a very young age, and taught me to be simple and honest. Their constant zeal for rational thinking gave me the initial conditions for my trajectory in both philosophy and physics. While my mother taught me the basics of algebra in sixth grade, it will not be an exaggeration to say that a large part of my intuition in physics was honed in my conversations with my father and brother during my childhood. Looking back, I feel immensely proud that as ten year olds, my brother and I discovered concepts like vectors and relative motion that we would go on to learn several years later in physics classes. I also want

to take this opportunity to thank the rest of my family and friends, beginning with my (late) grandparents, my uncle Mani, Sundararam & family, Sivaram & family, Janaki & family, Saraswati & family, Sarada & family, my late aunt Vani, my cousins Kiran, Mohan, Uma, Krishna, Kamu, Srikant, Vamsi, Sekhar, Pallavi, Katyayani, Durga, Lahari for the wonderful times together, and all the shared memories. Their passion in all their respective endeavours is inspiring. I also thank Sundari & family, Jyoti & family, Radhika & family, Rangarajan & family, Satyabala & family, Ramadoss & family, Subramaniam & family, KSN & family, Ayyagaris, YRB & family, the Gora family, the Peesapatis, and many other friends for their continued affection towards my family. My Ph.D. has been a long journey, and the patience of all my family and friends through this period has to be acknowledged. I want to thank Chandu Kaka for his benevolence and kind counsel. I also want to thank my uncle Rangarajan and Sri Peesapati Venkateswarlu for identifying my aptitude for science at a young age and encouraging me to take up physics. I am deeply grateful to Venkat uncle and Mallika aunty, and their children Sid and Priya for their affection, and being my family away from home. I spent long hours talking to my dear friend Divya Jain over the last three years. A special thanks to her for inspiring and 'conspiring' a transformation in both the extroverted and introverted aspects of my existence.

I thank all my friends in Maryland for the wonderful moments I shared with them. My long stint here binds them like family to me. I am indebted to Avinash for all his help when I first landed in the US, and for being a catalyst for my interest in Sanskrit. I have had wonderful company in Surya &Varadaa, Siddharth, Kavita & Nalin, Adi, Avinash, Dikpal, Rashmish, Madhura, Ashish, Shankar, Ranjan &

Sonali, Anita & Shane, Vitaley, Rangarajan, Anusha, Divya Gangaramani, Priya & Les, Sandeep & Trishna, Ashutosh and Deepa, and each of them has improved me in his/her own way. I thank Swarup for introducing me to Yoga and being an example in personal discipline. My dear friends Deepa & Srini staying nearby through my stay here helped deepen my long-standing bond with them. Among the many vivid memories that I carry of this place, the Grand Canyon hike and the cross-continent road trip to Berkeley with Surya, Varada and Dikpal, Sanskrit sessions with Avinash, the music sessions with Sid, Ranjan and Umamahesh, the meditation retreats with Ashish, the various food festivals with Shankar, Kavita & Nalin, critiquing movies with Adi, chess with Madhura, 100-mile bike rides and camping trips with Anita and Shane, and being chased by a black bear in Shenandoah while hiking with Vitaley are a few that I will cherish forever.

I want to specially thank my friend Auditya for being a continuous inspiration, be it physics or music or chess. Whenever I faced a dilemma, his words were like a beacon that pierced the mists. The group of Audi, Hari, Shree Krishna, Supradeepa, Sundeep, Chinmay, fondly called 'Gurunath-beat', has been largely responsible for sharpening my mathematical logic, and nurtured an overall refinement in my personality. I am honored to be in regular interaction with such extremely fertile minds. I want to thank Deepti Navaratna for making me privy to her musical musings, notwithstanding that her abilities are far far superior to mine. I have always been amazed at my friend Vijayaraghavan Bhashyam's zeal for learning and self-improvement and studying the Ramayana in the original with him has been sheer joy. I thank my dear friends Padmasini and Dheeraj for the wonderful time I had over my weekend visits

to NYC. Listening to Padma speak is a great way to stave off banality. I thank my friend Kiran for all the affection and moral support through thick and thin. I want to thank Pankaja for numerous thought-provoking conversations. I also want to thank my friends from college, the Incredible Alakites, Viri, Dheeraj, Chaitanya, Subbu, Vineeta, Nitya, Padmini, Prabha, Srividya, Lavanya, Bharadwaj, Uday, Bhargavi, Varun, Swaroop, Ashwini among many many others.

I want to thank my professors at my alma mater IIT Madras, Dr. Neelima Gupte, Dr. M.S.R Rao, Dr. Rangarajan, Dr. Balakrishnan, Dr. Suresh Govindarajan, Dr. Arul Lakshminarayanan, Dr. M.V. Satyanarayana, Dr. Deshmukh, Dr. Jyotirmaya Tripathi, Dr. T.T. Narendran, Prof. Mohan and late Dr. Dileep for their guidance and encouragement during my formative years at college. I also want to thank my teachers, Mr. M. P. Singh, Dr. K. S. Sastry, Dr. S. S. Sastry, Mr. S. K. Verma and others from high school who laid the foundation for my higher education.

I want to thank all my heroes– personalities that inspired me to pursue the numerous activities that I have dabbled in over the years. In physics, I have often drawn a fresh perspective in my frequent encounters with Einstein, Dirac, Feynman and Poincare among several others. In music, I grew up listening to Tyagaraja, Dikshitar and Syama Sastri, as rendered by Balamurali, M.S., Emani, Dwaram etc. Equally impactful has been the work of the constellation of Indian film composers like Shankar Jaikishen, Madan Mohan, Burman, OP Nayyar, Roshan, Ilaiyaraja, CR Subbaraman, singers like Lata, Rafi, Asha, Talat, Ghantasala, S. P. B., Ghulam Ali, Madhurani and many others. I have also had the fortune to expand my horizons listening to the music of the likes of Bach and Brahms from the west to Fairouz and

Shajarian in the middle east. In literature, I pored over the writings of Valmiki and Vyasa as well as Keats, Blake and Shakespeare. I was drawn to the visual styles of film makers like Kurosawa, Yimou *etc.* In my sporting activities, my imagination was captured by the achievements of Federer, Nadal, Djokovic, Sachin, McGrath, Anand, Alyokhine and their ilk. I am indebted to them all for enriching my experience.

And finally, I am indebted to all the great sages whose words have kindled the fire of inquiry in my mind – Krishna, Buddha, Sankara, JK, UG, Gibran, Thoreau, Melville, Whitman and Jed .... and Further.

Table of Contents

List of Tables

List of Figures

List of Abbreviations

cQED	circuit quantum electrodynamics
cavity QED	cavity quantum electrodynamics
ac/ AC	Alternating current
dc / DC	Direct current
CPW	coplanar waveguide
CW	continuous wave
CPB	Cooper-pair box
JJ	Josephson junction
IDC	Interdigital capacitance
MBE	Molecular Beam Epitaxy
IPA	Iso-propyl alcohol
DI	De-ionized (water)
NMP	N-Methyl-2-Pyrrolidone
MWO	Microwave Office
LNA	Low Noise Amplifier
HPF	High Pass Filter
LPF	Low Pass Filter
DR	Dilution Refrigerator
SEM	Scanning Electron Microscopy
AT	Autler-Townes
JC	Jaynes-Cummings
IBM	The International Business Machines Corporation
LPS	Laboratory for Physical Sciences

Chapter 1

Introduction

1.1 Introduction

Josephson junction-based superconducting circuits have been known to be potential candidates for quantum computation [1, 2] for about fifteen years [3]. The end of the twentieth century saw superconducting qubits emerge onto the quantum computation scene with an experimental demonstration of coherent control of Cooper-pair box (CPB) [3]. This result, and the large amount of work it stimulated soon established that macroscopic [4, 5, 6] circuits made of superconducting aluminum thin films, comprising one to a few Josephson junctions and fabricated using the conventional semiconductor lithographic techniques [7, 8], posed an attractive alternative for quantum information processing. The macroscopic nature of these circuits, and the ability to choose suitable design parameters, made classical control of the devices with conventional microwave electronics easier.

The first few years of the new millennium witnessed steady progress in the design and control of Josephson junction-based qubits. Different flavors of superconducting qubits were developed, using different quantum degrees of freedom of the Josephson junctions – charge [3, 9], flux[10] and phase [11, 12, 13]. Different techniques for qubit read-out [9, 13, 14, 15, 16] were also developed and remarkable progress was made in increasing the lifetime and coherence times of the qubits.

One big step, especially in the field of charge qubits, was the advent of circuit quantum electrodynamics (cQED) architecture [17, 18], where the qubit was embedded inside a coplanar waveguide (CPW) resonator. Through the 1980s and 1990s, Haroche *et al.* had done seminal experiments with single atoms interacting with the quantized electromagnetic field of a resonant cavity [19, 20, 21] – a field that came to be called cavity quantum electrodynamics (see Fig.1.1(a)). Circuit quantum electrodynamics (see Fig.1.1(b)), pioneered at Yale by Schoelkopf *et al.*, was the circuit analogue of cavity QED. When the qubit had a frequency detuned from that of the resonator, the resonator isolated the qubit from the vacuum fluctuations in free space, thereby improving its lifetime. As a result, the relaxation time T_1 of charge qubits improved from a few hundred nanoseconds [3, 22], to a few microseconds [17]. In the best cases, the Purcell protection [23, 24, 25, 26, 27] offered by the resonator to the qubit in the dispersively detuned limit, resulted in qubit lifetimes up to $T_1 \sim 200\,\mu$s [28].

While the lifetimes and coherence times improved overall, the coherence times of charge qubits remained short ($T_2 \sim 500\,$ns) compared to T_1, due to sensitivity to low-frequency charge noise [16, 22, 28, 29]. Charge qubits until that point had relied on operating at a "charge sweet-spot" for optimizing their coherence. This dependence on classical control channels for biasing the qubit led to decoherence due to coupling to noise on those channels. To circumvent this problem, the Yale group designed the 'transmon' [30] – short for "transmission-line shunted plasma oscillation qubit" – where a CPB was shunted with a large capacitance to lower its charging energy, thereby exponentially reducing its charge sensitivity. This brought the T_2

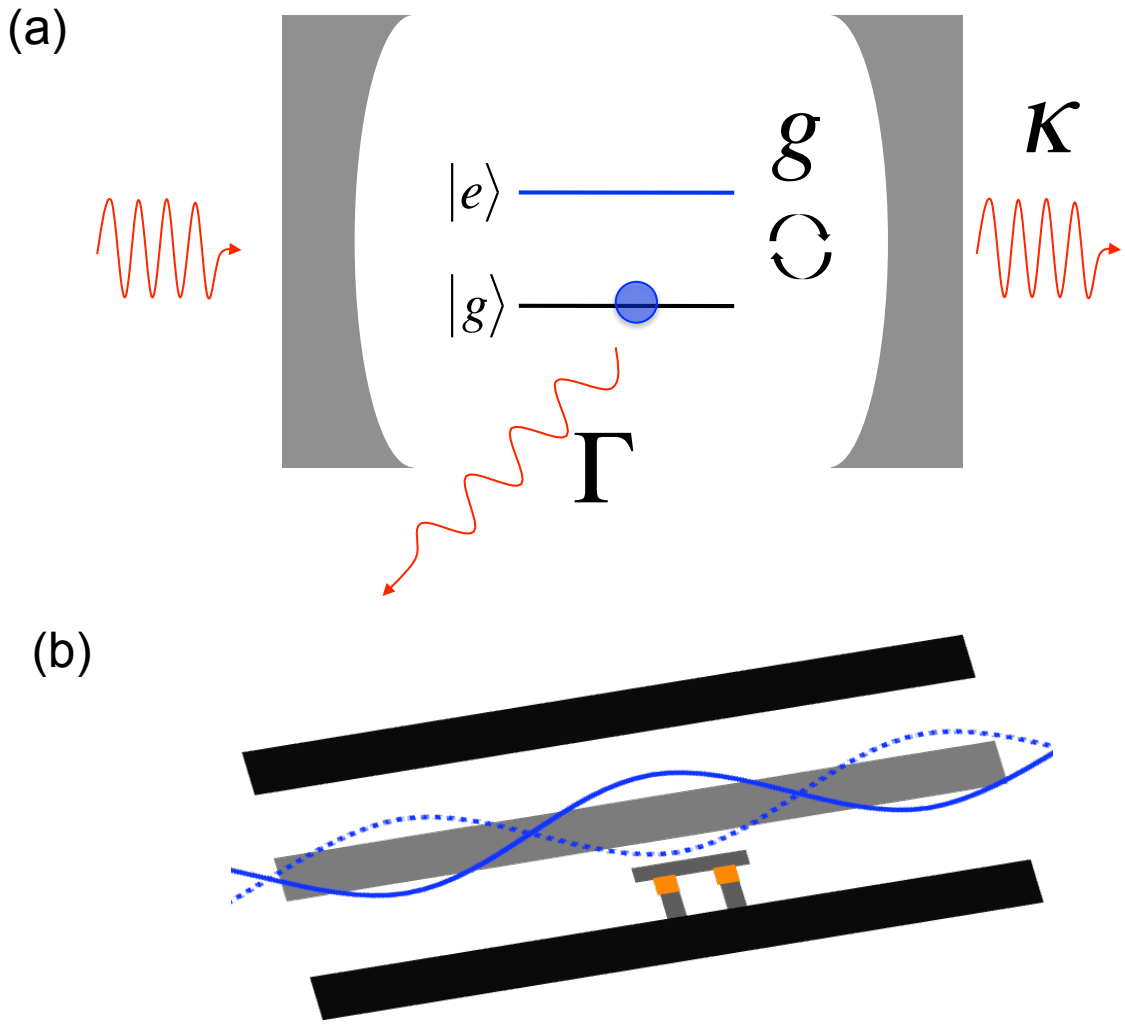

Figure 1.1: Representations of cavity and circuit quantum electrodynamics [18]. (a) A cavity quantum electrodynamics system where a two-level atom interacts with the radiation field of an optical cavity. (b) Circuit quantum electrodynamics system[17, 18] where a Cooper-pair box is coupled to the standing wave modes of a coplanar waveguide transmission line resonator. These vastly different architectures have essentially the same physics.

times into the microsecond range and placed transmons at the forefront of promising superconducting candidates

The ensuing period saw a concerted effort by many groups to investigate, understand and mitigate the factors causing decoherence. The Purcell effect, due to proximity to the higher resonant modes of the CPW read-out resonator[31], surface and interface dielectric losses [32, 33] and quasiparticle excitations caused by stray infrared radiation [34] were all found to be potential causes of relaxation. Purcell filters were designed [35, 36] to suppress the radiative loss mechanism. Increasing the physical dimensions of the transmon features was used to counter the surface and interface dielectric losses [37]. In addition, using new and cleaner materials like titanium nitride and epitaxial aluminum, and cleaner fabrication processes were found to improve the qubit coherence [38, 39].

A significant evolutionary breakthrough [40] on the coherence front was pioneered at Yale when the CPW resonator in the cQED architecture was replaced with a 3D superconducting aluminum microwave cavity and the transmon redesigned. With this change Paik *et al.* [40] measured a lifetime of $T_1 \sim 50\,\mu$s and a coherence time of $T_2 \sim 25\,\mu$s. This new architecture drastically reduced the participation of the surface and interface dielectric losses due to the increased mode volume of the cavity fields, and also reduced the coupling to spurious electromagnetic modes by dispensing with wire-bonds and other electrical connections in the vicinity of the qubit. A further improvement to the coherence time T_2 was achieved by Rigetti *et al.* at IBM [41] by replacing the superconducting aluminum cavity with a copper cavity, thereby improving the thermalization of the cavity field. This reduced the excess dephasing

caused by thermal photons in the resonator, and improved the coherence times of 3D transmons up to almost 100 μs.

While the improvement in coherence times was significant for quantum computation, cQED architectures with transmon qubits also led to a host of developments in quantum information processing. The large dipole moment of the artificial 'atom' interacting with the quantized electromagnetic field in the cQED architectures enabled operation in the strong coupling regime of cavity QED [20, 42]. This opened up new avenues for studying phenomena that were until then only accessible in atomic systems. Measurement of the Lamb-shift due to vacuum fluctuations [43], the observation of 'photon number-splitting' [21, 44, 45], the observation of Autler-Townes doublet and Mollow triplet states of a driven transmon system [46], as well as the large photon-number $\sqrt{n}$ nonlinearity in the Jaynes-Cummings vacuum Rabi splitting [47, 48] are some examples of the spectroscopic signatures of atom-field interactions in superconducting cQED devices [49]. The strong dispersive regime of the Jaynes-Cummings interaction [50] also led to the development of high fidelity read-out of the qubit state using the Jaynes-Cummings nonlinearity in the resonator [35, 51, 52]. This scheme is now extensively used by many groups for qubit read-out, including at LPS [53].

Another significant development was the demonstration of single-shot read-out using Josephson parametric amplifiers [54]. This led to pathbreaking measurements such as the experimental observation of quantum jumps [55], active suppression of decoherence and stabilization of Rabi oscillations through quantum feedback [56], and the mapping of quantum trajectories [57, 58] – all using transmons. Apart from this,

transmons have also found applications in the generation of non-classical microwave photon states [59, 60, 61], the development of a single microwave photon router [62], and a novel hybrid architecture using the coupling to surface acoustic modes of a piezoelectric substrate [63].

1.2 Overview of the thesis

In this thesis, I discuss my measurements of single $Al/AlO_x/Al$ transmon qubits coupled to superconducting lumped-element resonators made of thin film aluminum on a sapphire substrate in a cQED architecture. The overall aim of my work was to study the energy relaxation in transmon qubits that were read out using lumped-element resonators. This style of resonator was used in my earlier experiments with a CPB [28] with very encouraging results. On the one hand, the Cooper-pair box in [28] had a lifetime of $200\,\mu$s, which was the longest lifetime measured among superconducting qubits at that time. On the other hand, from measurements of Rabi oscillations, I observed that the lifetime of the CPB was strongly correlated with the coupling to the transmission line. The frequency dependence of the Rabi coupling was not fully understood at the time and motivated much of my later study, in which I designed, fabricated and measured transmon qubits coupled to lumped-element resonators. In my early transmon devices, I again found that the lifetime was limited by strong coupling to the transmission line. I examined the design using circuit analysis and microwave simulations and then made changes to the design to reduce the Rabi coupling. This study is one of the main aspects of this thesis.

In the spectroscopic measurements of my transmon devices, I observed interesting effects like the Autler-Townes effect involving the dressed states of the Jaynes-Cummings system and photon number-splitting [44]. When the transition between two quantum levels is driven strongly with a resonant drive field, the resulting pair of states can be viewed as being split by an amount equal to the Rabi frequency of the drive field. By probing the transitions to a third level in the system, this splitting can be observed spectroscopically. This is called the Autler-Townes (AT) effect [64]. Previously AT had been observed in superconducting systems [46, 65, 66], however the system of states involved in the effect in those experiments was the $|g\rangle$, $|e\rangle$ and $|f\rangle$ states of the transmon alone. In contrast, my observation of the Autler-Townes effect was the first involving both the transmon energy levels and the resonator photon-number levels (see Fig. 1.2). A detailed account of this experiment is given later in Chapter 6.

I also studied "photon number-splitting" of the transmon spectrum, where the ac Stark shift of the qubit frequency due to a single photon in the cavity is larger than the linewidth of the qubit transition. In particular I measured a nonlinear variation of the average photon occupancy of the resonator with the applied drive power. I examined this effect theoretically through extensive numerical simulations and a detailed account of this is another significant part of this thesis, covered in Chapter 6.

The lumped-element resonators I used in my devices behaved as a single-mode oscillator with frequency around 5 GHz, with no higher modes measured up to 30 GHz. The absence of higher resonator modes is thought to lower the possibility of enhanced

spontaneous emission through the multi-mode Purcell effect [31]. Another aspect in favor of the lumped-element architecture is the scalability. The on-chip footprint of a lumped-element resonator is typically about $400\,\mu\text{m} \times 400\,\mu\text{m}$, which is much smaller than the other resonator styles in vogue – CPW $\lambda/2$ resonators and 3D microwave cavities. Many groups have conventionally measured transmon qubits coupled to "distributed element" resonators, such as the CPW transmission line resonators [31, 37, 44], or more recently using 3D microwave cavities [40, 41, 66] and this makes my work with lumped-element resonators unique. While CPW resonators and 3D cavities are adequate when the number of qubits is small, scalability of the designs to include a large number of qubits becomes a concern as we approach a true quantum computing architecture. In this context, lumped-element resonators have a unique advantage.

In chapter 2, I begin with a theoretical introduction to the Hamiltonian formalism for the dynamics of an LC resonator circuit. I then derive the quantum mechanical Hamiltonian operator for the LC oscillator using Dirac's method of quantization [67] in both the driven and the undriven cases. Next, I extend the Hamiltonian formalism to non-dissipative, nonlinear circuits comprising a single Josephson junction. After reviewing the quantum dynamics of a capacitively shunted Josephson junction– popularly known as the 'transmon' – I set up the general Hamiltonian of a cQED architecture of a transmon coupled to a resonator [18, 68].

Chapter 3 extends the theory with a derivation of the Jaynes-Cummings Hamiltonian [50] from the cQED Hamiltonian under the rotating wave approximation. This is followed by a description of the physics in the strong dispersive regime of the Jaynes-

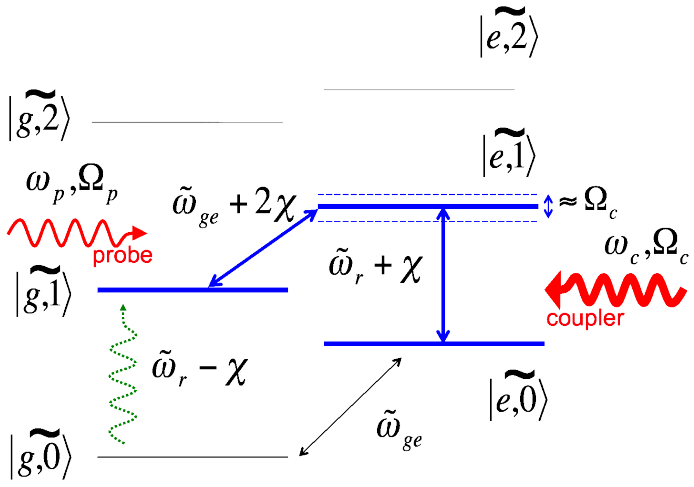

Figure 1.2: Autler-Townes mechanism of the dressed qubit-resonator states. Here, the $|\widetilde{e,0}\rangle \rightarrow |\widetilde{e,1}\rangle$ transition is a resonator-like transition, while the $|\widetilde{g,1}\rangle \rightarrow |\widetilde{e,1}\rangle$ transition is a qubit-like transition (see Chapter 6).

Cummings interaction. I then discuss the dissipative dynamics of the system through a system-bath master equation in the Born-Markovian approximation.

Chapter 4 marks the beginning of the experimental sections of the thesis with a detailed description of the design of the lumped-element resonator and transmon. I also give an overview of the fabrication procedure for the transmon-resonator devices that I built.

In Chapter 5, I detail the experimental set-up I used to measure devices at millikelvin temperatures. In this chapter, I also describe the Jaynes-Cummings read-out technique [35, 51, 52] that I used to measure the probability of the system being in the excited state.

Chapter 6 summarizes my spectroscopic measurements of transmons coupled to

lumped-element resonators. In particular, I describe my measurements of the photon occupancy of the resonator using the photon number-split spectrum of the transmon. Numerical simulations of the nonlinear variation of the photon occupancy with applied microwave power, using both a semi-classical steady-state solution and a steady state solution of the full system master equation, are compared to experimental data. In Chapter 6, I also give an account of the first experimental observation of the Autler-Townes effect involving the four lowest-lying dressed states of the Jaynes-Cummings system [53]. My experimental results are also shown to agree well with numerical simulations of the steady-state system master equation using two qubit energy levels and ten resonator levels.

In Chapter 7, I discuss time-domain measurements to characterize the coherence of my transmon devices coupled to lumped-element resonators. I found that my early designs had short lifetimes caused by strong coupling to the $50\,\Omega$ quantum dissipative environment. This coupling was characterized by the Rabi coupling to the input/output coplanar waveguide transmission line. I then motivate the modifications I made to the design to lower the Rabi coupling, based on a circuit analytical approach and simulations using Microwave Office. The results of the measurements on the new designs are shown, along with a discussion of possible new limits on the lifetime set by surface and interface dielectric losses.

Finally, in Chapter 8, I conclude with a summary of my main results and discuss future directions of research.

Chapter 2

Quantization of Superconducting Circuits

2.1 Overview

Quantum electrodynamics (QED) is the quantum mechanical theory of the interaction of charged particles with the electromagnetic field. At its heart is the fundamental interaction of a single photon, the quantum of the electromagnetic field, with a single electron, the quantum of electric charge. Over time, the meaning of the term QED has been extended to include interactions of the photon field with more complex systems, such as an atom. The behavior of an atom interacting with the light quanta of a resonant cavity field, is described by cavity quantum electrodynamics [42, 69]. With the advent of Josephson junction-based quantum circuits, the possibility of creating tunable man-made artificial 'atoms' became a reality. These artificial atoms can then be coupled to a resonant cavity [40], a transmission line resonator circuit [18] or to simple LC resonator circuits [53]. The interaction of the electromagnetic field of the resonator with the artificial atom, in the quantum limit, is the subject of *circuit quantum electrodynamics* (cQED). cQED is the underlying subject of this thesis.

The equations describing the classical dynamics of a circuit in a cQED architecture can be found using the well known Kirchhoff's circuit laws of voltages and currents. If we consider non-dissipative circuits, we know from classical mechanics

that a conservative system can be described using a Hamiltonian formalism [70]. Here we are interested in the quantum dynamics of the circuit. Given a classical Hamiltonian function for the circuit, we can quantize it using Dirac's recipe for canonical quantization. The goal of this chapter is to systematically reformulate Kirchhoff's *equations of motion* for a circuit in the Hamiltonian framework and then derive the quantum Hamiltonian generating the quantum dynamics of the circuit. To do this, I follow the approach of Devoret *et al.* [71]. To illustrate this process, I first discuss two linear circuits, the simple undriven LC oscillator, and the slightly more complex driven LC oscillator. I then consider nonlinear, non-dissipative circuits involving Josephson junctions and tie the two parts together to arrive at the Hamiltonian for a complete cQED system, a transmon coupled to a resonator.

2.2 Quantizing a resonator circuit - review of the simple harmonic oscillator

In physics classes, one can sometimes get the feeling that theoretical physics is the repeated study of the harmonic oscillator under different headers. In deference to that observation, let us start by looking at a simple LC resonator circuit comprising an inductor L and a capacitor C. The simple harmonic dynamics of such circuits is well known. As a first step towards formulating a Hamiltonian function, I demonstrate how to construct a Lagrangian for the circuit as a function of the generalized coordinates and velocities and then show how the dynamical equations can be derived using the Euler-Lagrange prescription [70].

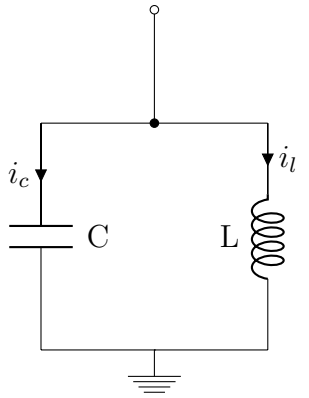

Figure 2.1: LC resonator circuit.

Consider the simple LC circuit shown in Fig. 2.1. Choosing the bottom node as the ground-reference, the voltage on the top-node is denoted by $v(t)$. By applying Kirchhoff's current conservation law to the top node, and making use of the constitutive relations for the inductor and capacitor , I arrive at the equation

$$i_c + i_l = 0 \tag{2.1}$$

and then write

$$C\dot{v} + i_l = 0 \tag{2.2}$$

or

$$C\dot{v} + \frac{\Phi}{L} = 0 \tag{2.3}$$

or

$$C\ddot{\Phi} + \frac{\Phi}{L} = 0 \tag{2.4}$$

where i_c is the current through the capacitor branch, i_l is the current through the inductor branch, Φ is defined as the time-integral of the node-voltage $v(t)$ according to

$$\Phi(t) = \int_{-\infty}^{t} v(\tau)\mathrm{d}\tau. \tag{2.5}$$

Equation 2.4 is also the equation of motion for a simple harmonic oscillator. Similar to the transition from Newton's equation of motion to a Lagrangian action principle in classical mechanics, the question to ask at this stage is if there exists an action integral that is minimized, or equivalently, if there exists a Lagrangian function (of the coordinates and velocities), that gives rise to the equations of motion. Given that this equation of motion has a simple form, it is easy to see that the Lagrangian is given by

$$\mathcal{L} = \frac{C\dot{\Phi}^2}{2} - \frac{\Phi^2}{2L}. \tag{2.6}$$

The Euler-Lagrange equation that results from Hamilton's principle, or the minimization criterion of the action integral $\mathcal{S} = \int_0^t \mathcal{L}d\tau$, are

$$\frac{d}{dt}\left(\frac{\partial\mathcal{L}}{\partial\dot{\Phi}}\right) = \frac{\partial\mathcal{L}}{\partial\Phi}. \tag{2.7}$$

It is easy to check that substituting Eq. 2.6 into Eq. 2.7 gives the correct equation of motion for the flux variable

$$C\ddot{\Phi} + \frac{\Phi}{L} = 0. \tag{2.8}$$

I now define the canonical momentum Q, as

$$Q \equiv \frac{\partial\mathcal{L}}{\partial\dot{\Phi}} = C\dot{\Phi}. \tag{2.9}$$

Note that this is just the charge on the top plate of the capacitor C. Thus the canonical momentum conjugate to the node flux Φ is just the node charge Q. I now use a Legendre transformation [70] from $\dot{\Phi}$ and Φ variables into the Q and Φ variables and write the Hamiltonian as

$$\mathcal{H} = Q\dot{\Phi} - \mathcal{L} \tag{2.10}$$

where the $\dot{\Phi}$ is now written in terms of Q. Upon simplification this gives

$$\mathcal{H} = \frac{Q^2}{2C} + \frac{\Phi^2}{2L}. \tag{2.11}$$

As one would have expected at the beginning, the Hamiltonian given by Eq. 2.11 can be mapped onto that of the classical mechanical spring-mass system,

$$\mathcal{H} = \frac{p^2}{2m} + \frac{1}{2}m\omega_r^2 x^2 \tag{2.12}$$

if I identify $p \leftrightarrow Q$,$x \leftrightarrow \Phi$, $m \leftrightarrow C$ and $\quad m\omega_r^2 \leftrightarrow 1/L$ and $\quad \omega_r = 1/\sqrt{LC}$.

To quantize this system, I employ the standard method of quantization as follows. I now demonstrate this with a mechanical system and then use the above analogy to map it to the electrical system. To begin with, following Dirac's recipe, I impose a commutation relation on the 'position' operator $\hat{x}$ and conjugate 'momentum' operator $\hat{p}$

$$[\hat{x}, \hat{p}] = i\hbar \tag{2.13}$$

and rewrite the Hamiltonian in terms of the $\hat{x}$ and $\hat{p}$ 'operators' as,

$$\mathcal{H} = \left(\frac{\hat{p}^2}{2m\omega_r} + \frac{m\omega_r}{2}\hat{x}^2\right)\omega_r. \tag{2.14}$$

I now define the scaled operators $\hat{X} = \sqrt{m\omega_r}\ \hat{x}$ and $\hat{P} = \hat{p}/\sqrt{m\omega_r}$ such that

$$[\hat{X}, \hat{P}] = i\hbar \tag{2.15}$$

$$\mathcal{H} = \left(\frac{\hat{P}^2}{2} + \frac{\hat{X}^2}{2}\right)\omega_r. \tag{2.16}$$

An advantage of using the scaled operators is that the Hamiltonian is explicitly symmetric in position and momentum, a feature that is characteristic of a harmonic system. I can now rewrite the above Hamiltonian as

$$\mathcal{H} = \frac{1}{4}\left\{(\hat{X} + i\hat{P})(\hat{X} - i\hat{P}) + (\hat{X} - i\hat{P})(\hat{X} + i\hat{P})\right\}\omega_r. \tag{2.17}$$

I can then define the operators

$$\hat{a} = \frac{\hat{X} + i\hat{P}}{\sqrt{2\hbar}} = \sqrt{\frac{m\omega_r}{2\hbar}}\left(\hat{x} + i\frac{\hat{p}}{m\omega_r}\right) \tag{2.18}$$

$$\hat{a}^\dagger = \frac{\hat{X} - i\hat{P}}{\sqrt{2\hbar}} = \sqrt{\frac{m\omega_r}{2\hbar}}\left(\hat{x} - i\frac{\hat{p}}{m\omega_r}\right) \tag{2.19}$$

which satisfy the commutation relation

$$[\hat{a}, \hat{a}^\dagger] = 1. \tag{2.20}$$

Rewriting the Hamiltonian in terms of the operators $\hat{a}$ and $\hat{a}^\dagger$, one obtains

$$\mathcal{H} = \frac{\hbar}{4}\left(4\hat{a}^\dagger\hat{a} + 2\right)\omega_r \tag{2.21}$$

giving us the celebrated Hamiltonian for a harmonic oscillator

$$\mathcal{H} = \hbar\omega_r\left(\hat{a}^\dagger\hat{a} + \frac{1}{2}\right). \tag{2.22}$$

It is important to note that, written in this form, this Hamiltonian is independent of the detailed construction of the system. This abstraction is what makes

it so universally applicable, while the specific definitions of the operators carry the information about the system. For an LC oscillator

$$\hat{a} = \sqrt{\frac{1}{2\hbar Z_r}} \left(\hat{\Phi} + i Z_r \hat{Q} \right) \tag{2.23}$$

$$\hat{a}^\dagger = \sqrt{\frac{1}{2\hbar Z_r}} \left(\hat{\Phi} - i Z_r \hat{Q} \right) \tag{2.24}$$

where $Z_r = \sqrt{L/C}$ is the characteristic impedance of the resonator. The operator $\hat{a}^\dagger \hat{a}$ quantifies the number of 'quanta'.

$$\hat{N} = \hat{a}^\dagger \hat{a} \tag{2.25}$$

and the eigenstates $|\psi_n\rangle$ of the system Hamiltonian are defined by

$$\mathcal{H} \, |\psi_n\rangle = \hbar\omega_r (\hat{N} + \frac{1}{2}) \, |\psi_n\rangle = \hbar\omega_r (n + \frac{1}{2}) \, |\psi_n\rangle \tag{2.26}$$

for n $\in \{0, 1, 2, \ldots\}$. The corresponding energy eigenvalues are equally spaced by $\hbar\omega_r$. Equal spacing of energy levels is a signature of a 'harmonic' system.

The operators $\hat{a}$ and $\hat{a}^\dagger$ are termed the 'annihilation' and 'creation' operators respectively, because they satisfy the commutation relations,

$$[\mathcal{H}, \hat{a}] = -\hat{a} \tag{2.27}$$

$$[\mathcal{H}, \hat{a}^\dagger] = \hat{a}^\dagger. \tag{2.28}$$

Their action on a given energy eigenstate of the system results in another eigenstate with one quantum less or more than the original state respectively

$$\hat{a}|\psi_n\rangle = \sqrt{n} \; |\psi_{n-1}\rangle \tag{2.29}$$

$$\hat{a}^\dagger|\psi_n\rangle = \sqrt{n+1} \; |\psi_{n+1}. \tag{2.30}$$

2.2.1 A useful canonical transformation

Before I conclude this section, I would like to note that there is a symmetry of the harmonic oscillator Hamiltonian under the exchange of coordinates and momenta, as seen explicitly in Eq. 2.16. I note in particular that the transformation of the scaled operators

$$\hat{X} \to \hat{P} \tag{2.31}$$

$$\hat{P} \to -\hat{X} \tag{2.32}$$

preserves the canonical commutation relations

$$[\hat{X}, \hat{P}] = i\hbar. \tag{2.33}$$

In terms of the annihilation and creation operators, the above transformation reads,

$$a \to -ia \tag{2.34}$$

$$a^\dagger \to ia^\dagger \tag{2.35}$$

and this preserves the commutation relation $[a, a^\dagger] = 1$. I use this property in the following sections to rewrite terms in the Hamiltonian in more recognizable forms.

2.2.2 A driven LC oscillator

In this section I consider a driven LC resonator (see Fig. 2.2). While the essence of the method employed to derive the Hamiltonian function for this circuit is the same as in the previous section, I take a more rigorous approach, as described in Devoret *et al.* [71]. For brevity, I not describe the general recipe here, but details can be found in Appendix A.

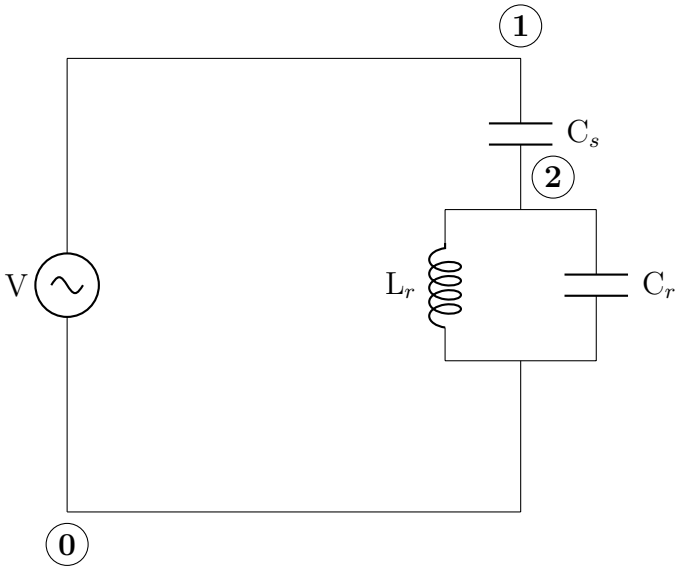

Figure 2.2: Driven LC resonator circuit.

For a connected network, one can define a *spanning tree* as a connected subgraph that includes all the nodes and has a unique path between any two nodes. One of the nodes in such a spanning tree can be chosen as a reference or 'ground' node with a voltage of zero assigned to it. Then the node variables for any given node in the spanning tree can be defined unambiguously in terms of the branch variables along the path connecting the given node to the ground node in the spanning tree. For convenience, I initially replace the ideal voltage source V in Fig. 2.2 with a large capacitance C_v as in Fig. 2.3b. In the final result, I take the simultaneous limit of the capacitance C_v and the charge on its top plate Q_v to infinity while keeping the ratio Q_v/C_v fixed at V.

To begin, I label the *branch* voltages and currents on the *spanning tree* of the circuit (drawn in red in Fig. 2.3a). I then assign zero voltage to the ground node (0)

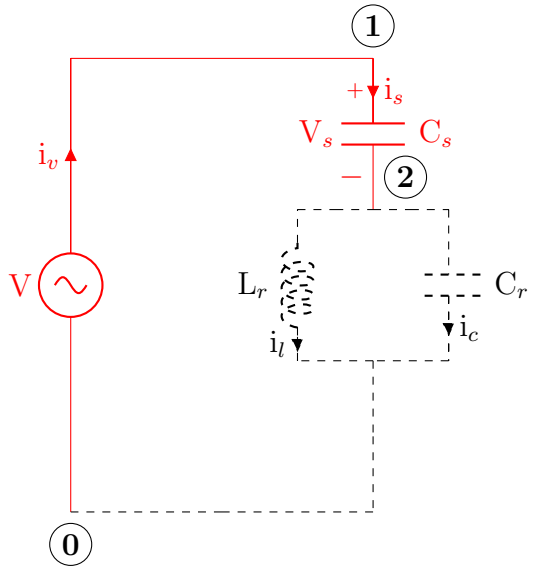

(a)

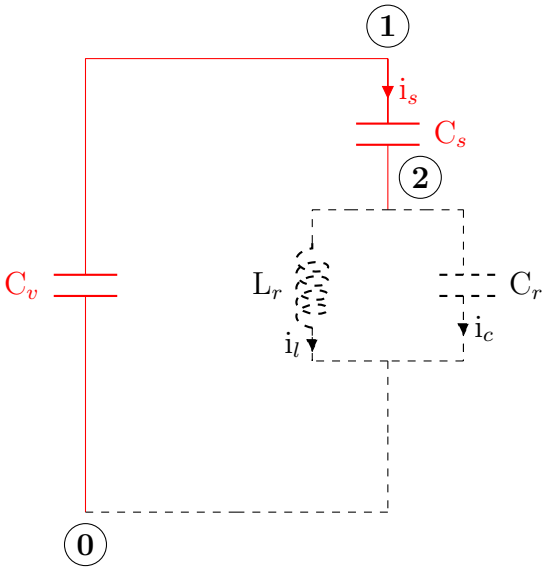

(b)

Figure 2.3: (a) Spanning tree of the driven LC resonator circuit. (b) Spanning tree with battery replaced by capacitor C_v.

and define the node voltages as (note the sign-convention)

$$V_0 = 0 \tag{2.36}$$

$$V_1 = V \tag{2.37}$$

$$V_2 = V - V_s. \tag{2.38}$$

I then define the node-fluxes as

$$\Phi_0 = 0 \tag{2.39}$$

$$\phi_1 = \int_{-\infty}^{t} V(\tau)\mathrm{d}\tau = \int_{-\infty}^{t} V_1(\tau)\mathrm{d}\tau \tag{2.40}$$

$$\phi_2 = \int_{-\infty}^{t} \left(V(\tau) - V_s(\tau)\right)\mathrm{d}\tau = \int_{-\infty}^{t} V_2(\tau)\mathrm{d}\tau. \tag{2.41}$$

Now, writing the current equations for nodes 1 and 2 from Fig. 2.3, and ignoring any static fluxes threading the resonator loop, I find

$$i_v = C_v\dot{V} = C_v\dot{V}_1 \tag{2.42}$$

$$i_s = C_s\dot{V}_s = C_s\left(\dot{V} - \dot{V}_2\right) \tag{2.43}$$

$$i_v + i_s = 0. \tag{2.44}$$

Therefore for node (1) I have,

$$C_v\dot{V}_1 + C_s(\dot{V}_1 - \dot{V}_2) = 0 \tag{2.45}$$

$$C_v\ddot{\phi}_1 + C_s(\ddot{\phi}_1 - \ddot{\phi}_2) = 0 \tag{2.46}$$

and for node (2) I have,

$$i_s = i_r + i_l \tag{2.47}$$

$$C_s(\ddot{\phi}_1 - \ddot{\phi}_2) = C_r\ddot{\phi}_2 + \frac{\phi_2}{L_r} \tag{2.48}$$

or

$$C_s(\ddot{\phi}_2 - \ddot{\phi}_1) + C_r\ddot{\phi}_2 + \frac{\phi_2}{L_r} = 0. \tag{2.49}$$

It can be shown that this set of equations can be derived by applying the Euler-Lagrange equations with the Lagrangian given by

$$\mathcal{L} = \frac{C_v(\dot{\phi}_1)^2}{2} + \frac{C_s\left(\dot{\phi}_1 - \dot{\phi}_2\right)^2}{2} + \frac{C_r(\dot{\phi}_2)^2}{2} - \frac{\phi_2^2}{2L_r}. \tag{2.50}$$

For example for node (**1**), we get

$$\frac{d}{dt}\left(\frac{\partial\mathcal{L}}{\partial\dot{\phi}_1}\right) - \frac{\partial\mathcal{L}}{\partial\phi_1} \equiv C_v\ddot{\phi}_1 + C_s(\ddot{\phi}_1 - \ddot{\phi}_2) = 0. \tag{2.51}$$

I can now define the node-charges as the conjugate momenta as:

$$Q_1 = \frac{\partial\mathcal{L}}{\partial\dot{\phi}_1} = C_v\dot{\phi}_1 + C_s(\dot{\phi}_1 - \dot{\phi}_2) \tag{2.52}$$

$$Q_2 = \frac{\partial\mathcal{L}}{\partial\dot{\phi}_2} = C_s(\dot{\phi}_2 - \dot{\phi}_1) + C_r\dot{\phi}_2. \tag{2.53}$$

Finally, I can write the circuit Hamiltonian as

$$\mathcal{H} = Q_1\dot{\phi}_1 + Q_2\dot{\phi}_2 - \mathcal{L} \tag{2.54}$$

$$\mathcal{H} = \frac{C_r + C_s}{2(C_rC_s + C_sC_v + C_vC_r)}Q_1^2 + \frac{C_v + C_s}{2(C_rC_s + C_sC_v + C_vC_r)}Q_2^2 + \frac{C_s}{(C_rC_s + C_sC_v + C_vC_r)}Q_1Q_2 + \frac{\phi_2^2}{2L_r}. \tag{2.55}$$

Next, I eliminate the capacitance C_v (representing the voltage source) by taking the limit $\underset{\substack{Q_1\to\infty\\ C_v\to\infty}}{\mathrm{Lim}} Q_1/C_v = V$. I also drop the subscript 2 in favor of r (for resonator), and ignore the first term, which is just the energy stored in the battery to arrive at

$$\mathcal{H} = \frac{Q_r^2}{2(C_r + C_s)} + \frac{\phi_r^2}{2L_r} + \frac{C_s}{C_r + C_s}\,Q_rV. \tag{2.56}$$

The first two terms of the Hamiltonian given by Eq. 2.56 are the same as the harmonic oscillator. The last term represents the *drive*. For $C_s \ll C_r$ I can treat the last term in the Hamiltonian as a perturbation. Following the standard procedure for quantization of a harmonic oscillator discussed in section Sec. 2.2, I get

$$H = \hbar\omega_r(a^\dagger a + \frac{1}{2}) + \frac{C_s}{C_r + C_s}\sqrt{\frac{2\hbar}{Z_r}}\,\frac{(a - a^\dagger)}{2i}V. \tag{2.57}$$

Note that the transformation $a \to -ia$ and $a^\dagger \to ia^\dagger$ preserves the canonical commutation relations. If the voltage source is a sinusoidal waveform generator $V = V_0 \sin(\omega t)$, I can rewrite this Hamiltonian in the form

$$H = \hbar\omega_r(a^\dagger a + \frac{1}{2}) - \hbar\Omega_r\,(a + a^\dagger)\cos(\omega t) \tag{2.58}$$

where $\Omega_r = 1/\left(2\hbar Z_r\right)^{1/2} C_s/(C_r + C_s)$.

2.3 Nonlinear circuits with Josephson junctions

The circuits considered above were *linear*, in the sense that the equations of motion are linear differential equations. In this section, I consider a dissipationless nonlinear element – a Josephson junction. Nevertheless, the recipe for quantizing the circuit is still applicable.

The basic logical element of a quantum computer is a quantum bit or *qubit*. A qubit is a quantum two-level system. As seen in the previous two sections, the linear circuits comprising capacitors and inductors have, at best, an equally spaced ladder of quantum levels. This means that a pair of states cannot be addressed uniquely using a classical driving field and hence a linear circuit cannot make a qubit. This leads us

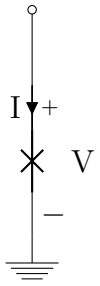

Figure 2.4: A pure Josephson junction.

to an essential requirement of nonlinearity in a circuit element to cause anharmonic spacing of quantum levels [2]. An ideal Josephson element is just such a nonlinear element.

2.3.1 A pure Josephson junction

2.3.1.1 Josephson relations

A pure Josephson junction, shown in Fig. 2.4 is a dissipationless nonlinear element that obeys the Josephson relations [72, 73]

$$I = I_c \sin(\varphi) \tag{2.59}$$

$$V = \frac{\hbar}{2e}\frac{d(\varphi)}{dt} \tag{2.60}$$

where φ is the gauge-invariant phase difference across the Josephson junction and I_c is the critical current of the Josephson junction – the maximum current that can be supported by the junction. The first relation is called the *dc* Josephson relation since it predicts a non-zero current when there is a constant phase difference between the two sides of the Josephson junction. The second relation is called the *ac* Josephson

relation since it predicts a voltage across the junction when the phase difference varies with time.

From the definition of node flux as the time integral of the node voltage Eq. 2.5, I can write the ac Josephson relation as

$$\dot{\phi} = \frac{\hbar}{2e}\frac{d(\varphi)}{dt}. \tag{2.61}$$

This gives us a definition for the phase difference across a Josephson element in terms of the flux threading it

$$\phi = \frac{\Phi_0}{2\pi}\varphi \tag{2.62}$$

or

$$\varphi = 2\pi\frac{\phi}{\Phi_0} \tag{2.63}$$

where $\Phi_0 = h/2e$ is a fundamental constant called the flux quantum.

Before I proceed to the Hamiltonian formalism, it is helpful to see how the DC Josephson relation leads to nonlinearity. An 'inductive' circuit element is one that has the current through the element governed by the flux threading it. Thus, a nonlinear relation such as Eq. 2.59 between the flux and the current for the Josephson junction makes the pure Josephson junction a nonlinear inductance. Taking the time derivative of the dc Josephson relation,

$$\frac{dI}{dt} = I_c \cos\left(2\pi\frac{\phi}{\Phi_0}\right)\frac{2\pi\dot{\phi}}{\Phi_0} \tag{2.64}$$

and rearranging gives

$$\dot{\phi} = V = \frac{\Phi_0 \dot{I}}{2\pi\sqrt{I_c^2 - I^2}}. \tag{2.65}$$

Equating this with a general V-I characteristic equation for an inductance,

$$V = L_J \dot{I} \tag{2.66}$$

I get an expression for the Josephson inductance that depends on the current, signifying nonlinearity:

$$L_J = \frac{\Phi_0}{2\pi\sqrt{I_c^2 - I^2}}. \tag{2.67}$$

2.3.1.2 Hamiltonian for a pure Josephson junction

I now derive the Hamiltonian that generates the above Josephson equations of motion. From the DC Josephson relation, which gives the current as a function of the phase difference, I can arrive at the Hamiltonian fairly directly. If Q is the node charge on the top node in Fig. 2.4, then

$$\dot{Q} = -I = -I_c \sin(\varphi) \tag{2.68}$$

and thus

$$-\frac{\partial H}{\partial \phi} = -I_c \sin\left(2\pi \frac{\phi}{\Phi_0}\right). \tag{2.69}$$

Integrating this gives

$$H = -\frac{I_c \Phi_0}{2\pi} \cos\left(2\pi \frac{\phi}{\Phi_0}\right) + f(Q) \tag{2.70}$$

where $f(Q)$ is the constant of integration and is a function of Q alone. For a pure Josephson element, I take this constant to be zero, and get the Hamiltonian

$$H = -E_J \cos\left(2\pi \frac{\phi}{\Phi_0}\right) \tag{2.71}$$

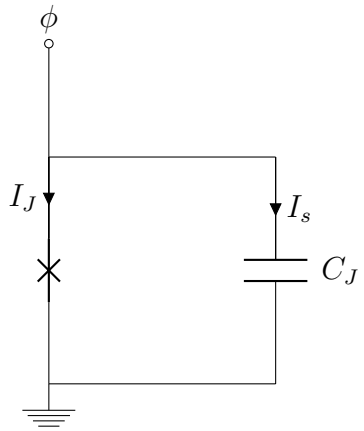

Figure 2.5: A capacitively shunted Josephson junction.

where $E_J = I_c\Phi_0/2\pi$ is the Josephson energy. Since ϕ is the coordinate, the Josephson energy term corresponds to a potential energy.

2.3.2 A capacitively shunted Josephson junction

While the Hamiltonian given by Eq. 2.71 captures the dynamics of a pure Josephson element, most practical realizations of Josephson elements, either in the trilayer sandwich architecture or the weak link architecture, include a capacitance between the superconducting terminals. This capacitance could be a stray capacitance, as often is the case with ultra-small junctions, or an intentional capacitive shunt, as in the case of a transmon. Starting from Kirchhoff's laws and the circuit in Fig. 2.5, I can write

$$I_J + I_s = 0 \tag{2.72}$$

$$C_J\ddot{\phi} + I_c \sin\left(2\pi\frac{\phi}{\Phi_0}\right) = 0 \tag{2.73}$$

This gives us the Lagrangian

$$\mathcal{L} = \frac{C_J \dot{\phi}^2}{2} + E_J \cos\left(2\pi \frac{\phi}{\Phi_0}\right). \tag{2.74}$$

From $\mathcal{L}$, the Hamiltonian can then be written in terms of $Q = C_J \dot{\phi}$ as

$$\mathcal{H} = \frac{Q^2}{2C_J} - E_J \cos\left(2\pi \frac{\phi}{\Phi_0}\right). \tag{2.75}$$

The first term in the Hamiltonian given by Eq. 2.75 represents the capacitive energy and gives an explicit functional form for the constant of integration that was discussed in Eq. 2.71 in the context of the pure Josephson element. Also note that in the limit $\theta = 2\pi \frac{\phi}{\Phi_0} \approx 0$ the Hamiltonian given by Eq. 2.75 reduces to

$$H \approx \frac{Q^2}{2C_J} + \frac{E_J \theta^2}{2} + \mathcal{O}(\theta^4). \tag{2.76}$$

To third order in θ Eq. 2.76 resembles a harmonic oscillator Hamiltonian. In the parameter regime where this approximation holds, the nonlinear terms in the potential energy can be treated as perturbative corrections to the unperturbed harmonic oscillator Hamiltonian. As I show in the next few sections, this is a good approximation in the transmon regime.

2.3.3 Capacitively-shunted Josephson junction with a gate bias voltage

I now consider the case of a gate-biased Josephson junction. The circuit I consider for this purpose is shown in Fig. 2.6. The voltage bias V_g is a low frequency signal and is to be distinguished from a drive that is at the characteristic frequency of

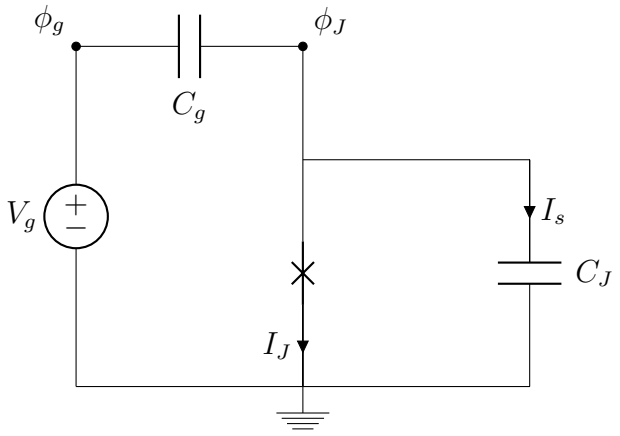

Figure 2.6: A gate biased Josephson junction.

the Josephson junction. This may be a controlled bias voltage applied by the experimenter or an unavoidable low-frequency *noise* source arising from the environment. I can write the Lagrangian for the circuit in Fig. 2.6 as follows.

$$\mathcal{L} = \frac{C_v\dot{\phi}_g^2}{2} + \frac{C_g(\dot{\phi}_g - \dot{\phi}_J)^2}{2} + \frac{C_J\dot{\phi}_J^2}{2} + E_J\cos\left(2\pi\frac{\phi}{\Phi_0}\right) \tag{2.77}$$

where C_v is the large capacitance that accounts for the ideal voltage source. I define the node charges as

$$Q_g = \frac{\partial\mathcal{L}}{\partial\dot{\phi}_g} = C_v\dot{\phi}_g + C_g(\dot{\phi}_g - \dot{\phi}_J) \tag{2.78}$$

$$Q_J = \frac{\partial\mathcal{L}}{\partial\dot{\phi}_J} = C_g(\dot{\phi}_J - \dot{\phi}_g) + C_J\dot{\phi}_J. \tag{2.79}$$

I can then write the Hamiltonian as

$$\mathcal{H} = Q_g\dot{\phi}_g + Q_J\dot{\phi}_J - \mathcal{L} \tag{2.80}$$

After taking the limit

$$\mathrm{Lim}_{\substack{Q_g\to\infty \\ C_v\to\infty}} \frac{Q_g}{C_v} = V_g \tag{2.81}$$

I arrive at the Hamiltonian

$$\mathcal{H} = \frac{(Q_J + C_g V_g)^2}{2C_\Sigma} - E_J \cos\theta \tag{2.82}$$

where $C_\Sigma = C_J + C_g$ is the effective capacitance of the Josephson junction and $\theta = 2\pi\phi/\Phi_0$ is the gauge-invariant phase difference across the Josephson junction.

In the superconducting state, the charge carriers are the Cooper pairs of electrons with charge $2e$. Therefore, I can write $Q_J = n(2e)$ where n stands for the number of Cooper pairs on the upper plate of the capacitance C_Σ of the Josephson junction. I can then write the Hamiltonian as

$$\mathcal{H} = 4E_c(n - n_g)^2 - E_J \cos\theta \tag{2.83}$$

where $n_g = -C_g V_g/2e$ is the excess number of Cooper pairs on the gate electrode due to the bias voltage and $E_c = e^2/2C_\Sigma$ is the capacitive charging energy required to add one electron to the Josephson junction. The Hamiltonian given by Eq. 2.83, thus, has two competing energy scales, namely the charging energy E_c and the Josephson energy E_J. The ratio E_J/E_c plays a crucial role in determining the dynamics of the device.

2.3.4 Quantizing the capacitively-shunted Josephson junction

In this section I describe the quantum dynamics generated by the Hamiltonian function given by Eq. 2.83. As in the case of the LC resonator, I quantize the Hamiltonian by imposing the canonical commutation relations on the operators for the

coordinate ($\hat{\phi}_J$) and the conjugate momentum ($\hat{Q}_J$):

$$[\hat{\phi}_J, \hat{Q}_J] = i\hbar. \tag{2.84}$$

In terms of the $\hat{\theta}$ and $\hat{n}$ operators, I have

$$[\hat{\theta}, \hat{n}] = i. \tag{2.85}$$

2.3.5 Charge representation

The Hamiltonian given by Eq. 2.83 can now be written in terms of the operators as

$$H = 4E_c(\hat{n} - n_g)^2 - E_J \cos(\hat{\theta}) \tag{2.86}$$

$$H = 4E_c(\hat{n} - n_g)^2 - \frac{E_J}{2}\left(e^{i\hat{\theta}} + e^{-i\hat{\theta}}\right). \tag{2.87}$$

From the commutation relation $[\hat{\theta}, \hat{n}] = i$ it follows that

$$[e^{i\hat{\theta}}, \hat{n}] = -e^{i\hat{\theta}}. \tag{2.88}$$

In the basis states of the 'charge' number operator, I can write

$$\hat{n}\,|n\rangle = n\,|n\rangle. \tag{2.89}$$

I can then arrive at some basic properties of $e^{i\hat{\theta}}$:

$$[e^{i\hat{\theta}}, \hat{n}]\,|n\rangle = -e^{i\hat{\theta}}|n\rangle \tag{2.90}$$

$$\hat{n}\,e^{i\hat{\theta}}\,|n\rangle = (n+1)e^{i\hat{\theta}}\,|n\rangle. \tag{2.91}$$

This shows the result that $e^{i\hat{\theta}}|n\rangle$ is an eigenstate of $\hat{n}$ with eigenvalue $n+1$. By choosing a unit normalization for $|n\rangle$, I then have

$$\langle n+1|\, e^{i\hat{\theta}}|n\rangle = 1, \quad \forall n \in \mathbb{Z} \tag{2.92}$$

and can then write:

$$e^{i\hat{\theta}} = \sum_{n=-\infty}^{+\infty} |n\rangle\langle n+1|. \tag{2.93}$$

The Hamiltonian in the charge representation then becomes:

$$H = 4E_c \sum_{n=-\infty}^{+\infty} (n-n_g)^2 |n\rangle\langle n| - \frac{E_J}{2}\left(\sum_{n=-\infty}^{+\infty} |n\rangle\langle n+1| + |n+1\rangle\langle n|\right). \tag{2.94}$$

In Eq. 2.94 one sees that the Josephson energy term comes into play through off-diagonal matrix elements between states with n Cooper-pairs and $n+1$ Cooper-pairs. It is clear that this term corresponds to the tunneling of Cooper-pairs across the Josephson junction. The charge representation is a convenient basis to work with numerically as well as for gaining a physical understanding of the system. In the 'Cooper-pair box regime' of $E_J/E_c \approx 1$ the infinite summation over charge states can be truncated to just two charge states (*eg.* $n=0$ and $n=1$) to describe the system (see Fig. 2.7(a)). In the 'transmon regime' (see Fig. 2.7(c)) where $E_J/E_c \approx 100$ the summation can be truncated to include around 5 or 6 charge states and still give sufficiently accurate numerical results, thereby making this a good basis the easiest to work with computationally.

2.3.6 Phase representation

Similar to the case of a free particle, where one uses a position and momentum representation, for a junction one can use the phase representation, which is dual to the charge representation [74, 75]. In the phase representation, the Schrodinger equation has closed form solutions in terms of Mathieu functions [68]. While they are not easy to work with in computations, the functional dependence of the energy eigenvalues and their anharmonicity on the ratio E_J/E_c is transparent in these solutions, shining light on some critical properties of the system.

From the commutation relation $[\hat{\theta}, \hat{n}] = i$, I can write the representation for the $\hat{n}$ operator in the $\hat{\theta}$ representation as [74]

$$\hat{n} = -i\frac{\partial}{\partial\hat{\theta}}. \tag{2.95}$$

It is not surprising that this looks strikingly similar to the momentum operator in the position basis for the free particle system. $\hat{\theta}$, like $\hat{x}$, is an operator with a continuous spectrum of eigenvalues defined by

$$\hat{\theta}|\theta\rangle = \theta|\theta\rangle, \quad \forall\theta \in (-\pi, \pi) \tag{2.96}$$

The basis states of $\hat{\theta}$ can be normalized according to

$$\langle\theta'|\theta\rangle = \delta(\theta' - \theta) \tag{2.97}$$

and the completeness relation is given by

$$\int_{-\pi}^{\pi} \mathrm{d}\theta\, |\theta\rangle\langle\theta| = 1 \tag{2.98}$$

In this representation, the Schrodinger equation can be written as

$$H\psi_n = E_n\psi_n \tag{2.99}$$

$$4E_c(-i\frac{\partial}{\partial\theta} - n_g)^2\psi_n - E_J\cos\theta\psi_n = E_n\psi_n. \tag{2.100}$$

The energy eigenvalues of this characteristic equation can be written analytically in terms of Mathieu's characteristic value functions [76, 30, 51] as

$$E_m(n_g) = E_c\, a_{2[n_g+k(m,n_g)]}\,(E_J/2E_c) \tag{2.101}$$

where $a_\nu(q)$ is the ν^{th} Mathieu's characteristic value function, and $k(m, n_g)$ is an integer-valued sorting function for the eigenvalues [30, 68, 76].

From Eq. 2.101, the energy associated with a transition from the $m = 0$ energy level to the m^{th} transmon energy level can be written as

$$E_{m0} = E_m - E_0. \tag{2.102}$$

A plot of the transition frequency E_{m0}/h in gigahertz vs n_g for the four lowest transitions with $m = 1, 2, 3$ and 4 for different values of E_J/E_c is shown in Fig. 2.7. For the Cooper-pair box regime ($E_J/E_c \simeq 1$) the transition energies (see Fig. 2.7(a)) show a strong dependence on the gate charge n_g, with the higher transitions ($m = 2, 3\ldots$) showing successively higher variation. As E_J/E_c is increased (see Fig. 2.7(b)) the E_{10} transition becomes less sensitive to n_g, while the higher transitions show significant variation. In the transmon regime [30] where $E_J/E_c \approx 100$ (see Fig. 2.7(c)), the four lowest transition energies are seen to be insensitive to changes in n_g. I also note that the spacing of the transition energies in the transmon regime is nearly harmonic.

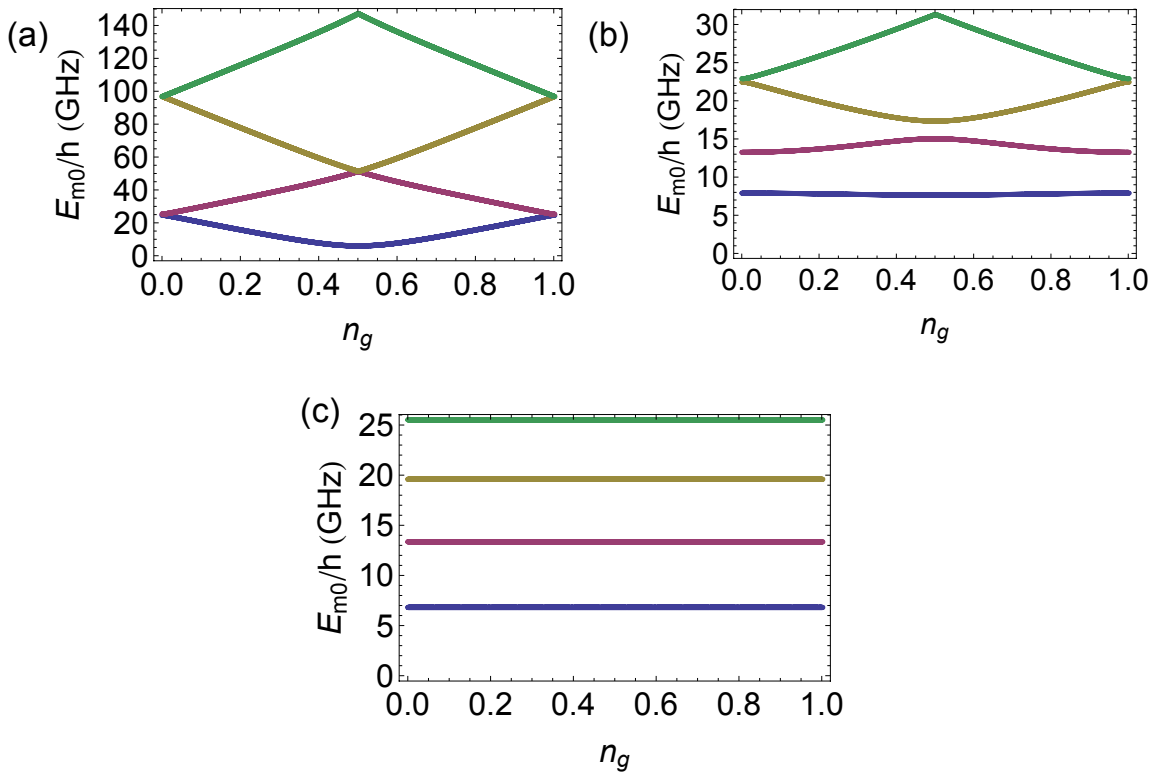

Figure 2.7: Transition frequencies of a Josephson junction as a function of the ratio E_J/E_c. All the transition frequencies are measured from the ground state, or '0' level of the system. The blue, purple, gold and green curves represent the transitions to levels m =1, 2, 3 and 4 respectively. (a) When $E_J/E_c = 1$, the charge-dispersion of the levels is significant, as seen from their dependence on the gate-charge n_g. (b) When $E_J/E_c = 10$, the lower transitions become less sensitive to the gate-charge. (c) When $E_J/E_c = 100$, the four transitions are very nearly flat, and thereby almost insensitive, to changes in gate-charge.

2.3.6.1 Charge dispersion

The most significant result of the Mathieu function solution given in Eq. 2.101 is that it provides an explicit functional form for the charge dispersion of the energy eigenvalues. The charge dispersion ϵ_m for the mth energy level is defined by

$$\epsilon_m = E_m\left(n_g = \frac{1}{2}\right) - E_m(n_g = 0) \tag{2.103}$$

and it can be used to quantify the dependence of the energy eigenvalue on the effective gate-bias charge n_g. This is useful for estimating the sensitivity of the device to uncontrollable low-frequency fluctuations of the gate voltage and charge noise. One can show that charge dispersion is exponentially suppressed as the value of E_J/E_c increases. In [68], it is shown that

$$\epsilon_m \simeq (-1)^m E_c \frac{2^{4m+5}}{m!}\sqrt{\frac{2}{\pi}}\left(\frac{E_J}{2E_c}\right)^{\frac{m}{2}+\frac{3}{4}} e^{-\sqrt{8E_J/E_c}}. \tag{2.104}$$

This means that in the large E_J/E_c limit, the charge dispersion is exponentially suppressed, as shown in Fig. 2.8(a).

The energy eigenvalues E_m for the lower eigenstates is given approximately by [30, 68]

$$E_m(n_g) \simeq E_m(n_g = \frac{1}{4}) + \frac{\epsilon_m}{2}\cos(2\pi n_g). \tag{2.105}$$

For ϵ_m sufficiently small, E_m can be treated as constant in n_g. This is typically a good approximation for the lower energy states of a transmon for $E_J/E_c \approx 100$. In the following section, I look at the "transmon limit" of the solutions and ignore any dependence on n_g.

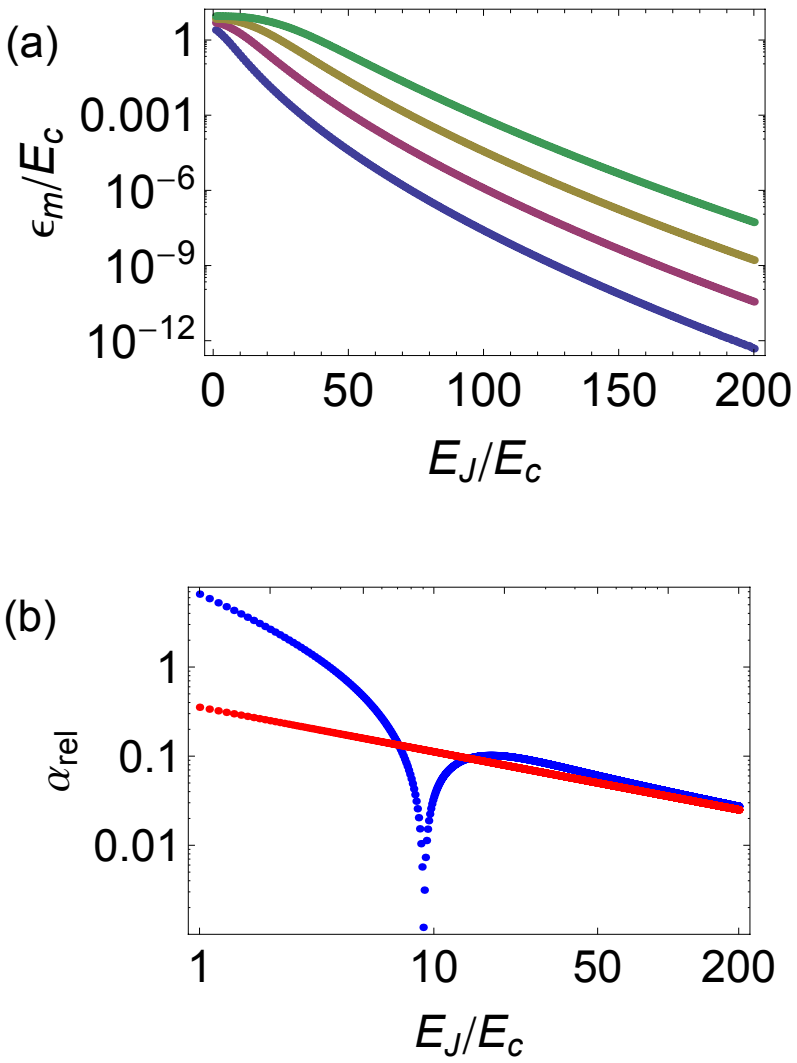

Figure 2.8: Plot of charge dispersion and anharmonicity of a capacitively shunted Josephson junction as a function of E_J/E_c. (a) Log-Linear plot of the normalized charge dispersion ϵ_m/E_c vs E_J/E_c. The blue, purple, gold and green curves correspond to the values $m = 1, 2, 3$ and 4 respectively. For large E_J/E_c the charge dispersion is exponentially suppressed. (b) Log-Log plot of the relative anharmonicity α_{rel} vs E_J/E_c. Anharmonicity decreases only as a power law as E_J/E_c increases. Blue curve is α_{rel} computed using Eq. 2.114. Red curve is the asymptotic expression given by $(8E_J/E_c)^{-1/2}$

2.3.7 Transmon regime

In the limit where $E_J/E_c \gg 1$ (typically around 50), I showed that the n_g dependence of the energy eigenvalues can be neglected. The Hamiltonian given by Eq. 2.83 can then be written as

$$H = 4E_c\,\hat{n}^2 - E_J\cos(\hat{\theta}). \tag{2.106}$$

In this same limiting case, I can also take θ to be close to zero and Taylor-expand the cosine in the potential up to the fourth power of θ.

$$H \approx 4E_c\,\hat{n}^2 + \frac{E_J}{2}\hat{\theta}^2 - E_J\frac{\hat{\theta}^4}{24}. \tag{2.107}$$

The Hamiltonian given by Eq. 2.107 is similar to that of a harmonic oscillator with an anharmonic term that can be treated perturbatively in the small θ limit. To diagonalize this Hamiltonian, I define 'annihiliation' and 'creation' operators analogous to the harmonic oscillator case

$$b = \left(\frac{E_J}{32E_c}\right)^{1/4}\left(\hat{\theta} + i\hat{n}\sqrt{\frac{E_J}{E_c}}\right) \tag{2.108}$$

$$b^\dagger = \left(\frac{E_J}{32E_c}\right)^{1/4}\left(\hat{\theta} - i\hat{n}\sqrt{\frac{E_J}{E_c}}\right). \tag{2.109}$$

Writing H in terms of these operators, I have

$$H = \sqrt{8E_JE_c}\left(b^\dagger b + \frac{1}{2}\right) - \frac{E_c}{12}\left(b + b^\dagger\right)^4. \tag{2.110}$$

Simplifying the last term and writing it in terms of $b^\dagger b \equiv m$, I get

$$H = \sqrt{8E_JE_c}\left(m + \frac{1}{2}\right) - \frac{E_c}{12}\left(6m^2 + 6m + 3\right). \tag{2.111}$$

The transition energies between levels can now be written as [30, 68]

$$E_{m+1,m} = E_{m+1} - E_m = \sqrt{8E_JE_c} - E_c(m+1). \tag{2.112}$$

2.3.7.1 Anharmonicity of energy levels

Another quantity of interest to us is the anharmonicity of the transmon energy levels. The quartic term in the transmon Hamiltonian given by Eq. 2.107 makes the system weakly anharmonic. This can be seen easily from the transition energy values in Eq. 2.112. For a perfectly harmonic system, all transition energies are equal. For a transmon, which is weakly anharmonic, the anharmonicity of the m^{th} energy level is

$$\alpha_m = E_{m+1,m} - E_{m,m-1} \simeq -E_c. \tag{2.113}$$

We can define the relative anharmonicity as

$$\alpha_{rel} \equiv \frac{\alpha_m}{E_{m+1,m}} = \frac{1}{\sqrt{8E_J/E_c} - (m+1)} \simeq (8E_J/E_c)^{-1/2} \tag{2.114}$$

for $m + 1 \ll \sqrt{8E_J/E_c}$.

From Eq. 2.114, we can see that asymptotically the anharmonicity decreases by a power law as E_J/E_c increases [30]. This power-law behavior is clearly seen in Fig. 2.8(b). The transmon regime corresponds to $E_J/E_c \geq 25$, where there is *sufficient* anharmonicity to allow rapid transitions, but very small charge dispersion to reduce sensitivity to environmental voltage and charge fluctuations.

2.3.8 The Cooper-pair box regime : $E_J/E_c \simeq 1$

Before I conclude this section it is useful to take a brief look at the Cooper-pair box regime – where the ratio $E_J/E_c \simeq 1$. In this limit, the dependence on the reduced gate bias charge n_g cannot be ignored. It can also be shown that, in this limit, the

infinite sum over charge basis states in the Hamiltonian given by Eq. 2.94 can be truncated to include just the $n = 0$ and $n = 1$ levels, if one considers $0 < n_g < 2$. This gives the Cooper-pair box Hamiltonian:

$$H_{CPB} = 4E_c\, n_g^2\, |0\rangle\langle 0| + 4E_c\, (n_g - 1)^2\, |1\rangle\langle 1| - \frac{E_J}{2}\left(|1\rangle\langle 0| + |0\rangle\langle 1|\right). \tag{2.115}$$

This is a two-state system and I can write the projection operators in terms of the Pauli spin-$\frac{1}{2}$ matrices using the transformations

$$|0\rangle\langle 0| \equiv \frac{I - \sigma_z}{2} \tag{2.116}$$

$$|1\rangle\langle 1| \equiv \frac{I + \sigma}{2} \tag{2.117}$$

$$|0\rangle\langle 1| + |1\rangle\langle 0| \equiv \sigma_x. \tag{2.118}$$

The Cooper-pair box Hamiltonian then becomes

$$H_{CPB} = -4E_c \left(n_g - \frac{1}{2}\right)\sigma_z - \frac{E_J}{2}\sigma_x. \tag{2.119}$$

The energy eigenvalues of this Hamiltonian are given by

$$E_\pm = \pm\sqrt{\left(4E_c\left(n_g - \frac{1}{2}\right)\right)^2 + \left(\frac{E_J}{2}\right)^2}. \tag{2.120}$$

The special place occupied by the $n_g = \frac{1}{2}$ point is transparent in this notation. Note that without the E_J term in the Hamiltonian, the energy eigenvalues are degenerate at $n_g = 1/2$, hence it is named the 'degeneracy point'. At this point, the island is equally likely to have zero "excess" Cooper pairs or one excess Cooper pair, *i.e.* there is a charge degeneracy at this point. This degeneracy is lifted by the Josephson coupling term. At $n_g = 1/2$ the difference between the two energy eigenvalues (Eq. 2.120) is E_J and in the neighborhood of the degeneracy point, the energy eigenvalues show a

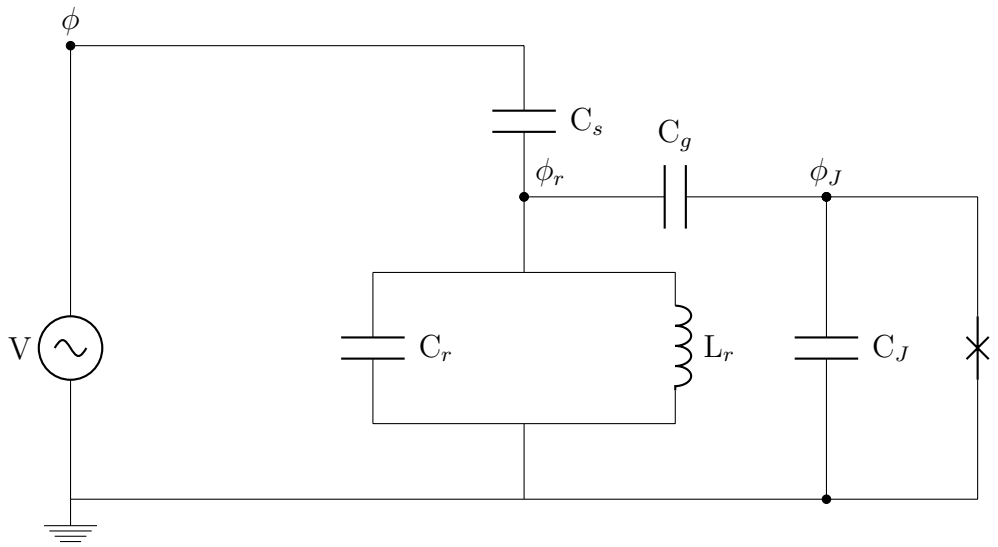

Figure 2.9: Transmon coupled to an LC resonator and drive voltage.

quadratic dependence in n_g. This quadratic variation of the energy eigenvalues with n_g makes it a favorable bias-point for the gate voltage. Hence the degeneracy point is also called the 'charge sweet-spot' for a Cooper-pair box.

2.4 Coupling a Josephson junction to a resonator - circuit quantum electrodynamics

2.4.1 Classical circuit Hamiltonian

We now have all the ingredients to couple a capacitively shunted Josephson junction to a resonator. The coupled circuit is shown in Fig. 2.9. The Lagrangian for

the circuit can be written as

$$\mathcal{L} = \frac{1}{2}C_v(\dot{\phi})^2 + \frac{1}{2}C_s(\dot{\phi} - \dot{\phi}_r)^2 + \frac{1}{2}C_g(\dot{\phi}_r - \dot{\phi}_J)^2 + \frac{1}{2}C_r(\dot{\phi}_r)^2 + \frac{1}{2}C_J(\dot{\phi}_J)^2 - \frac{1}{2L_r}(\phi_r)^2 + E_J\cos\left(2\pi\frac{\phi_J}{\Phi_0}\right) \tag{2.121}$$

where C_v is the large capacitance that accounts for the voltage source. I can define the node charges by

$$Q_v \equiv \frac{\partial\mathcal{L}}{\partial V} \tag{2.122}$$

$$Q_r \equiv \frac{\partial\mathcal{L}}{\partial V_r} \tag{2.123}$$

$$Q_J \equiv \frac{\partial\mathcal{L}}{\partial V_J}. \tag{2.124}$$

In terms of the node charges and fluxes, the Hamiltonian for the circuit takes the form

$$\mathcal{H} = \underbrace{\frac{Q_r^2}{2C_{res}} + \frac{\Phi_r^2}{2L_r}}_{\text{Resonator}} + \underbrace{\frac{Q_J^2}{2C_\Sigma} - E_J\cos\left(2\pi\frac{\phi_J}{\Phi_0}\right)}_{\text{Transmon}} + \underbrace{\beta_{rJ}Q_rQ_J}_{\text{coupling}} + \underbrace{\beta_rVQ_r + \beta_JVQ_J}_{\text{drive terms}} \tag{2.125}$$

where

$$C_{res} = C_r + C_s + \frac{C_JC_g}{C_J + C_g} \tag{2.126}$$

$$C_\Sigma = C_J + \frac{C_g(C_s + C_r)}{C_g + C_s + C_r} \tag{2.127}$$

$$\beta_r = \frac{C_s(C_b + C_g)}{C_b(C_g + C_r + C_s) + C_g(C_r + C_s)} \tag{2.128}$$

$$\beta_J = \frac{C_gC_s}{C_b(C_g + C_r + C_s) + C_g(C_r + C_s)} \tag{2.129}$$

$$\beta_{rJ} = \frac{C_g}{C_b(C_g + C_r + C_s) + C_g(C_r + C_s)}. \tag{2.130}$$

2.4.2 The general cQED Hamiltonian

The quantum version of the Hamiltonian in Eq. 2.125 is written as follows. Quantization of the resonator part of Eq. 2.125 gives Eq. 2.22. Quantizing the transmon part gives Eq. 2.111. For the coupling and drive terms in Eq. 2.125 I can replace the charge and flux variables with the quantum creation and annihilation operators using Eq. 2.24. For a sinusoidal drive voltage $V = V_0 \cos \omega t$ the cQED Hamiltonian can then be written as

$$\begin{aligned} H =& \hbar\omega_r \left(a^\dagger a + \frac{1}{2}\right) + \hbar\omega_J \left(b^\dagger b + \frac{1}{2}\right) - \frac{E_c}{12}\left(6\,(b^\dagger b)^2 + 6\,b^\dagger b + 3\right) \\ & - \hbar g(a - a^\dagger)(b - b^\dagger) - i\hbar\Omega_r(a - a^\dagger)\cos\omega t - i\hbar\Omega_J(b - b^\dagger)\cos\omega t \end{aligned} \tag{2.131}$$

where

$$\omega_r = \frac{1}{\sqrt{L_r C_{res}}} \tag{2.132}$$

$$E_c = \frac{e^2}{2C_\Sigma} \tag{2.133}$$

$$\hbar\omega_J = \sqrt{8E_J E_c} - E_c \tag{2.134}$$

$$g = \frac{e\beta_{rJ}}{\sqrt{\hbar Z_r}} \left(\frac{2E_J}{E_c}\right)^{1/4} \tag{2.135}$$

$$\Omega_J = \frac{e}{\hbar}\,\beta_J V_0 \left(\frac{8E_J}{E_c}\right)^{1/4} \tag{2.136}$$

$$\Omega_r = \frac{\beta_r V_0}{\sqrt{2\hbar Z_r}}. \tag{2.137}$$

I have also followed convention and used the symbol g to denote the transmon-resonator coupling.

By using the canonical transformation of the annihilation and creation operators, namely $a \rightarrow -ia$, $a^\dagger \rightarrow ia^\dagger$,$b \rightarrow -ib$, $b^\dagger \rightarrow ib^\dagger$, Eq. 2.131 can be written

as

$$H = \hbar\omega_r \left(a^\dagger a + \frac{1}{2}\right) + \hbar\omega_J \left(b^\dagger b + \frac{1}{2}\right) - \frac{E_c}{12}\left(6\,(b^\dagger b)^2 + 6\,b^\dagger b + 3\right)$$
$$+ \hbar g(a + a^\dagger)(b + b^\dagger) - \hbar\Omega_r(a + a^\dagger)\cos\omega t - \hbar\Omega_J(b + b^\dagger)\cos\omega t. \qquad (2.138)$$

The Hamiltonian given by Eq. 2.138 is analogous to that of an atom coupled to a cavity in cavity quantum electrodynamics [50, 68]. The resonator in this circuit plays the role of a cavity, and the Josephson junction coupled to it behaves as an artificial atom. The study of such circuits has therefore aptly been termed *circuit quantum electrodynamics*. The first two terms (containing Q_r and Φ_r) in Eq. 2.125 represent the familiar harmonic oscillator; the second two terms (containing Q_J and Φ_J) the Hamiltonian of a Josephson junction; the fifth term (containing $Q_r Q_J$) represents the coupling of the resonator with the Josephson junction; the last two terms represent the coupling of the drive voltage V to the resonator (term with $Q_r V$) and the Josephson junction (term with $Q_J V$) respectively. The Hamiltonian given by Eq. 2.138 is the generalized Rabi Hamiltonian for the driven cQED system and form the basis for the next chapter.

2.5 Conclusion

In this chapter, I derived the classical Hamiltonian for a dissipationless LC resonator circuit starting from the well known Kirchhoff's current and voltage equations. I then quantized the Hamiltonian using the canonical quantization procedure. I then applied this procedure to a Cooper-pair box and the transmon. I then put the pieces together and derived a general Hamiltonian for the transmon-resonator system.

Chapter 3

Circuit Quantum Electrodynamics

3.1 Overview

In this chapter I start with a brief discussion of the structure of the Rabi Hamiltonian that I derived in the Chapter 2. In the limit of a weak drive I derive the Jaynes-Cummings Hamiltonian by making a rotating wave approximation (RWA) [18, 51]. I then discuss the energy eigenstates of the Jaynes-Cummings system using a procedure for exact diagonalization and an approximate diagonalization in the 'dispersive' limit. From the time-dependent driven Jaynes-Cummings Hamiltonian in the dispersive limit, I derive a time-independent Hamiltonian by making a unitary transformation into a frame rotating with the drive fields. I then generalize the Jaynes-Cummings Hamiltonian to a multi-level system such as the transmon.

In the last section of this chapter, I briefly motivate the general method of coupling a system to a bath consisting of an infinite number of harmonic oscillators to model dissipation. I then present the system master equation (SME) for the density matrix of a harmonic oscillator that has dissipation. I next show that the steady state solutions of the driven, damped quantum harmonic oscillator are the well-known 'coherent states' [77] – eigenstates of the annihilation operator a. The coherent states are then shown to have a Poisson distribution of the photon number-states, in contrast to the exponential distribution found if the system is in thermal

equilibrium with a bath. I then make an analogy with the oscillator to write down the SME for a two-level system or qubit coupled to a dissipative environment, and finally obtain the SME for the coupled qubit-resonator dissipative system.

3.2 The Rabi Hamiltonian

In Chapter 2, starting from Kirchhoff's equations of motion for a circuit I derived an approximate low-energy quantum Hamiltonian for the coupled transmon-resonator system:

$$H = \hbar\omega_r \left(a^\dagger a + \frac{1}{2}\right) + \hbar\omega_J \left(b^\dagger b + \frac{1}{2}\right) - \frac{E_c}{12}\left(6\,(b^\dagger b)^2 + 6\,b^\dagger b + 3\right) \\ - \hbar\Omega_r(a + a^\dagger)\cos(\omega t) - \hbar\Omega_J(b + b^\dagger)\cos(\omega t) + \hbar g(a + a^\dagger)(b + b^\dagger). \qquad (3.1)$$

This Hamiltonian is referred to as the Rabi Hamiltonian [68]. The first term in Eq. 3.1 represents the resonator, the next two terms denote the transmon, the fourth term denotes the driving term for the resonator, the fifth term the driving term for the transmon, and the last term represents the coupling between the resonator and the transmon.

If we consider the first three terms to represent the unperturbed Hamiltonian H_0, the next three terms can be treated as a perturbation H'. In the eigenbasis of the 'number' states of the unperturbed Hamiltonian H_0, it can be seen that H' is purely off-diagonal. Below I make a further approximation to the Rabi Hamiltonian in Eq. 3.1 that is valid in the limit of 'weak driving', *i.e.* $\{\Omega_r, \Omega_J, g\} \ll \{\omega, \omega_r, \omega_J\}$.

3.2.1 The rotating wave approximation

For simplicity, consider first the driven resonator Hamiltonian.

$$H_r = \hbar\omega_r \left(a^\dagger a + \frac{1}{2}\right) - \hbar\Omega_r(a + a^\dagger)\cos(\omega t) \tag{3.2}$$

This Hamiltonian is written in the Schrodinger picture where the operators remain fixed in time, while the kets evolve in time. We can transform the Hamiltonian using a unitary transformation into the interaction or Dirac picture [67]. To do this, consider the unitary operator

$$U = e^{i\omega_r a^\dagger a\, t}. \tag{3.3}$$

Applying this transformation, the above Hamiltonian becomes [51]

$$H_{rI} = UHU^\dagger + i\hbar\dot{U}U^\dagger \tag{3.4}$$

$$= -\hbar\Omega_r \left(ae^{-i\omega_r t} + a^\dagger e^{i\omega_r t}\right)\cos(\omega t). \tag{3.5}$$

Expanding the cosine, we get

$$H_I = -\frac{\hbar\Omega_r}{2}\left(ae^{-i(\omega_r-\omega)t} + a^\dagger e^{i(\omega_r-\omega)t} + ae^{-i(\omega_r+\omega)t} + a^\dagger e^{i(\omega_r+\omega)t}\right). \tag{3.6}$$

When the drive frequency ω is on or near resonance with the resonator frequency ω_r, or $\omega \approx \omega_r$, the last two terms in the interaction Hamiltonian oscillate very rapidly compared to the first two terms. This results in the rapidly rotating terms averaging to zero over the relevant time-scales of evolution, and therefore they can be neglected. This approximation is called the *rotating wave approximation* (RWA) [18, 51]. The criterion for the validity of the RWA can also be stated as $\Omega_r \ll \{\omega, \omega_r\}$. After

applying the RWA, and transforming back into the Schrodinger picture, we find

$$H_r = \hbar\omega_r \left(a^\dagger a + \frac{1}{2}\right) - \frac{\hbar\Omega_r}{2}(ae^{i\omega t} + a^\dagger e^{-i\omega t}). \tag{3.7}$$

Reasoning on similar lines, the RWA can be applied to all three perturbation terms in Eq. 3.1 to give us

$$\begin{aligned} H = \hbar\omega_r \left(a^\dagger a + \frac{1}{2}\right) + \hbar\omega_J \left(b^\dagger b + \frac{1}{2}\right) - \frac{E_c}{12}\left(6\,(b^\dagger b)^2 + 6\,b^\dagger b + 3\right) \\ + \hbar g(ab^\dagger + a^\dagger b) - \frac{\hbar\Omega_c}{2}(ae^{i\omega_c t} + a^\dagger e^{-i\omega_c t}) - \frac{\hbar\Omega_p}{2}(be^{i\omega_p t} + b^\dagger e^{-i\omega_p t}) \end{aligned} \tag{3.8}$$

where a classical 'coupler' driving field of frequency ω_c and strength Ω_c drives the resonator and a classical 'probe' field of frequency ω_p and strength Ω_p drives the transmon. In my experiments, the resonator and transmon were far detuned and two separate drive tones were used to drive them. I use the nomenclature of probe and coupler fields here because Eq. 3.8 is useful for understanding the Autler-Townes effect which I shall discuss in the next section and Chapter 6.

If the anharmonicity of the transmon is sufficiently large, the Hilbert space can be truncated to include just the two lowest lying energy levels. In the two-level (qubit) approximation, the bosonic ladder operators $b, b^\dagger$ can be replaced by the Pauli spin matrices $\sigma_x, \sigma_y, \sigma_z$ and the Hamiltonian reduces to

$$\begin{aligned} H = \hbar\omega_r \left(a^\dagger a + \frac{1}{2}\right) + \frac{\hbar\omega_{ge}}{2}\sigma_z + \hbar g_{ge}(a\sigma^+ + a^\dagger\sigma^-) \\ - \frac{\hbar\Omega_c}{2}(ae^{i\omega_c t} + a^\dagger e^{-i\omega_c t}) - \frac{\hbar\Omega_p}{2}(\sigma^- e^{i\omega_p t} + \sigma^+ e^{-i\omega_p t}) \end{aligned} \tag{3.9}$$

where ω_{ge} is the ground to excited state transition frequency of the qubit, and g_{ge} is the coupling between the resonator and the qubit. The qubit raising and lowering

operators are defined as $\sigma^{\pm} = (\sigma_x \pm i\sigma_y)/2$ and satisfy $\sigma^+|g\rangle = |e\rangle$ and $\sigma^-|e\rangle = |g\rangle$. The Hamiltonian 3.9 that we call the driven *Jaynes-Cummings Hamiltonian* [50].

Thus, in the limit $\{\omega_r, \omega_{ge}, \omega_p, \omega_c\} \gg \{g, \Omega_c, \Omega_p\}$ when the RWA is valid, the Rabi Hamiltonian Eq. 3.1 becomes the driven Jaynes-Cummings Hamiltonian Eq. 3.9.

3.3 Jaynes-Cummings Hamiltonian

In this section I consider the undriven Jaynes-Cummings Hamiltonian

$$H_{JC} = \hbar\omega_r a^\dagger a + \frac{\hbar\omega_{ge}}{2}\sigma_z + \hbar g_{ge}(a\sigma^+ + a^\dagger\sigma^-). \tag{3.10}$$

This Hamiltonian was first discussed in detail by E. T. Jaynes and F. W. Cummings in the context of the dipole-coupling of an atomic transition to the electric field vector of the radiation field [50].

Let the energy eigenstates of the qubit be $|g\rangle$ and $|e\rangle$, and the energy eigenstates of the resonator be the number states $|n\rangle$. The product states denoted by $|g, n\rangle$ and $|e, n\rangle$ form a natural choice for the basis of the coupled system (see Fig. 3.1). In this basis, the coupling term is purely off-diagonal. An important feature of the Jaynes-Cummings coupling term is that it preserves the total number of excitations. From the matrix elements for the coupling term

$$\langle g, m|(a\sigma^+ + a^\dagger\sigma^-)|e, n\rangle = \sqrt{n+1}\,\delta_{m,n+1} \tag{3.11}$$

$$\langle e, n|(a\sigma^+ + a^\dagger\sigma^-)|g, m\rangle = \sqrt{m+1}\,\delta_{n,m+1}. \tag{3.12}$$

it can be seen that the coupling term mixes states with the same total number of

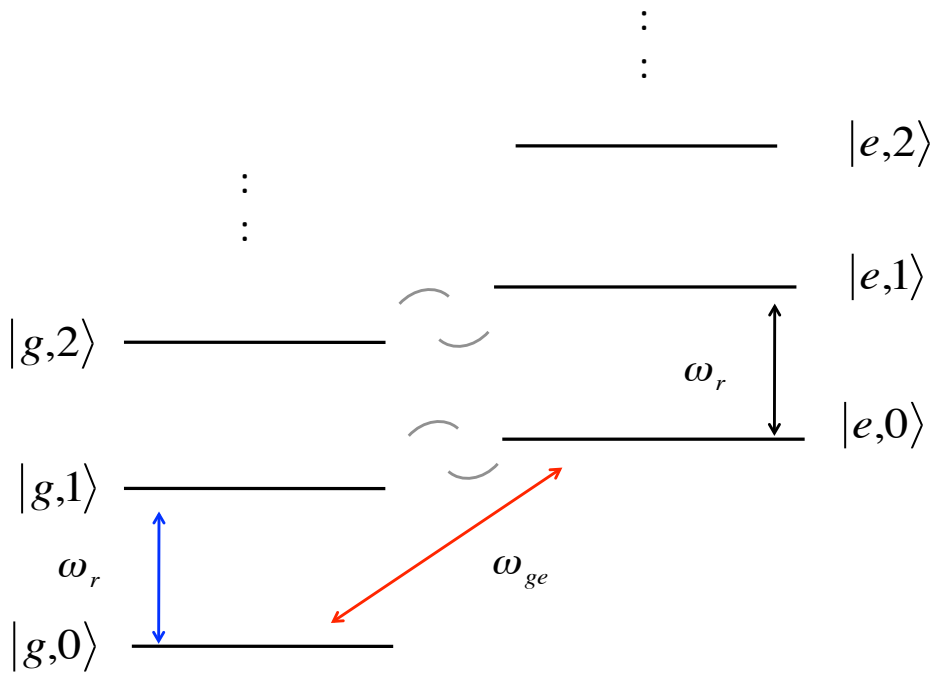

Figure 3.1: Energy levels of the bare states of the Jaynes-Cummings system

excitations. In contrast, the Rabi Hamiltonian we began with in Eq. 3.1 also allows addition or removal of two quanta due to the presence of the $a^\dagger b^\dagger$ and ab terms. The presence of these terms in the weak driving case leads to small Bloch-Siegert shifts [78, 43] in the energy levels.

It is useful to define an operator $\mathcal{N}$ for the total number of excitations as

$$\mathcal{N} = a^\dagger a + \frac{\sigma_z}{2} + \frac{1}{2} \tag{3.13}$$

where the additional 1/2 in the definition was chosen to make the number of excita-

tions zero for the ground state of the system, *i.e.*

$$\mathcal{N}|g,0\rangle = 0. \tag{3.14}$$

3.3.1 Dressed states and exact diagonalization

Due to the structure of the Jaynes-Cummings coupling term, the Hamiltonian has a block-diagonal form in the number basis with 2×2 blocks along the diagonal. The $\{|e,n-1\rangle, |g,n\rangle\}$ states span the n-excitation manifold for $n \geq 1$ and the Hamiltonian for this manifold is

$$\hbar \begin{bmatrix} (n-1)\omega_r + \omega_{ge}/2 & g_{ge}\sqrt{n} \\ g_{ge}\sqrt{n} & n\omega_r - \omega_{ge}/2 \end{bmatrix}. \tag{3.15}$$

The eigenvalues of this matrix are given by

$$E_{n,\pm} = (n - \frac{1}{2})\hbar\omega_r \pm \frac{\hbar}{2}\sqrt{\Delta^2 + 4g_{ge}^2 n} \tag{3.16}$$

where Δ is the *detuning* between the qubit and resonator frequencies

$$\Delta \equiv \omega_{ge} - \omega_r. \tag{3.17}$$

The corresponding eigenvectors are given by

$$|n,+\rangle = \cos(\theta_n)|e,n-1\rangle + \sin(\theta_n)|g,n\rangle \tag{3.18}$$

$$|n,-\rangle = -\sin(\theta_n)|e,n-1\rangle + \cos(\theta_n)|g,n\rangle \tag{3.19}$$

where the θ_n are defined by

$$\tan(2\theta_n) = \frac{2g_{ge}\sqrt{n}}{\Delta}. \tag{3.20}$$

The ground state is $|g,0\rangle$ with energy

$$E_0 = -\frac{\hbar\omega_{ge}}{2} \tag{3.21}$$

Note that the n in Eq. 3.15 – 3.20 represents the total number of excitations shared between the resonator and the qubit. It can also be shown that the Jaynes-Cummings Hamiltonian can be diagonalized [79] using the unitary transformation given by

$$\mathcal{T} = e^{\theta_n \mathcal{N}^{-1/2}(a\sigma^+ - a^\dagger\sigma^-)} \tag{3.22}$$

where again

$$\tan(2\theta_n) \equiv \frac{2g_{ge}\sqrt{\mathcal{N}}}{\Delta} \tag{3.23}$$

$$\mathcal{N} = a^\dagger a + \frac{\sigma_z}{2} + \frac{1}{2}. \tag{3.24}$$

The states $|n,\pm\rangle$ are called the *dressed states* of the Jaynes-Cummings system. The uncoupled qubit and resonator 'bare states' are 'dressed' due to the coupling. As we turn the coupling off, *i.e.* $g \approx 0$ and $\theta_n \approx 0$, the dressed states given by Eq. 3.19 become the bare states

$$|n,+\rangle \approx |e,n-1\rangle \tag{3.25}$$

$$|n,-\rangle \approx |g,n\rangle. \tag{3.26}$$

3.3.2 The dispersive limit and photon number-splitting

To gain more insight into the relevant parameter space of the Jaynes-Cummings Hamiltonian, it is helpful to define the critical number of photons

$$n_{crit} \equiv \frac{\Delta^2}{4g_{ge}^2}. \tag{3.27}$$

In terms of n_{crit}, we can write the energy eigenvalues as

$$E_{n,\pm} = \left(n - \frac{1}{2}\right)\hbar\omega_r \pm \frac{\hbar\Delta}{2}\left(1 + \frac{n}{n_{crit}}\right)^{1/2}. \tag{3.28}$$

and the mixing angle as

$$\tan 2\theta_n = \sqrt{\frac{n}{n_{crit}}}. \tag{3.29}$$

From these expressions, we see that the ratio n/n_{crit} is an important parameter in determining the eigenvalues and eigenvectors of the Hamiltonian.

The limit $n \ll n_{crit}$ is called the *dispersive limit*. From Eq. 3.27, we can see that this limit is more easily satisfied when $\Delta \gg g_{ge}$. In this limit, we can do a perturbation expansion of the expressions up to first order in the small parameter n/n_{crit} or equivalently up to second order in g_{ge}/Δ to get

$$E_{n,\pm} \approx \left(n - \frac{1}{2}\right)\hbar\omega_r \pm \frac{\hbar\Delta}{2}\left(1 + \frac{2g_{ge}^2 n}{\Delta^2}\right) \tag{3.30}$$

$$|n,+\rangle \approx |e,n-1\rangle + \frac{g_{ge}\sqrt{n}}{\Delta}|g,n\rangle \tag{3.31}$$

$$|n,-\rangle \approx -\frac{g_{ge}\sqrt{n}}{\Delta}|e,n-1\rangle + |g,n\rangle \tag{3.32}$$

Along the same lines, we can write the unitary transformation $\mathcal{T}$ as

$$\mathcal{T} \approx \exp\left\{\frac{g_{ge}}{\Delta}\left(a\sigma^+ - a^\dagger\sigma^-\right)\right\} \tag{3.33}$$

Applying this transformation to the Hamiltonian Eq. 3.10 and keeping terms up to second order in g_{ge}/Δ we get

$$\mathcal{T}H_{JC}\mathcal{T}^\dagger \approx \tilde{H}_{JC}^{(2)} = \hbar\omega_r a^\dagger a + \frac{\hbar\tilde{\omega}_{ge}}{2}\sigma_z + \hbar\chi(a^\dagger a)\sigma_z \tag{3.34}$$

where $\chi = g_{ge}^2/\Delta$ is called the 'dispersive shift' of the resonator frequency and $\tilde{\omega}_{ge} = \omega_{ge} + \chi$ is the Lamb-shifted qubit frequency. The mathematical details of this transformation are worked out in Appendix B.

The last term in the Hamiltonian given by Eq. 3.34 produces a shift in the resonator frequency that depends on the qubit state. When the qubit is in the excited state, the resonator has a frequency of $\omega_r + \chi$ and when the qubit is in the ground state, the resonator has a frequency of $\omega_r - \chi$. This can be seen by rearranging Eq. 3.34 to get

$$\tilde{H}_{JC}^{(2)} = \hbar(\omega_r + \chi\sigma_z)a^\dagger a + \frac{\hbar\tilde{\omega}_{ge}}{2} \tag{3.35}$$

This can also be seen from using Eq. 3.30 to write

$$E_{n,+} - E_{n-1,+} = \hbar(\omega_r + \chi) \tag{3.36}$$

$$E_{n,-} - E_{n-1,-} = \hbar(\omega_r - \chi) \tag{3.37}$$

From this we can deduce that in the dispersive limit, the coupled qubit-resonator system has two 'ladders' of resonator-like states (see Fig. 3.2). One ladder has a frequency spacing of $\omega_r - \chi$, corresponding to when the qubit is in the $|g\rangle$ state, and the other ladder has a frequency spacing of $\omega_r + \chi$, corresponding to when the qubit is in the $|e\rangle$ state.

The last term in Eq. 3.34 can also be thought of as an ac Stark shift of the qubit frequency due to the photons in the resonator. For every photon populating the resonator, the qubit frequency shifts by 2χ. The Hamiltonian given by Eq. 3.34 can again be rearranged to show this feature:

$$\tilde{H}_{JC}^{(2)} = \hbar\omega_r a^\dagger a + \frac{\hbar(\tilde{\omega}_{ge} + 2\chi a^\dagger a)}{2} \tag{3.38}$$

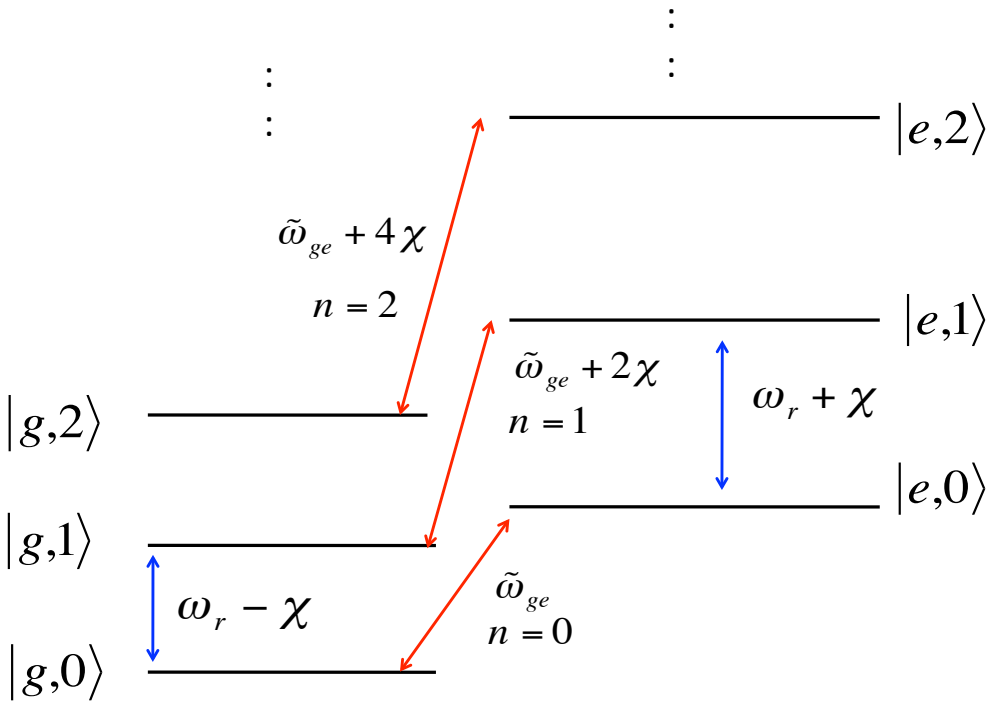

Figure 3.2: The Jaynes-Cummings ladder in the dispersive approximation

This can also be seen from Eq. 3.30 by writing

$$E_{n+1,+} - E_{n,-} = \hbar(\tilde{\omega}_{ge} + 2n\chi). \tag{3.39}$$

One implication of Eq. 3.39 is that in the limit $\chi \gg \{\Gamma, \kappa\}$ where Γ is the linewidth of the qubit transition and κ is the linewidth of the resonator, adding a single photon to the resonator shift the qubit frequency by more than a linewidth. In this limit if the resonator is in a superposition of photon number-states $|n\rangle$, the qubit spectrum shows a peak corresponding to each photon number-state in the superposition. This phenomenon is called *photon number-splitting* [44, 45]. The relative heights of the qubit peaks in the number-split spectrum will be proportional to the probability w_n of the corresponding photon number-state in the superposition. This effect can be used to perform quantum non-demolition measurements of the average number $\bar{n}$ of photons in the resonator where

$$\bar{n} = \frac{\sum_n w_n n}{\sum_n w_n}. \tag{3.40}$$

In section 3.6.3 I also show that when the resonator is driven coherently from the ground state [77], the probabilities $w(n)$ approach a Poisson distribution $w_n^{coh} = e^{-\bar{n}}(\bar{n})^n/n!$. On the other hand, for a finite temperature in the absence of coherent driving, w_n is just the usual thermal distribution [80, 44] $w_n^{th} = \bar{n}^n/(\bar{n}+1)^{n+1}$ (See Appendix C).

3.3.3 Dispersive transformation of the driven Jaynes-Cummings Hamiltonian

In this section, I consider the full Jaynes-Cummings Hamiltonian including the driving terms:

$$H = H_{JC} + H_d \tag{3.41}$$

$$= \hbar\omega_r \left(a^\dagger a + \frac{1}{2}\right) + \frac{\hbar\omega_{ge}}{2}\sigma_z + \hbar g_{ge}(a\sigma^+ + a^\dagger\sigma^-) - \frac{\hbar\Omega_r}{2}(ae^{i\omega_c t} + a^\dagger e^{-i\omega_c t}) - \frac{\hbar\Omega_p}{2}(\sigma^- e^{i\omega_p t} + \sigma^+ e^{-i\omega_p t}). \tag{3.42}$$

To this Hamiltonian, I apply the dispersive transformation given by

$$\mathcal{T} = e^{\Lambda} = e^{\lambda(a\sigma^+ - a^\dagger\sigma^-)} \tag{3.43}$$

where $\lambda = g_{ge}/\Delta$. To second order in λ, the transformed Hamiltonian becomes (see Appendix B, Eq. B.31)

$$\mathcal{T}H\mathcal{T}^\dagger \approx \tilde{H}^{(2)} \tag{3.44}$$

$$= \tilde{H}^{(2)}_{JC} + H_d \tag{3.45}$$

$$= \hbar\omega_r + \frac{\hbar\tilde{\omega}_{ge}}{2} + \hbar\chi(a^\dagger a)\sigma_z - \frac{\hbar\Omega_r}{2}(ae^{i\omega_c t} + a^\dagger e^{-i\omega_c t}) - \frac{\hbar\Omega_p}{2}(\sigma^- e^{i\omega_p t} + \sigma^+ e^{-i\omega_p t}). \tag{3.46}$$

3.3.3.1 In the rotating frame of the drives

The Hamiltonian given by Eq. 3.46 is time-dependent. To study the system in the steady-state, removing the explicit time-dependence of the Hamiltonian is very convenient. We can remove the explicit time-dependence in Eq. 3.46 by transforming

into a frame rotating with the drives, using a unitary transformation [18, 51] given by

$$U = e^{i\omega_c(a^\dagger a)t + i\frac{\omega_p\sigma_z}{2}t}. \tag{3.47}$$

The transformed time-independent Hamiltonian is given by

$$H_I = UHU^\dagger + i\hbar\dot{U}U^\dagger \tag{3.48}$$

$$= \hbar\tilde{\Delta}_c a^\dagger a + \frac{\hbar\tilde{\Delta}_p}{2} + \hbar\chi(a^\dagger a)\sigma_z - \frac{\hbar\Omega_c}{2}(a + a^\dagger) - \frac{\hbar\Omega_p}{2}(\sigma^- + \sigma^+) \tag{3.49}$$

where $\tilde{\Delta}_c \equiv \omega_r - \omega_c$ is the detuning of the coupler tone from the resonator frequency and $\tilde{\Delta}_p \equiv \tilde{\omega}_{ge} - \omega_p$ is the detuning of the probe tone from the qubit frequency. Clearly the Hamiltonian given by Eq. 3.49 is independent of time.

3.4 Generalized Jaynes-Cummings Hamiltonian

So far we have studied the Jaynes-Cummings Hamiltonian in the qubit approximation, *i.e.* an ideal two-level system coupled to an ideal harmonic oscillator. In contrast, the system I studied experimentally in this thesis comprised a transmon [30], which can be thought of as a multi-level artificial 'atom', coupled to a single harmonic mode of a superconducting resonator. The coupled transmon-resonator system can be modelled to a good approximation [68] by a Jaynes-Cummings Hamiltonian [50] generalized to a multi-level atom [45, 52]

$$H_{JC} = \hbar\omega_r(a^\dagger a) + \hbar\sum_{j=\{g,e,f...\}}\omega_j|j\rangle\langle j| + \hbar\sum_{j=\{g,e,f...\}} g_{j,j+1}(a^\dagger|j\rangle\langle j+1| + a|j+1\rangle\langle j|)\ . \tag{3.50}$$

Here ω_r is the bare resonator frequency, $a^\dagger\,(a)$ is the creation (annihilation) operator for the resonator mode, the transmon states $|j\rangle$ are labelled $\{g, e, f, ...\}$, and $g_{j,j+1}$

is the coupling strength of the $|j\rangle \leftrightarrow |j+1\rangle$ transition of the transmon with the resonator mode, assuming only coupling to quasi-resonance transitions.

This Hamiltonian can be approximately diagonalized in the dispersive limit [18, 79], $\Delta_{j,j+1} \equiv \omega_{j,j+1} - \omega_r \gg g_{j,j+1}$, where $\omega_{j,j+1} \equiv \omega_{j+1} - \omega_j$ is the frequency of the $|j\rangle \leftrightarrow |j+1\rangle$ transmon transition. To diagonalize the Hamiltonian, I use a unitary transformation similar to that used in the qubit case

$$U = \exp\left(\sum_{j=\{g,e,f\ldots\}} \lambda_{j,j+1}\left\{a|j+1\rangle\langle j| - a^\dagger|j\rangle\langle j+1|\right\}\right) \tag{3.51}$$

where $\lambda_{j,j+1} \equiv g_{j,j+1}/\Delta_{j,j+1}$. When the parameters $\lambda_{j,j+1} \equiv g_{j,j+1}/\Delta_{j,j+1} \ll 1$ we can then write the diagonal Hamiltonian $\tilde{H}_{JC} = UHU^\dagger$ as a perturbation expansion in $\lambda_{j,j+1}$. Further, when the transmon has sufficiently large anharmonicity ($\sim E_c$) compared to the strength of the driving field $\hbar\Omega_p$, I can truncate the transmon Hilbert space to a two level system with ground-state $|g\rangle$ and first-excited state $|e\rangle$. To account for the finite anharmonicity of the transmon I can also include perturbation shifts to the energy levels of the system due to the second-excited transmon state $|f\rangle$ [51]. The dispersively diagonalized Hamiltonian up to second order in $\lambda_{j,j+1}$ [18, 51] then becomes

$$\widetilde{H}^{(2)}_{JC} \approx \hbar\widetilde{\omega}_r(a^\dagger a) + \frac{\hbar\widetilde{\omega}_{ge}}{2}\sigma_z + \hbar\chi(a^\dagger a)\sigma_z\,, \tag{3.52}$$

where $\chi \simeq \chi_{ge} - \chi_{ef}/2$ is the effective dispersive shift of the resonator due to the transmon levels, $\chi_{j,j+1} \equiv g^2_{j,j+1}/\Delta_{j,j+1}$ are the partial couplings, $\widetilde{\omega}_r \simeq \omega_r - \chi_{ef}/2$ is the dressed resonator frequency, $\widetilde{\omega}_{ge} \simeq \omega_{ge} + \chi_{ge}$ is the dressed qubit transition frequency, and σ_z is the z-Pauli spin operator for the qubit. Comparing Eq. 3.34 with Eq. 3.52, I note that the higher transmon levels induce a Lamb-shift in the

resonator frequency, which was absent in the case of a pure two-level system.

I showed earlier, for the pure two level system case, that the n-excitation manifold of the Jaynes-Cummings Hamiltonian was spanned by the two states $\{|g,n\rangle, |e,n-1\rangle\}$. Diagonalizing the 2×2 block gave two different resonator frequencies for the qubit in the ground and excited states respectively. Similarly, in the generalized Jaynes-Cummings Hamiltonian coupling a resonator to an m-level system, the n-excitation manifold is spanned by the m states $\{|0,n\rangle, |1,n-1\rangle, \ldots, |m-1,n-m+1\rangle\}$. Diagonalizing the $m \times m$ block matrix gives m different eigenvalues, and thereby m different state-dependent frequencies for the resonator.

To include the coupler and probe drive tones I use the same method as in the qubit case. Since I am making a qubit approximation, the driving terms are unchanged from Eq. 3.49. Neglecting corrections to the driving terms to second order in λ, I can write the driven Jaynes-Cummings Hamiltonian in the rotating frame of the drives as

$$H_{tot} \approx \hbar\widetilde{\Delta}_c(a^\dagger a) + \frac{\hbar\widetilde{\Delta}_p}{2}\sigma_z + \hbar\chi(a^\dagger a)\sigma_z + \frac{\hbar\Omega_c}{2}(a+a^\dagger) + \frac{\hbar\Omega_p}{2}(\sigma^+ + \sigma^-) \qquad (3.53)$$

where $\widetilde{\Delta}_c = \widetilde{\omega}_r - \omega_c$ and $\widetilde{\Delta}_p = \widetilde{\omega}_{ge} - \omega_p$ are the detunings of the dressed resonator and spectroscopy tones.

3.5 System Master Equation - Overview

3.5.1 Basic principle of modelling dissipation in quantum systems

Until now I have considered systems that do not have any losses. Real quantum systems are affected by dephasing and dissipation. In classical mechanics, dissipation can sometimes be modelled in the equation of motion by including a term that is proportional to the velocity. A well known example of such a system is a driven mass and spring system experiencing an idealized drag force. The corresponding classical equation of motion for a particle of mass m attached to a spring with a spring constant $k = m\omega_0^2$, and acted upon by drag and a time-dependent force $F(t)$ is given by

$$m\ddot{x} + m\kappa\dot{x} + m\omega_0^2 x = F(t). \tag{3.54}$$

where κ is a linear dissipation coefficient. Since Eq. 3.54 is a linear differential equation that has an exact solution for a sinusoidal forcing term, we can solve it, in principle, for an arbitrary force. This equation is examined in greater detail in Appendix C.

The Schrodinger-Heisenberg-Dirac formulation of quantum mechanics uses a correspondence with the Hamiltonian approach to classical mechanics, but this formulation is not well-suited for studying dissipative systems. To overcome this difficulty, we assume the *system* is coupled to an environment or 'bath' that is modelled as an infinite collection of harmonic oscillators. The choice of harmonic oscillators for the microscopic degrees of freedom of the bath is done for reasons of convenience. In the final theory, the details of the microscopic interactions should not play any role in the

dissipation. In this model [6], information from the system is absorbed by the degrees of freedom of the bath. When the number of bath degrees of freedom is infinite, the time-scale for returning information from the bath to the system becomes arbitrarily long, consistent with dissipation and a loss of information from the system.

3.5.2 A brief review of the density operator formalism

An alternative to the usual wave function formalism of quantum mechanics involves the use of density operator ρ, as formulated originally by John von Neumann [68]. The density operator formalism is suitable for describing the dynamics of pure quantum states, which are coherent superpositions of the basis wave functions, as well as statistical mixtures of several pure states. The latter cannot be described using a wave function formalism but form the starting point for the density matrix formalism.

For convenience, consider the density operator in the diagonal representation:

$$\rho = \sum_i w_i |\psi_i\rangle\langle\psi_i| \tag{3.55}$$

where w_i is the probability for the system to be in the state $|\psi_i\rangle$. Since the w_i are probabilistic weights, they have to be non-negative, and their sum must be unity. In general, ρ has the following properties

$$\rho^\dagger = \rho \tag{3.56}$$

$$0 \leq w_i \leq 1 \tag{3.57}$$

$$\mathrm{Tr}(\rho) = \sum_i w_i = 1 \tag{3.58}$$

For a system in a well-defined quantum state $|\psi\rangle$ or a 'pure' state, the density operator reduces to

$$\rho_{pure} = |\psi\rangle\langle\psi| \tag{3.59}$$

Note that the kets $|\psi_i\rangle$ are taken to be in the Schrodinger picture, and from the Schrodinger equation of motion for the kets, an equation of motion for the density operator can be obtained:

$$i\hbar\frac{\partial\rho}{\partial t} = [H, \rho]. \tag{3.60}$$

In terms of the density operator ρ, mean value of a given observable A can be conveniently written as

$$\langle A\rangle = \mathrm{Tr}(\rho A). \tag{3.61}$$

Since the trace of an operator is invariant under unitary transformations, the average values are unaffected by what basis the operators are expressed in.

3.5.3 Master equation in the Born-Markovian approximation

I now follow and approach taken in [51] to write the master equation for an ideal system coupled to a bath of harmonic oscillators. Let $H = H_0 + H_d$ be the Hamiltonian of the isolated system where H_0 is the Hamiltonian for the undriven system with no coupling to the bath, and H_d is the Hamiltonian for the driving terms. Let H_E be the Hamiltonian of the environment or bath degrees of freedom and ϵV denote a weak coupling Hamiltonian between the system and the environment. I can now write

$$H_{tot} = H_0 + H_d + H_E + \epsilon V \tag{3.62}$$

with

$$H_E = \sum_k \hbar\omega_k b_k^\dagger b_k \tag{3.63}$$

$$\epsilon V = \hbar\left(\sum_k \left\{\epsilon_k S^\dagger b_k + \epsilon_k S b_k^\dagger\right\}\right) \tag{3.64}$$

and where $b_k, b_k^\dagger$ are the bosonic operators for an environmental mode k with frequency ω_k, ϵ_k is the coupling strength between the mode k and the system operator S which I assume is coupled to the bath through a single degree of freedom.

The master equation for the system density operator can be derived under the following assumptions :

1. I assume the coupling between the system and the environment is weak enough that the total density operator ρ_T of the 'universe' factorizes into a direct product of the density operator of the system ρ and that of the environment ρ_E at all times. Then

$$\rho_T = \rho \otimes \rho_E. \tag{3.65}$$

The density operator of the system is obtained by doing a *partial trace* over the environment degrees of freedom.

$$\rho(t) = \mathrm{Tr}_E(\rho_T(t)) \tag{3.66}$$

2. The coupling constants ϵ_k are sufficiently small that the coupling Hamiltonian ϵV can be treated using second order perturbation theory. This is called the *Born approximation* [51].

3. The bath operators b_k and $b_k^\dagger$ are treated in the *Markovian approximation*, which says that the correlation functions $\langle b_k b_l^\dagger \rangle$ decay on a time-scale that is much shorter than the time-scale of evolution of the density operator. In other words, the bath is assumed to be 'memory-less' on relevant time-scales. This enables us to write a linear equation for the evolution of the density operator ρ [51].

$$\dot{\rho} = L\rho. \tag{3.67}$$

4. In particular, for a thermal bath at temperature T the linear operator L can be written in the general form [68]

$$L\rho = -\frac{i}{\hbar}\left[H, \rho\right] + \sum_{\omega>0} \left(\kappa_i \mathcal{D}[A_i]\rho + e^{-\beta\hbar\omega} \kappa_i \mathcal{D}[A_i^\dagger]\rho \right) \tag{3.68}$$

where

$$\mathcal{D}[A_i]\rho \equiv A_i \rho A_i^\dagger - \frac{1}{2}\left(A_i^\dagger A_i \rho + \rho A_i^\dagger A_i \right) \tag{3.69}$$

and the operator A_i is chosen to be a lowering operator to be consistent with the choice of the Boltzmann factor in the above equation and $\beta = 1/k_B T$.

3.6 Master Equation for cQED systems

3.6.1 Dissipation in the resonator

With the above assumptions, for a damped driven harmonic oscillator (the resonator) interacting with a thermal bath at temperature T, the System Master

Equation 3.68 or SME can be written in the Schrodinger picture as [18, 68]

$$\dot{\rho} = -i\omega_0[a^\dagger a, \rho] + \frac{i\Omega_c}{2}[ae^{i\omega_c t} + a^\dagger e^{-i\omega_c t}, \rho] + \kappa_- \mathcal{D}[a]\rho + \kappa_+ \mathcal{D}[a^\dagger]\rho \tag{3.70}$$

where κ_- is the rate of loss of photons from the system resonator, and κ_+ is the rate of creation of photons due to thermal excitations in the system resonator. From the principle of detailed balance [81, 82], $\kappa_+/\kappa_- = e^{-\beta\hbar\omega_0}$. At zero temperature, $\kappa_+ = 0$ indicating the fact that the thermal bath cannot deliver energy to the system at $T = 0\,\mathrm{K}$.

For simplicity, I consider the $T = 0\,\mathrm{K}$ case henceforth. In this case Eq. 3.70 reduces to

$$\dot{\rho} = -i\omega_0[a^\dagger a, \rho] + \frac{i\Omega_c}{2}[ae^{i\omega_c t} + a^\dagger e^{-i\omega_c t}, \rho] + \kappa_- \mathcal{D}[a]\rho \tag{3.71}$$

From the master equation I obtain:

$$\frac{\mathrm{d}\langle a\rangle}{\mathrm{d}t} = \frac{\mathrm{dTr}(\rho a)}{\mathrm{d}t} \tag{3.72}$$

$$= \mathrm{Tr}(\dot{\rho} a) \tag{3.73}$$

$$= -i\omega_0\langle a\rangle - \frac{\kappa_-}{2}\langle a\rangle + \frac{i\Omega_c}{2}e^{-i\omega_c t} \tag{3.74}$$

This equation is identical to what one obtains from classical physics (see Appendix C). This is to be expected from Ehrenfest's theorem for mean values of quantum operators.

One can also derive a similar equation for the mean number of photons in the resonator

$$\frac{\mathrm{d}\langle a^\dagger a\rangle}{\mathrm{d}t} = -\kappa_-\langle a^\dagger a\rangle + \frac{i\Omega_c}{2}\left(\langle a^\dagger\rangle e^{-i\omega_c t} - \langle a\rangle e^{i\omega_c t}\right) \tag{3.75}$$

confirming that the rate of loss of photons is indeed κ_-. From this equation it is also clear that in the absence of driving ($\Omega_c = 0$), the initial number of photons populating the resonator decays exponentially to zero, and in the undriven steady state the resonator is in its ground state (no photons stored in it).

3.6.2 Coherent states of the harmonic oscillator

Before I discuss the steady state solution of the driven oscillator, a brief summary of the coherent states [77] of the harmonic oscillator is in order. A more detailed discussion is given in Appendix C.

Glauber [77] defined a coherent state $|\alpha\rangle$ as an eigenstate of the annihilation operator a, *i.e.*

$$a|\alpha\rangle = \alpha|\alpha\rangle \tag{3.76}$$

where α is the eigenvalue. Since a is a non-hermitian operator, α is in general a complex number. From the matrix elements of the operators a and $a^\dagger$ in the number basis, we can write the coherent state as [77]

$$|\alpha\rangle = e^{-|\alpha|^2/2} \sum_{n=0}^{\infty} \frac{\alpha^n}{\sqrt{n!}} |n\rangle. \tag{3.77}$$

The probability of having n photons in the resonator is given by the square of the magnitude of the coefficient of the ket $|n\rangle$ in the above expansion. This probability, denoted by w_n^{coh} is given by

$$w_n^{coh} = \frac{e^{-|\alpha|^2}|\alpha|^{2n}}{n!}. \tag{3.78}$$

We can also compute the average number of photons in a coherent state is:

$$\bar{n} = \langle\alpha|a^\dagger a|\alpha\rangle = |\alpha|^2. \tag{3.79}$$

In terms of $\bar{n}$ we have

$$w_n^{coh} = \frac{e^{-\bar{n}}\bar{n}^n}{n!}. \tag{3.80}$$

Thus the coherent state $|\alpha\rangle$ has a Poisson distribution of the number states.

Coherent states can be generated by a unitary transformation of the vacuum state $|0\rangle$. The unitary operator that achieves this is called the Glauber displacement operator [77, 51]:

$$D(\alpha) = e^{\alpha a^\dagger - \alpha^* a}. \tag{3.81}$$

Using the Baker-Campbell-Hausdorff formula [83], one can show that

$$D(\alpha) = e^{|\alpha|^2/2} e^{-\alpha^* a} e^{\alpha a^\dagger}. \tag{3.82}$$

Using this, one can then write

$$|\alpha\rangle = D(\alpha)|0\rangle = e^{-|\alpha|^2/2} \sum_{n=0}^{\infty} \frac{\alpha^n}{\sqrt{n!}} |n\rangle. \tag{3.83}$$

$D(\alpha)$ is called the 'displacement' operator because of the transformation properties of the bosonic operators $a, a^\dagger$ under $D(\alpha)$

$$D^\dagger(\alpha) a D(\alpha) = a + \alpha \tag{3.84}$$

$$D^\dagger(\alpha) a^\dagger D(\alpha) = a^\dagger + \alpha^*. \tag{3.85}$$

3.6.3 Coherent states as steady state solutions of the harmonically driven resonator

In this section I show that the coherent states discussed above are the steady state solutions of the master equation for the driven resonator. The simplest way to do this is by using the Glauber displacement operator. I begin by transforming the driven Hamiltonian using the unitary transformation $D^\dagger(\alpha)$ in Eq. 3.82:

$$\tilde{H} = D^\dagger(\alpha)HD(\alpha) + i\hbar\frac{\partial D^\dagger(\alpha)}{\partial t}D(\alpha) \tag{3.86}$$

$$= \hbar\omega_0(a^\dagger+\alpha^*)(a+\alpha) - \hbar\frac{\Omega_c}{2}[(a^\dagger+\alpha^*)e^{-i\omega_c t} + (a+\alpha)e^{i\omega_c t}] + i\hbar[(-\frac{\alpha^*}{2} - a^\dagger)\dot{\alpha} + (\frac{\alpha}{2}+a)\dot{\alpha}^*] \tag{3.87}$$

$$= \hbar\omega_0 a^\dagger a + \hbar a^\dagger[\omega_0\alpha - \frac{\Omega_c}{2}e^{-i\omega_c t} - i\dot{\alpha}] + \hbar a[\omega_0\alpha^* - \frac{\Omega_c}{2}e^{i\omega_c t} + i\dot{\alpha}^*]. \tag{3.88}$$

The transformed density matrix obeys [51]

$$\dot{\rho} = -\frac{i}{\hbar}[\tilde{H},\rho] + \kappa_-\mathcal{D}[a+\alpha]\rho \tag{3.89}$$

$$= -\frac{i}{\hbar}[\tilde{H},\rho] + \kappa_-\mathcal{D}[a]\rho + \frac{\kappa_-}{2}(\alpha^*[a,\rho] - \alpha[a^\dagger,\rho]). \tag{3.90}$$

Expanding $\tilde{H}$, we have

$$\dot{\rho} = -i\omega_0[a^\dagger a,\rho] + \kappa_-\mathcal{D}[a]\rho - i[a^\dagger,\rho]\left(\omega_0\alpha - \frac{\Omega_c}{2}e^{-i\omega_c t} - i\dot{\alpha} - i\frac{\kappa_-}{2}\alpha\right) - i[a,\rho]\left(\omega_0\alpha^* - \frac{\Omega_c}{2}e^{i\omega_c t} + i\dot{\alpha}^* + i\frac{\kappa_-}{2}\alpha^*\right) \tag{3.91}$$

where $\mathcal{D}$ is defined in Eq. 3.69.

To proceed, I note that we are free to choose α such that the terms in the

parentheses in Eq. 3.91 are zero, that is:

$$\omega_0\alpha - \frac{\Omega_c}{2}e^{-i\omega_c t} - i\dot{\alpha} - i\frac{\kappa_-}{2}\alpha = 0 \tag{3.92}$$

$$\omega_0\alpha^* - \frac{\Omega_c}{2}e^{i\omega_c t} + i\dot{\alpha}^* + i\frac{\kappa_-}{2}\alpha^* = 0. \tag{3.93}$$

Equations 3.92 and 3.93 are the same as Eq. C.13, the equations of motion of a classical oscillator. With this choice of α, the master equation for the density matrix becomes simply

$$\dot{\rho} = -i\omega_0[a^\dagger a, \rho] + \kappa_-\mathcal{D}[a]\rho \tag{3.94}$$

which is nothing but the master equation for an undriven oscillator.

We know that the steady state solution for the undriven oscillator is the ground state or vacuum state $|0\rangle$. However to arrive at Eq. 3.94 we began by transforming the Hamiltonian H using the displacement operator $D^\dagger(\alpha)$. If the untransformed steady state solution is $|\psi_{ss}\rangle$, then we can write

$$D^\dagger(\alpha)|\psi_{ss}\rangle = |0\rangle. \tag{3.95}$$

Noting that $D^\dagger(\alpha) = D(-\alpha)$, Eq. 3.95 can be written as

$$D(-\alpha)|\psi_{ss}\rangle = |0\rangle. \tag{3.96}$$

Applying the operator $D(\alpha)$ on both sides, we get

$$|\psi_{ss}\rangle = D(\alpha)|0\rangle = |\alpha\rangle. \tag{3.97}$$

Thus we have the result that the steady state of a driven, damped oscillator that is initially in the ground state $|0\rangle$ is given by the coherent state $|\alpha\rangle$ where α satisfies the classical equation of motion in Eq. 3.92.

3.6.4 Modelling dissipation in a qubit

Following the same scheme used for the resonator, the master equation for a two-level qubit coupled to a thermal bath of temperature T can be written as [51]

$$\dot{\rho} = -\frac{i}{\hbar}[H, \rho] + \Gamma_{-}\mathcal{D}[\sigma^{-}]\rho + \Gamma_{+}\mathcal{D}[\sigma^{+}]\rho + \frac{\gamma_{\varphi}}{2}\mathcal{D}[\sigma_z]\rho \tag{3.98}$$

where the operator $\mathcal{D}$ is defined in Eq. 3.69 and

$$H = \frac{\hbar\omega_{ge}\sigma_z}{2} - \frac{\hbar\Omega_p}{2}\left(\sigma^{-}e^{i\omega_p t} + \sigma^{+}e^{-i\omega_p t}\right) \tag{3.99}$$

is the driven qubit Hamiltonian. The coefficient Γ_{-} represents the rate of qubit *relaxation* and Γ_{+} is the rate of thermal excitation of the qubit. As in the oscillator case, the two rates Γ_{-} and Γ_{+} are related by the Boltzmann factor $\Gamma_{+}/\Gamma_{-} = e^{-\beta\hbar\omega_{ge}}$. The coefficient γ_{φ} denotes the rate of pure *dephasing* of the qubit which has been included in an *ad hoc* fashion. When the environment is at a very low temperature compared to the qubit frequency $k_B T \ll \hbar\omega_{ge}$, the up-rate Γ_{+} can be neglected.

The lifetime T_1 of the qubit is the time-scale for energy loss of the qubit. We can define T_1 from the down-rate Γ_{-} and up-rate Γ_{+} as

$$T_1 = \frac{1}{\Gamma_{-} + \Gamma_{+}} \tag{3.100}$$

The dephasing time T_{φ} is defined as

$$T_{\varphi} = \frac{1}{\gamma_{\varphi}} \tag{3.101}$$

Similarly, a coherence time T_2 for the qubit can be defined as the time-scale on which a "spin-echo" signal decays [103, 68]. This decay involves the time-scale for qubit relaxation along the energy axis or along a direction transverse to the energy axis. The T_2 time is therefore dependent on both the relaxation and dephasing rates, and one can show that [51]

$$T_2 = \frac{2}{\Gamma_- + \Gamma_+ + 2\gamma_\varphi} \tag{3.102}$$

Equation 3.102 yields a well-known relation between the three time-scales:

$$\frac{1}{T_2} = \frac{1}{2T_1} + \frac{1}{T_\varphi} \tag{3.103}$$

From this relation, we see that the T_1 places an upper bound on T_2 given by

$$T_2 \leq 2T_1 \tag{3.104}$$

3.6.5 Master equation for the coupled transmon resonator system

I can now put all the pieces together and write a master equation for a coupled transmon-resonator system that has dissipation and dephasing. I make the dispersive approximation and truncate the qubit Hilbert space to the two lowest energy levels. In the Schrodinger picture, the master equation for the driven system can be written as

$$\dot{\rho} = -\frac{i}{\hbar}[H, \rho] + \kappa_- \mathcal{D}[a]\rho + \kappa_+ \mathcal{D}[a^\dagger]\rho + \Gamma_- \mathcal{D}[\sigma^-]\rho + \Gamma_+ \mathcal{D}[\sigma^+]\rho + \frac{\gamma_\varphi}{2}\mathcal{D}[\sigma_z]\rho \tag{3.105}$$

where $\mathcal{D}$ is defined in Eq. 3.69 and

$$H = \hbar\tilde{\omega}_r a^\dagger a + \frac{\hbar\tilde{\omega}_{ge}\sigma_z}{2} + \hbar\chi(a^\dagger a)\sigma_z - \frac{\hbar\Omega_c}{2}(ae^{i\omega_c t} + a^\dagger e^{-i\omega_c t}) - \frac{\hbar\Omega_p}{2}(\sigma^- e^{i\omega_p t} + \sigma^+ e^{-i\omega_p t}). \tag{3.106}$$

To study the steady state of the system, we can transform into a frame rotating with the drives using Eq. 3.47 and remove the explicit time dependence in Eq. 3.106. The master equation in this time-independent picture becomes

$$\dot{\rho} = -i\tilde{\Delta}_c[a^\dagger a, \rho] - \frac{i\tilde{\Delta}_p}{2}[\sigma_z, \rho] - i\chi[(a^\dagger a)\sigma_z, \rho] + \frac{i\Omega_c}{2}[a + a^\dagger, \rho] + + \frac{i\Omega_p}{2}[\sigma^- + \sigma^+, \rho] + \kappa_-\mathcal{D}[a]\rho + \kappa_+\mathcal{D}[a^\dagger]\rho + \Gamma_-\mathcal{D}[\sigma^-]\rho + \Gamma_+\mathcal{D}[\sigma^+]\rho + \frac{\gamma_\varphi}{2}\mathcal{D}[\sigma_z]\rho \tag{3.107}$$

where $\tilde{\Delta}_c \equiv \tilde{\omega}_r - \omega_c$ and $\tilde{\Delta}_p \equiv \tilde{\omega}_{ge} - \omega_p$ are the detunings of the drive tones from the resonator and qubit transitions respectively.

The first three terms in Eq. 3.107 represent the evolution of the density matrix ρ under the undriven Jaynes-Cummings Hamiltonian, the terms containing Ω_c and Ω_p represent the driving terms for the resonator and the qubit respectively. The term containing κ_- represents the photon decay in the resonator, and the term containing κ_+ represents the thermal excitation of photons in the resonator. Similarly, the terms containing κ_- and $\kappa+$ represent the relaxation and thermal excitation of the qubit. The last term containing γ_φ represents the dephasing in the qubit.

In Chapter 6, I solve Eq. 3.107 in the steady state to numerically study the Autler-Townes effect. The steady-state condition $\dot{\rho} = 0$ reduces Eq. 3.107 to a set of coupled linear equations in the elements of the density matrix ρ. The solution of

the resulting linear equations gives the steady-state density matrix for the coupled, driven, dissipative system.

The various parameters in the SME can be determined from independent measurements, as will be discussed in detail in Chapter 6 and 7. The dispersive shift χ is measured from qubit spectroscopy. The resonator drive amplitude Ω_c can be determined from the average photon occupancy in the resonator. The qubit drive amplitude Ω_p can be measured from the Rabi oscillations of the qubit. The resonator dissipation coefficients κ_- and κ_+ are determined from the resonance line-shape of the resonator. The qubit decay-rate $1/T_1 = \Gamma_- + \Gamma_+$ is determined from the T_1 decay of the qubit excited state probability, and is approximately equal to the rate Γ_- at low temperatures for qubit frequencies in the 4-8 GHz range. The dephasing rate of the qubit γ_φ is determined from the decay of the Ramsey fringes.

Chapter 4

Device design and fabrication

Overview

In this chapter, I first describe the components of the cQED devices I used. I then discuss my design of the devices using the simulation tools Microwave Office (AWR Corp.) to simulate the microwave properties of the devices and FastCap (Fast Field Solvers) to generate a dc capacitance matrix for the conductors in the architecture. From the capacitance matrix I computed the device parameters using a circuit quantization method [30, 68]. Finally, I describe the procedure I used to fabricate the devices.

4.1 Device design

4.1.1 Device description

4.1.1.1 The resonator

The circuit quantum electrodynamics architecture that I studied consisted of two principal components – a resonator and a transmon qubit. The resonator was made of a 100 nm thick aluminum film on a 500 μm thick sapphire substrate and consisted of a meandering inductor with an inductance of $L_r \sim 2$ nH and an interdig-

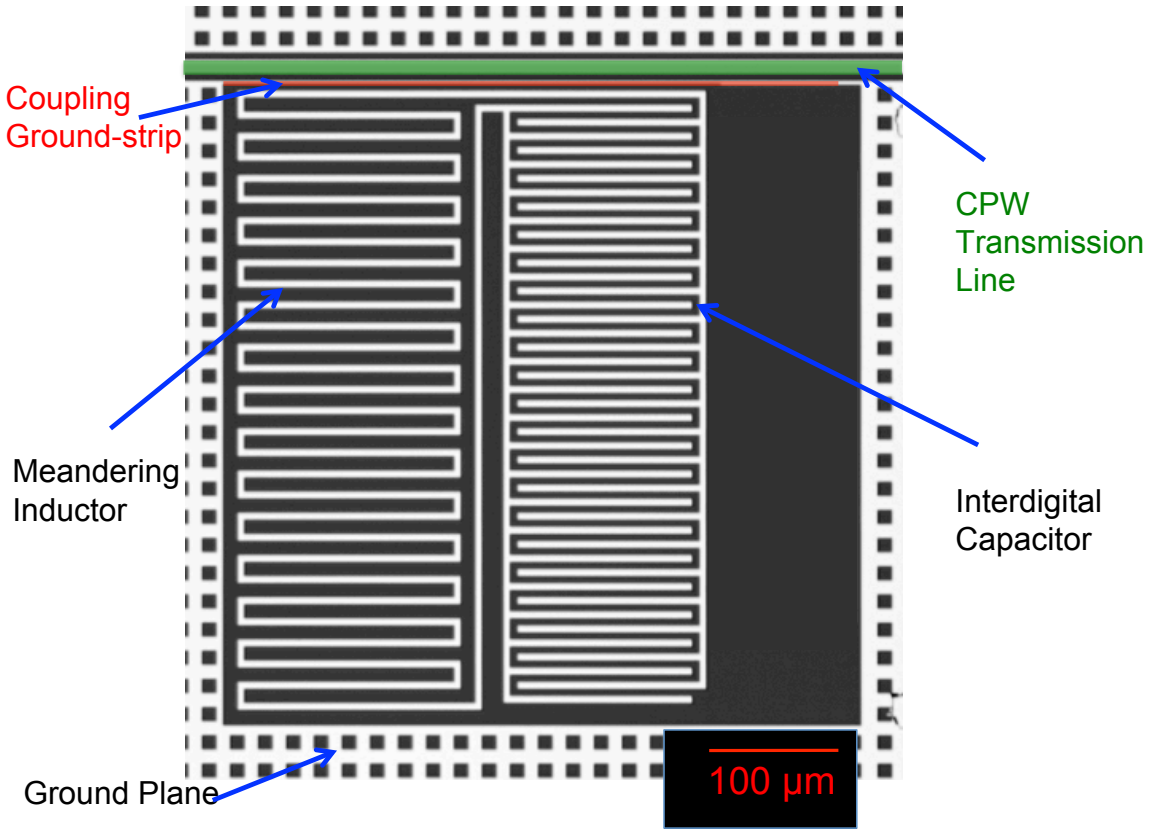

Figure 4.1: Colorized mircrograph of a lumped element resonator made of aluminum on sapphire substrate.

itated capacitor (IDC) with a capacitance of $C_r \sim 400\,\mathrm{fF}$ [75]. This gave a resonance frequency $\omega_r/2\pi \approx 5\,\mathrm{GHz}$ at a convenient place in the microwave region of the electromagnetic spectrum. A laser confocal micrograph of one of my resonators is shown in Fig. 4.1. The width and separation between the capacitor fingers was $5\,\mu\mathrm{m}$, and the length of the fingers was $160\,\mu\mathrm{m}$. The overall dimensions of the resonator were about $400\,\mu\mathrm{m} \times 400\,\mu\mathrm{m}$. I built two main types of resonators. One variation, called LEv5 (see Fig. 4.1), had a resonator frequency around 5.4 GHz, and another variation, called LEv6 has the resonator frequency around 7 GHz.

The bulk dielectric constant of sapphire is $\epsilon \approx 11$. For the IDC, this gives an effective dielectric constant of $\epsilon_{eff} \sim (\epsilon + 1)/2 = 6$. Since the refractive index n of a medium varies as $\sqrt{\epsilon_{eff}} \sim 2.5$, the effective speed of light on the chip is a factor 2.5 smaller than that in free space. The wavelength of 5 GHz radiation in the resonator is around 2.4 cm, which is significantly larger than the dimensions of the resonator. In this case, a *lumped-element* approximation can be used for the resonator, since the spatial variation of the field over the length scale of the resonator, can be ignored.

The LC resonator was coupled to a coplanar waveguide transmission line (shown in green in Fig. 4.1) with a $10\,\mu\mathrm{m}$ center conductor separated from a coplanar ground-plane by a gap of $5\,\mu\mathrm{m}$. The transmission line was used for input and output of microwaves to the device and was designed to have an impedance of $Z_0 = 50\,\Omega$ [75]. A narrow strip of ground plane between the resonator and the transmission line (shown in red in Fig. 4.1) determined the strength of coupling of the resonator to the transmission line. I varied the width of the ground-strip between $2\,\mu\mathrm{m}$ and $15\,\mu\mathrm{m}$ in my designs, which gave coupling quality factors Q_e between 15,000 and 70,000 for

the resonators. I also used perforations in the ground plane around the resonator to prevent the trapping of magnetic flux vortices.

An ideal lumped-element resonator, being an LC oscillator, has a unique characteristic frequency. This simple electromagnetic mode-structure renders it convenient for analytical study. Moreover, the small on-chip dimensions of the resonator make it a potential candidate for scalable architectures for quantum computation and quantum information processing purposes. As be discussed below, standard lithographic techniques used for semiconductor circuits can be utilized, making their fabrication reliable and reproducible.

4.1.1.2 The transmon

Each of the transmon devices I measured had a single Josephson junction, shunted with a large capacitance (see Fig. 4.2). The Josephson junction was formed from a trilayer of Al/ AlO_x/Al. The nominal area of the junction was 150 nm $\times$ 150 nm. As shown in Chapter 2, the Josephson junction behaves as a nonlinear inductance L_J, and the inductive energy scale is set by the Josephson energy E_J. The Josephson energy can be estimated from the room-temperature resistance R_J of the Josephson junction using the Ambegaokar-Baratoff formula [74],

$$E_J = \frac{R_Q}{R_J}\frac{\Delta_{Al}}{8} \tag{4.1}$$

where $R_Q = h/e^2 \simeq 26\,\mathrm{k}\Omega$ is the resistance quantum and $\Delta_{Al}/h = 52\,\mathrm{GHz}$ is the superconducting energy gap of Aluminum.

For the shunt capacitance C_b, I used an interdigital design (IDC) as shown

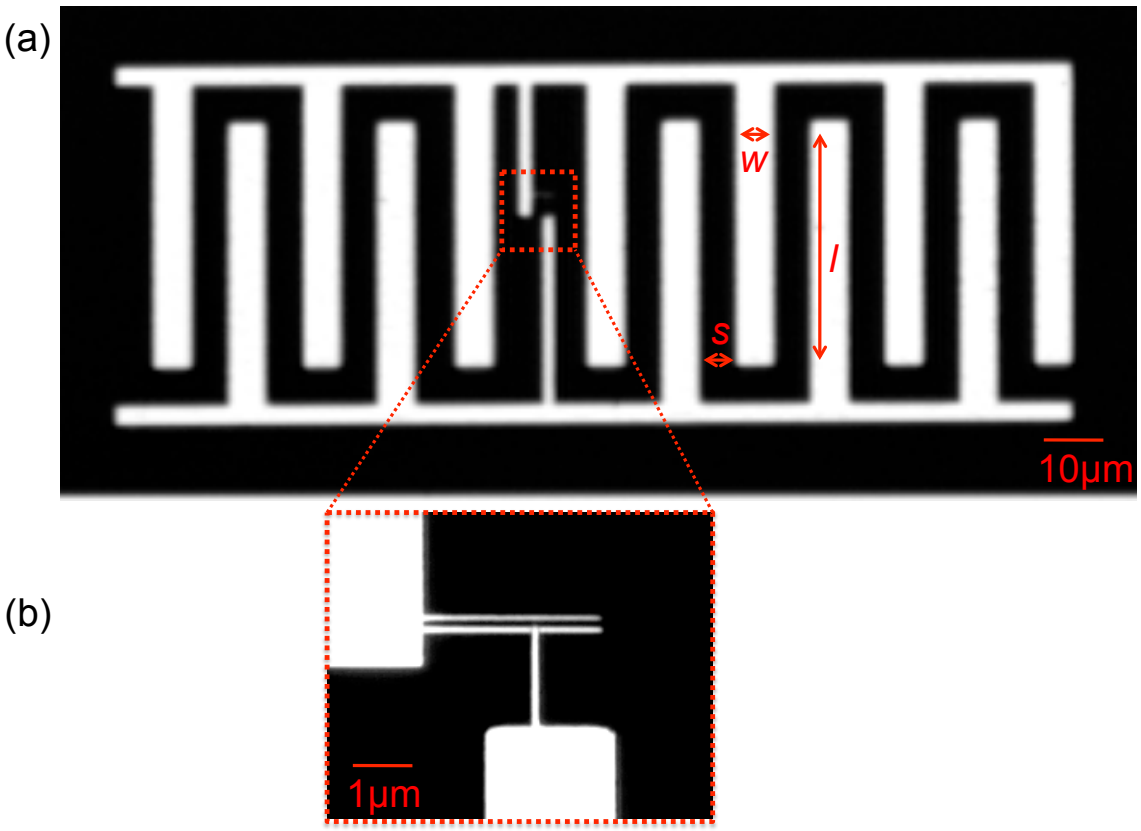

Figure 4.2: Micrograph of a Transmon. (a) Transmon with a single Josephson junction shunted by a large interdigital capacitor. (b) Detailed view of the single $Al/AlO_x/Al$ Josephson junction which had an area of 150 nm × 150 nm.

in Fig. 4.2. Typically the IDC had $N \sim 12$ fingers and each finger had a length $l \sim 70\,\mu$m, a width $w \sim 10\,\mu$m and was separated by $s = w \sim 10\,\mu$m from its neighbors. A preliminary estimation of the capacitance C_b of the IDC was made using the expression [84]

$$C_b = \frac{\epsilon_{eff}}{18\pi}\left[\frac{K(k)}{K'(k)}\right](N-1)l \tag{4.2}$$

where the elliptical integrals are given by

$$K(k) = \int_0^{\pi/2}\left(1 - k\sin^2 t\right)^{-1/2}\mathrm{d}t \tag{4.3}$$

$$K'(k) = \int_0^{\pi/2}\left(1 - \sqrt{1-k^2}\sin^2 t\right)^{-1/2}\mathrm{d}t \tag{4.4}$$

and where

$$k = \tan^2\left(\frac{w\pi}{4(w+s)}\right). \tag{4.5}$$

For the parameters listed above, one finds $C_b \approx 40\,\mathrm{fF}$.

For measuring the transmon state, I coupled the transmon to the lumped element resonator in a cQED architecture. The resonator also protects the transmon from the $50\,\Omega$ dissipative environment of the CPW transmission line [24, 31] (see Chapter 7). The layout of one of my transmon-resonator devices is shown in Fig. 4.3.

The effective capacitance C_Σ shunting the Josephson junction determines the charging energy E_c of the transmon from

$$E_c = \frac{e^2}{2C_\Sigma}. \tag{4.6}$$

Measurements on my devices showed that the charging energy was around $E_c/h \approx 300\,\mathrm{MHz}$ (see Chapter 6). This gave a transmon capacitance of $C_\Sigma \sim 60\,\mathrm{fF}$, roughly

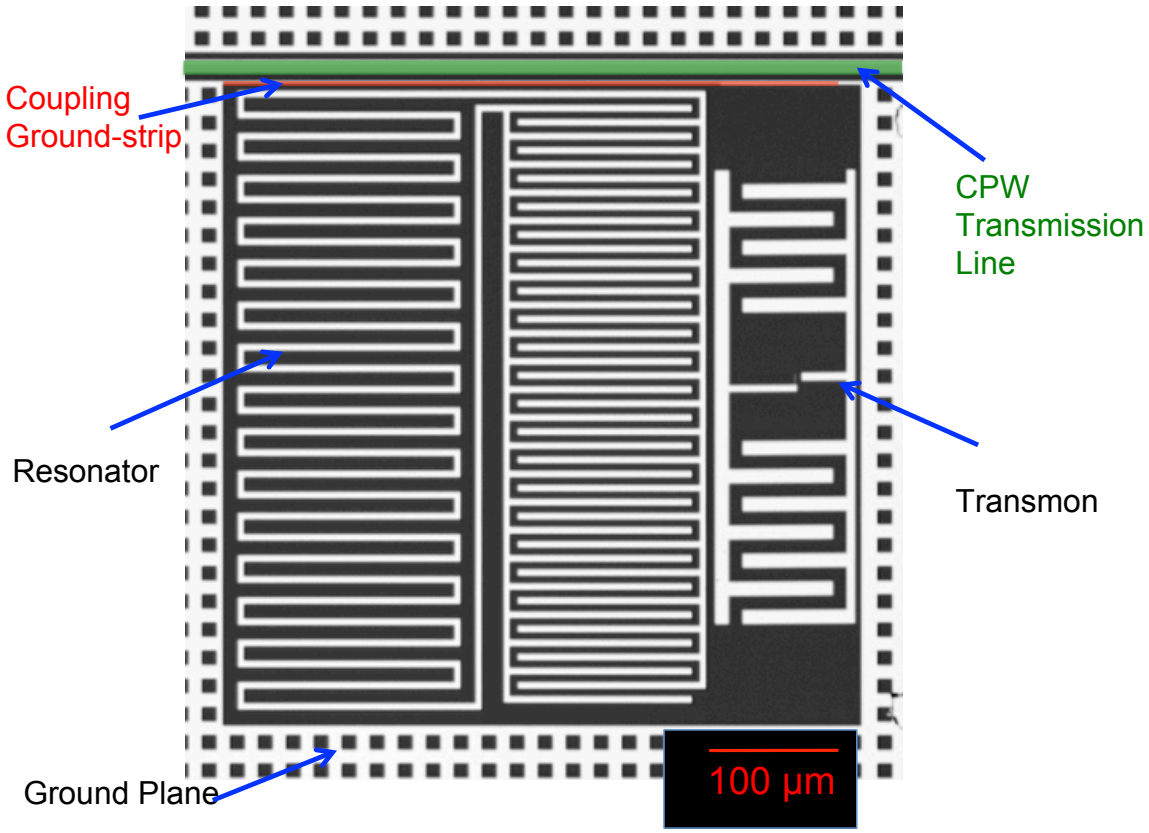

Figure 4.3: Colorized micrograph of device LEv5-7 showing a transmon coupled to a lumped-element resonator.

double the interdigital capacitance. The additional capacitance is due to the transmon junction and the capacitance coupling the transmon to the resonator and the ground plane. In order to determine C_Σ more accurately, I calculated the capacitance matrix for the device geometry in FastCap, as described in the next section. From the charging energy E_c and the Josephson energy E_J, the transmon ground-to-first excited state transition frequency can then be estimated using [30]

$$\hbar\omega_{ge} \approx \sqrt{8E_J E_c} - Ec. \tag{4.7}$$

4.1.2 Simulations using Microwave Office

To refine the design of my resonator and transmon, I used Microwave Office (AWR Corp.) to simulate the RF properties of the devices. Microwave Office is an easy-to-use simulation tool that is well-suited for simulating planar structures. For these simulations, I drew a 1 mm $\times$ 1 mm area that included resonator, transmon IDC, transmission line and the ground planes were drawn using contiguous polygons in the layout editor of the simulator (see Fig. 4.4). To simplify the simulations, I did not perforate the ground plane. To simulate the superconducting properties of the aluminum thin film, I assigned the material as a 'perfect conductor'. The thickness of the perfect conductor layer was specified to be 100 nm. To simulate the sapphire substrate, I used a dielectric layer of thickness 500 μm with dielectric properties of sapphire – a dielectric constant $\epsilon \approx 11$ and a loss-tangent $\tan\delta \sim 1\times10^{-7}$ [28]. Above the perfect conductor layer, I used a 500 μm layer of vacuum. A perfect conducting metallic box enclosing the 1 mm $\times$ 1 mm area provided the boundary conditions for

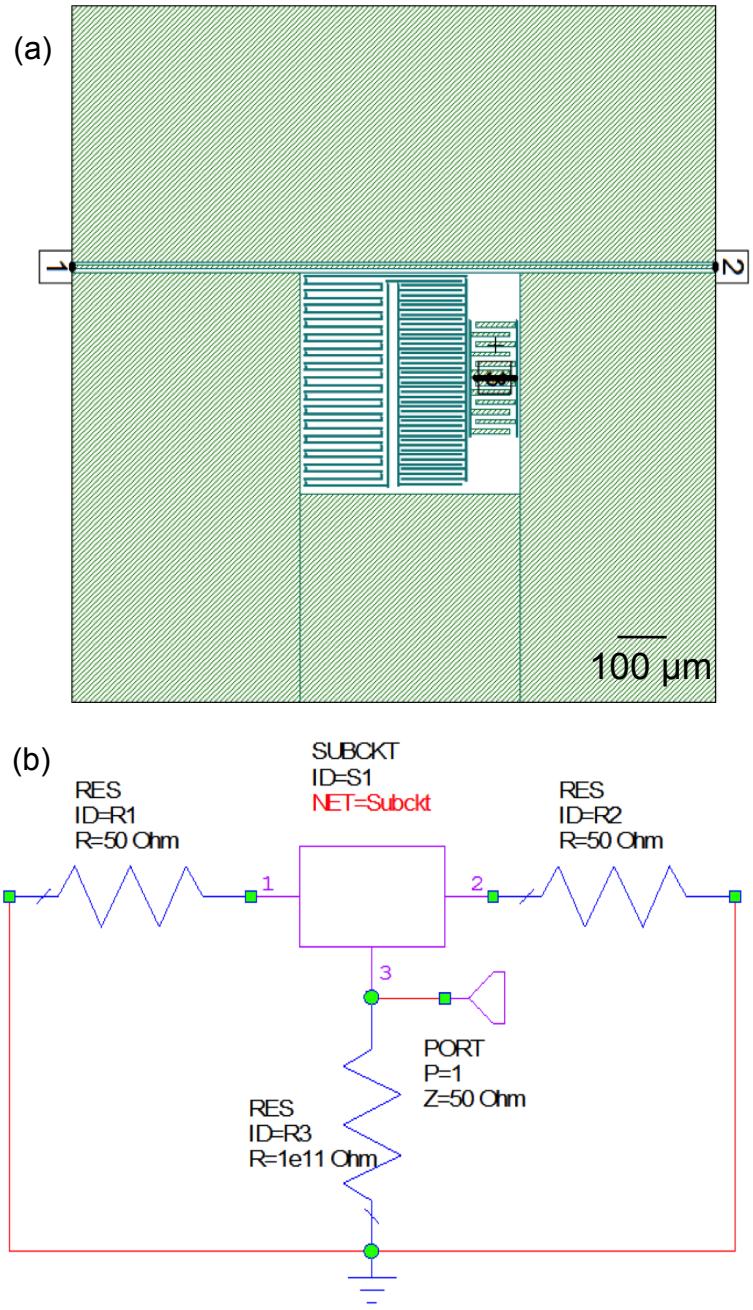

Figure 4.4: Layout and circuit schematic for simulation in Microwave Office simulations. (a) 1 mm × 1 mm layout including the resonator, transmon, transmission line and ground plane. Ports 1 and 2 at the ends of the transmission line were used for simulating $S_{21} = V_2/V_1$. (b) Circuit schematic used for simulating the admittance $Y_{33}(\omega)$ across the Josephson junction (port 3).

the simulation, with on-chip ground plane extended all the way to the boundary walls.

4.1.2.1 S_{21} of the resonator

To get the resonant frequency and external quality factor of the resonator, I simulated the ratio of output-to-input voltage as a function of frequency through the transmission line. For a two-port network, the scattering matrix or S-matrix is a 2×2 matrix that specifies the input-output characteristics of ports 1 and 2. The quantity that measures the transmission through the network is $S_{21} \equiv V_{out}/V_{in}$ [75].

To compute S_{21}, I placed "edge ports" at the end of the transmission line as shown in Fig. 4.4. For an S_{21} simulation, port 3 was not included. With port 1 as the in-port (excitation port) and port 2 as the out-port $S_{21} = V_2/V_1$ was simulated. When the frequency of the excitation was swept close to the resonant frequency of the resonator, the S_{21} showed a characteristic resonance dip or 'notch' centered around the resonant frequency (see Fig. 4.5(a)). I used an exponential sweep algorithm to speed up the computation compared to a linear sweep. As a general rule, the grid size was at least as small as the smallest feature in the device geometry. Microwave Office (v9) does not use an adaptive mesh. In practice this limited the overall dimensions of the geometry that could be simulated. With a 2.5 μm mesh, a 1 mm side for the square geometry, and an exponential sweep-algorithm with 10,000 frequency steps, the simulation typically ran for about an hour. With a 5 μm grid size of the same layout, the simulation took about 5 min. I note that the exponential sweep algorithm was most effective when the sweep-range was not too large compared to the line width of

the resonance. It was also more effective when the sweep range was symmetric about the resonance.

Figures 4.5(a)-(c) show the real and imaginary parts (blue points) of S_{21} close to the resonant frequency for a simulation of the layout shown in Fig. 4.4. The width of the ground-strip between the resonator and the transmission line for this particular design was about $2.5\,\mu$m. I used the Diameter Correction Method delineated in [85] to fit the complex S_{21} to the expression

$$S_{21}(\omega) = 1 - \frac{Q_L/|Q_e|e^{i\phi}}{1 + 2iQ_L\left(\frac{\omega-\omega_0}{\omega_0}\right)} \tag{4.8}$$

where Q_L is the total quality factor of the resonator, Q_e is the external quality factor due to the coupling to the transmission line, and ϕ is a complex phase factor that accounts for the asymmetry of the resonance lineshape.

The fits to Re$[S_{21}]$ (in-phase) and Im$[S_{21}]$, along with the fit to the circle in the complex plane of S_{21} are shown in red in Fig. 4.5. From the fits, the resonance frequency ω_r, the total quality factor Q and the external quality factor Q_e are determined. From Q_L, Q_e and the expression

$$\frac{1}{Q_L} = \frac{1}{Q_e} + \frac{1}{Q_i} \tag{4.9}$$

the intrinsic quality factor Q_i due to loss in the resonator can be found. From the S_{21} fits in Fig.4.5, one finds a resonator frequency $\omega_r/2\pi = 5.465\,\text{GHz}$, the total quality factor $Q_L = 19,000$ and an external quality factor of $Q_e = 22,000$. I note that the experimentally measured value of $Q_e = 20,000$ for a resonator with layout in Fig. 4.4 was in reasonable agreement with the simulated value.

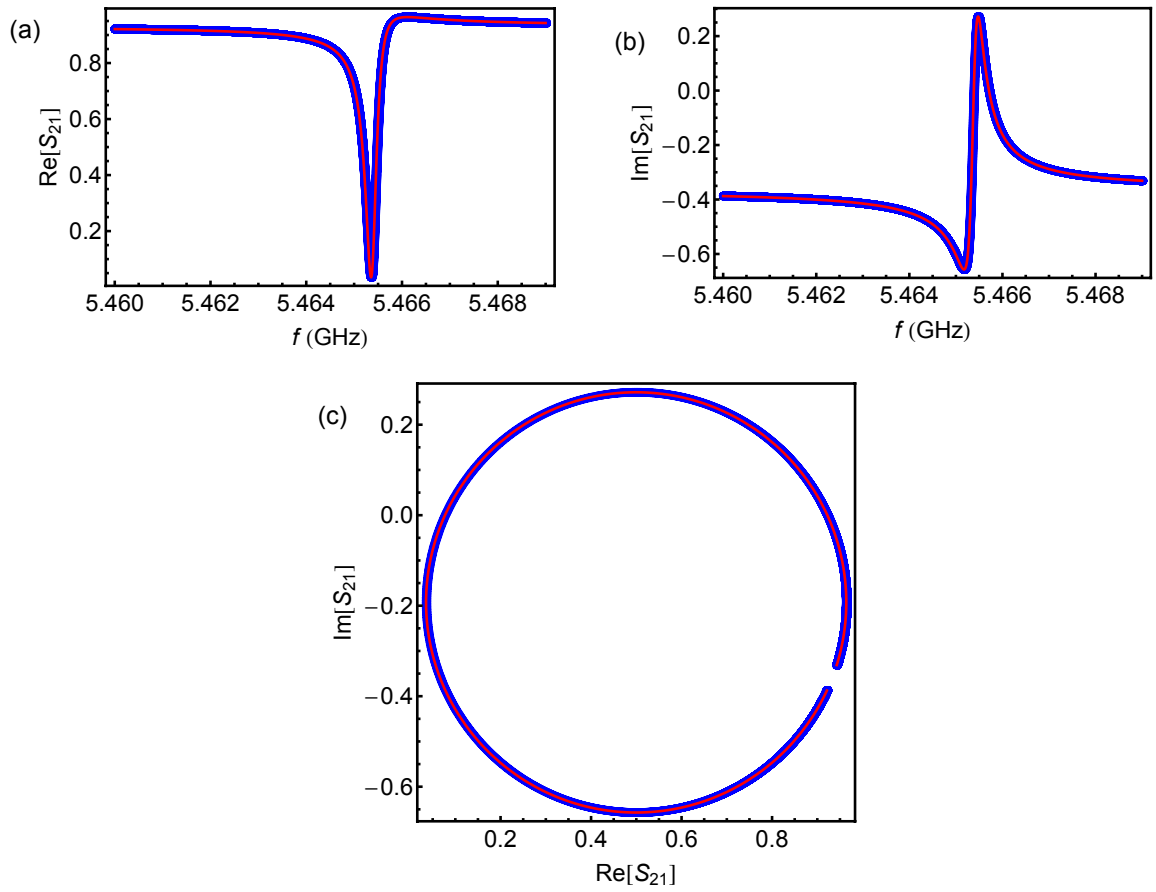

Figure 4.5: Blue curves show plot of S_{21} vs f simulated using Microwave Office for the resonator shown in Fig. 4.4. (a) Real part of S_{21}. (b) Imaginary part of S_{21}. (c) Parametric plot of $\mathrm{Re}[S_{21}]$ vs $\mathrm{Im}[S_{21}]$. The fits (Red curves) using Eq. 4.8 to the simulated results gave $\omega_r/2\pi = 5.465\,\mathrm{GHz}$, total quality factor $Q_L = 19,000$ and external quality factor $Q_e = 20,000$.

Table 4.1: Comparison of measured resonator parameters vs Microwave Office simulations.

Device Name	$\omega_r/2\pi$ (GHz) Measured	$\omega_r/2\pi$ (GHz) Simulated	Q_e Measured	Q_e Simulated
LE5-56	5.435	5.45	35,114	36,315
LE5-7	5.476	5.465	19,600	22,000
LE5-ZK9	5.460	5.465	20,000	22,000
LE5-15	5.331	5.48	18,460	20,000
LE5-17	5.345	5.47	58,064	64,000
LE6-1	7.208	7.18	73,000	74,000
LE6-7	7.201	7.18	56,000	74,000
LE6-2	7.195	7.13	69,000	74,000
LE6-3	7.189	7.13	69,000	74,000

Table 4.1 gives a comparison of the measured parameters vs the simulated parameters for all my resonators. I note that the agreement between simulation and data was typically within 3% for ω_r and within 10% for Q_e.

4.1.3 FastCap simulations of the capacitance matrix

To achieve the desired spectroscopic parameters of the transmon, it was necessary to set the charging energy of the transmon accurately. As described earlier, the interdigital capacitance C_b contributed about 50% of the total capacitance C_Σ of the

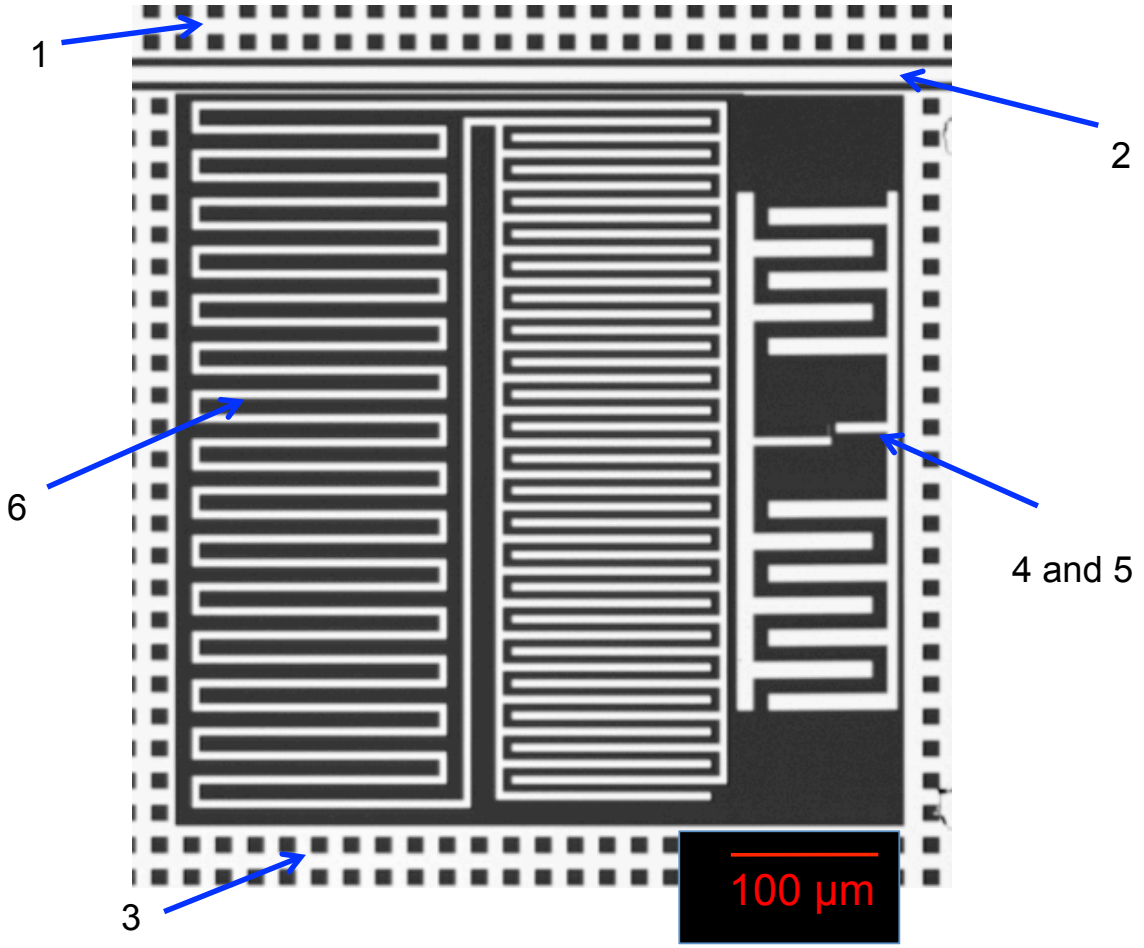

Figure 4.6: Micrograph of device LEv5-7. The conductors in the geometry are labeled to represent the indices of the capacitance matrix elements.

transmon. The remainder included contributions from coupling capacitance to the resonator and the ground plane. In order to estimate C_Σ, I used FastCap (Fast Field Solvers).

FastCap is a Fortran based dc-field solver [109]. For complex geometries, one bottle neck in using FastCap is the difficulty in generating the '.lst' list file for the geometry, which can subsequently be compiled and run using FastCap. To construct the ".lst" file, I used a graphical editor called XIC (Whiteley Research Inc.) The

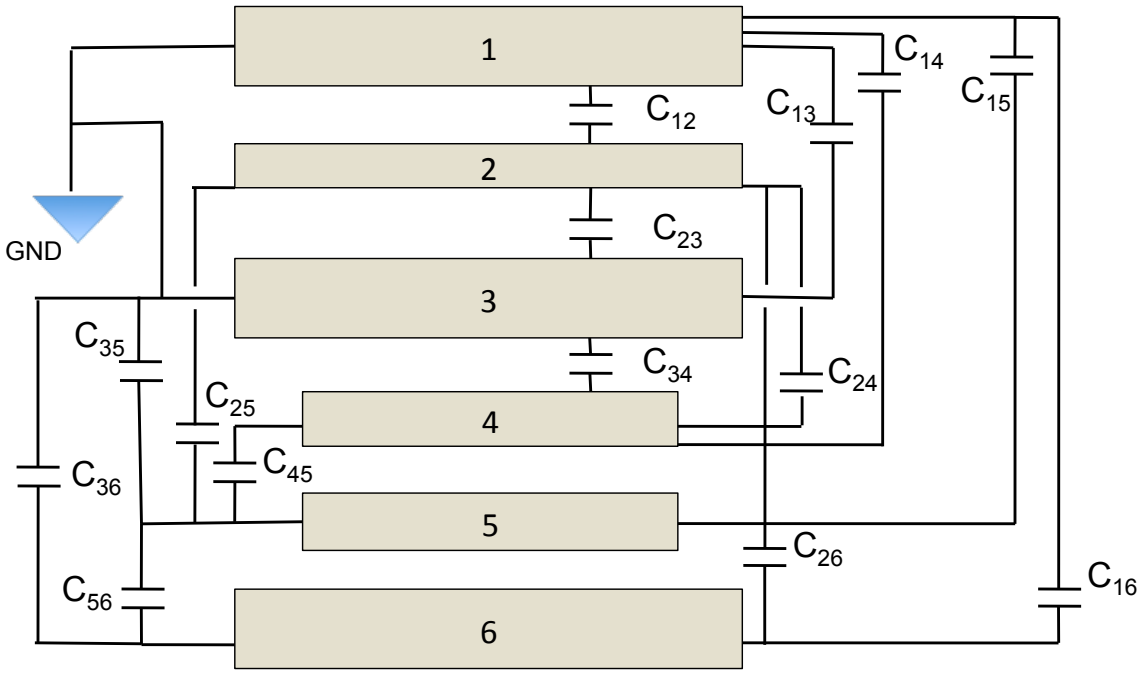

Figure 4.7: Full capacitance network for the layout of conductors shown in Fig. 4.6.

layout of the resonator was exported from Microwave Office a file in the '.dxf' format. This '.dxf' file was imported into XIC. I then drew the transmon IDC within XIC. The thickness of the metal layer was chosen to be 100 nm. The dielectric constant of the substrate was set to be 11, close to that of sapphire. I then chose a mesh-size of 1 μm and generated a '.lst' file.

The total number of contiguous conductors in my device geometry was six (see Figs. 4.6 and 4.7) – one transmission line, one resonator, two ground planes on either side of the transmission line and two pads of the IDC of the transmon. Upon running the list-file using FastCap, a 6×6 capacitance matrix was generated. The capacitance matrix from FastCap for the layout shown in Fig. 4.4 was:

$$
C = \begin{array}{c} \\ 1 \\ 2 \\ 3 \\ 4 \\ 5 \\ 6 \end{array}
\begin{array}{c}
\begin{array}{cccccc} 1 & 2 & 3 & 4 & 5 & 6 \end{array} \\
\left(\begin{array}{cccccc}
439 & -115.9 & -140.7 & -2.175 & -1.815 & -32.69 \\
-115.9 & 234.2 & -99.3 & -0.34 & -0.194 & -13.21 \\
-140.7 & -99.3 & 617.7 & -30.63 & -11.78 & -140.5 \\
-2.175 & -0.34 & -30.63 & 88.55 & -45.52 & -8.01 \\
-1.815 & -0.1947 & -11.78 & -45.52 & 88.24 & -27.61 \\
-32.69 & -13.21 & -140.5 & -8.01 & -27.61 & 235.6
\end{array}\right)
\end{array}
\text{fF} \qquad (4.10)
$$

The capacitance matrix in Eq. 4.10 is in the Maxwell capacitance matrix format [109]. A capacitance matrix for a set of conductors has to be symmetric. In addition, the Maxwell capacitance matrix has the property that the diagonal entries are all positive, and the off-diagonal entries are negative. The sum of the entries in each row or each column of the matrix gives the 'self-capacitance' or capacitance-to-infinity of each conductor. The magnitudes of the off-diagonal entries denote the mutual capacitances between any two conductors. For the capacitance matrix in Eq. 4.10, the self-capacitances for all the conductors other than the ground planes (1 and 3) were found to be quite small ($\sim 5\,\text{fF}$). Therefore, I ignored the self-capacitance of the conductors and considered only the mutual capacitance between any two conductors. For six conductors, there were 15 mutual capacitances. A schematic of the capacitance network is shown in Fig.4.7.

I used the circuit quantization method discussed in Chapter 2 and Appendix A on the full capacitance network (see Fig. 4.7) to write a Hamiltonian for the transmon-

resonator coupled circuit that has the form

$$\mathcal{H} = \frac{Q_r^2}{2C_{res}} + \frac{\Phi_r^2}{2L_r} + \frac{Q_J^2}{2C_\Sigma} - E_J \cos\left(2\pi\frac{\phi_J}{\phi_0}\right) + \beta_{rJ} Q_r Q_J + \beta_r V Q_r + \beta_J V Q_J. \quad (4.11)$$

where the subscript r denotes the resonator, J denotes the transmon Josephson junction and V denotes the voltage on the CPW transmission line. The coefficients β_r, β_J and β_{rJ} depend only on the capacitance values (see Chapter 2). The capacitance C_Σ can then be determined from the coefficient of Q_J^2. Similarly, the transmon-resonator coupling can be determined from the coefficient of the term $Q_r Q_J$. From the capacitance matrix in Eq. 4.10, using the circuit Hamiltonian I determined $E_c/h = 257\,\mathrm{MHz}$ and $g/2\pi = 60\,\mathrm{MHz}$ for device LEv5-7. In Appendix-E, I present the Mathematica (Wolfram Research) routine that I developed to calculate the parameters of the Hamiltonian for a full capacitance matrix (generated using FastCap) comprising all six conductors.

Table 4.2 shows a comparison between the measured device parameters and the simulated values. Although the agreement is good in general, I note that FastCap simulates the low-frequency capacitance network and may not be able to fully capture the behavior at microwave frequencies. I also note that for devices LEv6-2 and LEv6-3 (see Chapter 7, Fig. 7.27), the simulated values of g did not agree well with experiment. This was probably caused by an asymmetrical placement of the pattern between the plates of the resonator IDC. This brought the transmon around $5\,\mu$m closer to one plate of the resonator IDC compared to the other plate. Whether this explains the large g needs to be examined further.

Table 4.2: Table showing the measured transmon parameters vs the parameters values from simulations using FastCap.

Device Name	E_c/h (MHz) - Measured	E_c/h (MHz) - Simulation	$g/2\pi$ (MHz)- Measured	$g/2\pi$ (MHz) - Simulation
LE5-56	430	450	78	74
LE5-7	274	257	88	60
LE5-ZK9	250	274	70	60
LE5-15	234	260	65	67
LE5-17	250	239	44	67
LE6-1	314	312	40	32
LE6-7	330	312	44	32
LE6-2	578	450	129	35
LE6-3	578	450	129	35

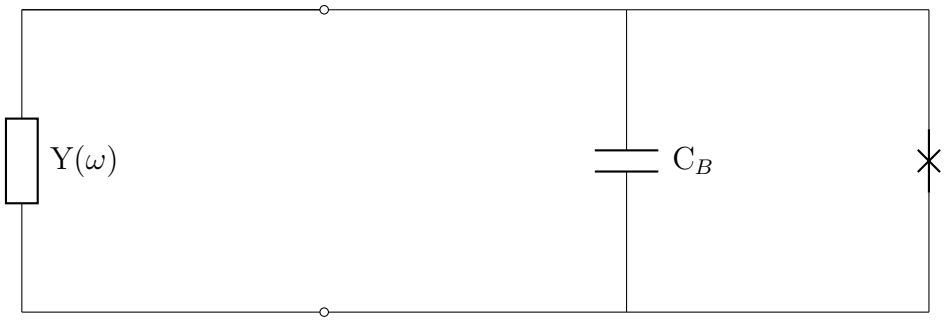

Figure 4.8: Schematic of a transmon qubit coupled to a frequency-dependent environmental admittance Y(ω)

.

4.1.4 Simulation of T_1 vs f for the transmon using Microwave Office

One of the key design quantities of interest for a transmon is the effective admittance across the Josephson junction. If the total capacitance shunting the Josephson junction is C_b and the rest of the circuit can be condensed into an effective admittance $Y(\omega)$ across the junction (see Fig. 4.8), the RC decay time-constant of the circuit can be expressed classically as

$$T_1 = \frac{C_B}{\mathrm{Re}[Y(\omega)]}. \tag{4.12}$$

In the semiclassical approximation, this expression also gives the lifetime of the excited state of the transmon. In my devices, the input and output of the transmission line acted as $50\,\Omega$ dissipative environments. Coupling to this environment contributed to the decay rate of the transmon excited state. One goal of my design was to reduce the transmon's decay rate by coupling to the transmission line.

To estimate the admittance across the Josephson junction using Microwave

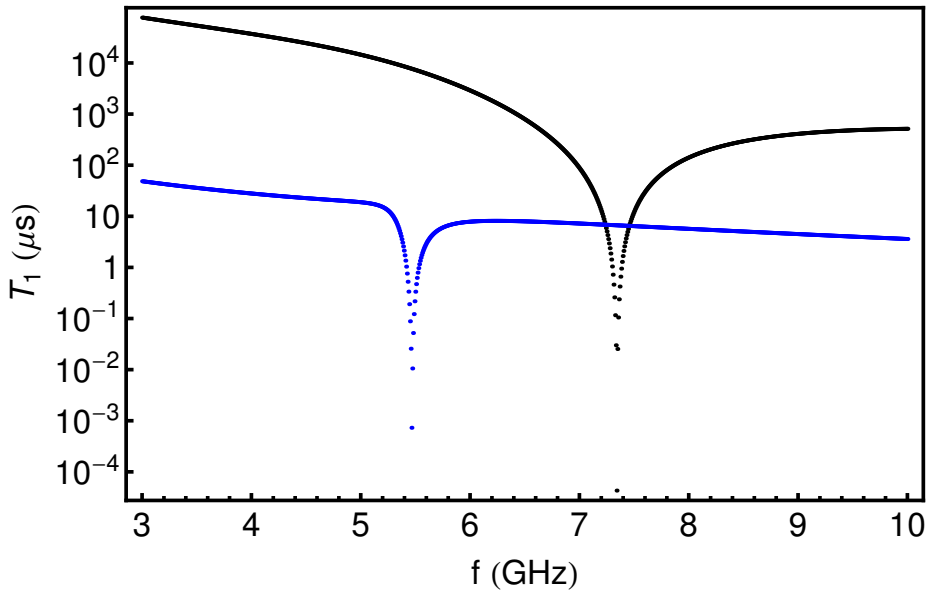

Figure 4.9: Plot of T_1 vs f simulated using MWO. T_1 was calculated using Eq. 4.13. Black curve – simulation of a device geometry similar to that of device LEv5-7. Blue curve – simulation of a device geometry similar to device LEv6-7 (see Chapter 7)

Office, I placed an internal port (3) in place of the Josephson junction (see Fig. 4.4(a)). This internal port acted as a simple voltage source. The admittance $Y_{33}(\omega)$ across the port was then computed as the ratio of the current generated to the voltage applied. For this simulation, the device geometry was embedded as a subcircuit into a circuit schematic as shown in Fig. 4.4(b). To simulate the dissipative environment, I replaced ports 1 and 2 with 50 Ω resistors. The lifetime of the transmon excited state was then computed using

$$T_1 = \frac{C_B}{\mathrm{Re}[Y_{33}(\omega)]}. \tag{4.13}$$

Figure 4.9 shows a plot of the T_1 thus computed for two different layouts. In these simulations, the dielectric loss in the substrate was ignored *i.e.* $\tan\delta = 0$. The

blue curve shows the prediction from Microwave Office for T_1 for device LEv5-7 (see Fig. 4.3). The black curve shows the T_1 prediction from Microwave Office for the device LEv6-7. A detailed discussion of these particular T_1 simulations using MWO is given in Chapter 7.

The above simulations allowed me to estimate the key transmon and resonator parameters for a given design and choose designs that looked most promising.

4.2 Device Fabrication

4.2.1 Photolithography mask design

Following the design procedure described above, the device layout (except for the transmon) was generated using the graphical layout editor L-Edit (Tanner EDA). Figure 4.10 shows one such layout drawn using L-Edit. The full layout comprised two layers, one for the superconducting areas (blue areas in Fig. 4.10) and the other for the normal metal areas (purple in Fig. 4.10). The superconducting layer (blue in Fig. 4.10) included the resonator, a continuous transmission line, pads for wirebonding to the sample box, the ground plane and alignment marks – both local and global – for aligning the subsequent Ti/Au layer. The Ti/Au normal metal layer (purple in Fig. 4.10) included the test-junction pads and transmon alignment markers to be used during e-beam lithography. Each layer was separately exported into a GDS format and sent to the manufacturer of the photolithography mask (Advanced Reproductions Corporation).

Two 5 inch soda-lime reticles, one for each layer, were manufactured for use with

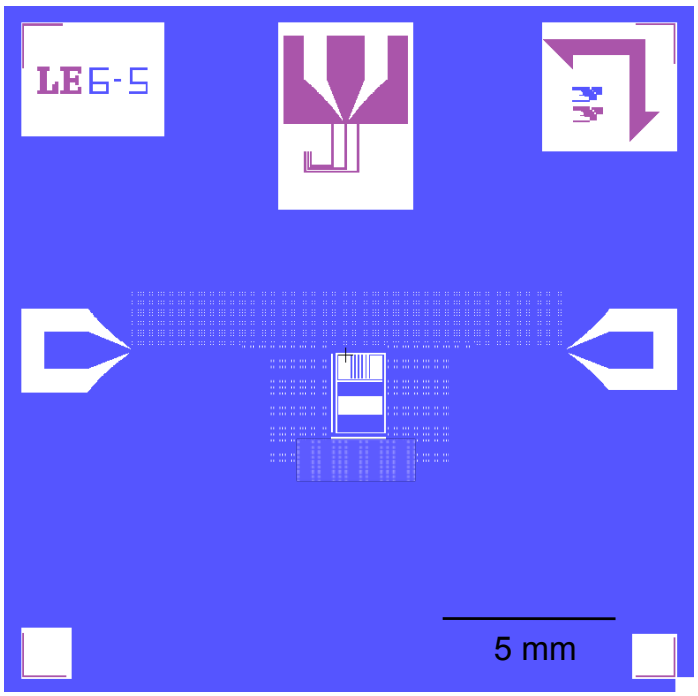

Figure 4.10: Layout of of a single device designed using L-Edit. Blue represents aluminum. Purple represents Ti/Au. The pattern on the mask is scaled up by a factor 5 relative to the actual device dimensions.

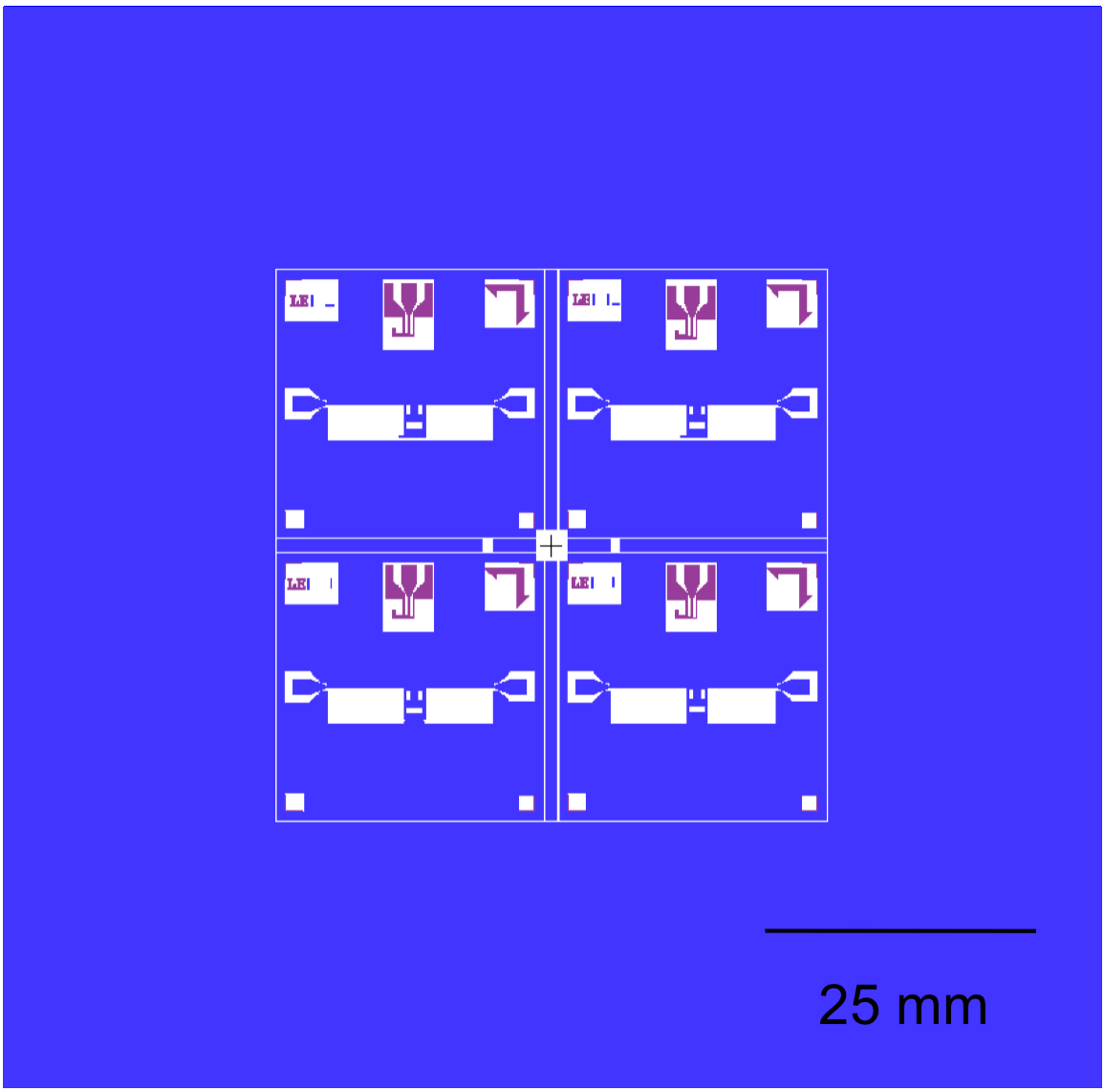

Figure 4.11: Layout of a photolithography mask designed using L-Edit. Blue represents aluminum. Purple represents Ti/Au. The pattern on the mask is scaled up by a factor 5 relative to the actual device dimensions. Each array contained 4 devices. The array was "stepped" across a 3 inch diameter sapphire wafer 49 times to produce a wafer with 96 devices.

a 5X stepper, which means that the features on the mask were five times the size of the actual features to be patterned on the wafer (see Fig. 4.11). Both the reticles had the chrome-side facing down with the polarity of the mask depending on the method used for metallization. The mask for the superconducting layer was made with a data-dark polarity suitable for an etching process after patterning a positive photo-resist, and the mask for the normal metal layer was made with a data-clear polarity suitable for a lift-off process after patterning a bi-layer of positive photo-resists.

4.2.2 Overview of the fabrication procedure

The device fabrication procedure involved three main steps:

1. Deposition, photolithography, etching and lift-off to define the resonator and ground plane superconducting aluminum (Al) and normal metal titanium-gold (Ti/Au) layers on a c-plane sapphire substrate.

2. Preparation of the sample for electron beam lithography.

3. Electron-beam (e-beam) lithography of the transmon, followed by aluminum double-angle evaporation and lift-off.

The fabrication recipe evolved over the course of my dissertation and the account given here represents the recipe used for the majority of the devices (all except LEv5-56 as discussed below).

4.2.3 Photolithography of the superconducting (Al) layer.

To begin, I took a clean 3 inch diameter c-plane oriented sapphire wafer (Kyocera corporation) with a single-sided polish. On the polished side of the wafer, I deposited a 100 nm thick layer of aluminum. For devices LEv1 through LEv5, this layer was deposited in a high-vacuum environment ($\sim 10^{-7}$ torr) in a thermal evaporator that is dedicated to evaporating aluminum. For devices LEv6, a 100 nm epitaxial layer of aluminum was grown in a molecular beam epitaxy (MBE) chamber maintained at an ultra-high vacuum ($\sim 10^{-9}$ torr) by the MBE group at LPS [110].

Figure 4.12 shows the key steps in the photolithography process for the aluminum layer. To pattern this layer, I used a positive photo-resist, OIR 906-10 (Fujifilm), spun at 3000 rpm for 60 s in a spinner hood. The wafer was then pre-baked at 120 °C for 60 s on a hot plate. After cooling to room temperature, it was mounted on a chuck by coarsely aligning the flat of the wafer with that of the chuck. The chuck was then mounted on the stage of a GCA ALS Waferstep 200 i-line stepper for exposure to 350 nm light. As the aluminum for the resonator and ground plane was the first layer to be processed, local alignment was not required in this step. The pattern on the reticle was scaled down five times using the optics in the stepper and stepped across the wafer with an exposure of 0.65 s for each cell.

Following this, the wafer was post-baked for 60 s on a hot plate set to 140 °C. The photo-resist was then developed for 60 s in a beaker of OPD 4262 (Fujifilm), followed by a rinse in deionized water (DI) for another 60 s. Since OIR 906-10 is a positive photo-resist, the areas exposed to UV light through the reticle are dissolved

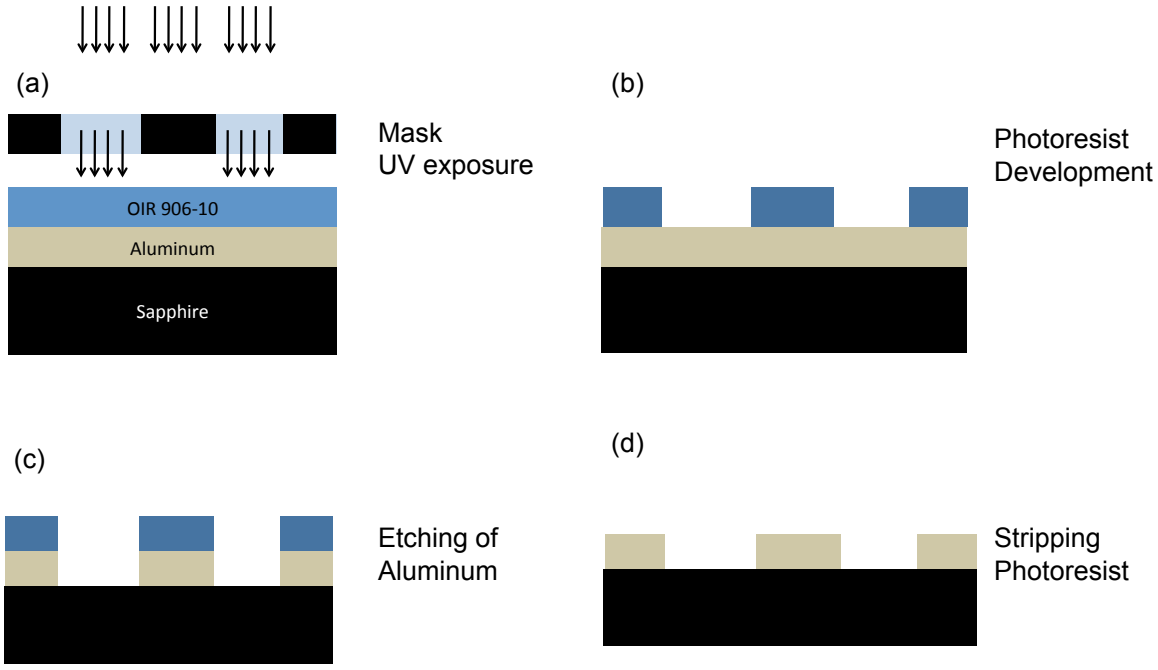

Figure 4.12: Procedure for patterning the aluminum layer.

away by the developer, leaving photo-resist intact in the unexposed areas.

After development I used a commercial aluminum etchant (1-5%HNO_3+65-75%H_3PO_4+5-10%Acetic acid) at room temperature, to etch the aluminum that was not covered by the photoresist. I found that the etchant removed the 100 nm thick aluminum film within a period of 2 min 15 s. To ensure that the film was fully etched, I etched for an additional 15 s, for a total etching time of 150 s.

To stop the etching, I immersed the wafer in a beaker of DI water for 60 s, followed by a rinse under running DI water for another 60 s, followed by drying with nitrogen. At this stage, there was still photo-resist on the undeveloped and unetched parts of the wafer. To strip this resist off, I soaked the wafer in a beaker of acetone for over 10 min followed by a thorough rinse with methanol and isopropanol (IPA) and

then blow-dried the wafer thoroughly with nitrogen. This completed the patterning of the resonator, transmission line and the ground plane of the device.

After patterning the aluminum layer, I checked the adhesion of the aluminum film to the substrate using the "scotch-tape test". I affixed a piece of scotch-tape about 0.5 in from the edge of the wafer and peeled off the tape to check if the aluminum film was also peeling off along with it, indicating poor adhesion. I repeated this at a few places along the circumference of the wafer and only those wafers where the Al film did not peel off were then considered for the next steps of fabrication listed below.

4.2.4 Photolithography of the normal metal (Ti/Au) layer.

Since Al ($Z = 13$) has a low atomic number, and sapphire is Al_2O_3, thin films of Al on a sapphire substrate are typically not readily visible to an e-beam microscope. On the other hand, Gold ($Z = 79$) on sapphire is readily visible to an e-beam. Therefore, to facilitate alignment of the transmon pattern with the resonator during e-beam writing, I added Ti/Au alignment marks [75] to my pattern.

I also used the Ti/Au layer for contact pads for test-junctions that I built to determine the Josephson energy of the Josephson junctions. Since measuring the actual transmon junctions was not possible without damaging the device, I made a pair of test junctions on the same chip as the actual transmon and measured the resistance of a set of test junctions at room temperature. Since all the junctions on a chip underwent the same fabrication process, nominally they were expected to be

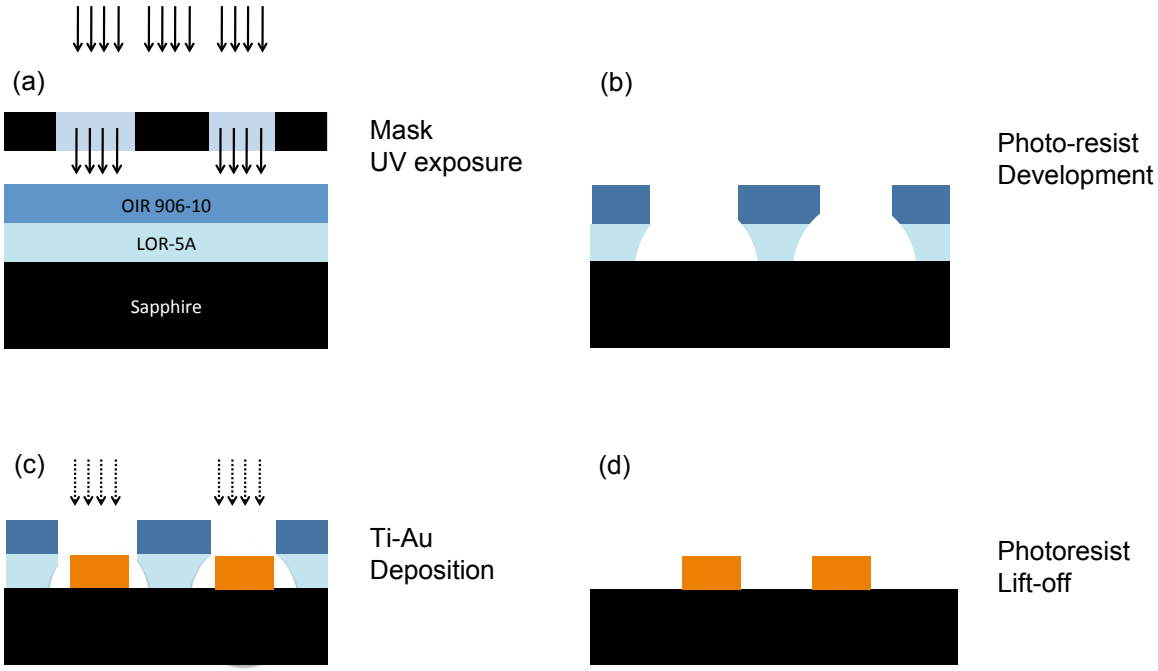

Figure 4.13: Procedure for fabrication of Ti/Au layer

identical. The leads of these test junctions are connected to large pads that enable wirebonding to the sample box. These pads were made with gold to provide good electrical contact between the external probes and the test junctions.

Figure 4.13 depicts the key steps in the procedure that I used for patterning the Ti/Au layer. I used a photo-resist bi-layer consisting of a bottom layer of LOR-5A(MicroChem), and a top layer of OIR 906-10 (Fujifilm). The LOR 5A was spun at 4000 rpm for 60 s in the spinner hood. I then baked the wafer for 60 s on a hot plate set to 195 °C. After allowing the wafer to cool to room temperature, I spun OIR 906-10 resist at 3000 rpm for 60 s. The wafer was then prebaked on a hot plate set to 120 °C.

The exposure in the stepper for this layer of processing was more involved than

for the previous Al layer because the reticle for patterning the Ti/Au layer needed to be carefully aligned with the Al pattern on the wafer. Using global alignment marks located at diametrical end points of the wafer in the aluminum pattern, I first performed a global alignment manually. It was important to do this alignment as accurately as possible and in practice I could achieve an accuracy as fine as 1 μm Having done the global alignment, I used the μ-DFAS local alignment feature of the stepper to *map* the microscopic alignment corrections for each individual cell. This allowed me to achieve accuracies to within a few hundred nanometers. After reviewing the statistics of the alignment over all the cells on the wafer, each cell was exposed for 0.65 s.

Following this, the wafer was post-baked for 60 s at 140 °C and developed in OPD 4262 for 60 s. A 10 nm thin film of Ti followed by a 100nm layer of Au was evaporated in a CHA Systems Mark-40 e-beam evaporator. A lift-off of the photo-resist bilayer was done to finish the process. For the lift-off, I used two baths of Remover PG heated to 70 °C. The wafer was immersed in the first bath for a duration of 1.5 hr to ensure that most of the resist lifted off. The wafer was held at an angle in the beaker with the front face down to ensure that the peeled-off metal film did not land on the wafer again. No agitation or stirring was used in this step. After most of the resist lifted off in the first bath, the wafer was transferred quickly to the second bath where it is left for around 20 min. While in this bath, I agitated the wafer manually once every 2 min to ensure a thorough cleaning of the surface. The wafer was then rinsed in IPA and DI water alternatingly, with the last rinse in IPA, and then blow-dried thoroughly. The wafer was then visually inspected under an optical microscope using

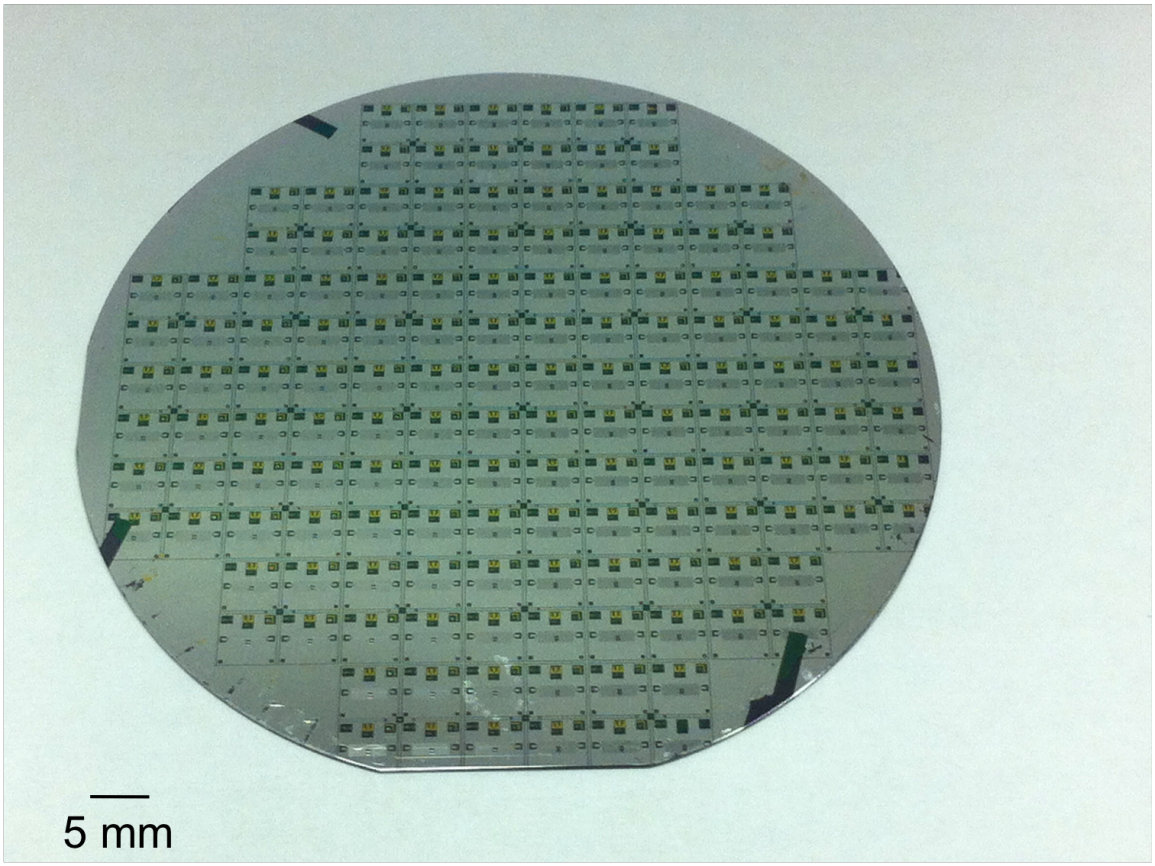

Figure 4.14: A patterned 3 inch sapphire wafer with 96 devices

a Nomarski filter. This step marked the end of the photolithography stage of the fabrication. Figure 4.14 shows a patterned 3 inch diameter sapphire wafer after the completion of the photolithography of the aluminum and Ti/Au layers.

4.2.5 Photolithography for device LEv5-56

The fabrication steps described above were used for making all of my devices except LEv5-56. Device LEv5-56 (see Fig. 4.15) was the first transmon qubit made at LPS. ;I note that the length, width and separation between the transmon IDC fingers were very small ($\sim 1\,\mu$m) for LEv5-56 compared to my later transmons (see Fig. 4.2).

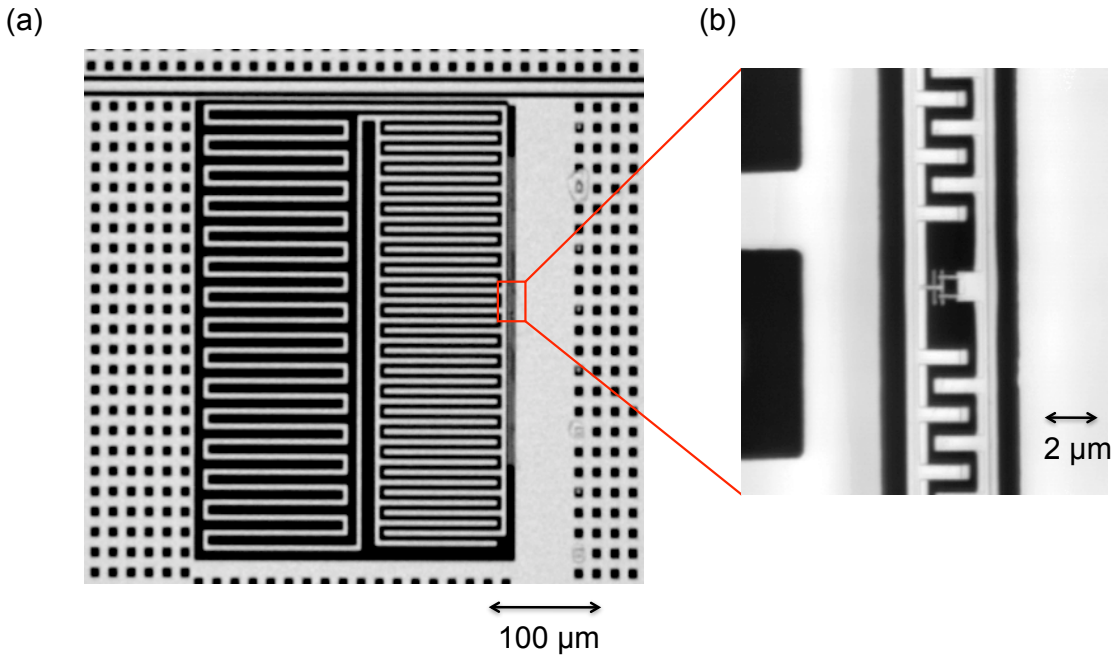

Figure 4.15: Micrograph of device LEv5-56. (a) Transmon LEv5-56 coupled to lumped element resonator. (b) Detailed view of the transmon showing the Josephson junctions forming the SQUID loop, and the transmon IDC.

The main differences in its fabrication were in the photolithography step, due to using a contact aligner instead of a stepper for the exposure of the resist, and using a lift-off process for the aluminum layer. The photolithography mask for both the aluminum and Ti/Au patterns had a data-clear polarity suitable for a lift-off process. Unlike in the case of the stepper, the features on the mask that was used with a contact aligner had the same dimensions as those of the actual features to be patterned on the wafer.

For LEv5-56, I took a clean 3 inch diameter c-plane sapphire wafer (Kyocera corp.) I used a photo-resist bi-layer consisting of a bottom layer of LOR-5A and a top layer of OIR 906-10. First the LOR 5A was spun at 4000 rpm for 60 s in the spinner

hood. The wafer was then baked for 60 s on a hot plate at 195 °C. After allowing the wafer to cool to room temperature, the OIR 906-10 resist layer was spun at 3500 rpm for 90 s. The wafer was then prebaked for 60 s on a hot plate at 90 °C.

For exposure, I used a Karl Suss MJB3 contact aligner, with a UV light exposure duration of 4 s, followed by a post-bake on a hotplate at 120 °C. The resist was then developed in OPD 4262 for 60 s. A 100 nm thick layer of Al was thermal-evaporated onto the wafer, and to finish the process, the resist stack was lifted off in two baths of Remover PG at 70 °C.

The same sequence of steps were repeated to process the Ti/Au layer, with the Al deposition replaced by an e-beam evaporation of 10 nm of Ti followed by 100 nm of Au in a CHA system Mark-40 evaporator. The main disadvantage in using the contact aligner for a multi-layer lithography process was the possibility of significant misalignment between the different layers. Because of this, the LEv5-56 Ti/Au pattern had a different alignment relative to the Al pattern on each chip from the wafer. This misalignment needed to be compensated for during the e-beam lithography. In the case of large patterns, such as the transmon shunt capacitor, this misalignment got amplified, rendering the fabrication process quite difficult. This is what prompted me to use the stepper for the fabrication of the rest of my samples.

4.2.6 Preparation of the sample for e-beam writing

For e-beam writing, I used a resist bi-layer of MMA(8.5)MMA EL11 (MicroChem) on the bottom and ZEP 520A DR2.3 (Zeon Chemicals) on the top. The top

resist layer of ZEP has a lower sensitivity to electron-beam exposure compared with the bottom resist layer of MMA. Upon e-beam exposure, ZEP provided the desired resolution for the pattern, while MMA provided the required amount of undercut for performing a *lift-off* after aluminum evaporation.

The MMA was spun at 1000 rpm for 60 s, giving it a thickness of about 900 nm. The wafer was then baked for 5 min at 180 °C. After letting the wafer cool to room temperature, ZEP was spun at 5000 rpm for 60 s. This gave the ZEP layer a thickness of nearly 100 nm. The wafer was then baked again for 5 min at 180 °C. To further remove solvent from the resist, the wafer was next *hard-baked* in an oven at 180 °C for at least 30 min.

To avoid charging of the resist during e-beam writing, I deposited an anti-charging layer of Al, about 10 nm thick, in a thermal evaporator. I note that depositing this layer in an e-beam evaporator could have exposed the e-beam resist, so I used a thermal evaporator instead. To protect the devices during dicing, I spun a 5 μm thick protective layer of FSC-M (blue resist) at 2000 rpm for 60 s, followed by baking at 120 °C for 5 min.

The wafer was diced into 5 mm $\times$ 5 mm individual chips using the semi-automatic mode of a Disco DAD321 dicing saw. Two of my wafers were diced using a hubless vitrified glass-bonded diamond blade VT07-SD400-VC100-75 (Disco). This blade was not dressed before use, even though that is recommended. The VT-07 blade was 200 μm thick and gave a kerf of around 250 μm with about 25 μm of chipping at a feed-rate of 2 mm/s and a spinning rate of 20,000 rpm. For another wafer, I used a 2 inch hubbed resin-bonded diamond blade CX-010-325-080-H (Dicing Blade Technol-

ogy). The CX blade was 250 μm thick and without dressing, it gave a kerf of around 310 μm with about 30 μm of chipping at a feed rate of 0.75 mm/s and a spinning rate of 22,000 rpm. I found that dressing the CX blade helped bring the cut-width down to 270 μm with a chipping of around 20 μm. While dicing, the wafer was held together by an adhesive backing tape, which also facilitated a good vacuum with the chuck-table and helped secure the chips during dicing.

After dicing, individual chips were carefully separated from the adhesive tape using precision-tipped tweezers. The FSC-M protective resist was then removed by rinsing in acetone for around 40 s, followed by successive rinsing in methanol and isopropanol for 30 s each. I only removed the blue resist shortly before e-beam writing because we found that it offered protection to the chips from physical damage due to dust and scratches and also protected the e-beam resist from unwanted exposure [75].

4.2.7 Electron-Beam Lithography

Electron beam writing was carried out in a JEOL 6500F Scanning Electron Microscope equipped with a beam blanker to facilitate writing. I used Nanometer Pattern Generation System (NPGS) software to write the patterns, which were designed using Design CAD LT 2000 software. My CAD designs were integrated with an NPGS run-file which controlled the beam dosages and dwell times.

The beam was first focused on a small scratch that I placed on the chip in a corner using a diamond-tipped scribe. This scratch was used to help me adjust the

coarse focus up to a magnification of 30,000. The final focusing was achieved through burning contamination spots about 100 μm to 150 μm away from the location of the pattern. The typical diameter of a contamination spot at the best focus was about 10 nm. If the focusing was done too far from where the CPB pattern was written, the focus might not be perfect while writing, resulting in under-exposure of the resist.

Along with the transmon pattern, I also wrote a test junction pattern (see Fig. 4.10) which was I used to tune the oxygen exposure parameters (chamber pressure and duration of exposure). By measuring the room-temperature tunnel junction resistance using an ohmmeter with external probes, I obtained an estimate for $E_{J,max}$ for the CPB using Eqn. 4.14 and tuned the oxidation parameters to achieve the target values for the resistance (typically about 15 kΩ). The test junctions had the same nominal dimensions as the transmon junctions and the resistances should be nominally identical. The position for writing the transmon was determined by first locating the Ti/Au alignment markers on the chip at a magnification of around 90X. Care was taken not to expose the area that was going to be patterned. A finer alignment was then done on NPGS through an alignment step. NPGS was then used to control the electron beam through a beam-blanker to write the desired pattern onto the resist. For writing the transmon junction and pads, I used a magnification of around 200X and a measured beam-current of 20 pA. For writing the test junctions, I used a magnification of 700X and a measured beam-current of around 20 pA.

4.2.8 Development of the e-beam pattern

Figure 4.16 shows the key steps in the fabrication procedure I used for my transmon devices. After e-beam writing, the two layers of resist were developed independently in separate development steps. First, the anti-charging layer of aluminum was stripped by rinsing the chip in OPD4262 for 60 s, followed by rinsing in deionized water for another 60 s. The top layer of ZEP was then developed in ZED-N50 (Amyl Acetate) for 3 min, followed by rinsing in isopropanol for 60 s. Next the MMA was developed (see Fig. 4.16) in a 5:1 volume mixture of isopropanol and deionized water for 150 s, followed by rinsing in isopropanol for 60 s. In the above steps, the chip was held in the beaker using tweezers and agitated gently. The chip was then blown dry. A laser confocal microscope was used to image the pattern after each layer of resist was developed. This enabled me to effectively isolate the steps that needed to be fine-tuned.

4.2.9 Aluminum double angle evaporation - Oxidation parameters and lift-off

After the patterns were developed, I transferred the chip to a thermal evaporator. The evaporator was evacuated to a base pressure of 1×10^{-7} Torr. Double angle evaporation with an intermediate oxidation step was employed to fabricate the Al/AlO_x/Al Josephson junctions. The first Al evaporation was done at an angle of -20° for a thickness of 30 nm at an average rate of 0.5 nm/s. This formed the bottom island of the transmon Josephson junction. The aluminum was deposited directly on

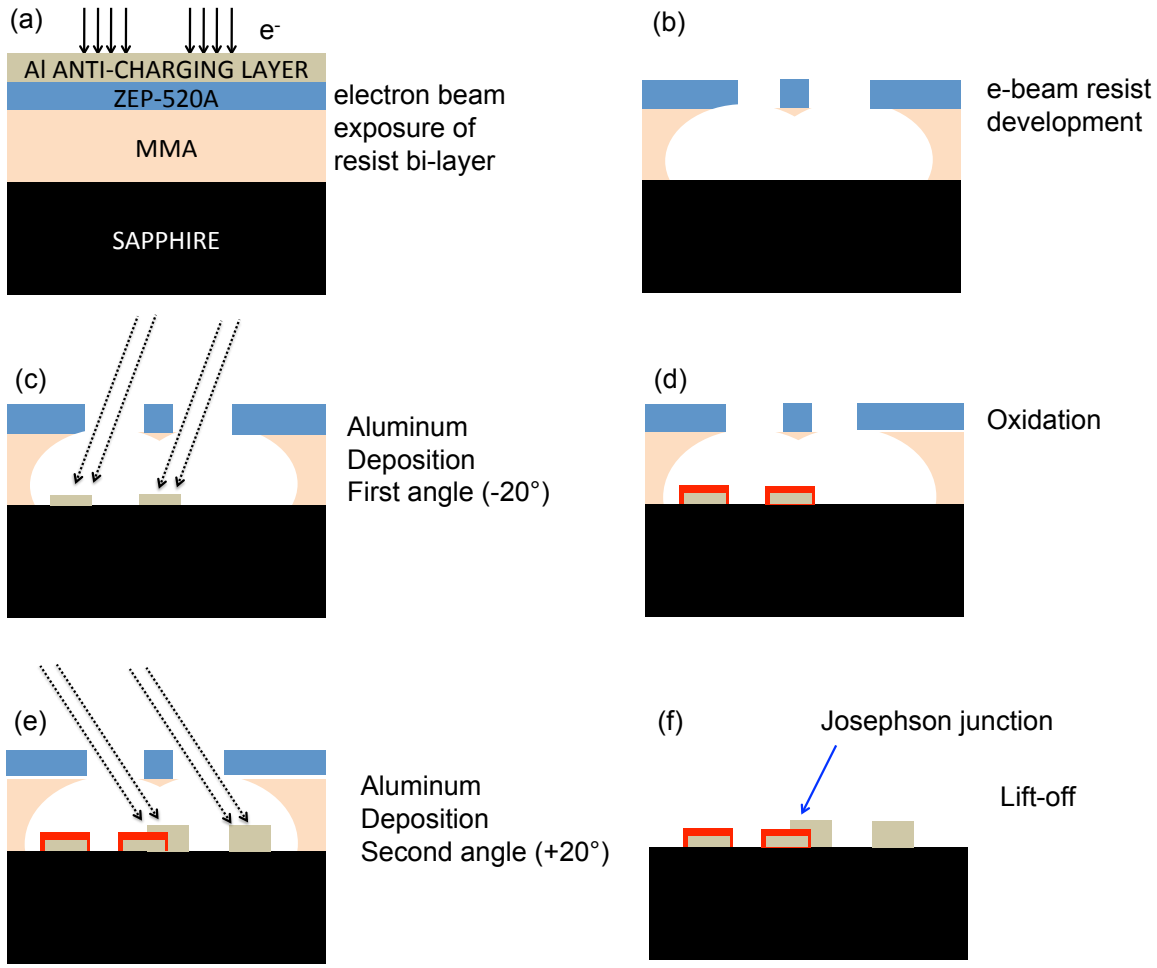

Figure 4.16: Fabrication of $Al/AlO_x/Al$ transmon devices

the sapphire substrate through the window in the developed resist (see Fig. 4.16). Note that the angle of evaporation depends on the thickness of the resist layer used.

An oxide layer was then grown *in situ* by letting O_2 gas into the chamber of the evaporator at an average pressure of 150 millitorr for a duration of 4 min. Both the pressure of oxygen in the chamber and the time of exposure determined the resistance of the Josephson junction. On top of the oxide layer, a 50 nm thick layer of Al was then evaporated, this time at a $+20^\circ$ angle, thus forming the top island of the transmon Josephson junction.

The next step was to lift off the e-beam resist. For the LEv5 devices, I used N-Methyl-2-Pyrrolidone (NMP) for lift-off. The chip was immersed metal-side-up in a beaker of NMP heated to 80°C for about 60 min without any agitation. After most of the aluminum film was lifted off in the first beaker, the chip was quickly transferred into a second beaker of NMP heated up to 80° C. This second immersion was done for 20 min while gently agitating it once every 2 min for a duration of 30 s each time. The second immersion was done to ensure that the lift-off process was complete and there was no residual resist on the chip. Once the NMP cooled to around 60° C, the chip was rinsed repeatedly in IPA and DI water, with the last rinse in IPA, and then blow-dried thoroughly.

For the LEv6 devices, I used Microposit Remover 1165 for the lift-off. Microposit Remover 1165 is an NMP-based resist remover with additional surfactants in it that help break the polymerized resist membranes. I placed the chip metal-side-up in a beaker of Microposit 1165 heated to 80 °C and left it there for about 6 to 8 hr without any disturbance. After almost all the aluminum was lifted off in the first beaker, I

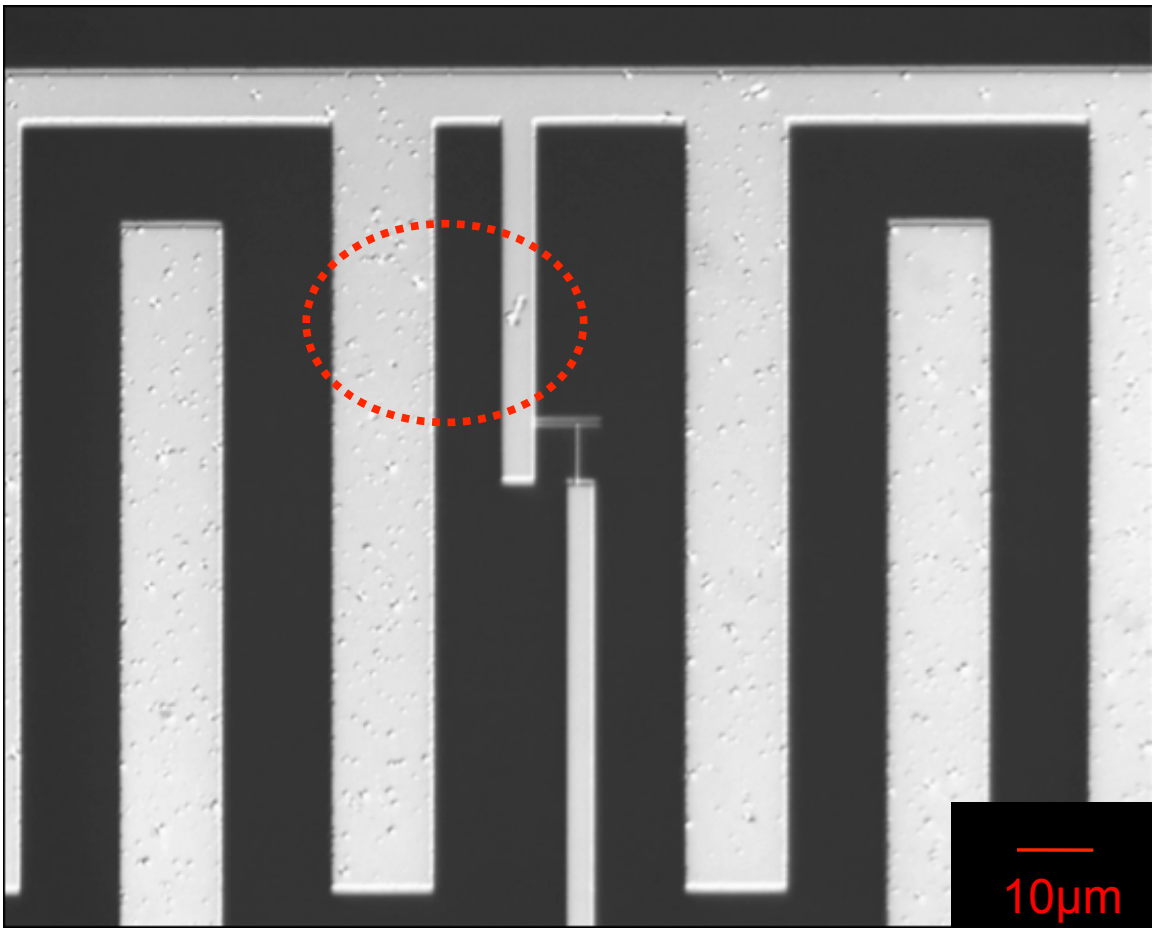

Figure 4.17: Micrograph of a device showing damage due to ultrasonic agitation. The red circle highlights an area of the interdigital capacitor where the aluminum film looks rough due to damage caused by ultrasonication for over 2 min.

transferred the chip to a second beaker of Microposit heated up to 80 °C and let it soak for another 1 hr with regular agitation. The chip was then rinsed repeatedly in IPA and DI water, with the last rinse in IPA, before being blow-dried thoroughly.

At no stage in the lithography process was ultrasonication used since it was found to damage the aluminum film on occasions (see Fig.4.17). Before measuring, a prospective device was inspected under the laser confocal microscope to ensure that there were no visible defects in the chip that would render the chip unusable.

I note that despite inspecting the devices using confocal microscopy and Nomarski microscopy, resist residue in small areas around the junctions could not always be detected. When I looked at some devices under a scanning electron microscope, I found a thin film of resist residue close to the Josephson junction (see Fig. 4.18). A systematic study of the causes of such residual contaminants is beyond the scope of this thesis. In Chapter 7, I show that surface dielectric losses may be limiting the lifetimes of my transmons. In the light of that observation, a closer look of the fabrication process could be useful in figuring out how to eliminate residual contaminants and improve the performance of the devices.

4.2.10 Tuning the E_J of a Josephson junction

I required the fundamental transition frequency of my transmon devices to lie in the range of 4 GHz to 8 GHz consistent with the band width of the measurement apparatus (see Chapter 5). While the charging energy E_c of the transmon is determined by the design of the shunt capacitance and its placement relative to the resonator and

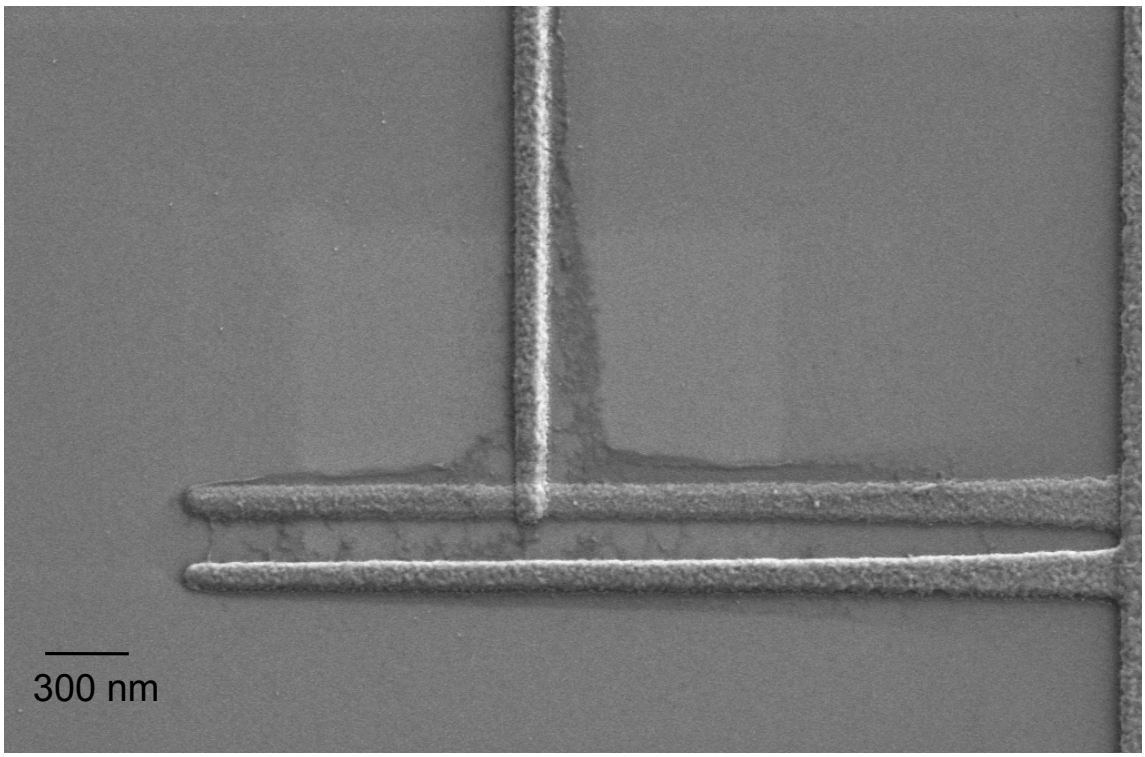

Figure 4.18: Scanning electron micrograph showing a single Josephson junction with resist residue after fabrication.

the ground planes, the Josephson energy E_J is determined by the oxidation parameters during double-angle evaporation. For my single-junction transmons the E_J could be tuned using an external flux bias.

In order to tune the junction resistance, I measured the junction resistance at room temperature. The resistance of the transmon junctions could not be measured directly. For this purpose I fabricated test junctions on the same chip as the transmon. The test junctions were designed to have nominally the same geometry as the transmon junction and since they were developed, metallized and oxidized in the same step as the transmon, they were expected to have, nominally, identical parameters to the transmon junction. The test-junctions were located far away from the transmon junction, but on the same chip, so that measuring them would not damage the transmon.

I used the Ambegaokar-Baratoff formula [74] to determine the Josephson energy E_J in terms of the resistance of the tunnel barrier R_J,

$$E_J = \frac{R_Q}{R_J}\frac{\Delta_{Al}}{8} \tag{4.14}$$

where $R_Q = h/e^2 \simeq 26\,\mathrm{k}\Omega$ is the resistance quantum and $\Delta_{Al} \simeq 200\,\mu\mathrm{eV}$ is the superconducting energy gap for Aluminum. Using $\Delta_{Al}/h = 52\,\mathrm{GHz}$, and a typical value of $R_J = 10\,k\Omega$ I find a typical $E_J/h = 17\,\mathrm{GHz}$ for the junction.

The ground-to-first excited state transition frequency f_{ge} of the transmon can then be computed using the expression

$$hf_{ge} = \sqrt{8E_JE_c} - E_c \tag{4.15}$$

For the above numerical values, and for an E_c/h of 200 MHz, I get a transition

frequency of 5 GHz for the transmon.

By measuring the R_J of each test-junction I fabricated, I estimated the E_J, and thereby the expected transition frequency, and tuned the oxidation exposure to increase or reduce the junction resistance accordingly. A larger resistance of the junctions means a smaller critical current and hence a smaller E_J. Needless to say that the actual spectroscopically measured E_J for the transmon was slightly different (10% to 15%) from that estimated from the room-temperature resistance of the test-junctions in all the transmons except for device LEv5-56. This was probably due to difference in the areas between the transmon junctions and the test junctions. This was due to changes in the resistance between room temperature and millkelvin temperatures, as well as microscopic differences in the different junctions. Table 4.3 shows the E_J values measured spectroscopically vs the E_J values estimated from the room temperature resistance R_J for my transmon devices.

Table 4.3: Table of measured E_J and E_J estimated from room-temperature tunnel junction resistance. † - device LEv5-56 had a split CPB allowing flux-tunability of the E_J. For this device, the $E_J^{max}/h \approx 87\,\mathrm{GHz}$. * - Device LEv5-ZK9 had a split CPB allowing flux-tunability of the E_J. For this device, the $E_J^{max}/h \approx 26\,\mathrm{GHz}$.

Device Name	R_J ($\mathrm{k}\,\Omega$)	E_J/h (GHz) - Predicted	E_J/h (GHz) - Measured
LEv5-56†	8.5	20	87
LEv5-7	7.04	24	29.4
LEv5-ZK9*	6.0	28.1	25.9
LEv5-15	19.0	8.89	10.5
LEv5-17	19.0	8.89	6.1
LEv6-1	16.2	10.4	12.2
LEv6-7	16.2	10.4	16.0
LEv6-2	9.5	17.7	20.5
LEv6-3	9.5	17.7	20.5

Chapter 5

Experimental set-up

5.1 Overview

In this chapter, I first describe how I packaged my devices in preparation for measurement. I then describe the two main components of the experimental setup that I used for measuring my devices at millikelvin temperatures – the dilution refrigerator and the measurement electronics. Finally I discuss the two methods I employed to read out the state of the qubit.

5.2 Packaging the Device

The fabrication of my transmon-resonator devices was discussed in detail in the previous Chapter. To select a device for measurement, I first inspected the device optically using laser confocal microscopy (Keyence) and Nomarski microscopy.

For packaging most of my devices (except LEv6-2 and LEv6-3), I used a copper sample box (see Figs. 5.1 - 5.3). After selecting a sample device for measurement, I glued it to a sample box (see Fig. 5.2) using silver paste (SPI Products). The sample box used UT-47 copper coaxial cables for input and output microwaves. This was done to avoid magnetic materials found in common SMA connectors that could cause unwanted magnetic field gradients across the chip. The coplanar microwave

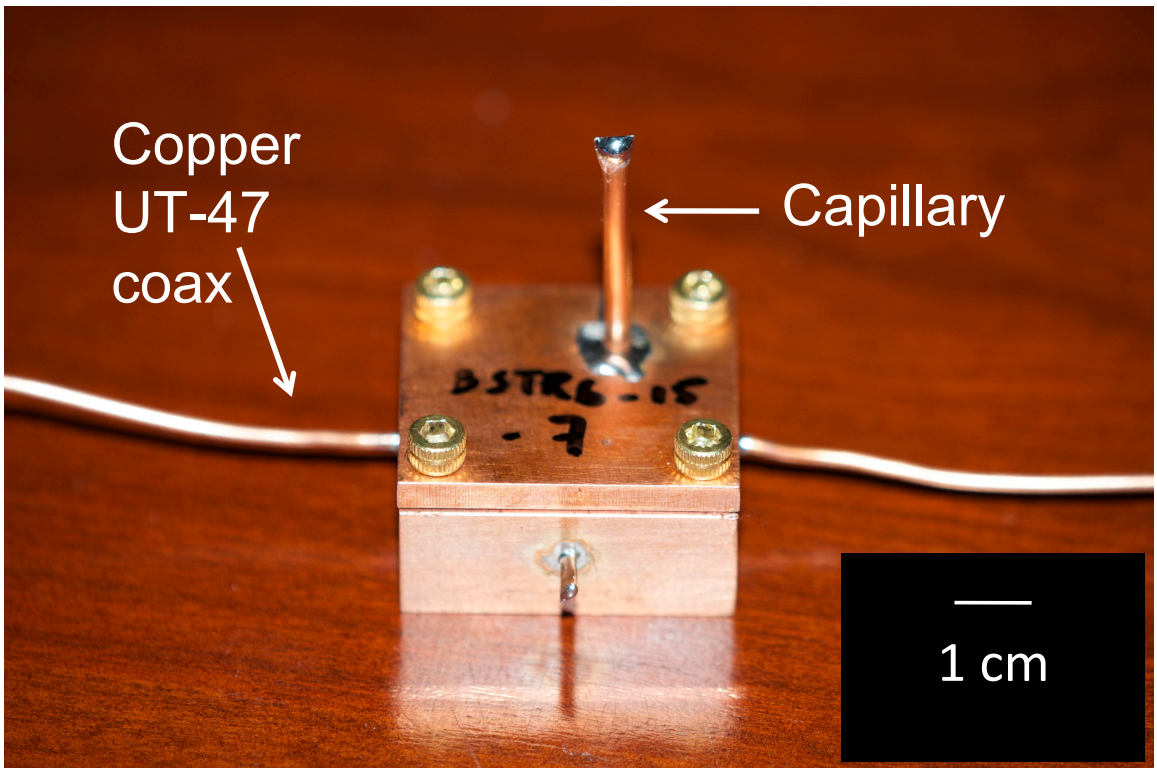

Figure 5.1: Photograph of copper sample box showing the coaxial connectors and the capillary for backfilling He gas. The box was sealed air-tight by pinching the capillary and soldering over the pinched area. An indium gasket was used between the two halves of the box to make it air-tight and prevent RF leakage.

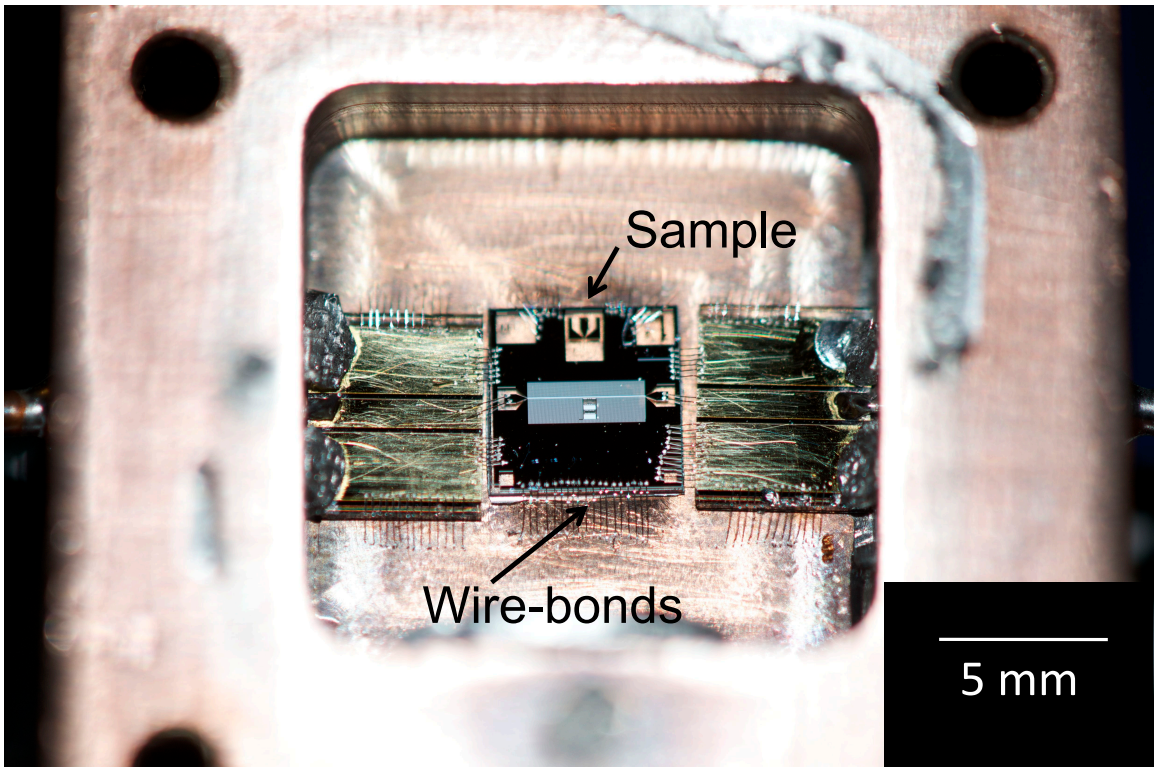

Figure 5.2: Photograph of copper sample box with sample showing wire-bonds. The sample is glued using silver paste. The microwave launchers (on the left and right side of the sample) and the ground plane of the box are connected to the device through wire-bonds. The microwave launchers are made of Ti-Au on quartz. The center conductor of the UT-47 copper coaxial connectors is soldered directly onto the center conductor of the launcher.

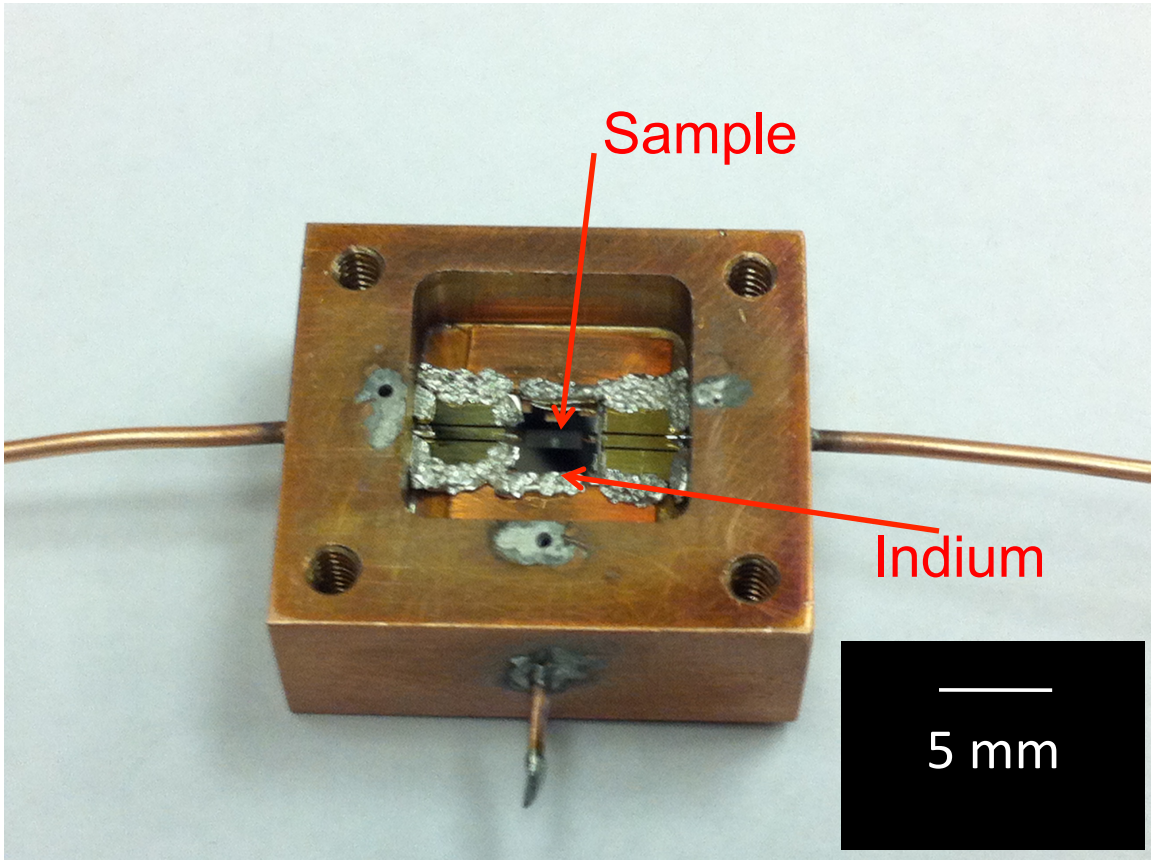

Figure 5.3: Photograph of copper sample box with indium ground contact. A lump of Indium was pressed between the on-chip ground plane and the sample box to achieve continuous ground contact.

launchers were made of Ti-Au on a sapphire substrate (see Fig. 5.2). The ground plane of the launchers was wire-bonded to the box to ensure ground contact. The center- conductor of the copper coaxial cable was soldered directly on to the center-strip of the coplanar microwave launchers of the box (see Fig. 5.2). For devices LEv6-2 and LEv6-3, I used an aluminum sample-box with non-magnetic SMA connectors.

After the silver paste was allowed to dry, securing the chip to the sample box, the on-chip coplanar transmission line and the on-chip continuous ground plane were wire-bonded with aluminum wire using a West-Bond wedge bonder (see Fig. 5.2). In some of our sample boxes, I found spurious resonances arising from improper ground contact. To ensure good ground contact, I pressed a lump of indium into those places where the ground plane of the box came in contact with the ground plane of the microwave launchers, in addition to the wire-bonds. In one case (device LEv6-1), I pressed a lump of indium between the ground plane of the device and the ground of the sample box, instead of using aluminum wire-bonds, to achieve a continuous ground contact (see Fig. 5.3).

The sample box was then sealed with a gasket made of indium wire. For some devices (LEv5-7, LEv5-15, LEv5-17, LEv6-1, LEv6-7), the lid of the copper sample box had a capillary made of copper through which the box was evacuated and He-4 gas was back-filled into the box. The capillary was then pinched and sealed with solder (see Fig. 5.1). This was done to reduce the amount of water vapor in the box.

Once the box was sealed air-tight (see Fig. 5.1), I inspected the box for microwave leakage. To do this, I connected the microwave input of the box to the excitation port 1 of a vector network analyzer (VNA), and terminated the microwave

output with a 50 Ω terminator. A horn was connected to the port 2 of the VNA. By measuring the S_{21} transmission of the microwaves over a wide range of frequencies between 300 kHz and 20 GHz, I was able to check for microwave leakage. Typically the leakage was below -100 dB from $0 - 20$ GHz. The device thus packaged was mounted on the cold stage of a dilution refrigerator for microwave characterization at millikelvin temperatures.

5.3 Dilution Refrigerator

The hermetically sealed copper box was attached to the mixing chamber of a dilution refrigerator. The dilution refrigerator was situated inside a copper shielded room to protect the device from electromagnetic radiation from surrounding electrical and electronic equipment (see Fig. 5.4). For some of my devices (see Table 5.1), I used an Oxford Kelvinox 100 dilution refrigerator with a base temperature of 20 mK. For other devices, I used a Leiden CF-450 cryogen-free dilution refrigerator, which used a pulse-tube compressor to cool the He-4 gas to 4 K in a closed cycle. Devices LEv5-7 was measured in both refrigerators.

5.3.1 Attenuation in the Oxford Kelvinox100 dilution refrigerator

To isolate the device from thermal noise at higher temperatures, the input microwave line to the device has a 10 dB attenuator mounted at 4 K, 20 dB at 0.7 K, and 30 dB at 20 mK on the mixing chamber (see Fig. 5.4). K&L low-pass filters with a 11 GHz cutoff were placed on the input and output of the sample box at the

Table 5.1: Table of devices and the dilution refrigerator they were measured in.

Device Name	Dilution Refrigerator
LEv5-56	Oxford Kelvinox100
LEv5-7	Oxford Kelvinox100 and Leiden CF-450
LEv5-ZK9	Oxford Kelvinox100
LEv5-15	Leiden CF-450
LEv5-17	Leiden CF-450
LEv6-1	Oxford Kelvinox100
LEv6-7	Oxford Kelvinox100
LEv6-2	Leiden CF-450
LEv6-3	Leiden CF-450

20 mK stage to further filter high frequency radiation. On the output microwave line, two 18 dB isolators (Pamtech Inc.) with bandwidths from 4 to 8 GHz were placed in series at 20 mK. The output microwave signal then goes to a 3 dB attenuator and then to a high electron mobility transistor (HEMT) amplifier (Caltech) at 4 K.

5.3.2 The Leiden CF-450 dilution refrigerator

The Oxford dilution refrigerator required the cryogen, liquid helium, to be replenished externally. The other system I used was a Leiden CF-450 cryogen-free dilution refrigerator (see Fig. 5.5). On this refrigerator, the input microwave line had a 20 dB attenuator mounted at 3 K, 10 dB at 50 mK, and 32 dB at 20 mK on the

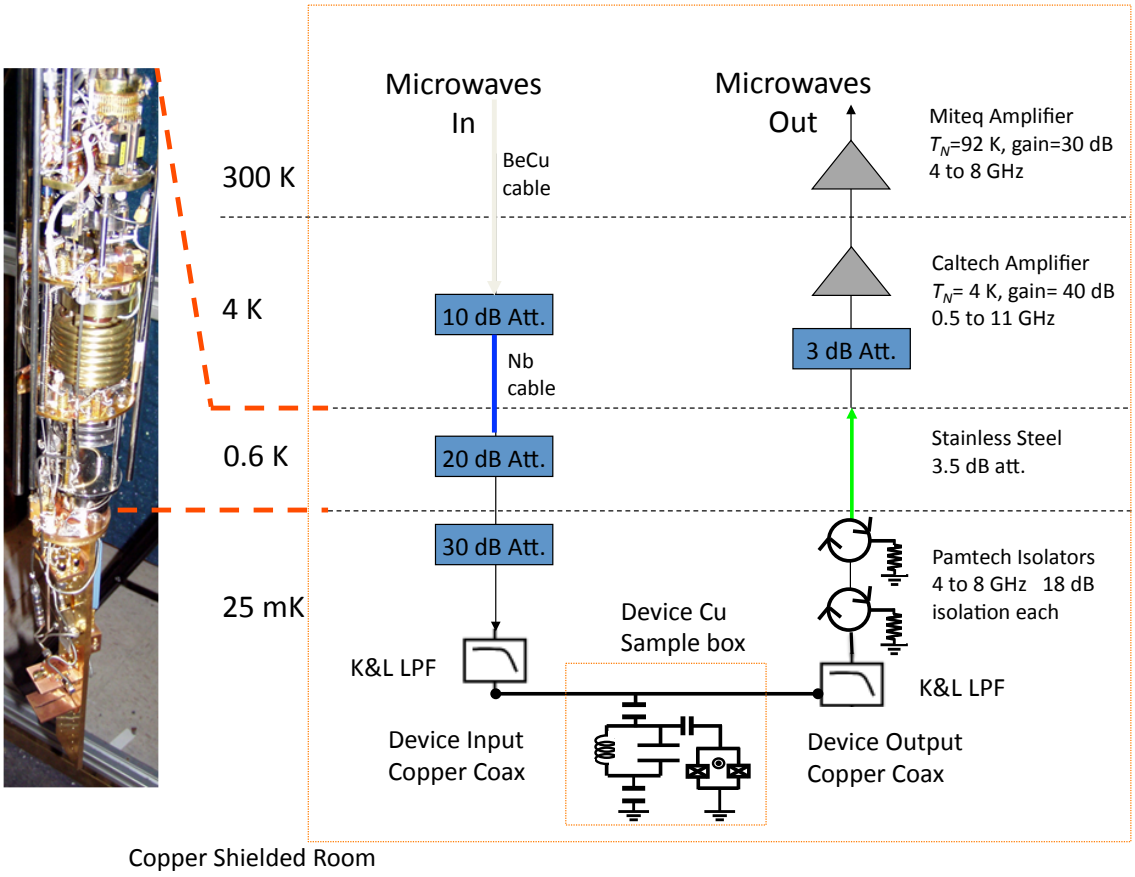

Figure 5.4: Schematic of attenuation, isolation and amplification in the Oxford Kelvinox-100 dilution refrigerator.

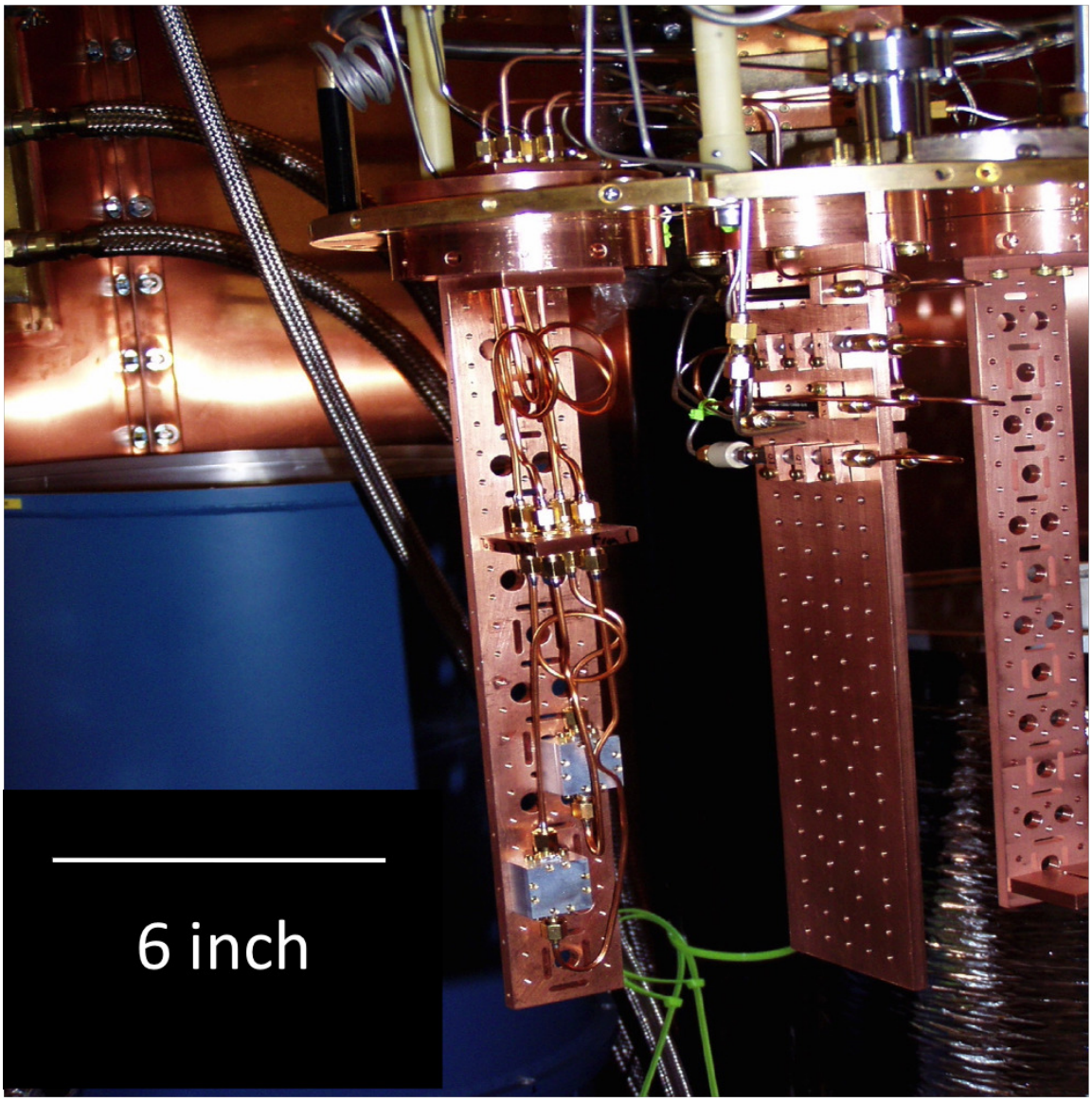

Figure 5.5: Photograph of the cold stage of the Leiden dilution refrigerator.

mixing chamber. K&L low-pass filters with a 11 GHz cut-off were used on the input and output of the sample box at 20 mK. The microwave line had two 18 dB isolators (Pamtech Inc.) with bandwidths from 4 to 12 GHz were placed in series at 20 mK.

5.4 Heterodyne Measurement Set-up

For measuring my devices, I applied up to three microwave tones to the input line (see Fig. 5.6). For consistency of terminology, I refer to them as the probe, coupler, and read-out tones. The probe tone was the spectroscopy tone that was usually close to the qubit transition frequency. The coupler tone was used to coherently drive the resonator in the low photon number limit. The read-out tone was on resonance with the bare cavity frequency f_r, typically at a power that was about 50 dB larger than the power of the coupler tone.

For my basic transmon spectroscopy and time-domain measurements discussed in Chapters 6 and 7, I applied just the probe and read-out tones (see Fig. 5.7). In most of the measurements, the read-out and probe tones were pulsed on and off, as described in the next section. When a measurement required the coupler tone, like in the photon number-splitting measurement and the measurement of the Autler-Townes effect (see Chapter 6), the coupler tone was applied continuously for the duration of the measurement (see Fig. 5.6).

I used a combination of Agilent 83732B, Agilent 83650B, Agilent E8257D and Agilent E8267D microwave signal generators to supply the microwave tones. A 10 MHz Rubidium frequency standard (Stanford Research Systems FS725) supplied the

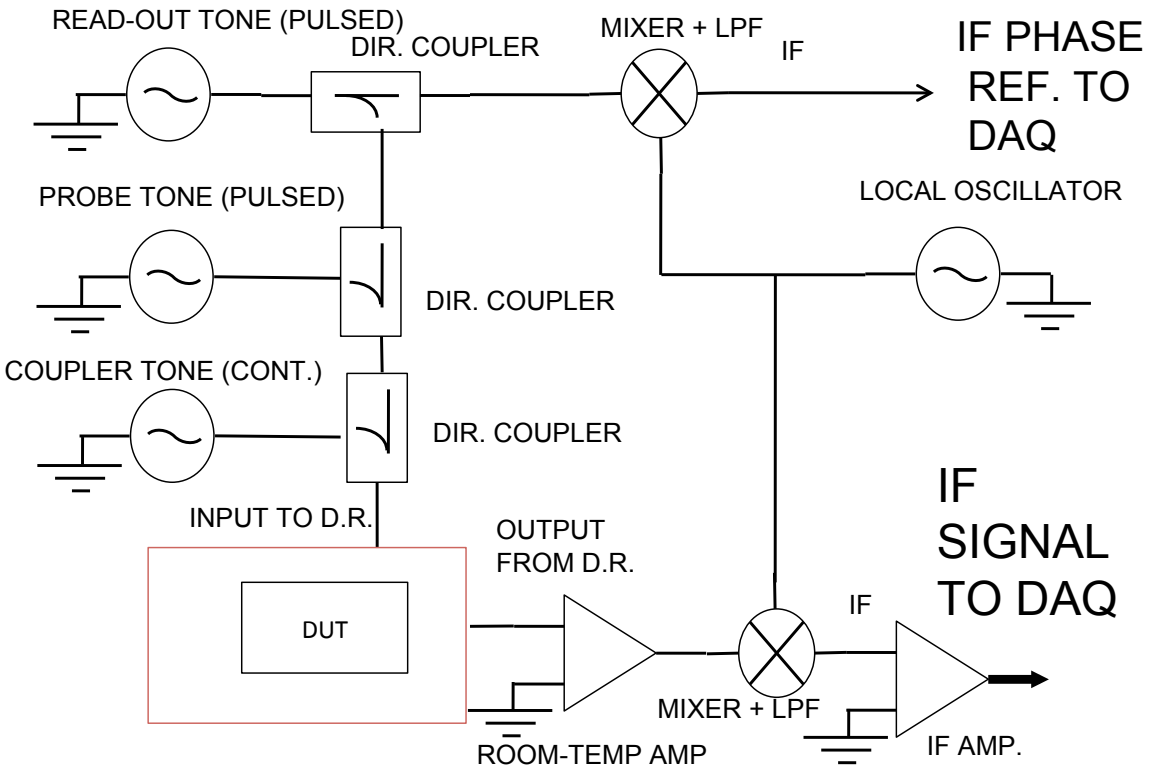

Figure 5.6: Schematic of the measurement setup outside the dilution refrigerator used for Number-splitting and Autler-Townes measurements. This set- up had three microwave tones input to the device (see Chapter 6). The read-out and probe tone are pulsed. The weak coupler tone is continuously applied ($\sim -145\,\mathrm{dBm}$).

clock reference for the signal generators. Each microwave tone was routed through a channel of a three-channel step attenuator (Aeroflex) in order to control the amplitude of the respective tone at the input to the refrigerator. The output from the attenuator channels was fed to the input line to the device using room-temperature directional couplers. For this purpose I used Mac-Technology C3205 series of directional couplers with an operational frequency range between 4 and 8 GHz and a coupled output power ranging between 6 dB (see Fig. 5.7) and 30 dB less than the input. The insertion loss for these directional couplers was less than 2 dB.

The microwave tones were then input to the refrigerator. A schematic of the attenuation and amplification inside the dilution refrigerator is shown in Fig. 5.4. A microwave tone input to the input line of the refrigerator went through different temperature stages with different attenuation. The output signal from the device was amplified by 40 dB using a HEMT LNA (Caltech) at 4 K. The dominant component of the output signal (RF) was at the read-out frequency with weak components at the probe and coupler tones. This signal was then demodulated using a heterodyne set-up as described below (see Fig. 5.7).

In the heterodyne set-up, the signal was first amplified by 38 dB using a room-temperature low noise amplifier (Miteq AMF-4F 4-8 GHz) and mixed down to an intermediate frequency (IF) of around 10 MHz using a double side-band mixer (Marki microwave) (see Fig. 5.7). The local oscillator (LO) frequency input to the mixer was generated by a microwave signal generator (Agilent 83732B). The frequency of the LO was chosen to be above the read-out frequency by an amount equal to the IF frequency (typically 10 MHz). The high frequency (RF + LO) output of the mixer

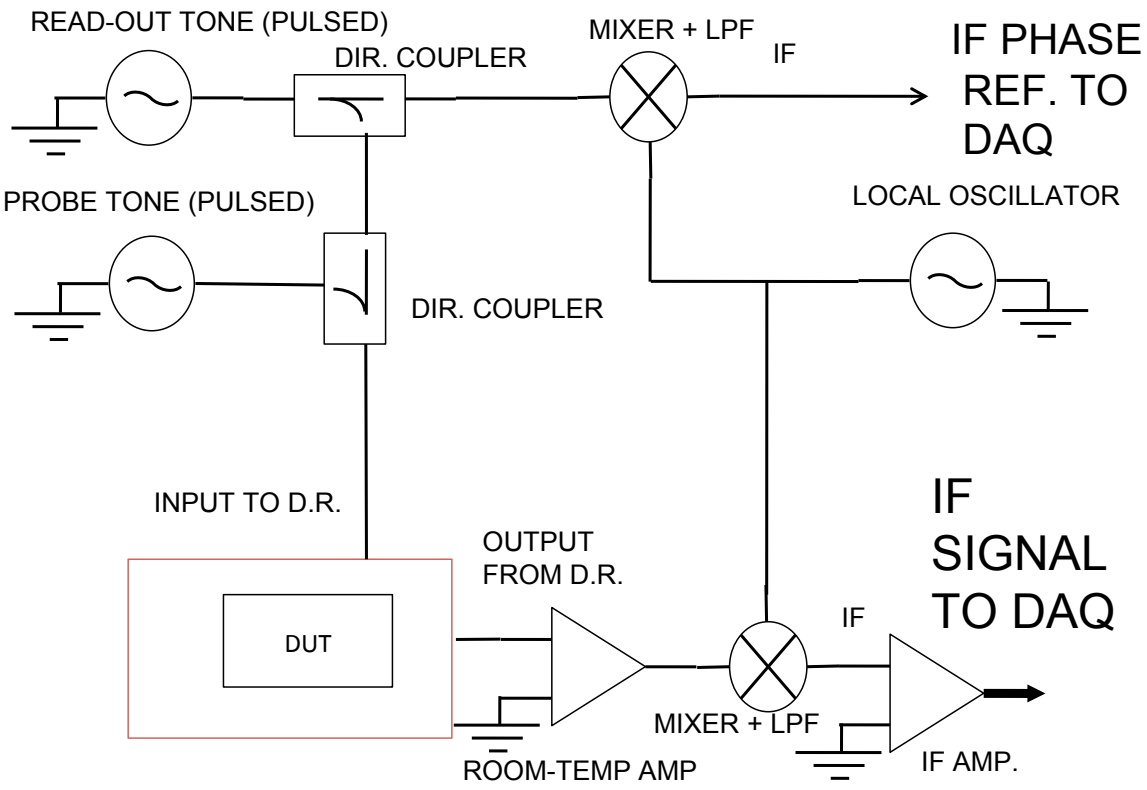

Figure 5.7: Schematic of measurement set-up external to the dilution refrigerator used for basic pulsed spectroscopy and time-domain measurements. The read-out and probe tone were pulsed for high- power Jaynes-Cummings read-out. Both tones were continuously applied during low-power dispersive read-out.

was filtered out using a low-pass filter (Minicircuits SLF-25). The low frequency (IF) component of the mixer output was sent to an IF amplifier and the amplified IF signal was then sent to an Agilent Aquiris data acquisition card (DAQ) for digitization. The DAQ digitized the 10 MHz IF signal at 1 GSa/s, with a resolution of 1 ns.

In order to have phase reference, a reference signal was generated at the IF frequency by power-splitting the read-out tone and sending it directly to a double side-band mixer (see Fig. 5.7). The low-pass filtered IF component of the mixer output was then sent to the DAQ, where the digitized signal from the device and the reference signal acquired by the DAQ were demodulated numerically into the in-phase (I) and out-of-phase (Q) quadrature voltages. The I and Q voltages were then averaged separately and written to a data file.

In most of my measurements, I pulsed the read-out and probe tones. To do this, I used two Agilent 33250A arbitrary waveform generators to generate the pulse sequence, which was then used to gate the read-out and probe signal generators in the pulsed mode of operation. The pulse output of the read-out signal generator was also used to trigger the DAQ. The instruments were controlled and programmed using LabView. Using this set-up I measured my transmons as described below.

5.5 Reading out the transmon state using the resonator

I used two methods to read out the state of my transmons – (a) A low power dispersive read-out and [44, 17] (b) a high power Jaynes-Cummings read-out [35, 52, 51]. Both these methods rely on the Jaynes-Cummings interaction between the

qubit and the resonator. While the dispersive read-out is operated in the low-power linear regime, the Jaynes-Cummings read-out is operated in the high power nonlinear regime of the interaction.

5.5.1 The low power dispersive read-out

The main principle of this read-out follows from the Jaynes-Cummings Hamiltonian in the dispersive approximation

$$H_{JC}^{(2)} \approx \hbar\omega_r a^\dagger a + \frac{\hbar\tilde{\omega}_{ge}}{2}\sigma_z + \hbar\chi a^\dagger a\sigma_z. \tag{5.1}$$

One can see from Eq. 5.1 that the resonator frequency changes by an amount $\pm\chi$ depending on the state of the qubit (see Fig. 5.8). This shift in the resonator frequency can be directly used to read out the qubit state. In practice, a weak continuous read-out tone is applied at the frequency $\omega_r - \chi$ (5.459 GHz in Fig. 5.8) while a second probe or spectroscopy tone is scanned around the qubit transition frequency. The amplitude of the transmitted read-out tone is continuously monitored while varying the frequency of the probe tone. When the probe tone comes near resonance with the qubit transition, there is an increase in the transmission of the read-out tone.

This read-out has the advantage of being nearly QND [18] since the demolition of the wave function is given by g/Δ which is a small fraction in the dispersive limit (see Chapter 3). This read out was used in [44] to perform a QND counting of the number of photons in the resonator.

The last term in Eq. 5.1 also represents an ac Stark shift of the qubit frequency depending on the number of photon stored in the resonator. Since the dispersive

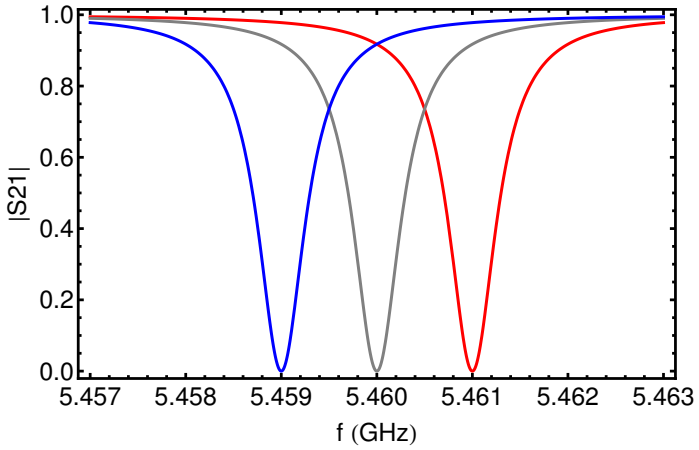

Figure 5.8: Theory plot of qubit state-dependent frequency shift of the resonator. Gray curve is for the bare resonator. Blue curve is the resonance dispersively shifted when the qubit is in the ground state. Red curve is the resonance dispersively shifted when the qubit is in the excited state.

read-out is operated in the continuous mode, the spectroscopy of the qubit reveals the ac Stark-shifted frequency. To find the unshifted qubit frequency, the amplitude of the read-out tone has to be made very low so that, on average, less than one photon is stored in the resonator in the steady state. The small amplitude of the transmitted signal necessitates a large number of averages (1000,000) per data point to achieve good SNR above the amplifier noise levels. This precludes this read-out scheme from being used for single shot measurements.

In my experiments, I employed the low-power dispersive read-out to locate the qubit transition initially (see Chapter 6), before setting up the high power read-out. When the amplitude of the read-out tone was very low ($\sim -150\,\mathrm{dBm}$), the qubit transition frequency was close to the qubit frequency without an ac Stark shift. The

high power Jaynes- Cummings read-out required a knowledge of the qubit transition frequency. Therefore the low-power read-out was a necessary step before the high-power read-out could be used.

5.5.2 High power read out – The Jaynes-Cummings nonlinearity

5.5.2.1 Two-level qubit coupled to a resonator

The Jaynes-Cummings interaction facilitates another type of read-out of the qubit state which was discovered at Yale by Reed *et al.* [35, 52, 51]. This read-out relies on a fundamental property of the Jaynes-Cummings nonlinearity – that the dispersive shift of the resonator frequency goes to zero in the limit of large photon number. To understand this read-out, I first consider a qubit coupled to a resonator.

In the limit of large photon number $n \gg n_{crit}$, the dispersive approximation breaks down. Therefore I consider the Jaynes-Cummings Hamiltonian in its original form,

$$H_{JC} = \hbar\omega_r a^\dagger a + \frac{\hbar\omega_{ge}}{2}\sigma_z + \hbar g(a^\dagger\sigma^- + a\sigma^+) \tag{5.2}$$

The n-excitation manifold of this Hamiltonian in the basis of states $|g,n\rangle, |e,n-1\rangle$ has the form of a 2×2 matrix:

$$\hbar\begin{bmatrix} (n-1)\omega_r + \omega_{ge}/2 & g_{ge}\sqrt{n} \\ g_{ge}\sqrt{n} & n\omega_r - \omega_{ge}/2 \end{bmatrix}. \tag{5.3}$$

The eigenvalues of this matrix are given by

$$E_{n,\pm} = (n-\frac{1}{2})\hbar\omega_r \pm \frac{\hbar}{2}\sqrt{\Delta^2 + 4g_{ge}^2 n} \tag{5.4}$$

where $\Delta \equiv \omega_{ge} - \omega_r$ is the detuning between the qubit and resonator frequencies.

From Eq. 5.4, it can be seen that a resonator coupled to a TLS has two qubit state-dependent resonator frequencies, given by

$$\hbar\omega_r^g = E_{n,-} - E_{n-1,-} \tag{5.5}$$

$$\hbar\omega_r^e = E_{n,+} - E_{n-1,+} \tag{5.6}$$

Figure 5.9 shows a plot of the frequencies $f_r^g = \omega_r^g/2\pi$ and $f_r^e = \omega_r^e/2\pi$ as a function of n, found from on Eq. 5.6 for bare parameter values $\omega_r/2\pi = 5.464\,\text{GHz}$, $g/2\pi = 70\,\text{MHz}$ and $\omega_{ge}/2\pi = 4.982\,\text{GHz}$. This set of parameters correspond to device LEv5-ZK9 (see Chapter 6). From Fig. 5.9, it can be seen that the state-dependent frequency of the resonator depends on n, approaching the bare resonator frequency f_r for $n \gg n_{crit}$. It can also been seen for a pure TLS, the frequencies f_r^g and f_r^e are symmetric about the bare resonator frequency $f_r = 5.464\,\text{GHz}$ for all values of n.

I now consider the case where the resonator is driven with a tone frequency f_d and amplitude ϵ_d (in units of frequency). Since the resonator has two frequencies f_r^g and f_r^e, the average photon number stored in steady state also depends on the qubit state. Semi-classically, this qubit state-dependent photon number can be written as [45]

$$\bar{n}_i = \frac{\epsilon_d^2}{(f_r^i(\bar{n}_i) - f_d)^2 + (\kappa/2)^2} \tag{5.7}$$

where κ is the rate of photon-loss in the resonator, $\bar{n}_g$ is the photon occupancy with the atom in the $|g\rangle$ excited state, and $\bar{n}_e$ is the photon occupancy when the quit is in the $|e\rangle$ state. Since the frequencies f_r^i depend on the photon number $\bar{n}$ themselves, Eq. 5.7 has to be be solved self-consistently to find the atom state-dependent photon

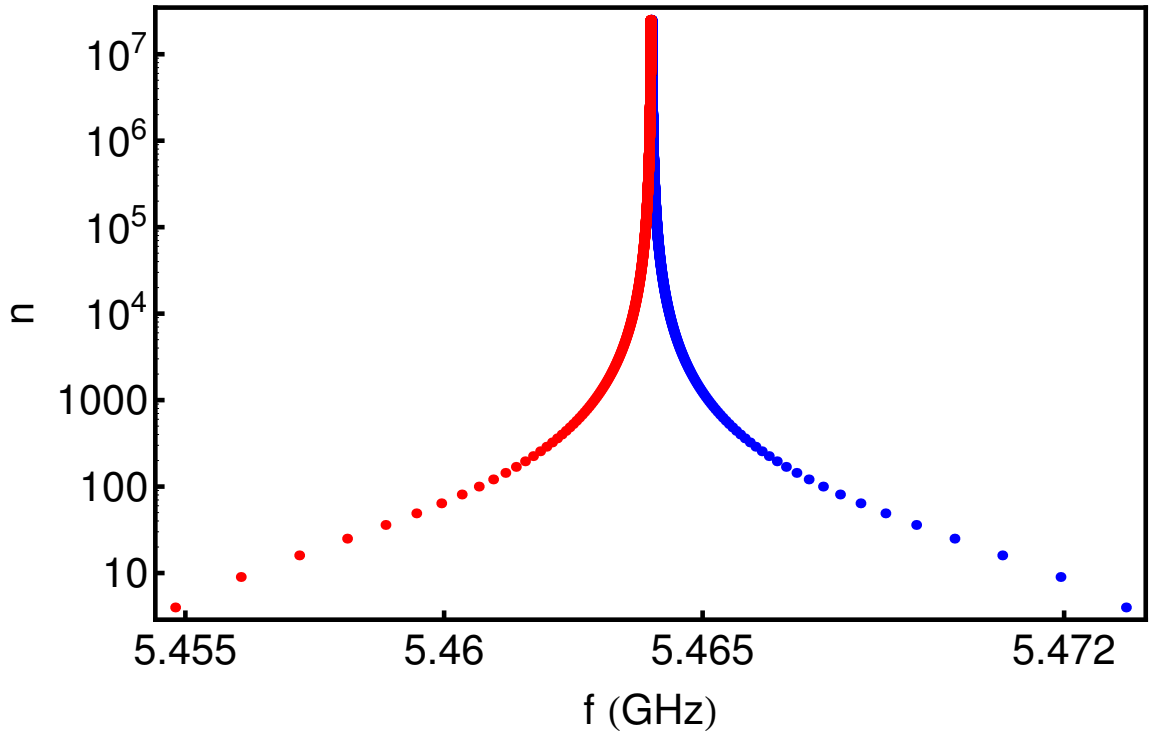

Figure 5.9: Plot of simulated f_r^g (blue) and f_r^e (red) of the resonator coupled to a pure TLS. The parameters for the bare Hamiltonian were $\omega_r/2\pi = 5.464\,\mathrm{GHz}$, $g/2\pi = 70\,\mathrm{MHz}$ and $\omega_{ge}/2\pi = 4.982\,\mathrm{GHz}$, corresponding to those of device LEv5-ZK9.

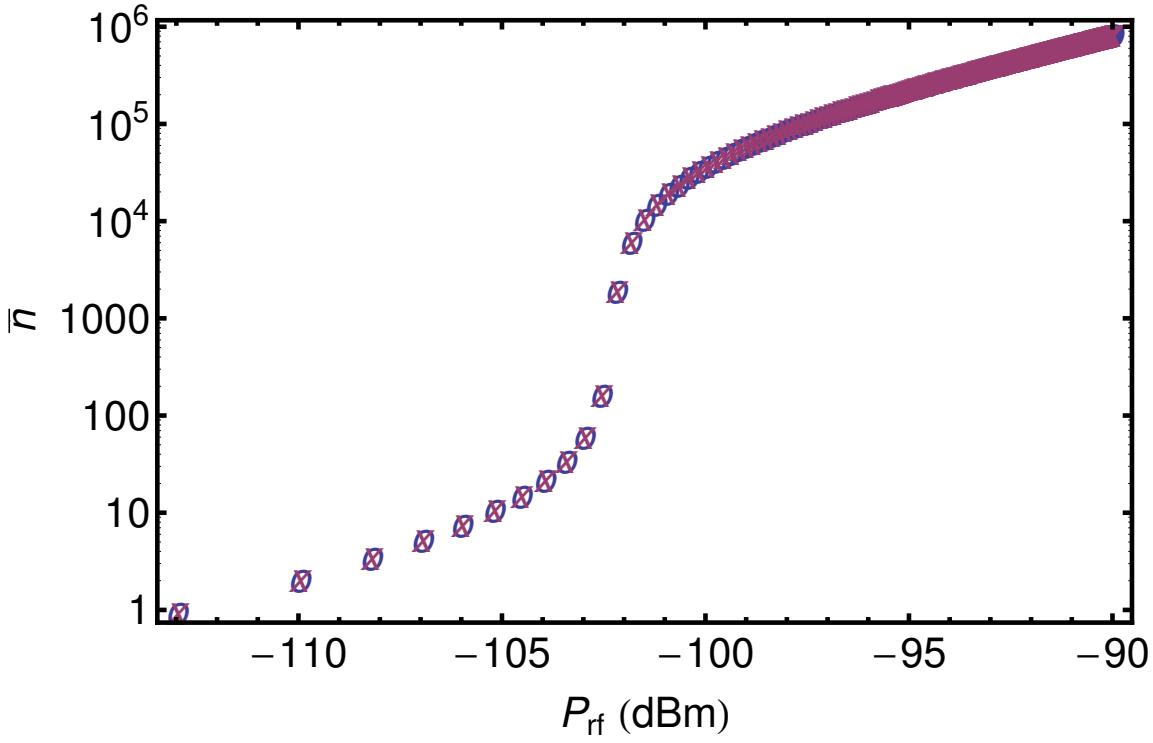

Figure 5.10: Log-Log plot of average photon number $\bar{n}$ at the bare resonator frequency vs drive power P_{rf} for a qubit coupled to a resonator, calculated from Eq. 5.7. The blue circles are $\bar{n}_g$ for qubit in the ground state. The purple 'x' are $\bar{n}_e$ for qubit in the excited state. The two curves overlap for the qubit case. P_{rf} is calibrated using $P_{rf} = 4\hbar Q_e \epsilon_d^2$ and $Q_e = 20,000$.

occupancy $\bar{n}_i$ in the resonator.

If the drive frequency is resonant with the bare resonator frequency ($f_d = f_r$), then because of the symmetry of f_r^g and f_r^e with respect to f_r, the photon numbers $\bar{n}_g$ and $\bar{n}_e$ are equal. This is shown in Fig. 5.10 where the curves for $\bar{n}_g$ and $\bar{n}_e$ overlap.

5.5.2.2 Multi-level system coupled to resonator

The system that I studied in my dissertation is a transmon coupled to a resonator. Since a transmon is a multi-level system, its interaction with a resonator is described using the generalized Jaynes- Cummings Hamiltonian that was discussed in Chapter 3. For a general m-level system interacting with a resonator, the n-excitation manifold of the generalized Jaynes-Cummings Hamiltonian is formed by m uncoupled atom-resonator basis states $\{|n,0\rangle, |n-1,1\rangle, \ldots, |n-m+1, m-1\rangle\}$. Therefore, there are m atom state-dependent resonator frequencies denoted by $f_r^i(\bar{n}_i)$ for $i \in \{0, \ldots m-1\}$. The qubit- resonator system discussed in the previous section was for the particular case $m = 2$.

Similar to the qubit case, the resonator now has m different frequencies, each corresponding to the transmon being in a different state. From the m eigenvalues of the Hamiltonian in the n-excitation manifold $\{E_{n,0}, E_{n,1}, ...E_{n,m-1}\}$, the m state-dependent resonator frequencies can be calculated, as in the TLS case, using

$$\hbar\omega_r^k = E_{n,k} - E_{n-1,k} \tag{5.8}$$

Figure 5.11 shows a plot for the frequencies f_r^g and f_r^e for the transmon in the $|g\rangle$ $(k = 0)$ and $|e\rangle$ $(k = 1)$ states respectively, found using the diagonalization procedure just described, for bare parameters $f_r = 5.464\,\text{GHz}$, $g_{ge}/2\pi = 70\,\text{MHz}$, and $\omega_{ge}/2\pi = 4.982\,\text{GHz}$. The striking difference between Fig. 5.11 and Fig. 5.9 is that the frequencies are no longer symmetric about the bare frequency f_r (5.464 GHz in Fig. 5.11).

If I now consider driving the resonator at the bare resonator frequency, since

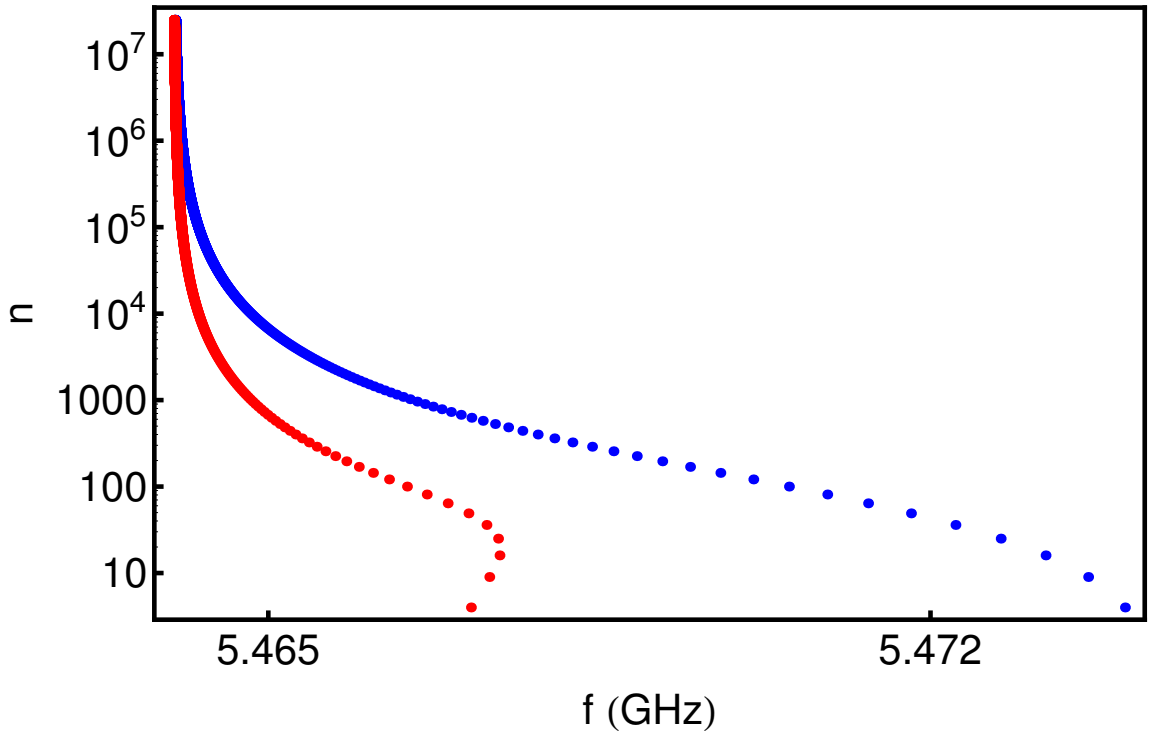

Figure 5.11: Plot of simulated f_r^g (blue) and f_r^e (red) for a resonator coupled to a four-level system vs photon number n. The parameters for the bare generalized Jaynes-Cummings Hamiltonian were $\omega_r/2\pi = 5.464\,\mathrm{GHz}$, $g/2\pi = 70\,\mathrm{MHz}$, $\omega_{ge}/2\pi = 4.982\,\mathrm{GHz}$, with $m = 4$ levels in the transmon Hamiltonian, corresponding to those of LEv5-ZK9.

the frequencies f_r^g and f_r^i are not symmetric about $f_d = f_r$, we have the result that $\bar{n}_g \neq \bar{n}_e$. Figure 5.12 shows a plot of $\bar{n}$ as a function of the drive power ($P_{rf} \sim \epsilon_d^2$), where ϵ_d is the amplitude of the drive expressed in frequency units. At a power of $P_{rf} \sim -102\,\mathrm{dBm}$ in Fig. 5.12, the photon occupancy with the transmon in $|g\rangle$, $\bar{n}_g$ (blue dots), is roughly a factor of 10^5 smaller than the photon occupancy in the resonator when the transmon is in $|e\rangle$. This large difference in the photon number gives rise to a large difference in the output signal and enables one to distinguish the occupancy of $|g\rangle$ from $|e\rangle$.

5.5.3 Implementing the high power Jaynes-Cummings read-out

I used a pulsed scheme to implement the Jaynes-Cummings read-out [35] of the transmon state. The pulse sequence is shown in Fig. 5.13. Initially, a read-out pulse of duration $5\,\mu$s is applied on resonance with the bare resonator frequency f_r. This pulse serves as a calibration for the transmitted signal voltage assuming, the qubit is in the ground state. After allowing the photons in the resonator to decay fully by waiting for around $80\,\mu$s (the decay time of the resonator was $1/\kappa \approx 1.5\,\mu$s), a probe or spectroscopy pulse was applied for a duration of $10\,\mu$s, on resonance with the qubit transition frequency, and at an amplitude large enough to saturate the transmon $|g\rangle \rightarrow |e\rangle$ transition. About 10 ns after turning off the probe pulse, a second read-out pulse was sent. The difference in the average transmitted voltage V_{out} between the two read-out pulses is proportional to the probability of the excited state P_e [35]. This way, the transmon state can be read out using the Jaynes-Cummings read-out.

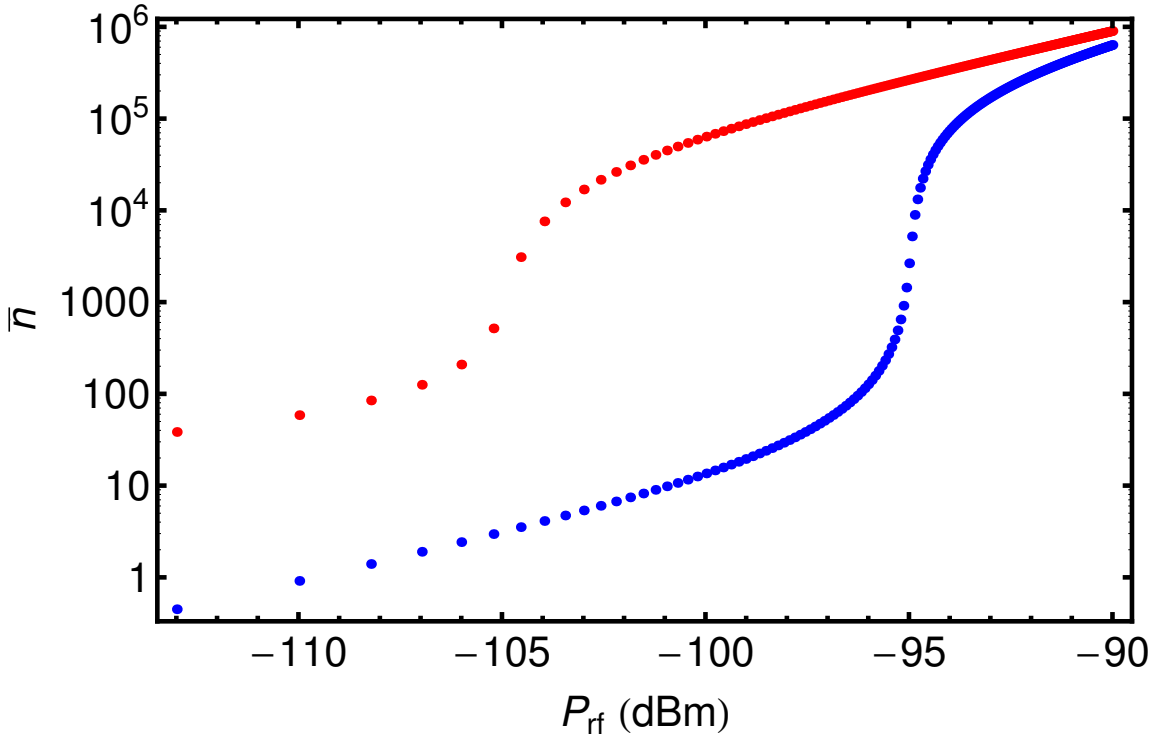

Figure 5.12: Log-Log plot of average photon number $\bar{n}$ at the bare resonator frequency vs drive power P_{rf} for a multilevel system coupled to a resonator, calculated from Eq. 5.7 for $m = 4$. The frequencies f_r^g and f_r^e were calculated by diagonalizing the generalized Jaynes- Cummings Hamiltonian with 4 levels in the transmon, for parameter values $f_r = 5.464\,\text{GHz}$, $g_{ge}/2\pi = 70\,\text{MHz}$, and $\omega_{ge}/2\pi = 4.982\,\text{GHz}$. The blue dots are $\bar{n}_g$ for qubit in the ground state. The red dots are $\bar{n}_e$ for qubit in the excited state. P_{rf} is calibrated using $P_{rf} = 4\hbar Q_e\,\epsilon_d^2$, for $Q_e = 20,000$.

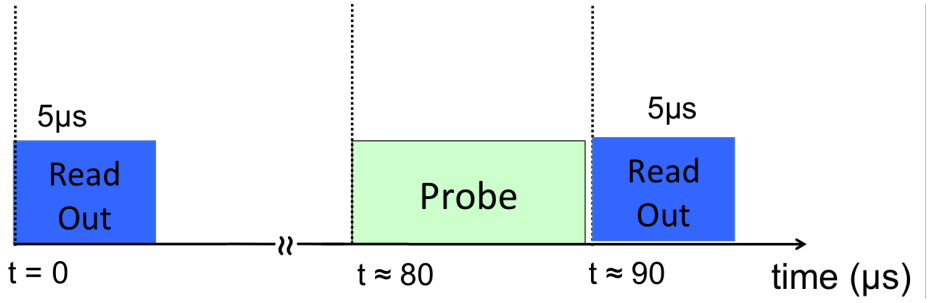

Figure 5.13: Pulse sequence for high power Jaynes-Cummings Read-out.

5.5.4 Optimizing the read-out

5.5.4.1 Optimizing the read-out power

As shown in Fig. 5.12, the transmon state-dependent photon occupancy of the resonator is maximally different at an optimal drive power. To determine this optimal read-out power, I repeated the pulse sequence shown in Fig. 5.13 for different values of the read-out power. Figure 5.14 shows a plot of the difference between the mean amplitude of the two read-out pulses V_{out} as a function of the applied drive power P_{rf} as measured on the CPW transmission line for device LEv5-ZK9. For a transmission measurement, when the transmon is in $|g\rangle$ a large transmissivity (blue curve) is observed and when the transmon is in an excited state ($|e\rangle$, $|f\rangle$ etc) a small transmissivity is observed (red curve). This behavior is seen in Fig. 5.14. From this transmission s-curve, the optimal read-out power can be determined ($\sim$ -97 dBm in Fig. 5.14).

I note that the microwave power to have a single photon, on average, in this resonator was roughly 1 aW or -150 dBm, while the power of the read-out tone in this

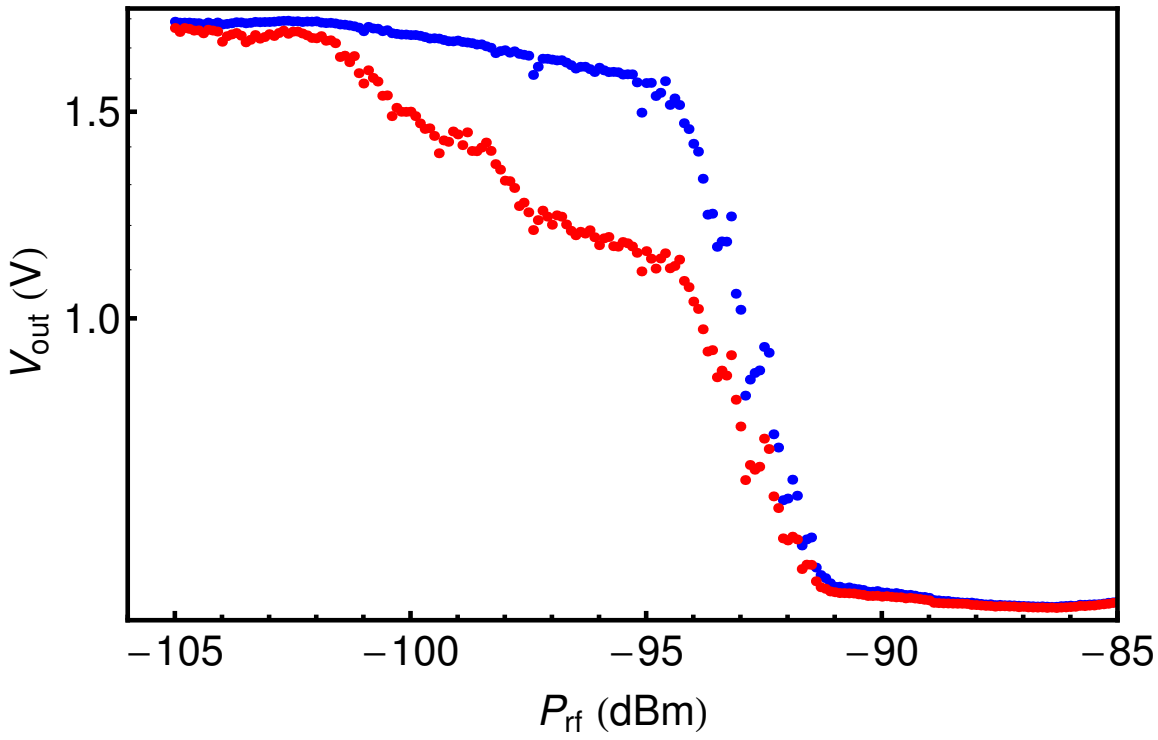

Figure 5.14: Plot of measured transmitted pulsed microwave voltage amplitude at $f_r = 5.464\,\text{GHz}$, as a function of the drive power P_{rf} for device LEv5-ZK9. The blue curve is the transmitted voltage for the calibration read-out pulse, corresponding to when transmon is in $|g\rangle$. The red curve is the transmitted voltage for the read-out pulse after qubit excitation corresponding to transmon in $|e\rangle$. At $P_{rf} = -97\,\text{dBm}$, the difference between the transmitted voltages is maximum.

scheme was about six orders of magnitude higher, offering a significant advantage in the SNR compared to the dispersive read-out.

5.5.4.2 Optimizing the read-out pulse-width

The read-out contrast can be further optimized by varying the width of the read-out pulses. In order to do this, I initially sent a read- out pulse of length $5\,\mu$s to calibrate the output voltage with the qubit in the ground state. After waiting for about $80\,\mu$s ($1\kappa \approx 1.5\,\mu$s), I prepared the qubit in the excited state by sending a π- pulse at the qubit frequency. The length of the π-pulse was determined from Rabi oscillations discussed in Chapter 7. About 10ns after turning off the qubit π-pulse, I sent a second read-out pulse of $5\,\mu$s length. This pulse sequence is similar to the one shown in Fig. 5.13, with the long ($10\,\mu$s) probe pulse replaced by a π-pulse. This constitutes a single shot of the measurement. The average transmitted voltage for each read-out pulse was then recorded. Repeating this process several times ($\sim 500,000$), I obtained data for a histogram showing the distribution of output voltages for both read- out pulses.

Figure 5.15(a) shows the histogram for the transmitted voltage for the calibration read-out pulse of width $5\,\mu$s for device LEv6-7. This histogram characterizes the output voltage when the transmon is in the ground state. From Fig. 5.15 (a), about 85% of the counts are within the larger lobe centered around 0.032 V. Therefore this is the single-shot read-out voltage corresponding to the transmon being in $|g\rangle$. Figure 5.15(b) shows the histogram for the transmitted voltage for the second read-out

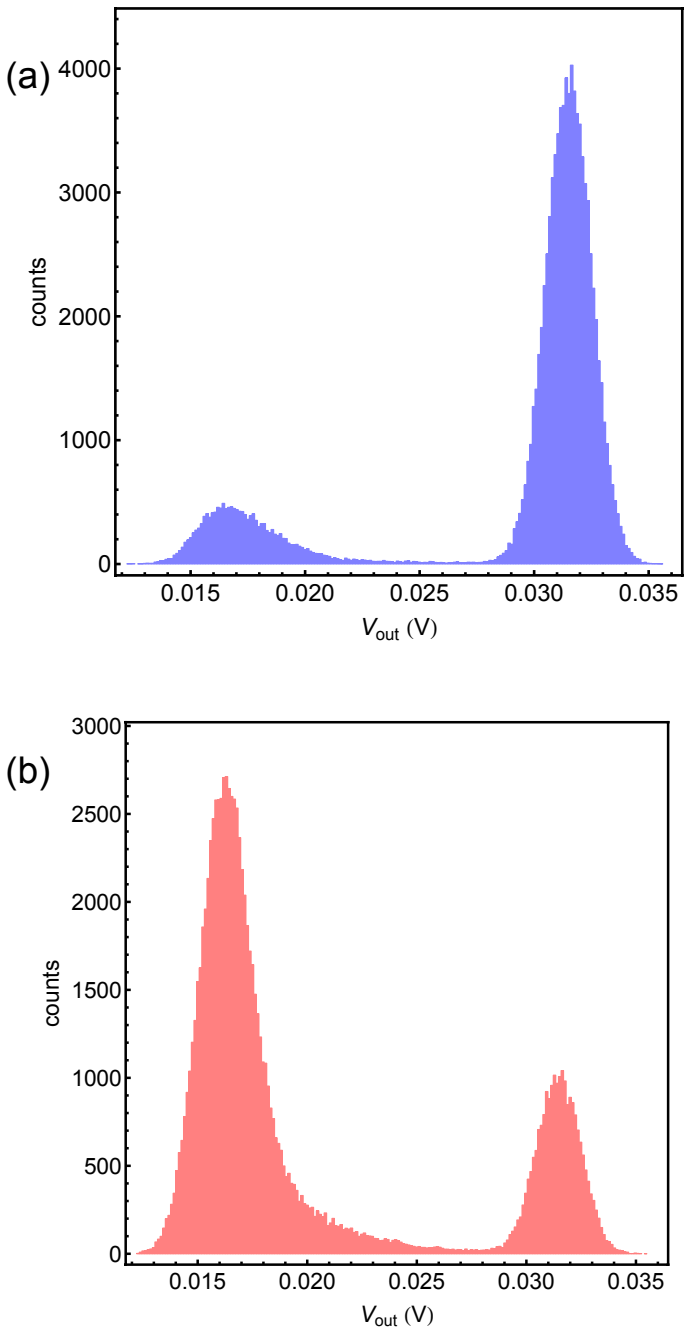

Figure 5.15: Histogram of measured transmitted voltages of read- out pulses for device LEv6-7. (a) Histogram of transmitted voltage for the calibration pulse, with qubit in $|g\rangle$. (b) Histogram of transmitted voltage for read-out pulse after qubit preparation in $|e\rangle$ using a $\pi-$pulse.

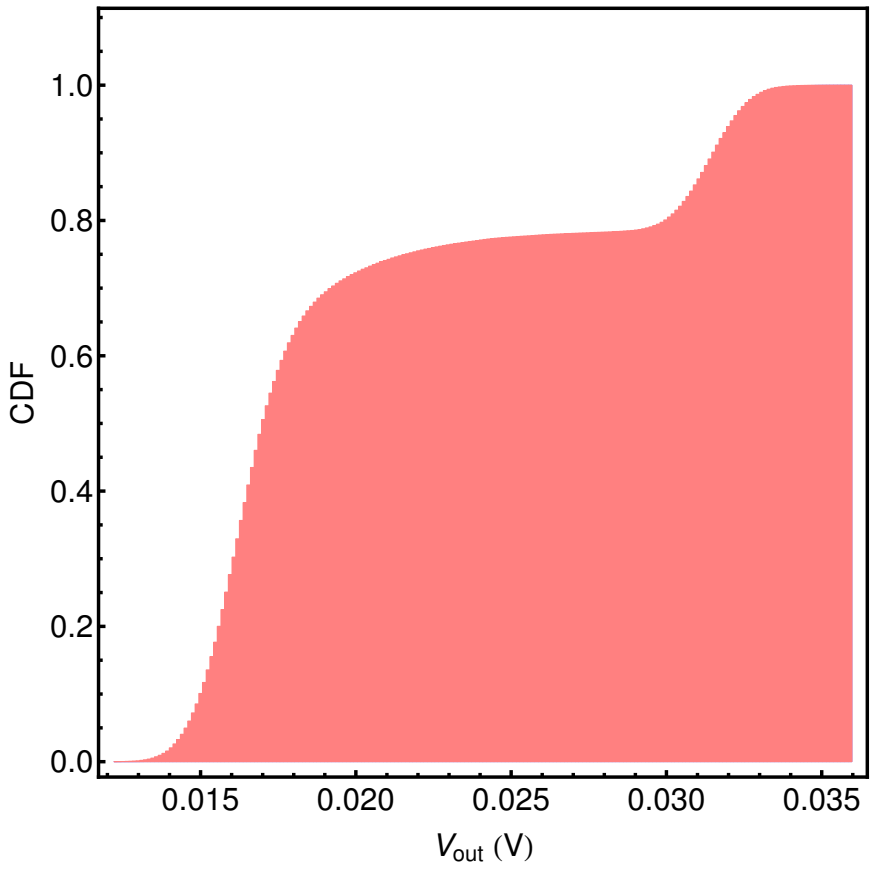

Figure 5.16: Cumulative distribution function of the output voltage histograms for device LEv6-7. Read-out fidelity from the CDF is about 55%.

pulse of width 5 μs for device LEv6-7. This histogram characterizes the output voltage when the transmon is in the excited state. From Fig. 5.15(b), about 70% of the counts are within the larger lobe centered around 0.018 V, so this is the single-shot read-out voltage corresponding to the transmon being in $|e\rangle$.

From the cumulative distribution of the two histograms (see Fig. 5.16) the read-out fidelity for $|e\rangle$ was found to be 55%. The rather low fidelity is caused by the short relaxation time of the device and the presence of "false counts" denoted by the smaller lobe of the ground state histogram in Fig. 5.15(a). This lobe represents

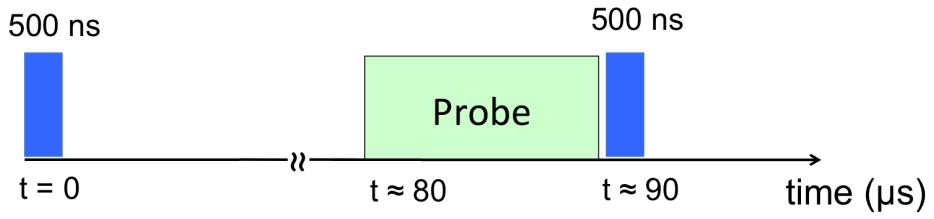

Figure 5.17: Pulse sequence for single shot measurement on device LEv6-7 using a pulse-width of 500 ns for the read-out pulses.

those instances when the qubit was reported to be in the excited state even though no excitation was applied. The cause for such "false counts" is not yet understood and is worth examining in the future.

Measurement of single-shot histograms can be used to optimize the read-out pulse-width using the read-out fidelity as a metric. Figure 5.18 shows the histograms for device LEv6-7 when the read-out pulse-width was only 500 ns. The pulse sequence for this measurement is shown in Fig. 5.17. The voltage histograms for the transmon in $|g\rangle$ (blue) and $|e\rangle$ (red) states are not as well resolved as in Fig. 5.15. The fidelity for reading out $|e\rangle$ in this case was around 15%.

By varying the pulse-width, I found that a read-out pulse-width of about 5 μs was optimal, with a maximum read-out fidelity of close to 55%. Increasing the pulse-width beyond 5 μs did not improve the fidelity [35]. The optimal pulse length depends on the decay rate of the resonator. In my case, the photons in the resonator decay on a time- scale $1/\kappa \sim 1.5\,\mu$s.

Some aspects of the Jaynes-Cummings read-out are not yet fully understood. I

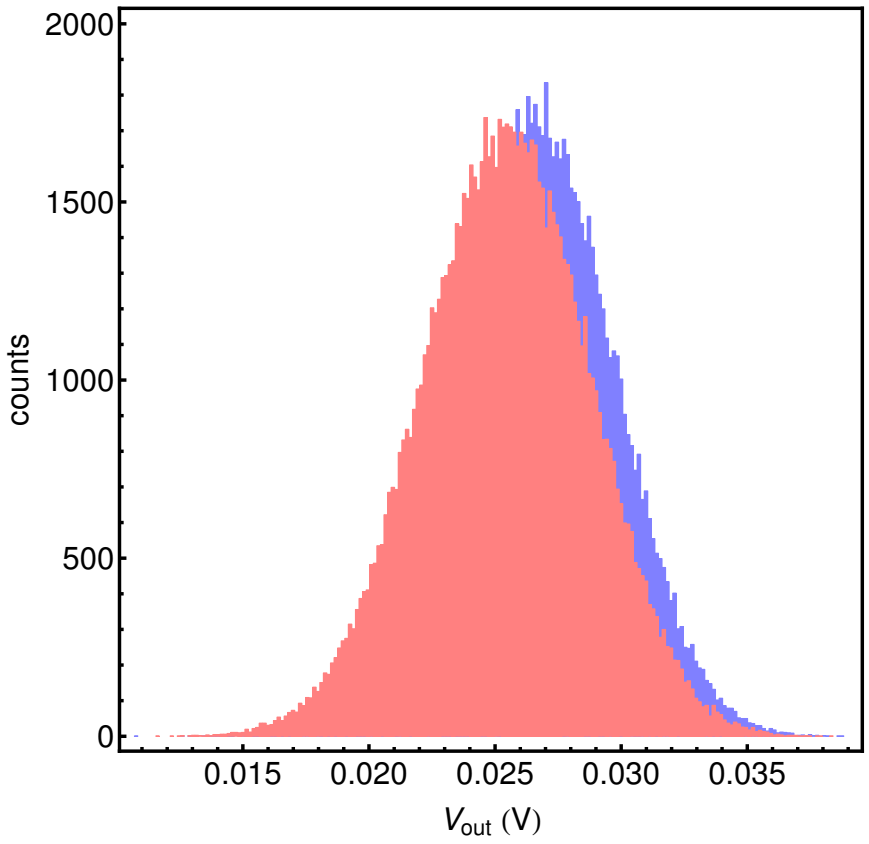

Figure 5.18: Histogram of measured transmitted microwave voltage amplitude for read-out pulses of width 500 ns for device LEv6-7.

found that this read-out performed better when the qubit transition frequency was below the resonant frequency of the resonator. This is probably because the closest qubit transition to the resonator, in this case, is the fundamental $|g\rangle \rightarrow |e\rangle$ transition. All higher transitions are farther detuned from the resonator making their "pull" on the resonator frequency small compared to that due to the $|g\rangle \rightarrow |e\rangle$ transition. I did not make a quantitative study of this aspect. Another aspect of the high power read-out that is not fully understood is that of false counts that I mentioned earlier (see Fig. 5.15(a)). One concern is that this read-out applied high power microwaves to the input line of the device. While I did not notice any change in the temperature of the mixing chamber of the dilution refrigerator, it will be interesting to examine if this read-out causes heating that could affect the coherence of devices.

5.6 Summary

In this Chapter, I described the experimental set-up I used for measuring transmons. In particular, I described the package used to mount the device. I then described the elaborate dilution refrigerator set-up including how it filtered out thermal noise from high temperature stages. I next described the amplification and heterodyne demodulation of the signal. Finally I discussed the two main read-out methods employed in my measurements and explained the principle of their operation for reading out the qubit state.

Chapter 6

Spectroscopic measurements of transmon-resonator cQED devices

6.1 Overview

In this chapter, I begin by discussing my spectroscopic measurements of lumped-element resonators (mainly LEv6-1). Then I discuss spectroscopy of transmon qubits (mainly LEv5-56, LEv5-ZK9, LEv6-1 and LEv6-7) coupled to lumped-element resonators. Using these results, I show how the 'bare' and 'dressed' parameters of the coupled transmon-resonator system can be determined. I then describe the measurements I made of photon number-splitting of the transmon spectrum under coherent driving and the nonlinear relation between the photon number and applied coupler power. I found that even in the absence of a coherent coupler tone, a weak n=1 photon peak appears, indicating a small thermal population of photons in the resonator. I was able to observe the Autler-Townes splitting of this n=1 photon peak in the presence of a coupler tone. I show that this effect can be understood based on an Autler-Townes mechanism involving the four lowest lying dressed resonator-transmon levels. I did a full master equation simulation with two transmon levels and up to ten resonator levels and found good qualitative and quantitative agreement with data.

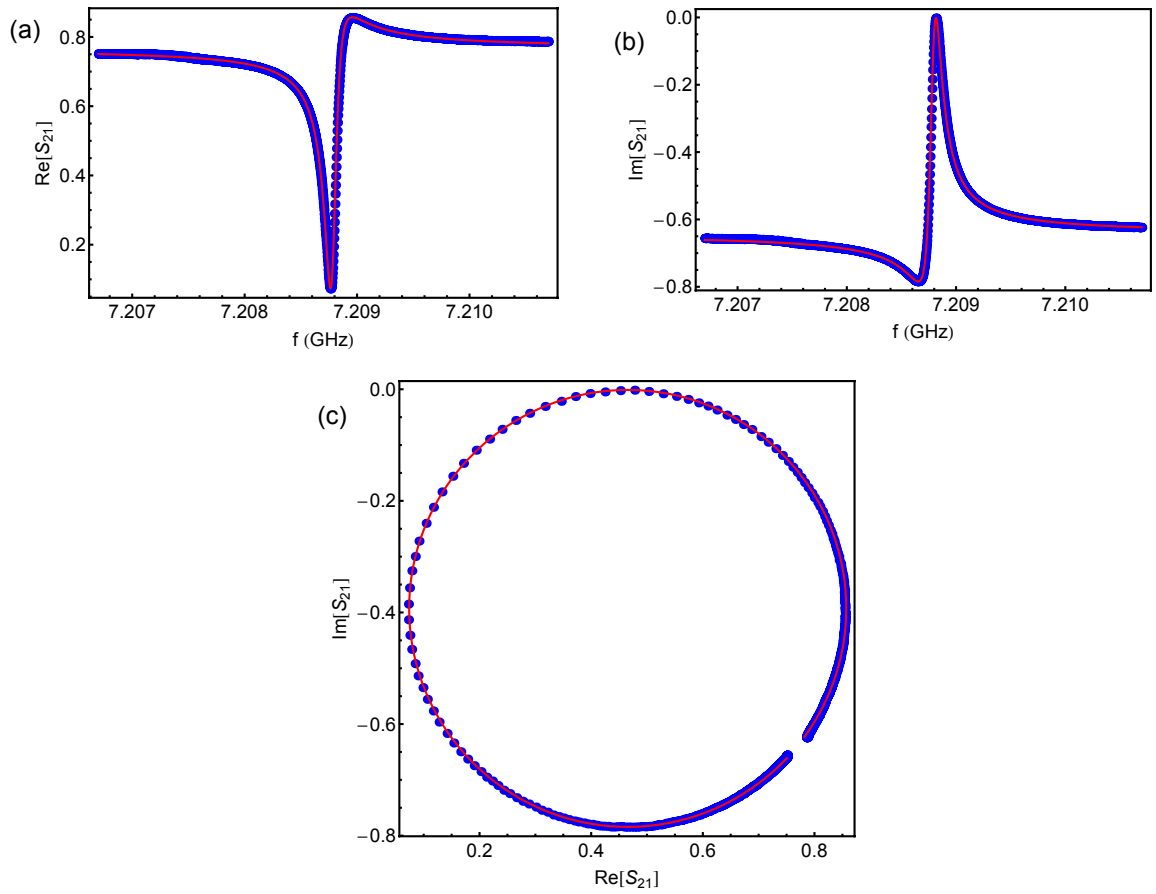

Figure 6.1: Plots of S_{21} vs f for device LEv6-1 with fit. (Blue dots) Measured data for an applied power of $P_{rf} = -100\,\mathrm{dBm}$. (Red curve) Fit using Eq. 6.1 with $f_r = 7.2087\,\mathrm{GHz}$, $Q_L = 56,000$, $Q_e = 73,000$ and $Q_i = 200,000$. (a) Plot of $\mathrm{Re}(S_{21})$ vs f. (b) Plot of $\mathrm{Im}(S_{21})$ vs f. (c)Parametric plot of $\mathrm{Im}(S_{21})$ vs $\mathrm{Re}(S_{21})$ in the complex plane of S_{21}

.

Table 6.1: Measurement sequence for transmon-resonator devices.

	Measurement	Parameters measured
1	S_{21} vs f – resonator	ω_r, Q_L, Q_c, Q_i
2	S_{21} vs f vs P_{rf} – resonator	ω_r, $\omega_r - \chi_{ge}$, χ_{ge}
3	low power dispersive spectroscopy – qubit	$\tilde{\omega}_{ge}$, $\chi_{ge} - \chi_{ef}/2$
4	S-curve –Jaynes-Cummings read-out optimization	Optimal read-out power
5	Pulsed spectroscopy – Jaynes-Cummings read-out	$\tilde{\omega}_{ge}$, $\tilde{\omega}_{gf}/2$, E_c, E_J
6	Time-domain measurements of qubit	T_1, T_2^*, f_{Rabi} etc.

6.2 The resonator

Table 6.1 shows the sequence of measurements I made after cooling a device to base temperature and the parameters I obtained from each measurement. The first measurement performed on a device after cooling was spectroscopy of the resonator. To do this, microwaves were input to the refrigerator and the phase and amplitude of the transmitted microwaves on the output were observed. In particular, I measured the output-to-input voltage ratio $S_{21} = V_2/V_1$ as described in Chapter 5. For my devices, when the microwave frequency was scanned near the the resonance frequency of the resonator, microwaves are absorbed by the resonator and the resonance appears as a 'notch' or dip in S_{21}. For example, Fig. 6.1 shows S_{21} for device LEv6-1 for an input power of around -100 dBm.

Following M. Khalil *et al.* [85], the complex S_{21} data was fit using the Diameter

Correction Method using the the expression

$$S_{21}(\omega) = 1 - \frac{Q_L/|Q_e|e^{i\phi}}{1 + 2iQ_L\left(\frac{\omega-\omega_r}{\omega_r}\right)} \tag{6.1}$$

where Q_L is the total or loaded quality factor of the resonator, Q_e is the external quality factor due to the coupling to the CPW transmission line, and ϕ is a complex phase factor that accounts for the asymmetry of the resonance lineshape [85]. The fits to the $\mathrm{Re}[S_{21}]$ (in-phase) and $\mathrm{Im}[S_{21}]$, along with the fit to the circle in the argand plane of S_{21} for device LEv6-1 are shown in Fig. 6.1 (as red curves).

From the fits, I find the resonance frequency ω_r, the total quality factor Q_L and the external quality factor Q_e. Using the expression

$$\frac{1}{Q_L} = \frac{1}{Q_e} + \frac{1}{Q_i} \tag{6.2}$$

I can then find Q_i or the intrinsic quality factor due to loss in the resonator. From the S_{21} fits for device LEv6-1 (see Fig. 6.1), I determined $\omega_r/2\pi = 7.2087\,\mathrm{GHz}$, $Q_L = 56,000$, $Q_e = 73,000$ and $Q_i = 200,000$. The quality factor Q_L is also related to the total decay-rate of photons stored in the resonator according to $Q_L = \omega_r/\kappa$, giving $\kappa = 2\pi(126)\,\mathrm{kHz}$ for this device. In the presence of strong asymmetry in the resonance lineshape, an accurate determination of Q_i becomes difficult using Eq. 6.2 as the external quality factor is a complex quantity. In such cases, as shown in [85], $|Q_e|$ can be replaced by $\mathrm{Re}[Q_e]$.

I also measured at S_{21} at very low powers, around $-150\,\mathrm{dBm}$, which typically correspond to the single-photon limit for the resonator. This data for device LEv6-1 is shown in Fig. 6.2. The external and intrinsic quality factors for this low-power data are $Q_e = 70,000$ and $Q_i = 180,000$. The shift in the resonance frequency by

Table 6.2: Measured resonator parameters of LEv5 and LEv6 devices. The last column gives the values of Q_e found in Microwave Office simulations (see Chapter 4).

Device Name	$\omega_r/2\pi$ (GHz)	Q_L	Q_i	Q_e	Q_e (MWO)
LEv5-56	5.435	29,862	199,644	35,114	36,315
LEv5-7	5.476	15,300	180,000	19,600	22,000
LEv5-ZK9	5.460	18,000	180,000	20,000	22,000
LEv5-15	5.331	15,000	80,000	18,460	20,000
LEv5-17	5.345	45,000	200,000	58,064	64,000
LEv6-1	7.208	56,000	200,000	73,000	74,000
LEv6-7	7.201	43,000	213,000	56,000	74,000
LEv6-2	7.195	52,000	187,000	69,000	74,000
LEv6-3	7.189	50,000	181,000	69,000	74,000

about 1 MHz between the high power and low power measurements is caused by the interaction with the qubit, and will be discussed in the next section. A summary of the resonator measurements for all my devices is shown in Table 6.2

6.2.1 S_{21} vs f vs P_{rf}

The second set of measurements I made on each device was to find S_{21} as a function of frequency f and input microwave power P_{rf}. Figure 6.3 shows this data for device LEv6-1. Each horizontal scan represents S_{21} around the resonator's resonance frequency for a given input power, and the scan was repeated by stepping the

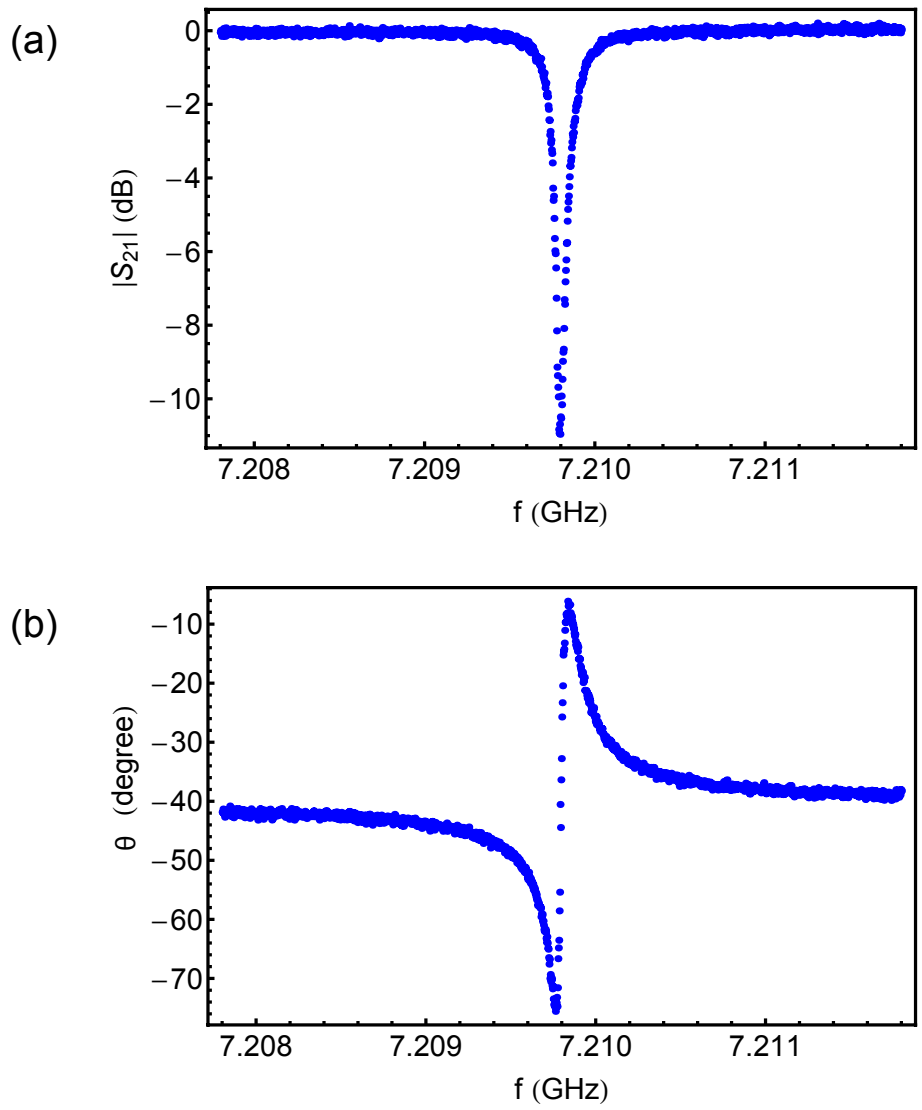

Figure 6.2: S_{21} vs f for device LEv6-1 for an input power $P_{rf} = -150\,\mathrm{dBm}$ (a) Log of $|S_{21}|$ in dB vs frequency f (b) Phase θ of S_{21} in degrees vs f.

input power through the values given along the y-axis. It can be seen in Fig. 6.3 that the resonator has two frequencies, one corresponding to the bare resonator (~ 7.2088 GHz) at high drive powers ($P_{rf} \sim -100\,\mathrm{dBm}$), and the other corresponding to the dispersively shifted frequency with the transmon in the ground state, due to the Jaynes-Cummings interaction (see Chapter 5). At low powers and low photon numbers, the resonator frequency is dispersively shifted due to coupling to the transmon, as described in Chapter 5. This qubit pull on the cavity diminishes to zero as the number of photons increases and above a threshold power $\sim -110\,\mathrm{dBm}$, the bare resonator frequency is recovered. Beyond this power, the resonator behaves linearly, as if it were uncoupled to the transmon.

As shown in Chapter 3, using the generalized Jaynes-Cummings Hamiltonian, up to second order in the dispersive approximation, the dispersively shifted frequency is given by

$$\tilde{\omega}_r - \chi \approx \omega_r - \chi_{ge} \tag{6.3}$$

Knowing both ω_r and $\tilde{\omega}_r - \chi$ from experiment, one can estimate $\chi_{ge} \equiv g_{ge}^2/\Delta_{ge}$. For device LEv6-1, $\chi_{ge}/2\pi \approx 1\,\mathrm{MHz}$. To determine g_{ge} and Δ_{ge}, I needed to perform qubit spectroscopy, which I discuss in the next section. In the intermediate power regime, between -120 dBm and $-110\,\mathrm{dBm}$, the resonator is classically bistable and this results in greater transmission and a suppression of the characteristic resonance dip [68].

For comparison, the blue curve superposed on the data in Fig. 6.3 is a plot of

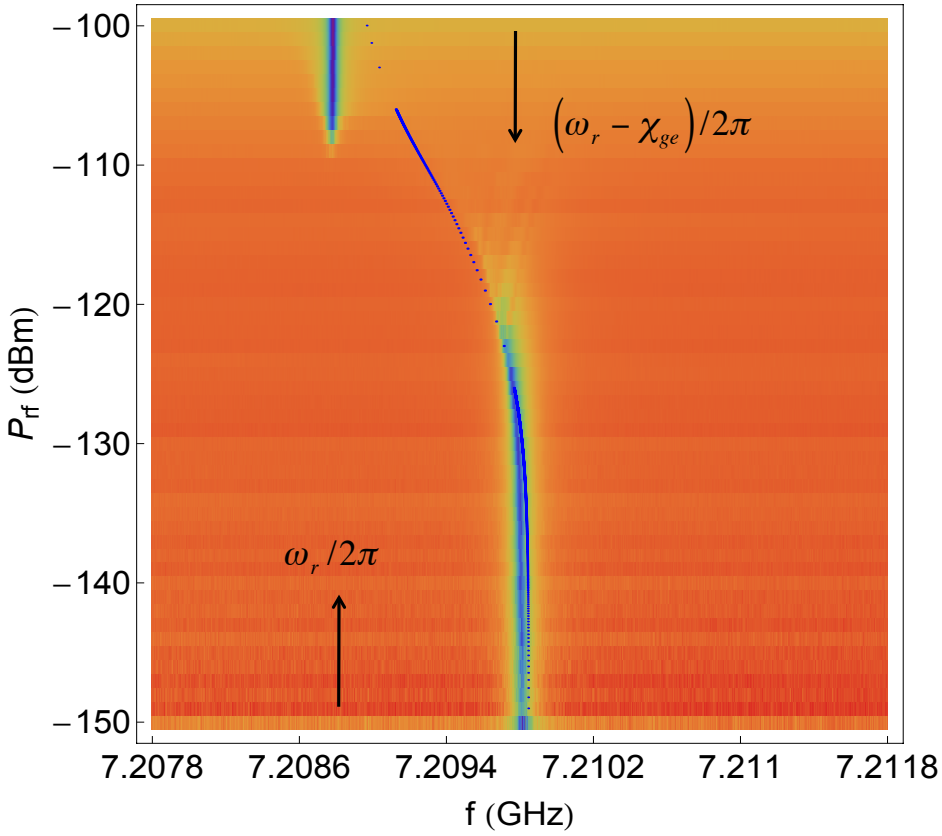

Figure 6.3: Plot of Log-magnitude of S_{21} transmission of the microwaves near the resonator frequency, while varying the drive power. At low powers, we can see the dispersively shifted resonator frequency $\sim 7.21\,\mathrm{GHz}$. At large drive powers, the bare resonator frequency is recovered at ~ 7.2087 GHz. For this device, the qubit transition frequency was at $\tilde{\omega}_{ge}/2\pi = 5.4\,\mathrm{GHz}$.

the calculate resonator frequency f_r^g, when the transmon is in the ground state, using Eq. 5.8 (see Chapter 5). For the parameters of the generalized Jaynes-Cummings Hamiltonian, I used $\omega_r/2\pi = 7.2087\,\mathrm{GHz}$, $\omega_{ge}/2\pi = 5.4\,\mathrm{GHz}$, and $g_{ge}/2\pi = 43\,\mathrm{MHz}$. For this calculation, the n-excitation manifold of the generalized Jaynes-Cummings Hamiltonian, with ten qubit levels in the manifold, was diagonalized numerically. The resonator frequency with the transmon in the ground state was selected from the ten possible eigenvalues. The parameters of the Hamiltonian were determined from Transmon spectroscopy, which is the subject of the next section.

6.3 Transmon spectroscopy

6.3.1 Low power continuous spectroscopy

As described in Chapter 5, to locate the qubit transition frequency $\tilde{\omega}_{ge}$, I first performed a low-power continuous dispersive read-out of the device.

By measuring S_{21} at low input powers ($\sim -140\,\mathrm{dBm}$) close to the single photon limit of the resonator, the dispersively shifted frequency $\tilde{\omega}_r - \chi$ of the resonator can be found (see Fig. 6.2). This was chosen as the low-power read-out frequency. Figure 6.4 shows a simple illustration of the low-power dispersive read-out scheme. To avoid ac Stark-shifting the transmon frequency, the amplitude of the read-out tone was chosen to have nearly one photon stored in the resonator. While monitoring the transmission of microwaves at the read-out frequency, the probe tone was swept in frequency to do spectroscopy. When the probe tone excites the qubit $|g\rangle \rightarrow |e\rangle$ transition, there is increased transmission of the read-out frequency (see Chapter 5), showing a peak

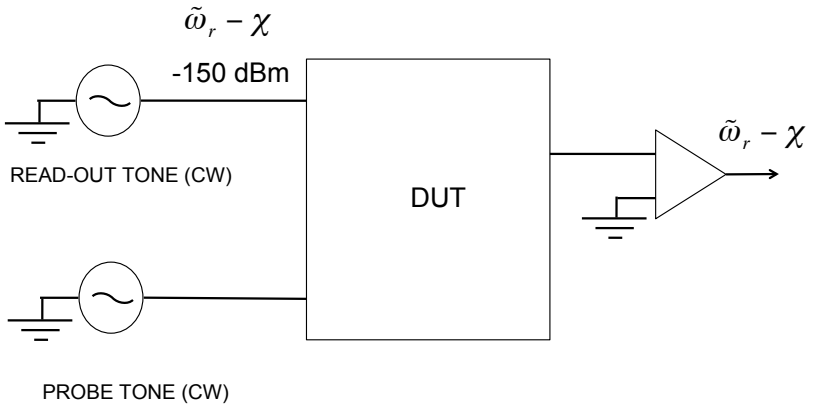

Figure 6.4: Block diagram of the low-power dispersive read-out set-up.

around the qubit frequency.

Since the read-out tone was very weak, this method required a lot of averaging and each spectroscopic point was averaged around 200,000 times for good SNR. The power of the probe tone was initially chosen to be high ($\sim -100\,\mathrm{dBm}$) in order to excite the qubit transition. Once the spectral peaks were located, the probe power was reduced in steps to isolate the peak corresponding to $\tilde{\omega}_{ge}$.

Figure 6.5(a) shows spectroscopy of the transmon device LEv5-56 (see Fig. 4.15) using the low-power dispersive read-out for a coupler power $P_{rf} = -148\,\mathrm{dBm}$ and a probe power of $-120\,\mathrm{dBm}$. The broad spectral feature around 6.4 GHz corresponds to the transmon $|g\rangle \rightarrow |e\rangle$ transition. By reducing the power of the probe tone, the multiphoton transitions are less and less prominent in the spectroscopy isolating the $\tilde{\omega}_{ge}$ peak.

Figure 6.5(b) shows a detailed plot of the qubit transition spectrum for device LEv5-56 using the low-power dispersive read-out. This spectrum reveals the photon-number splitting peaks [44]. Because of the continuous coupler tone of power $P_{rf} =$

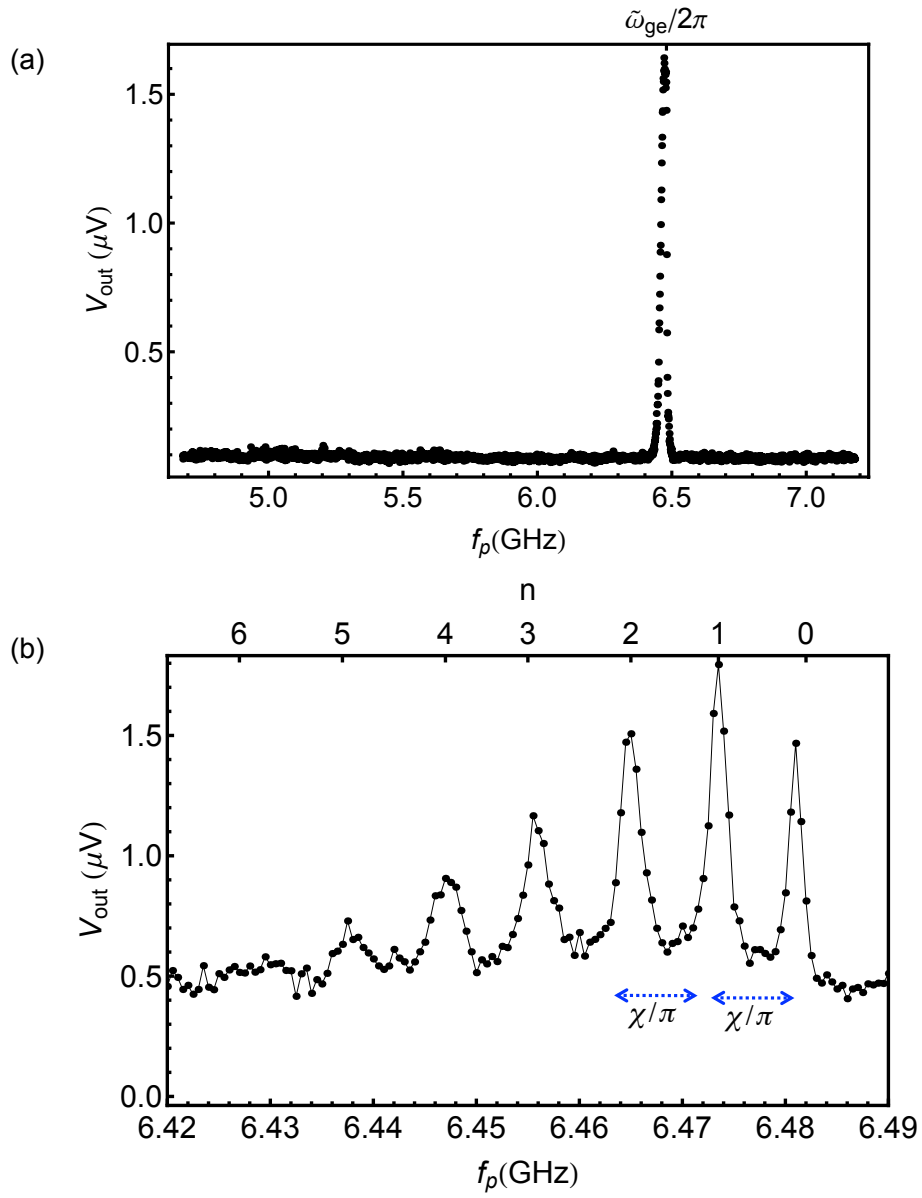

Figure 6.5: Spectroscopy of transmon device LEv5-56 using a low-power continuous dispersive read-out and monitoring transmission at $\omega_r - \chi_{ge}$. (a) Spectrum over a wide frequency range. Read-out power $P_{rf} = -148\,\mathrm{dBm}$, Probe power $-120\,\mathrm{dBm}$ at the device. (b) Detailed spectrum close to the qubit transition revealing photon number-splitting of the spectrum. $P_{rf} = -148\,\mathrm{dBm}$ with an average photon population of $\bar{n} = 2.1$ in the resonator. Power of the probe tone is $-140\,\mathrm{dBm}$ at the CPW transmission line of the device.

$-148\,\mathrm{dBm}$ on resonance, the resonator is driven into a coherent state, with the weights of the individual photon-number states following a Poisson distribution. When the resonator-qubit coupling is strongly dispersive (such that the ac Stark shift per photon on the qubit frequency is greater than the spectral linewidth), every additional photon in the resonator contributes to a well-resolved peak in the qubit spectrum. This phenomenon has been termed photon number-splitting [44].

In the Fig. 6.5(b), the peak on the right-most at $6.482\,\mathrm{GHz}$ corresponds to the qubit transition frequency $\tilde{\omega}_{ge}$ when there are no photons in the resonator. The peak at $6.473\,\mathrm{GHz}$ corresponds to the ac Stark shifted peak due to $n = 1$ photon in the resonator, given by $\tilde{\omega}_{ge} + 2\chi$, for $\chi/2\pi = -4.5\,\mathrm{MHz}$. Similarly for the $n = 2$, $n = 3$ and other peaks. As shown in Chapter 3, the number-weighted average of the peak heights gives the average number of photons in the resonator. For the data shown in Fig. 6.5, the average number of photons stored in the resonator in steady state is $\bar{n} \approx 2.1$

From the number-split spectrum, two additional pieces of information can be extracted. First, the location of the $n = 0$ photon peak gives the qubit transition frequency $\tilde{\omega}_{ge}$ accurately. This is helpful for setting up the high power read-out discussed in the next section. Second, the measured separation between the successive photon number peaks gives the effective ac Stark shift due to a single photon. In the second order dispersive approximation of the generalized Jaynes-Cummings Hamiltonian, this ac Stark shift is given by

$$2\chi \approx 2\chi_{ge} - \chi_{ef} \tag{6.4}$$

where $\chi_{ge} = g_{ge}^2/(\tilde{\omega}_{ge} - \omega_r)$ and $\chi_{ef} = g_{ef}^2/(\tilde{\omega}_{ef} - \omega_r)$. As described in the previous section, from the S_{21}-vs-power measurement, I was able to extract χ_{ge}. Using the photon number-splitting measurement, I can now extract χ_{ef} using Eq. 6.4. Since we measure $\tilde{\omega}_{ge}$ from spectroscopy, we also know $\Delta_{ge} \equiv \tilde{\omega}_{ge} - \omega_r$ and we can now determine χ_{ef}. For device LEv5-56 $\chi_{ge}/2\pi = 3.6\,\mathrm{MHz}$, $\Delta_{ge}/2\pi = 1000\,\mathrm{MHz}$, and $g_{ge}/2\pi \approx 60\,\mathrm{MHz}$. Using the measured ac Stark shift from the number-split spectrum, and $\chi/2\pi = -4.5\,\mathrm{MHz}$, and from Eq. 6.4, I get $\chi_{ef}/2\pi = 16.2\,\mathrm{MHz}$.

I note that in this low-power technique the average number of photons in the resonator is being counted without relaxing the state of the resonator. A metric for *demolition* is given by the smallness of the ratio g_{ge}/Δ_{ge} – the smaller the ratio, the more QND the measurement. For device LEv5-56, $g_{ge}/\Delta_{ge} \approx 0.05 \ll 1$ making the measurement near QND.

Another aspect of this read-out is that since the read-out or coupler tone has such a small number of photons, to achieve a good SNR the signal has to be averaged many ($\sim$ 1,000,000) times. The data set in Fig. 6.5 (b) was taken over nearly 12 hours. This makes the read-out very slow and inefficient with the amplifiers in our set-up. In the next section, I describe transmon spectroscopy using the Jaynes-Cummings read-out [35] which achieves significant speed up of data acquisition along with drastic improvement in the SNR.

6.3.2 Pulsed spectroscopy using Jaynes-Cummings read-out

The principle of the Jaynes-Cummings read-out [35, 52, 51] and the protocol for implementing the read-out were discussed in detail in Chapter 5. To summarize, the transmissivity of the microwaves at frequency ω_r depends on the state of the transmon. At an optimal power of the microwaves, a high transmissivity is observed when the transmon is in the ground state, while a low transmissivity is observed when the transmon is in one of the excited states. By measuring the output transmission of the read-out pulses, both for the transmon in $|g\rangle$ and $|e\rangle$, the optimal read-out power can be determined. I term this the "transmission s-curve measurement".

The transmission s-curve measurement for device LEv6-7 is shown in Fig. 6.6. Microwaves at the bare resonator frequency $\omega_r/2\pi = 7.2016\,\mathrm{GHz}$ show a larger transmissivity when the qubit is in the ground state (blue trace) than when the qubit is in the excited state (red trace), in the range of powers $-108\,\mathrm{dBm} \leq P_{rf} \leq -97\,\mathrm{dBm}$. At $P_{rf} = -100\,\mathrm{dBm}$, the difference between the blue and red traces is maximal, making it the optimal read-out power. Note that the power of the read-out tone used in this method ($P_{rf} = -100\,\mathrm{dBm}$) is about 50 dB higher than the power of the read-out tone in the low power dispersive read-out discussed in the previous section. This large signal amplitude improves the SNR of the read-out and allows us to use a smaller number of averages (50,000), thereby speeding up data acquisition. I note that the Jaynes-Cummings read-out is strongly projective unlike the low power dispersive read-out and characterizes a strong measurement of the qubit state.

The transmon spectrum for device LEv6-7 measured using the pulsed Jaynes-

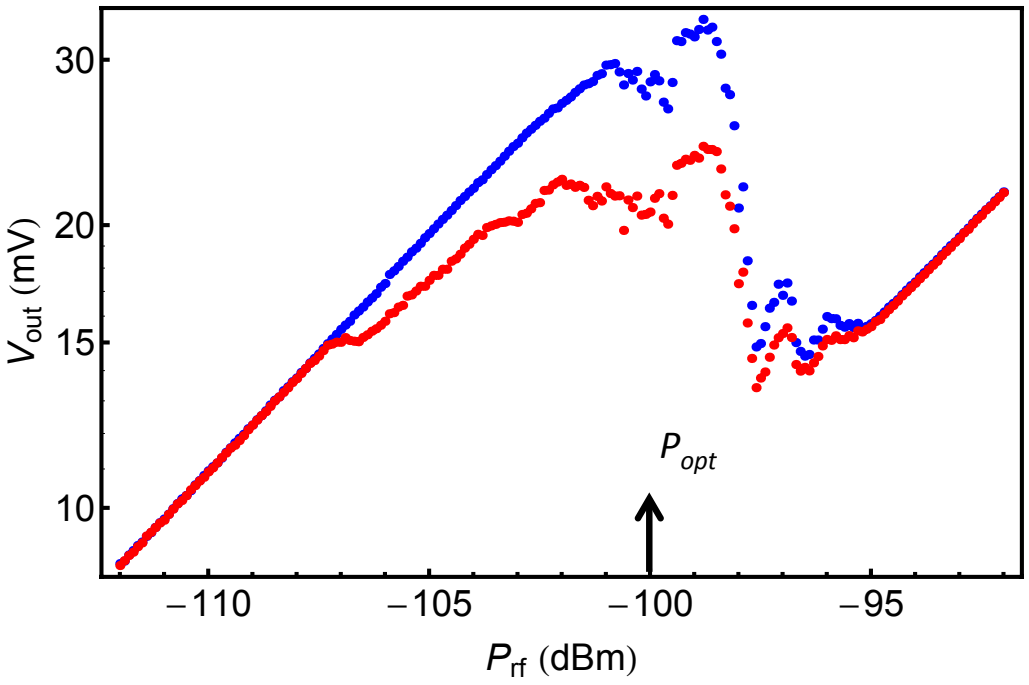

Figure 6.6: Transmission s-curve for device LEv6-7. Microwaves at the bare resonator frequency $\omega_r/2\pi = 7.2016\,\text{GHz}$ show a larger transmissivity when the qubit is in the ground state (blue) than when the qubit is in the excited state (red) in the range of powers $-108\,\text{dBm} \leq P_{rf} \leq -97\,\text{dBm}$. At $P_{rf} = -100\,\text{dBm}$, the difference between the blue and red traces is maximal, making it the optimal read-out power.

Cummings read-out is shown in Fig. 6.7. When the probe power is high ($\sim -90\,\mathrm{dBm}$) the spectrum (see Fig. 6.7(a)) shows a prominent broad peak corresponding to $\tilde{\omega}_{ge}/2\pi \approx 6.26\,\mathrm{GHz}$. The relatively narrow peak at $\tilde{\omega}_{gf}/4\pi \approx 6.15\,\mathrm{GHz}$ corresponds to a two-photon transition from ground state $|g\rangle$ to the second excited state $|f\rangle$ of the transmon. Similarly, the peak at $\tilde{\omega}_{gh}/6\pi \approx 5.95\,\mathrm{GHz}$ corresponds to a three-photon transition from the ground $|g\rangle$ to the third excited state $|h\rangle$ of the transmon. From the measured values of $\tilde{\omega}_{ge}$, $\tilde{\omega}_{gf}/2$ and $\tilde{\omega}_{gh}/3$, using Eq. 2.101, I find the transmon Josephson energy $E_J/h = 16\,\mathrm{GHz}$ and the charging energy $E_c/h = 330\,\mathrm{MHz}$ for device LEv6-7.

For comparison, Fig. 6.7(b) shows the spectrum measured with a low power spectroscopy tone ($\sim -120\,\mathrm{dBm}$). At such weak qubit excitation, only the $|g\rangle \rightarrow |e\rangle$ transition is probable, yielding only the one peak at $\tilde{\omega}_{ge}$.

Figure 6.8 shows a false color plot of S_{21} as a function of the frequency f and input microwave power P_{rf} for device LEv6-7 when the qubit is prepared in a statistically mixed state with $50\%|e\rangle$ and $50\%|g\rangle$. At the lowest powers $P_{rf} < -135\,\mathrm{dBm}$, the resonator has the frequency $\tilde{\omega}_r/2\pi - \chi/2\pi = 7.204\,\mathrm{GHz}$ corresponding to when the qubit is in the ground state $|g\rangle$, and $\tilde{\omega}_r + \chi/2\pi = 7.2028\,\mathrm{GHz}$ corresponding to when the qubit is in the excited state $|e\rangle$. The different parameters $(\omega_r, \chi_{ge}, \chi_{ef}, \tilde{\omega}_r)$ that can be determined from this measurement are marked in the figure. As P_{rf} is increased, the dispersive shift of the resonator frequency changes, as discussed in detail in Chapter 5. For $P_{rf} \approx -110\,\mathrm{dBm}$, the resonant absorption of the resonator is suppressed due to the classical bistability [51]. The blue and red curves superposed on the data in Fig. 6.8 are from a numerical calculation of the resonator frequency f_r^g cor-

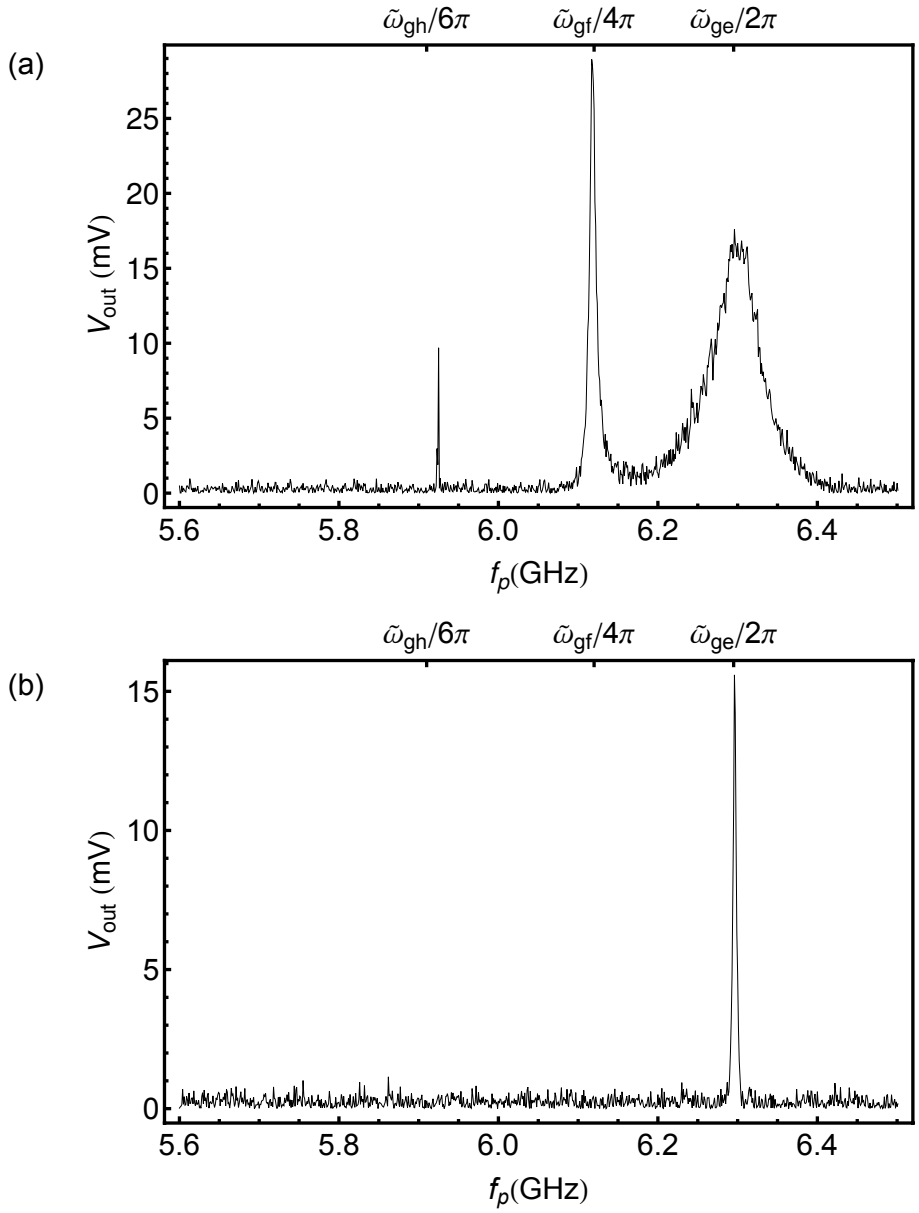

Figure 6.7: Transmon spectroscopy of device LEv6-7 using a pulsed Jaynes-Cummings read-out with the read-out tone $P_{rf} = -100\,\text{dBm}$ at the CPW transmission line. (a) Spectrum with a power of $-90\,\text{dBm}$ for the probe tone. $\tilde{\omega}_{ge}/2\pi = 6.26\,\text{GHz}$. Multiphoton transitions to higher transmon states are seen at $\tilde{\omega}_{gf}/2(2\pi) = 6.15\,\text{GHz}$ and $\tilde{\omega}_{gh}/3(2\pi) = 5.95\,\text{GHz}$. (b) Spectrum with a power of $-120\,\text{dBm}$ for the probe tone. Only the main qubit transition seen at $\tilde{\omega}_{ge}/2\pi = 6.26\,\text{GHz}$.

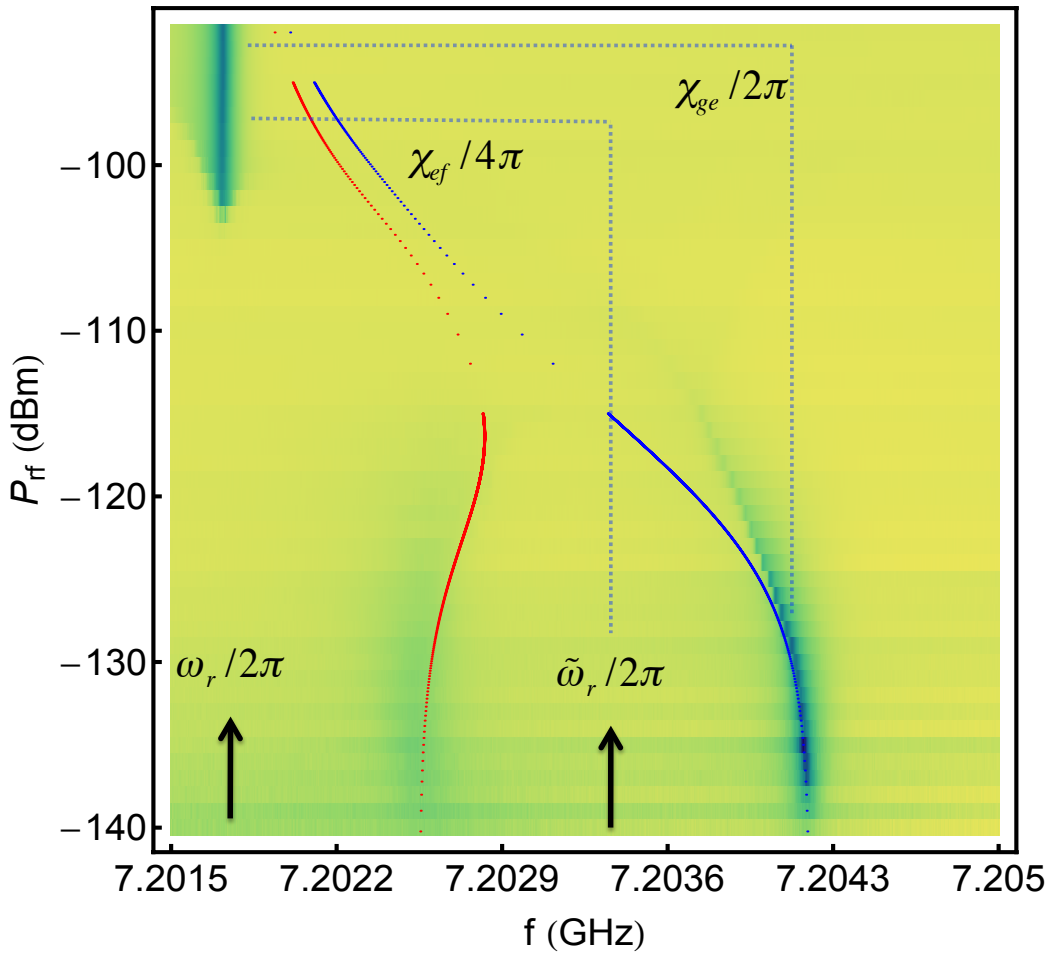

Figure 6.8: Measured S_{21} vs f vs P_{rf} for device LEv6-7, with the qubit prepared in a mixed state containing 50% $|e\rangle$ and 50% $|g\rangle$. The blue and red curves in Fig. 6.8 are a numerical calculation of the resonator frequency as a function of P_{rf} corresponding to when the qubit is in the $|g\rangle$ state and $|e\rangle$ state respectively. To calculate these frequencies, I diagonalized the generalized Jaynes-Cummings Hamiltonian with 10 transmon levels, for the parameters $\omega_r/2\pi = 7.2016\,\text{GHz}$, $\omega_{ge}/2\pi = 6.26\,\text{GHz}$, $E_c/h = 330\,\text{MHz}$ and $g_{ge}/2\pi = 54\,\text{MHz}$.

responding to when the qubit is in the $|g\rangle$ state and $|e\rangle$ state respectively as a function of P_{rf}. To calculate these frequencies, I diagonalized the n-excitation manifold of the generalized Jaynes-Cummings Hamiltonian with 10 transmon levels, for the parameters $\omega_r/2\pi = 7.2016\,\mathrm{GHz}$, $\omega_{ge}/2\pi = 6.26\,\mathrm{GHz}$, $E_c/h = 330\,\mathrm{MHz}$, $g_{ge}/2\pi = 54\,\mathrm{MHz}$. The photon number n in the simulation (blue and red curves in Fig. 6.8) was calibrated to the drive power P_{rf} using the relation $n \approx (Q_L/Q_e)P_{rf}/\kappa\hbar\omega_r$, which is valid in the low-power limit.

A summary of the spectroscopically measured parameters for all my transmon devices is given in Table 6.3.

6.4 Photon number-splitting and Aulter-Townes effect in dressed states

6.4.1 Background and motivation

In this section, I present some new spectral features I observed [53] in device LEv5-ZK9 which was coupled to a quasi-lumped element resonator. I note that this sample was fabricated by Zach Keane. Due to strong coupling and the AC stark shift from individual photons in the resonator, discrete peaks in the transmon spectrum can be observed in our devices - a phenomenon that has been referred to as "photon number-splitting" [44, 45]. Unlike the measurement of photon number-splitting in a superconducting qubit described in the previous section, I utilized improvements in the read-out [35] to investigate this effect while also varying the detuning of the tone associated with photons in the resonator [45]. During this investigation, in the absence of a coherent drive field on the resonator, I observed a weak $n = 1$ photon

Table 6.3: Table of spectroscopically measured parameters for LEv5 and LEv6 transmons. † Device LEv5-56 had a split CPB allowing flux-tunability of E_J with $E_J^{max}/h \approx 87\,\mathrm{GHz}$. * Device LEv5-ZK9 had a split CPB allowing flux-tunability of E_J with $E_J^{max}/h \approx 26\,\mathrm{GHz}$.

Device Name	$\omega_{ge}/2\pi$ (GHz)	E_J/h (GHz)	E_c/h (MHz)	$g_{ge}/2\pi$ (MHz)	Δ_{ge}/h (GHz)	E_J/E_c	Charge dispersion ϵ_1 (MHz)
LEv5-56†	6.5	13	430	78	+ 1.065	30.23	-0.922
LEv5-7	8.001	29.4	274	88	+2.525	107.23	-3×10^{-6}
LEv5-ZK9*	4.982	12.4	250	70	-0.482	49.6	-0.011
LEv5-15	4.18	10.5	234	65	-1.151	44.8	-0.027
LEv5-17	3.5	6.1	250	44	-1.845	24.4	-1.9925
LEv6-1	5.4	12.2	314	43	-1.8087	38.85	-0.115
LEv6-7	6.26	16	330	54	-0.941	48.48	-0.02
LEv6-2	9.995	20.5	578	129	+2.8	35.46	-0.415
LEv6-3	9.989	20.5	578	129	+2.8	35.46	-0.415

spectral peak due to a thermal population of photons in the resonator [34, 87, 80]. Upon pumping the system with an additional electromagnetic field at the dressed frequency of the resonator I observed a splitting of the thermal $n = 1$ photon peak with a size that increases linearly as I increased the microwave drive amplitude. I show that these observations are consistent with an Autler-Townes effect [64] associated with dressing of the $|\widetilde{e,0}\rangle \leftrightarrow |\widetilde{e,1}\rangle$ transition due to the strong 'coupler' field.

These results were published in the article [53], sections of which are reproduced here. In section 6.4.2, I describe the experimental set-up used for the experiment. In section 6.4.3, I discuss the results of the experiment and compare them with simulations of the master equation with two qubit levels and ten resonator levels.

While the Autler-Townes effect had been observed in superconducting qubits [46, 65, 66], to my knowledge this was the first experimental observation of this effect involving both the photon number states in the resonator and the states of the transmon. A potential application of this effect is a fast microwave router for quantum computation [89, 90]. Finally, the Autler-Townes effect can be a precursor to observing electromagnetically induced transparency (EIT) [91] which had not been observed in superconducting devices at the time of these observations [92]. The ability to engineer the coherence of the states of the resonator, independent of the states of the qubit, could provide additional flexibility in realizing EIT as has been theoretically proposed by Ian *et al.* [93].

6.4.2 Experiment

6.4.2.1 Device description

Figure 6.9 shows a colorized image of device LEv5-ZK9. The transmon (shown in red in Fig. 6.9) is coupled to a superconducting lumped-element resonator (shown in blue) [28], which is in turn coupled to a coplanar waveguide transmission line (shown in purple) used for excitation and measurement. The transmon is formed from two Josephson junctions (total junction area $\approx 100 \times 100$ nm^2) shunted by an interdigitated capacitor with finger widths of 10 μm, lengths of 70 μm, and separation between fingers of 10 μm. The junctions are connected to form a superconducting loop with a nominal loop area of $4 \times 4.5\,\mu$m^2. The Josephson junction loop was placed close to a shorted current bias line (green region in Fig. 6.9) to finely tune the critical current of the parallel junctions and hence the transition frequency of the qubit.

6.4.2.2 Experimental parameters

All the spectroscopic and time-domain measurements described below were performed using the high-power pulsed Jaynes-Cummings read-out technique described in Chapter 5. For coherently driving the resonator, a weak coupler tone ($P_{rf} \sim -150\,$dBm) resonant with $(\tilde{\omega}_r - \chi)/2\pi = 5.474\,$GHz was kept continuously on during the measurement. The read-out tone, at the bare resonator frequency $\omega_r/2\pi = 5.464\,$GHz and amplitude about 50 dB stronger than the coupler and probe tones, was pulsed on and off. A block diagram showing the different microwave tones is seen in Fig. 6.10. From spectroscopic and time-domain measurements the

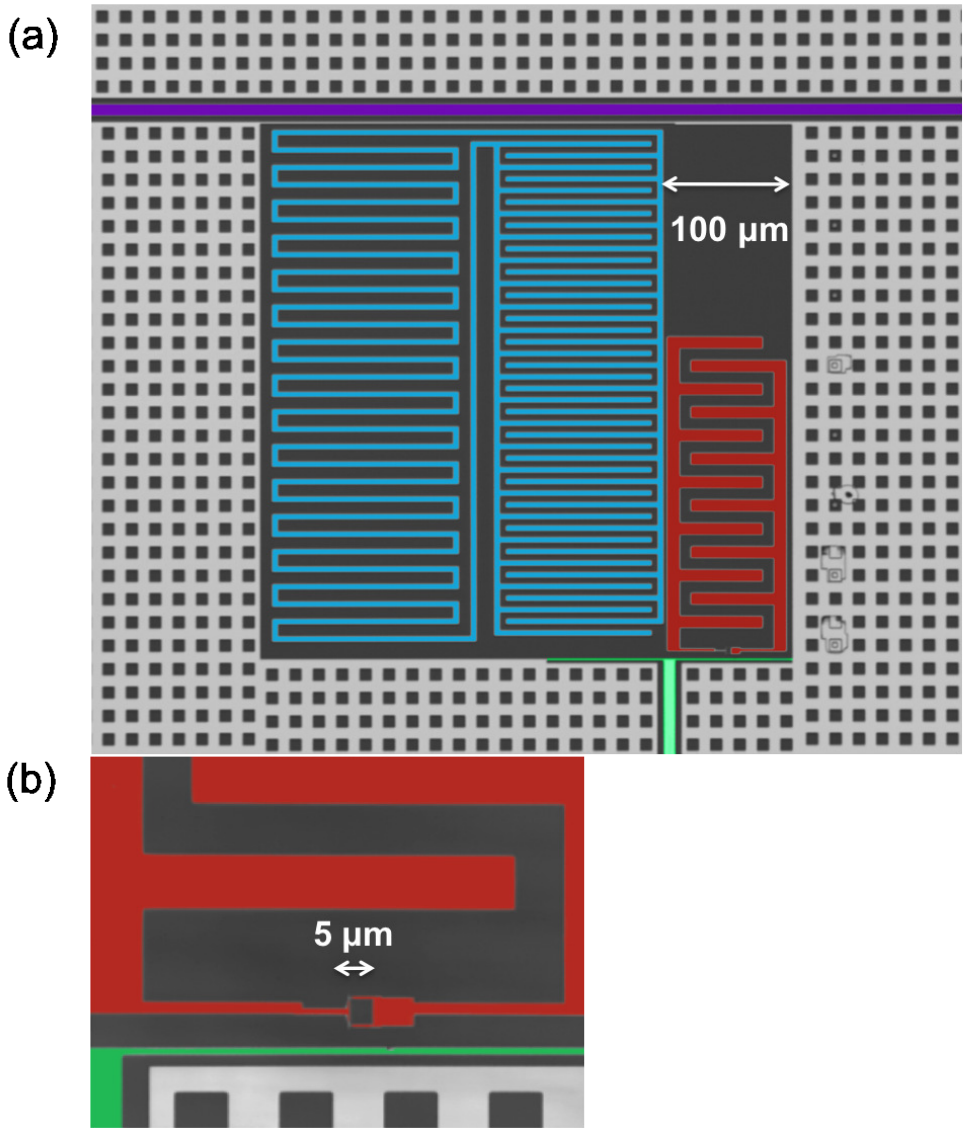

Figure 6.9: Colorized micrograph of device LEv5-ZK9. (a) A lumped element resonator (blue) and transmon (red) are coupled to a coplanar waveguide transmission line (violet) and surrounded by a perforated ground plane (gray). The resonator consists of a meandering inductor and an interdigitated capacitor. The transmon has two Josephson junctions in parallel to allow the transition frequency to be tuned with an external magnetic field and an on-chip flux bias (green). (b) Detailed view of transmon's Josephson junctions and flux bias line.

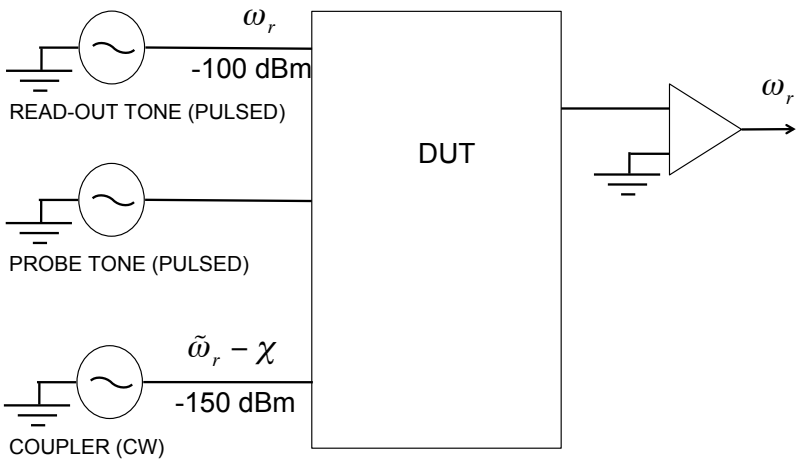

Figure 6.10: Block diagram showing the three tones used for number-splitting and Autler-Townes measurements of LEv5-ZK9. The read-out and probe tones were pulsed and the weak coupler tone was continuously applied.

main system parameters were determined. The resonator had a bare resonant frequency $\omega_r/2\pi = 5.464\,\mathrm{GHz}$, internal quality factor $Q_I = 190,000$, and a loaded quality factor $Q_L \equiv \omega_r/\kappa = 18,000$ with $\kappa = 2\pi(300)\,\mathrm{kHz}$. The normal-state resistance of the two Josephson junctions in parallel yielded a maximum Josephson energy $E_{J,max}/h \approx 25\,\mathrm{GHz}$ and the transmon had a Coulomb charging energy of $E_c/h = 250\,\mathrm{MHz}$. This gave a maximum ground-to-first excited state transition frequency $\omega_{ge,max}/2\pi \simeq (\sqrt{8E_{J,max}E_c} - E_c)/h = 7.1\,\mathrm{GHz}$ for the qubit.

The qubit transition frequency was tuned using a combination of an external superconducting magnet and the on-chip flux bias to $\widetilde{\omega}_{ge}/2\pi = 4.982\,\mathrm{GHz}$, which corresponds to a detuning of $\Delta_{ge}/2\pi = -482$ MHz from the bare resonator frequency. From spectroscopic measurements of the qubit, I found the effective dispersive shift $\chi/2\pi = -4.65\,\mathrm{MHz}$. From the measurement of the bare and dressed resonator

frequencies, and the effective dispersive shift χ, I determined $\chi_{ge}/2\pi = -10$ MHz and $\chi_{ef}/2\pi = -10.7\,\mathrm{MHz}$ respectively. From Eq. 6.4 gave $g_{ge}/2\pi = 70\,\mathrm{MHz}$ and $g_{ef}/2\pi = 89$ MHz.

For better numerical simulations of the experimental data, I did a perturbation expansion of the dispersive transformation of the system Hamiltonian up to the fourth order [52]. To this order, Kerr-type terms appear in the Hamiltonian, which can be written in the form:

$$H_{JC}^{(4)} \approx \hbar\tilde{\omega}_r a^\dagger a + \hbar\frac{\tilde{\omega}_{ge}}{2}\sigma_z + \hbar\chi a^\dagger a\sigma_z + \hbar\zeta(a^\dagger a)^2\sigma_z + \hbar\zeta'(a^\dagger a)^2 \tag{6.5}$$

where the resonator-qubit cross-Kerr coefficient ζ and the resonator self-Kerr coefficient ζ' [45, 52] are determined from:

$$\zeta \approx (\chi_{ef}\lambda_{ef}^2 - 2\chi_{ge}\lambda_{ge}^2 + 7\chi_{ef}\lambda_{ge}^2/4 - 5\chi_{ge}\lambda_{ef}^2/4) \tag{6.6}$$

$$\zeta' \approx (\chi_{ge} - \chi_{ef})(\lambda_{ge}^2 + \lambda_{ef}^2) \tag{6.7}$$

where $\lambda_{ge} = g_{ge}/\Delta_{ge}$ and $\lambda_{ef} = g_{ef}/\Delta_{ef}$. For the parameters of my experiment, the Kerr coefficients from Eq. 6.6 and Eq. 6.7 are $\zeta/2\pi = 85\,\mathrm{kHz}$ and $\zeta'/2\pi = -23\,\mathrm{kHz}$. The effect of these nonlinearities is small in the context of the Autler-Townes effect, but they played a significant role in the photon number-splitting experiment.

The Kerr coefficients can also be numerically estimated from a simulation of the transmon state-dependent frequency shifts of the resonator (see Fig. 6.11). From the Hamiltonian given by Eq. 6.5, the photon-number dependent frequency of the resonator is given by

$$\omega_r(n) = \tilde{\omega}_r + \chi\sigma_z + \zeta(a^\dagger a)\sigma_z + \zeta'(a^\dagger a). \tag{6.8}$$

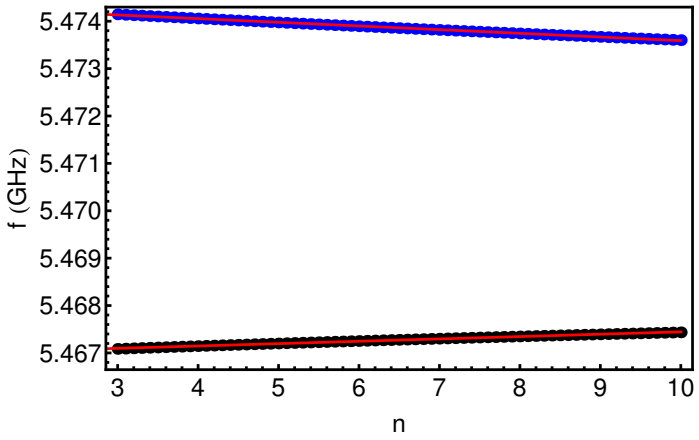

Figure 6.11: Plot of simulated transmon state-dependent resonator frequency as a function of photon number for device LEv5-ZK9. (Blue dots)– resonator frequency with the qubit in the ground state f_r^g. (Black dots)– resonator frequency with the qubit in the excited state f_r^e. The generalized Jaynes-Cummings Hamiltonian with $\omega_r/2\pi = 5.464\,\mathrm{GHz}$, $\omega_{ge}/2\pi = 4.982\,\mathrm{GHz}$, $E_c/h = 250\,\mathrm{MHz}$, $g_{ge}/2\pi = 70\,\mathrm{MHz}$ was diagonalized with 10 transmon levels included in the basis. Red curve shows the linear fit. Using Eq. 6.9 and Eq. 6.10, and the slope of the linear fit, $\zeta/2\pi = 63\,\mathrm{kHz}$ and $\zeta'/2\pi = -13\,\mathrm{kHz}$ can be determined.

For a qubit in the ground and first excited states, the photon-number dependence of the resonator frequency is explicitly given by

$$\omega_r^g(n) = \tilde{\omega}_r - \chi + (\zeta' - \zeta)n \tag{6.9}$$

$$\omega_r^e(n) = \tilde{\omega}_r + \chi + (\zeta' + \zeta)n. \tag{6.10}$$

In Fig. 6.11, the transmon state-dependent resonator frequency is plotted for the transmon in the $|g\rangle$ and $|e\rangle$ levels (blue and black dots respectively) as a function of photon number. The frequencies were numerically calculated by diagonal-

izing the generalized Jaynes-Cummings Hamiltonian, with 10 transmon levels with bare parameters $\omega_r/2\pi = 5.464\,\mathrm{GHz}$, $\omega_{ge}/2\pi = 4.982\,\mathrm{GHz}$, $E_c/h = 250\,\mathrm{MHz}$ and $g_{ge}/2\pi = 70\,\mathrm{MHz}$. In the small photon number limit, the resonator frequencies with the transmon in the $|g\rangle$ and $|e\rangle$ states are given by Eq. 6.9 and Eq. 6.10. The calculated resonator frequencies (blue and black curves in Fig. 6.11) were fit to a straight line (as shown by the red curves in Fig. 6.11). From the slope of the line Kerr shifts were calculated using Eq. 6.9 and Eq. 6.10 to be $\zeta/2\pi = 63\,\mathrm{kHz}$ and $\zeta'/2\pi = -13\,\mathrm{kHz}$, which agrees well with the values estimated from experiment.

Time-domain coherence measurements performed at a resonator-qubit detuning of ($\Delta_{ge}/2\pi = -482$ MHz) revealed a qubit relaxation time $T_1 = 1/(\Gamma_- + \Gamma_+) = 1.6\ \mu$s and a Rabi decay time $T' = 1.6\ \mu$s for the first excited state of the qubit. From these measurements, the pure dephasing rate was estimated at $\gamma_\phi \equiv 1/T_\phi \approx 2 \times 10^5\,\mathrm{s}^{-1}$. The time-domain measurements will be discussed in detail in Chapter 7, but these numbers will be used for my simulations in this chapter.

6.4.3 Photon number-splitting

6.4.3.1 Photon number-splitting - data

Figure 6.12(a) shows the measured spectrum (black dots) of the transmon LEv5-ZK9 with no drive field applied to the resonator. The spectrum shows the dressed qubit ground-to-first excited state transition at $\widetilde{\omega}_{ge}/2\pi = 4.982\,\mathrm{GHz}$. The smaller spectroscopic peak detuned by -9.3 MHz at $(\widetilde{\omega}_{ge} + 2\chi)/2\pi = 4.973\,\mathrm{GHz}$ is due to one photon of frequency $\widetilde{\omega}_r - \chi/2\pi = 5.474$ GHz occasionally being present in the

resonator [80], presumably from thermal excitations. From the relative areas under the two spectral peaks (see Eq. 6.12), I estimated a fractional thermal population of $n_{th} = 0.1$ photons, corresponding to a temperature of about 120 mK for the resonator. This effective temperature is much higher than the base temperature ~ 20 mK of the dilution refrigerator, possibly due to a leakage of infrared photons [34, 87], or due to insufficient cooling of an attenuator stage on the input or output microwave lines.

Upon driving the resonator with a coupler tone at $\Omega_c/2\pi = 5.474$ GHz, which was resonant with the transition $|\widetilde{g,0}\rangle \leftrightarrow |\widetilde{g,1}\rangle$, I increased the mean occupancy of the resonator from its equilibrium value and create a coherent state. Since the coherent state is a superposition of photon number (Fock) states, the qubit spectrum has multiple peaks, one for each Fock state. When applying a power of $P_{rf} = 2.5$ aW at the dressed resonator frequency (see Fig. 6.12(b)), an increase in the height of the $\widetilde{\omega}_{ge}+2\chi$ peak was observed and a spectral peak at $\widetilde{\omega}_{ge}+4\chi$ appeared. The peak at $\widetilde{\omega}_{ge}$ was still the largest. Figure 6.12(c) shows the spectrum for an applied resonator drive power of 160 aW. In this case, more spectral peaks were observed and the $\widetilde{\omega}_{ge} + 2\chi$ was the largest.

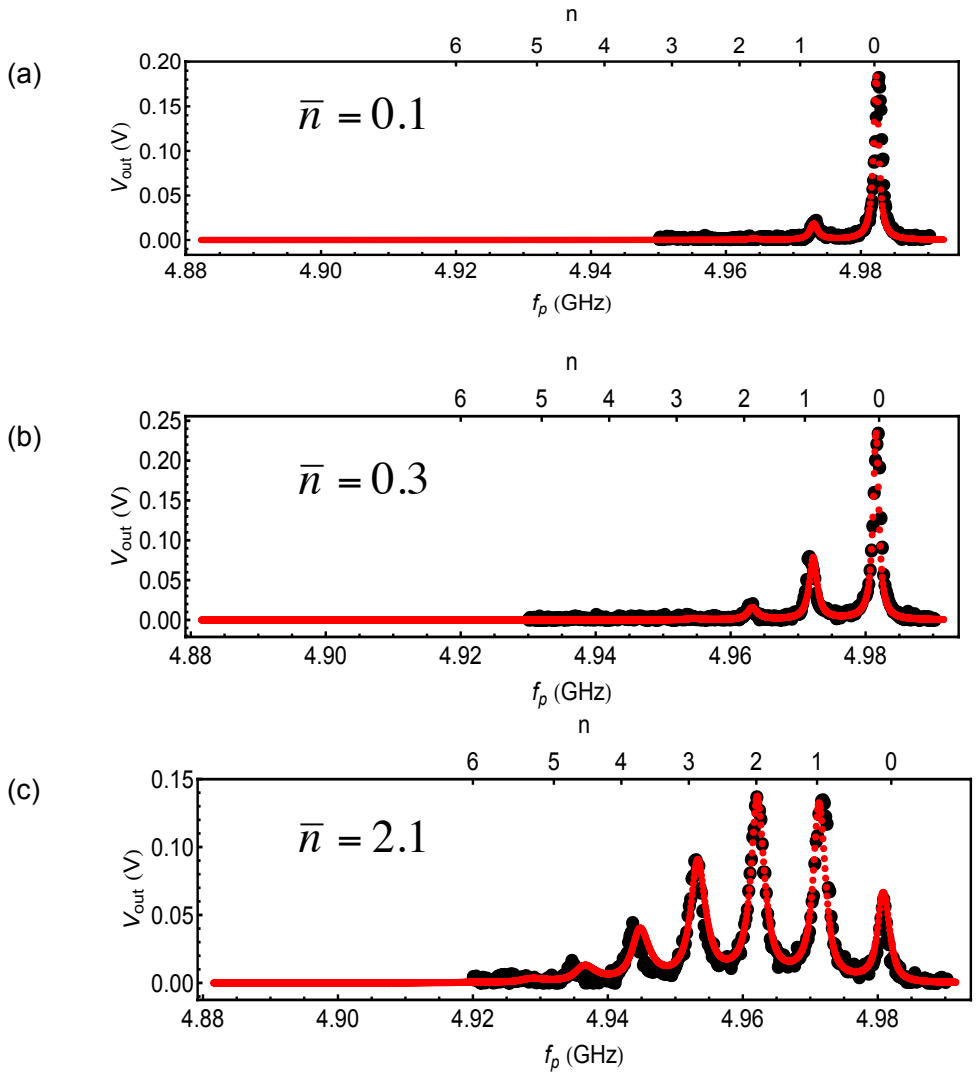

Figure 6.12: Photon number-splitting in the transmon spectrum for device LEv5-ZK9. (Black dots) - data. (Red dots) - Steady-state solution of the master equation Eq. 6.11 with parameters determined in Sec. 6.4.2.2. (a) Spectroscopy with no coupler tone applied. The primary qubit transition frequency is seen at $\widetilde{\omega}_{ge}/2\pi = 4.982\,\mathrm{GHz}$. The spectroscopic peak at 4.973 GHz is due to a thermal population $n_{th} = 0.1$ photons in the resonator. (b) A coupler tone applied at $\omega_c/2\pi = 5.474\,\mathrm{GHz}$ and power $P_{rf} = 2.5\,\mathrm{aW}$ produces a population with an average of $\bar{n} = 0.3$ photons stored in the resonator. (c) A coupler tone of power $P_{rf} = 160\,\mathrm{aW}$ gives $\bar{n} = 2.1$ photons stored in the resonator.

6.4.3.2 Photon number-splitting - master equation simulation

The photon number-splitting of the spectrum was also numerically simulated by solving the full system master equation in the steady state

$$\begin{aligned}\dot{\rho} = &- i\tilde{\Delta}_c[a^\dagger a, \rho] - \frac{i\tilde{\Delta}_p}{2}[\sigma_z, \rho] - i\chi[(a^\dagger a)\sigma_z, \rho] - i\zeta[(a^\dagger a)^2\sigma_z, \rho] - i\zeta'[(a^\dagger a)^2, \rho] \\ &+ \frac{i\Omega_c}{2}[a + a^\dagger, \rho] + + \frac{i\Omega_p}{2}[\sigma^- + \sigma^+, \rho] \\ &+ \kappa_-\mathcal{D}[a]\rho + \kappa_+\mathcal{D}[a^\dagger]\rho + \Gamma_-\mathcal{D}[\sigma^-]\rho + \Gamma_+\mathcal{D}[\sigma^+]\rho + \frac{\gamma_\varphi}{2}\mathcal{D}[\sigma_z]\rho \end{aligned} \tag{6.11}$$

where the operator $\mathcal{D}[A_i]\rho \equiv A_i\rho A_i^\dagger - \frac{1}{2}\left(A_i^\dagger A_i\rho + \rho A_i^\dagger A_i\right)$ (see Chapter 3). The steady state condition $\dot{\rho} = 0$ reduces this master equation into a set of coupled linear equations in the elements of the density matrix ρ, the solution of which was carried out numerically. In Appendix F I present the Mathematica routine that I used to do the numerical simulation of the steady-state system master equation.

The parameters entering the Hamiltonian and the decoherence terms were experimentally determined as described in Sec. 6.4.2.2 from spectroscopic and time-domain measurements. The Jaynes-Cummings Hamiltonian included the fourth order (in g_{ge}/Δ_{ge}) Kerr-type terms to achieve better accuracy. The master equation also modeled a thermal excitation in both the resonator and the qubit through terms involving the $a^\dagger$ and $b^\dagger$ operators for the resonator and transmon respectively. Figure 6.13 shows that the overlay of the data with the numerical simulation is in excellent quantitative agreement.

6.4.3.3 $\bar{n}$ vs P_{rf} - data

From Fig. 6.12, I calculated the average number of photons ($\bar{n}$) by fitting the spectral peak associated with each Fock state and using the relative peak areas to weight each Fock state according to:

$$\bar{n} = \frac{\sum_n w_n n}{\sum_n w_n}. \tag{6.12}$$

The relative weights w_n were found to follow a Poisson distribution once the resonator was pumped into a coherent state [44]. Figure 6.13 shows the average number of photons versus the applied power. For very weak driving $P_{rf} < 1\,\text{aW}$, the thermal photon population $n_{th} = 0.1$ is the dominant contribution to $\bar{n}$. Above an applied power of $P_{rf} > 1\,\text{aW}$, $\bar{n}$ monotonically increases. For small applied powers in this region, $\bar{n} \approx (Q_L/Q_e)P_{rf}/(\hbar\tilde{\omega}_r\kappa_-)$ where the leading factor renormalizes the power P_{rf} applied to the transmission line to the power stored in the resonator and Q_e is the quality factor due to external coupling. Using this linear relation and the excess photon number population from the applied coupler tone in Fig. 6.12(b), an attenuation of $\alpha = 65\,\text{dB}$ is calculated for the input microwave line. I note that the nominal total attenuation on the input microwave line was 60 dB, agreeing reasonably well with the estimated attenuation (65 dB) using the photon-number analysis.

6.4.3.4 $\bar{n}$ vs P_{rf} - semi-classical linear theory

For comparison with data, I also studied the variation of the average photon number $\bar{n}$ with P_{rf} using a semi-classical approach. The mean occupancy of photons in the

resonator, when it is driven with a tone of fixed frequency ω_c, and applied power P_{rf} is given by the Lorentzian line-shape of the resonance as

$$\bar{n} = \frac{P_{rf}/4\hbar Q_e}{\delta^2 + (\kappa_-/2)^2}, \tag{6.13}$$

where $\delta = \omega_c - (\tilde{\omega}_r - \chi)$ is the detuning of the coupler drive from the resonance frequency $(\tilde{\omega}_r - \chi)$. When δ is a constant, this equation gives a linear relation between $\bar{n}$ and P_{rf}. As I will show shortly, $\delta(\bar{n})$ is in general a function of $\bar{n}$, giving a nonlinear dependence for $\bar{n}$ on P_{rf}. The gray curve in the Fig. 6.13 represents the linear model given by $\bar{n} = 0.1 + (Q_L/Q_e)P_{rf}/\kappa\hbar\omega_r$, which was obtained by setting $\delta = 0$ in Eq. 6.13. The additional 0.1 is to account for the equilibrium thermal photon population n_{th} in an *ad hoc* way in the simulation. Clearly, the experimental data deviates from the linear model even at an average occupancy of one photon in the resonator. Note that the critical number of photons for $g_{ge}/2\pi = 70\,\mathrm{MHz}$ and $\Delta_{ge}/2\pi = -482\,\mathrm{MHz}$ is $n_{crit} = \Delta_{ge}^2/4g_{ge}^2 \simeq 12$. Therefore, the deviation from linearity happens at $\bar{n} \ll n_{crit}$. This fact was also predicted in [45].

6.4.3.5 $\bar{n}$ vs P_{rf} - steady-state master equation simulation

The red squares in Fig. 6.13 represent the average photon number computed by applying Eq. 6.12 to spectra numerically simulated using the master equation Eq. 6.11 (see Fig. 6.12). It can be seen that the master equation simulation does capture the deviation from linearity. This is because the Hamiltonian used in the evolution equation included the Kerr-type nonlinear terms. The simulated average photon number deviates from the data at higher powers, likely due to contribution from higher

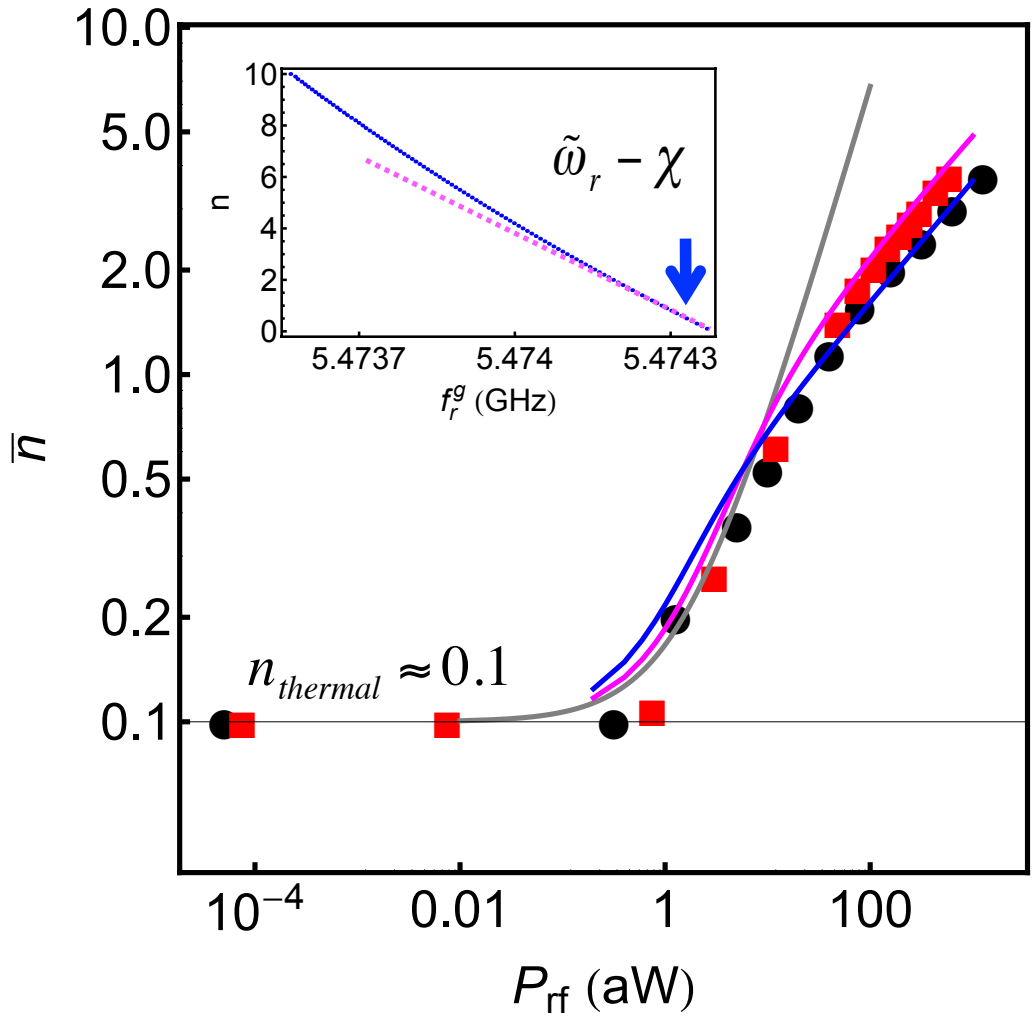

Figure 6.13: Average photon number $\bar{n}$ in the resonator as a function of the applied microwave power P_{rf} for LEv5-ZK9. Black dots show $\bar{n}$ from applying Eq. 6.12 to the measured spectra. Gray curve is the classical linear model $\bar{n} = 0.1 + (Q_L/Q_e)P_{rf}/\kappa\hbar\omega_r$. The red squares represent $\bar{n}$ computed by applying Eq. 6.12 to the spectra simulated using Eq. 6.11. The magenta curve is the solution of Eq. 6.14. The blue curve is the solution of Eq. 6.15. Note that $n_{crit} \simeq 12$ for this device ($g_{ge}/2\pi = 70\,\mathrm{MHz}$ and $\Delta_{ge}/2\pi = -482\,\mathrm{MHz}$). Inset shows the calculated $\omega_r^g/2\pi$ from exact diagonalization (blue points) and the lowest order nonlinear approximation given by Eq. 6.9 (magenta).

order nonlinearities which have been ignored in the master equation simulation.

6.4.3.6 $\bar{n}$ vs P_{rf} - semi-classical theory with lowest order nonlinearity

The magenta curve in Fig. 6.13 is the solution of the equation

$$\bar{n} = 0.1 + \frac{P_{rf}/4\hbar Q_e}{\{(\zeta' - \zeta)\bar{n}\}^2 + (\kappa_-/2)^2}, \tag{6.14}$$

where the lowest order approximation $\delta = \omega_c - (\tilde{\omega}_r - \chi) \approx (\zeta' - \zeta)\bar{n}$ from Eq. 6.9 is used. The Kerr-type coefficients $\zeta/2\pi = 85\,\text{kHz}$ and $\zeta'/2\pi = -23\,\text{kHz}$ are estimated from spectroscopy using Eq. 6.6 and Eq. 6.7. Equation 6.14 is then solved in a self-consistent manner to compute $\bar{n}$. This semi-classical simulation (magenta) with the lowest order Kerr-type nonlinearity is seen to agree well with the solution of the system master equation (red squares), where the system Hamiltonian included nonlinearities up to the order of the Kerr-type terms.

This shows that the nonlinear variation of $\bar{n}$ with P_{rf} arises due to the Jaynes-Cummings nonlinearity. As seen from Eq. 6.9, this qubit-induced nonlinearity in the resonator results in a change in the resonance frequency as $\bar{n}$ is varied. The inset to Fig. 6.13 shows the calculated frequency $\omega_r^g/2\pi$ of the resonator (blue points) when the qubit is in $|g\rangle$, using an exact diagonalization of the generalized Jaynes-Cummings Hamiltonian (see Eq. 3.50). The "bare" parameters of the Hamiltonian were determined from spectroscopic measurements (see Sec. 6.4.2.2) and for the calculation, we used up to 10 transmon levels for greater accuracy. The magenta points in the inset correspond to the lowest order approximation to the nonlinearity given by Eq. 6.9.

6.4.3.7 $\bar{n}$ vs P_{rf} - semi-classical theory with full nonlinearity

Finally, the blue curve in Fig. 6.13 is a solution of the nonlinear equation

$$\bar{n} = 0.1 + \frac{P_{rf}/4\hbar Q_e}{[\delta(\bar{n})]^2 + (\kappa_-/2)^2}, \tag{6.15}$$

where the detuning $\delta(n) = \omega_c - \omega_r^g(n)$ is calculated from an exact diagonalization of the generalized Jaynes-Cummings Hamiltonian (Eq. 3.50) with 10 transmon levels in the calculation. The ω_r^g thus calculated is shown as the blue curve in the inset to Fig. 6.13. Equation 6.15 can be solved self-consistently to compute the mean occupancy $\bar{n}$ as a function of P_{rf}. This semi-classical solution for $\bar{n}$ is plotted as the blue curve in Fig. 6.13, and it is seen to be in very good agreement with the experimental data. I note that in the experiment, the coupler frequency is fixed at $\omega_c = \tilde{\omega_r} - \chi = 2\pi(5.474)\,\text{GHz}$ (indicated by the blue arrow in the inset). The change in the resonance frequency with $\bar{n}$ is the cause of the nonlinear power-dependence of $\bar{n}$. Conversely, if the coupler frequency were adjusted to always drive on resonance, $\bar{n}$ would agree with the classical linear model (gray curve in Fig. 6.13).

I also note that the *ad hoc* manner in which the thermal population $n_{th} = 0.1$ is included in this study is not technically correct. This approximation breaks down when the coherent population due to the drive is close to the thermal population $n_{th} \approx 0.1$. This may be the reason for the deviations of the theory from experimental data when $\bar{n}$ lies between 0 and 0.3 in Fig. 6.13. A complete theory encompassing both coherent and thermal population of photons is beyond the scope of this thesis.

6.4.4 Two tone spectroscopy

In the last section I discussed driving the resonator on resonance using a weak coupler tone at ($\tilde{\omega}_r - \chi$), setting up a coherent state. I also varied the detuning of the coupler tone. Figure 6.14 shows two-tone spectroscopy of the qubit as I varied the frequency of the coupler tone. In this plot, the vertical bands at frequencies $\omega_s/2\pi = 4.982\,\mathrm{GHz}$ and 4.973 GHz are just the $n = 0$ and $n = 1$ photon peaks as seen in Fig. 6.12. The prominent diagonal band seen between the $n = 0$ and $n = 1$ photon bands in this figure corresponds to a two-photon 'blue' sideband transition from the $|\widetilde{g,0}\rangle$ to $|\widetilde{e,1}\rangle$ [94]; the sum of the frequencies (Ω_p, Ω_c) of the drive photons along this diagonal band is equal to the corresponding transition frequency.

In general, a diagonal band with slope $-1/n$ should appear in Fig. 6.14 when the detunings of the drives satisfy $\widetilde{\Delta}_p - n\widetilde{\Delta}_c = n\chi$ corresponding to the sideband transition $|g, n-1\rangle \leftrightarrow |e, n\rangle$ (see Fig. 6.15). For example, the sideband transition $|\widetilde{g,0}\rangle \leftrightarrow |\widetilde{e,1}\rangle$ level appears as a band of slope -1 and the $|\widetilde{g,1}\rangle \leftrightarrow |\widetilde{e,2}\rangle$ transition appears as a faintly visible band of slope $-1/2$ in Fig. 6.14.

I also note a faint splitting in the spectrum shown in Fig. 6.14 at the point $(\tilde{\omega}_{ge} + 2\chi, \tilde{\omega}_r + \chi)$. From its occurence at $(\tilde{\omega}_{ge} + 2\chi, \tilde{\omega}_r + \chi)$, I inferred that the three levels involved in the process were $|\widetilde{e,0}\rangle$, $|\widetilde{e,1}\rangle$ and $|\widetilde{g,1}\rangle$ (see Fig. 6.15). Using additional measurements of the variation of the splitting size with the coupler power (as discussed in the next section), I concluded that this splitting was due to an Autler-Townes mechanism involving these three dressed Jaynes-Cummings states. This splitting will be examined closely in the next section.

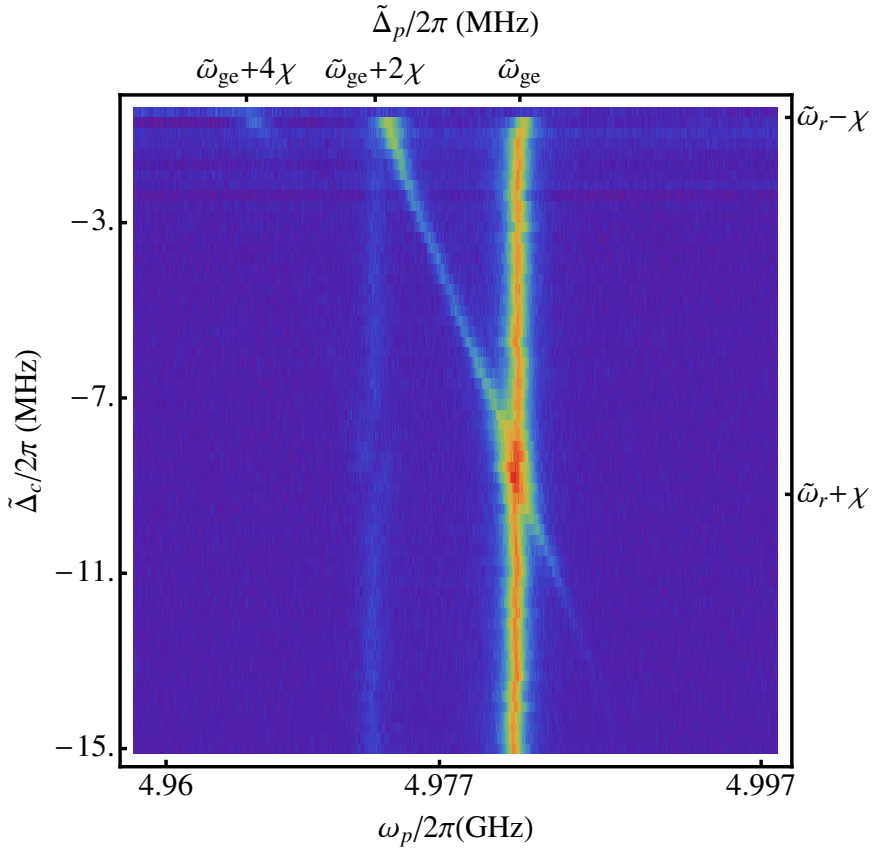

Figure 6.14: Two-tone spectroscopy of the transmon-resonator system as a function of probe and coupler frequency in device LEv5-ZK9. False color plot of qubit excited state probability versus probe frequency $\omega_p/2\pi$ and detuning of the coupler drive $\tilde{\Delta}_c/2\pi$ at a coupler power of 160 aW. Red corresponds to increase in the probability of occupying the excited state of the qubit. The qubit transition $|g\rangle \rightarrow |e\rangle$ is seen as a vertical band at $\Omega_p/2\pi = \widetilde{\omega}_{ge}/2\pi = 4.982$ GHz. The spectral peak when a thermal photon is present in the resonator is seen as a vertical band at 4.973 GHz. The diagonal band between $n = 0$ and $n = 1$ photon peaks is due to the sideband two-photon transition from $|\widetilde{g,0}\rangle \rightarrow |\widetilde{e,1}\rangle$. An analogous sideband transition $|\widetilde{g,1}\rangle \rightarrow |\widetilde{e,2}\rangle$ is faintly visible with a slope -1/2 towards the top-left portion of the figure. Note also the small Autler-Townes splitting of the thermal-photon peak at $(\widetilde{\omega}_{ge} + 2\chi, \widetilde{\omega}_r + \chi)$ in the plot.

6.4.5 Autler-Townes splitting in the dressed Jaynes-Cummings system

6.4.5.1 Autler-Townes mechanism

When the transition between two quantum levels is driven strongly with a resonant drive field, the resulting 'dressed' system can be equivalently viewed as two split levels, with splitting equal to the Rabi frequency of the drive field (see Fig. 6.15). This splitting can be observed spectroscopically by probing transitions to a third level in the system, which comprises the Autler-Townes effect [64]. In this section, I take a closer look at the driven Hamiltonian to understand the mechanism of the Autler-Townes splitting of the $n = 1$ photon peak observed in our experiment. The Kerr-type nonlinearities are neglected in this model.

I begin by truncating the set of basis states of the Jaynes-Cummings Hamiltonian to the four lowest dressed levels $|\widetilde{g,0}\rangle$, $|\widetilde{e,0}\rangle$, $|\widetilde{g,1}\rangle$ and $|\widetilde{e,1}\rangle$ (see Fig. 6.15). In the experiment, the $|\widetilde{e,0}\rangle \leftrightarrow |\widetilde{e,1}\rangle$ transition is driven by a strong 'coupler' field with strength Ω_c and detuning $(\widetilde{\omega}_r + \chi) - \Omega_c \equiv \widetilde{\Delta}_c + \chi$, and the $|\widetilde{g,1}\rangle \leftrightarrow |\widetilde{e,1}\rangle$ is 'probed' by a weak field of strength Ω_p and detuning $(\widetilde{\omega}_{ge} + 2\chi) - \Omega_p \equiv \widetilde{\Delta}_p + 2\chi$ (see Fig. 6.15).

In this truncated basis, the Hamiltonian can be represented by the matrix

$$H^{(2)}_{4-\text{levels}}/\hbar \approx \begin{pmatrix} -\widetilde{\Delta}_p/2 & 0 & 0 & 0 \\ 0 & \widetilde{\Delta}_p/2 & 0 & \Omega_c/2 \\ 0 & 0 & \widetilde{\Delta}_c - \widetilde{\Delta}_p/2 - \chi & \Omega_p/2 \\ 0 & \Omega_c/2 & \Omega_p/2 & \widetilde{\Delta}_c + \widetilde{\Delta}_p/2 + \chi \end{pmatrix}, \tag{6.16}$$

where I have made the RWA and excluded transitions detuned from the drives. Equation 6.16 is written in the interaction picture of the driving tones to remove the explicit

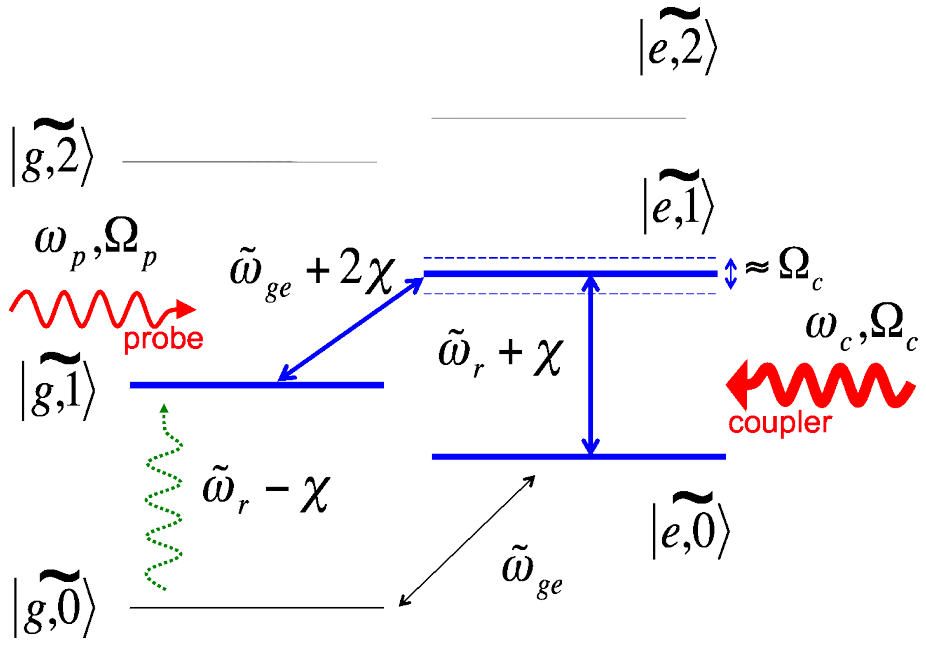

Figure 6.15: Autler-Townes mechanism of the dressed qubit-resonator states. The four lowest levels of the dispersively coupled transmon-resonator system are shown here. The three levels $|\widetilde{e,0}\rangle$, $|\widetilde{g,1}\rangle$, and $|\widetilde{e,1}\rangle$ form a lambda system. The $|\widetilde{e,0}\rangle \leftrightarrow |\widetilde{e,1}\rangle$ transition is driven with amplitude Ω_c and frequency ω_c by the coupler, and the $|\widetilde{g,1}\rangle \leftrightarrow |\widetilde{e,1}\rangle$ transition is driven by the probe tone with amplitude Ω_p and ω_p. In our experiment, the $|\widetilde{g,1}\rangle$ level is thermally populated (green) in the absence of a drive field.

time-dependence. When the probe and coupler drives are exactly resonant with the respective transitions, the detunings obey $\tilde{\Delta}_p + 2\chi = 0$ and $\tilde{\Delta}_c + \chi = 0$. Under this condition the eigenvalues of Eq. 6.16 show a splitting equal to

$$\delta = (\Omega_c^2 + \Omega_p^2)^{1/2}, \tag{6.17}$$

and for $\Omega_p \ll \Omega_c$, this gives an Autler-Townes splitting linear in the coupler Rabi frequency $\delta \simeq \Omega_c \sim (P_{rf})^{1/2}$, where P_{rf} is the drive power of the coupler tone.

6.4.5.2 Observation of Autler-Townes effect in dressed states

In Fig. 6.14, there is a small splitting in the thermal $n = 1$ photon peak when the frequencies of the probe and coupler tones are $(\omega_p, \omega_c) \simeq (\widetilde{\omega}_{ge} + 2\chi, \widetilde{\omega}_r + \chi)$. Here I follow the convention of Sec. 6.4.5.1 and refer to the strengths of the probe and coupler tones in terms their Rabi frequencies Ω_p and Ω_c. The Rabi oscillations at zero detuning on the $|\widetilde{g,0}\rangle \rightarrow |\widetilde{e,1}\rangle$ transition were used to quantify Ω_p. For the coupler tone, the following relation between Ω_c and P_{rf} was used (see Appendix C) [45]

$$\Omega_c = \left(\frac{P_{rf}}{\hbar Q_e}\right)^{1/2}. \tag{6.18}$$

Figures 6.16(a)-(c) show measurements of the splitting in the thermal $n = 1$ photon peak as I varied the strength of the coupler tone while keeping the strength of the probe tone fixed $\Omega_p/2\pi \simeq 0.3\,\mathrm{MHz}$. 6.16(a) shows that when I applied a coupler tone with strength $\Omega_c/2\pi \simeq 1.3\,\mathrm{MHz}$, I observed a splitting in the thermal $n = 1$ photon peak with a splitting size that was almost equal to Ω_c. In figure 6.16(b), we lower the strength of the coupler to $\Omega_c/2\pi \simeq 1\,\mathrm{MHz}$ and I noticed a corresponding

decrease in the splitting size to $\sim 1\,\mathrm{MHz}$. Upon further lowering the strength of the coupler to $\Omega_c/2\pi \simeq 0.6\,\mathrm{MHz}$, the splitting decreased in size to $\sim 0.6\,\mathrm{MHz}$.

The splitting size can be understood based on an Autler-Townes mechanism (see Sec. 6.4.5.1) involving the levels shown in Fig. 6.15. To begin, the $|\widetilde{g,1}\rangle$ level is populated due to thermal excitation of photons in the resonator [34, 87]. Subsequently the probe and coupler tones are applied on resonance with the transitions $|\widetilde{g,1}\rangle \leftrightarrow |\widetilde{e,1}\rangle$ and $|\widetilde{e,0}\rangle \leftrightarrow |\widetilde{e,1}\rangle$ respectively. In the presence of the two drive fields, the $|\widetilde{e,1}\rangle$ level splits into a pair of levels separated by $\delta = (\Omega_p^2 + \Omega_c^2)^{1/2}$ (Eq. 6.17). In the limit $\Omega_c \gg \Omega_p$ this splitting is almost equal to Ω_c and I observed the splitting spectroscopically upon probing the $|\widetilde{g,1}\rangle \leftrightarrow |\widetilde{e,1}\rangle$ transition.

The simple model Hamiltonian in Eq. 6.16 also predicts the overall 'shape' of the observed splitting in the (Ω_p, Ω_c) plane (see Figs. 6.16(a)-(c)). When $\tilde{\Delta}_p + 2\chi = 0$ and $\tilde{\Delta}_c + \chi \neq 0$, only the $|\widetilde{g,1}\rangle \leftrightarrow |\widetilde{e,1}\rangle$ transition is resonantly driven, while the influence of level $|\widetilde{e,0}\rangle$ is energy suppressed. This explains the vertical band corresponding to the $n = 1$ photon peak at $4.973\,\mathrm{GHz}$. When $\tilde{\Delta}_p + 2\chi = \tilde{\Delta}_c + \chi \neq 0$, the difference of the drive frequencies corresponds to the $|\widetilde{e,0}\rangle \leftrightarrow |\widetilde{g,1}\rangle$ transition. This two-photon 'red' sideband transition [94] explains the slope of +1 for the splitting in the Fig. 6.16.

For direct comparison with the data, Figs. 6.16(d)-(f) show results from steady state simulations of the system-bath master equation Eq. 6.11 in the region around the thermal $n = 1$ photon peak when driving the coupler with a strength of $\Omega_c/2\pi =$ 1.3 MHz, 1 MHz, and 0.6 MHz respectively. The parameters $\chi, \Omega_c, \Omega_p, \zeta, \zeta', \kappa_-, \kappa_+, \Gamma_-, \Gamma_+$ and γ_ϕ in the master equation were determined from independent experiments (section 6.4.2.2) and the system master equation was then solved for ρ in the steady

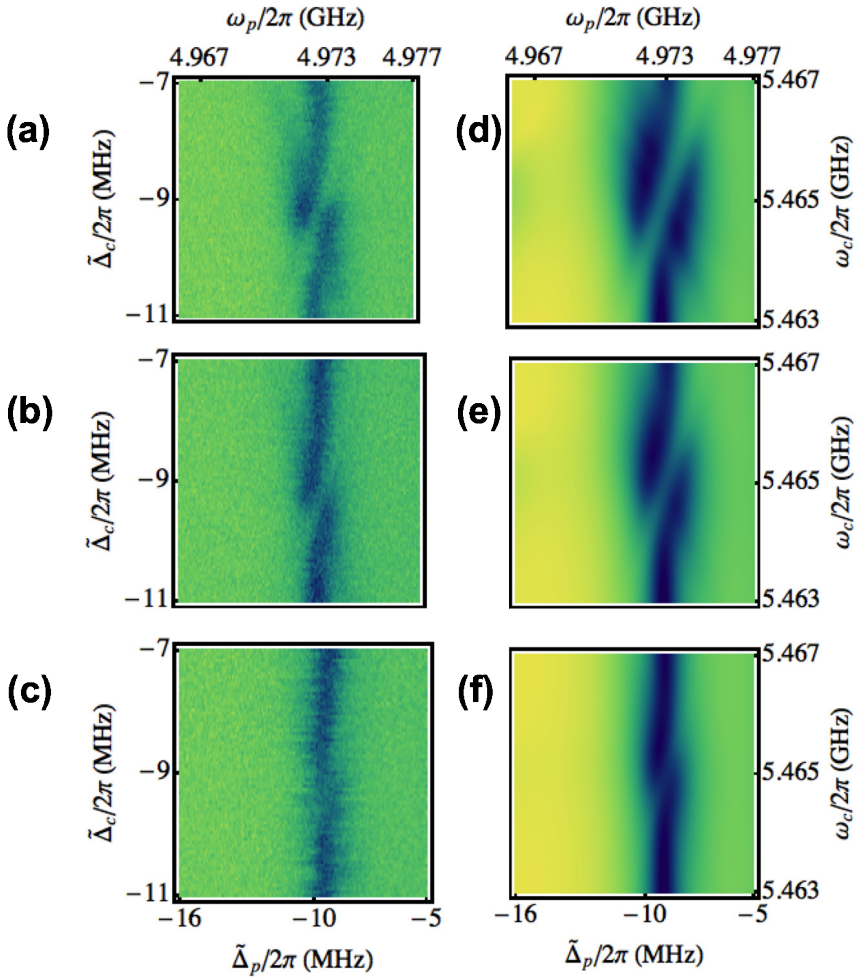

Figure 6.16: Two-tone spectroscopy of Autler-Townes splitting. False color plots of measurements of the qubit excited state probability P_e versus detuning of the applied probe ($\tilde{\Delta}_p/2\pi$) and coupler ($\tilde{\Delta}_c/2\pi$) on the n = thermal photon peak. (a)-(c) Data showing the Autler-Townes splitting of the thermal $n = 1$ photon peak for three different strengths of the coupler drive. Splitting for a coupler amplitude of (a) $\Omega_c/2\pi \sim 1.3\,\mathrm{MHz}$, (b) $\Omega_c/2\pi \sim 1\,\mathrm{MHz}$, and (c) $\Omega_c \sim 0.6\,\mathrm{MHz}$. (d)-(f) Corresponding false color plots of $\mathrm{Tr}(\rho\sigma_z)$ from numerical simulations of the steady-state master equation for the resonator-transmon system for amplitudes of the coupler drive (d) $\Omega_c/2\pi = 1.3\,\mathrm{MHz}$, (e) 1 MHz, and (f) 0.6 MHz.

state. Here I plot $P_e = \mathrm{Tr}(\rho.\sigma_z)$ to simulate the qubit state-projective read-out in our experiment [52, 35, 51]. For this simulation I actually included the two lowest qubit levels $|g\rangle, |e\rangle$, the ten lowest resonator levels, the resonator self-Kerr and qubit-resonator cross-Kerr terms in the simulation. The population in the $n = 1$ Fock state of the resonator and the $|e\rangle$ state of the transmon due to finite temperature were taken into account through the excitation rates $\kappa_+ \approx \kappa_-/10$, $\Gamma_+ \approx \Gamma_-/10$ in the system master equation.

Finally, Fig. 6.17 shows the experimentally measured splitting vs the Rabi frequency of the coupler. The Rabi frequency of the coupler Ω_c was calibrated using Eq. 6.18. The root-mean-square voltage $V_{rf} = (Z_0 P_{rf})^{1/2}$ of the coupler tone on the CPW transmission line was calculated by assuming $Z_0 = 50\,\Omega$ for the impedance of the transmission line. The red curve in the Fig. 6.17 is the splitting size $\delta/2\pi \simeq (\Omega_c^2 + \Omega_p^2)^{1/2}/2\pi$ predicted by Eq. 6.17 for a fixed $\Omega_p/2\pi \simeq 0.3\,\mathrm{MHz}$ and it agrees well with the experimental data. Here I note that the observed Autler-Townes splitting is nearly linear (see blue dashed line) in the amplitude of the coupler drive voltage V_{rf} and is almost equal to the Rabi frequency of the coupler field, as expected from Eq. 6.17.

I note that the simple model also predicts an Autler-Townes splitting of the $n = 0$ photon qubit peak when the probe and coupler frequencies are $(\Omega_p, \Omega_c) \simeq (\tilde{\omega}_{ge}, \tilde{\omega}_r + \chi)$. I see a hint of this splitting in Fig. 6.14 but it is not fully resolved because of the line-width of the qubit $|\widetilde{g, 0}\rangle \leftrightarrow |\widetilde{e, 0}\rangle$ transition. The Autler-Townes mechanism for the splitting in the $n = 0$ photon peak involves the $|\widetilde{g, 0}\rangle$, $|\widetilde{e, 0}\rangle$, $|\widetilde{e, 1}\rangle$ levels (see Fig. 6.15). The three-level subsystem forms a 'ladder' configuration, with

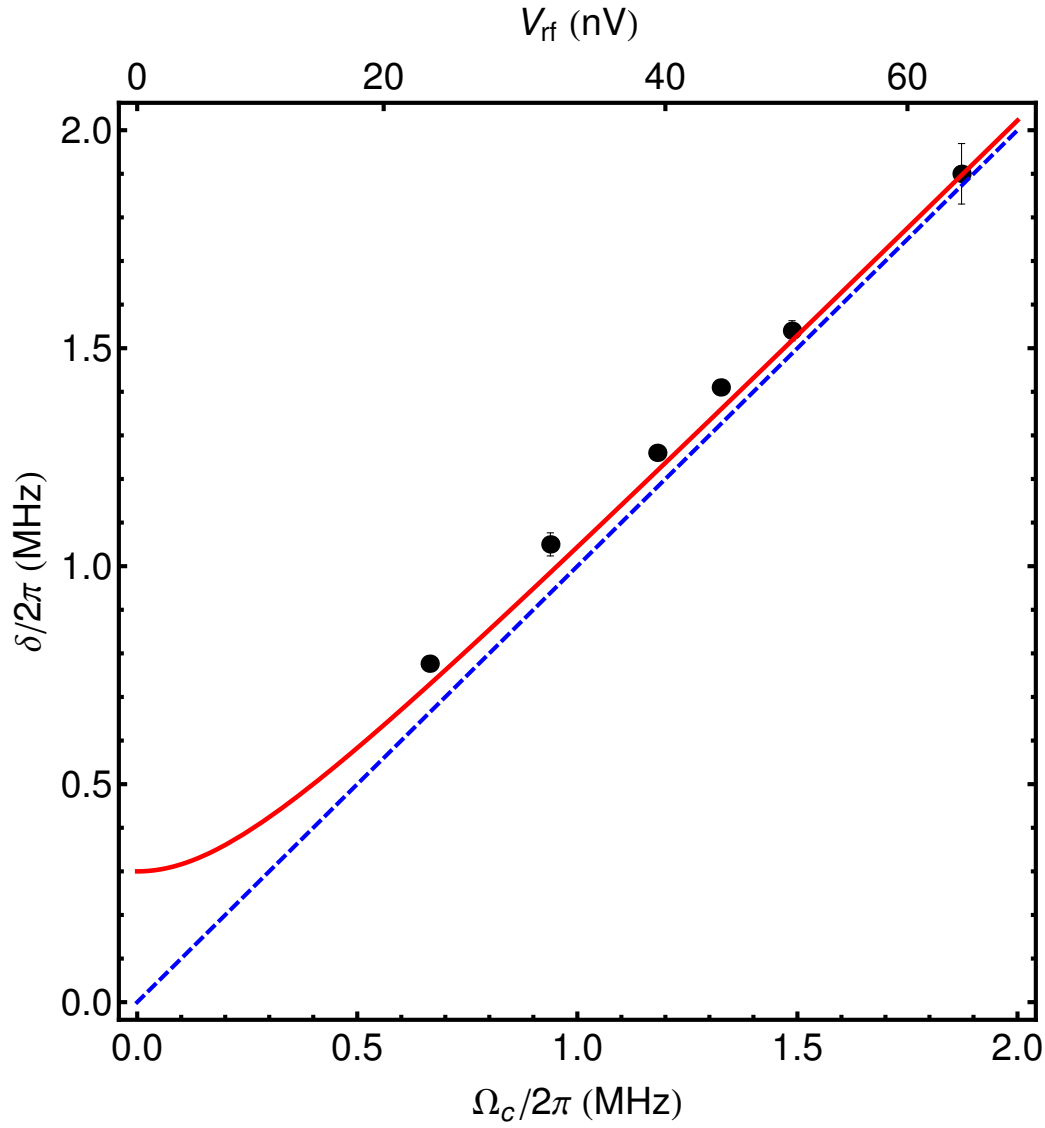

Figure 6.17: Plot of Autler-Townes splitting size $\delta/2\pi$ versus drive amplitude of the coupler field $\Omega_c/2\pi$. Measured Autler-Townes splitting (black circles) in the thermal $n = 1$ photon peak increases linearly with the voltage of the coupler drive $V_{rf} \propto (P_{rf})^{1/2}$ at the CPW transmission line. The Rabi frequency Ω_c of the coupler is calibrated from P_{rf} using Eq. 6.18. The red curve is predicted splitting size from Eq. 6.17 where $\Omega_p/2\pi = 0.3\,\mathrm{MHz}$ was calibrated from Rabi oscillations and Ω_c was calibrated from data in Fig. 6.14. Blue dashed curve shows line with slope +1 for comparison.

the $|\widetilde{e,0}\rangle \leftrightarrow |\widetilde{e,1}\rangle$ transition driven strongly with a 'coupler' tone and the $|\widetilde{g,0}\rangle \leftrightarrow |\widetilde{e,0}\rangle$ transition weakly 'probed'.

6.5 Conclusion

In this chapter I discussed spectroscopic measurements of resonator-transmon cQED devices and showed how the various parameters of the coupled system were determined spectroscopically. In particular I studied photon number-splitting in the spectrum of device LEv5-ZK9, a transmon coupled to a lumped element resonator in the strong dispersive regime. The nonlinearities in the photon occupancy were compared to results from a numerical solution of the system master equation, as well as through a semiclassical steady-state solution to the driven oscillator. Higher order corrections to the dispersive approximation were shown to play a prominent role in causing the nonlinear power-dependence of the photon occupancy. In the absence of a coherent field driving the resonator, I observed an average thermal population $n_{th} = 0.1$ of microwave photons in the resonator, corresponding to an effective temperature of 120 mK. I observed additional photon number peaks with weights w_n (6.12) in the qubit spectrum when a coherent coupler tone is applied to the resonator. In the presence of a strong coupler field and a weak probe field, I observed an Autler-Townes spitting of the thermal $n = 1$ photon peak. The size of the splitting increased linearly with the amplitude of the coupler tone as expected for an Autler-Townes effect in the 'lambda' system comprising the $|\widetilde{g,1}\rangle$, $|\widetilde{e,0}\rangle$, $|\widetilde{e,1}\rangle$ levels of the dressed Jaynes-Cummings transmon-resonator system. Numerical simulations of the steady state

system-bath master equation for the density matrix with two qubit levels and up to ten resonator levels agreed well with the experimental observations.

In atomic systems, observing the Autler-Townes effect can be a precursor to seeing electromagnetically induced transparency or absorption (EIT/EIA) [91, 93]. EIT (EIA) gives rise to exotic phenomena such as 'slow-light' [95], and its use as a sensitive probe for the decoherence of a quantum state was proposed [96]. Clear observation of EIT in superconducting systems typically requires engineering the coherence of the three 'atom' states independently [96], and how this can be done is an open question in superconducting qubit research. Ian *et al.* [93] theoretically explored the possibility of achieving EIT in dressed qubit-resonator system due to the inherent tunability of the coherences. Since the Autler-Townes effect is closely related to EIT [65, 93, 97, 98], this observation of the Autler-Townes effect in a dressed qubit-resonator system was a big step in this direction. In fact, as I was writing my thesis, Novikov *et al.* [111] reported seeing EIT effects in a transmon-resonator system.

Chapter 7

Transmon coherence measurements

7.1 Overview

A perfectly isolated quantum system in an eigenstate of the Hamiltonian remains in that state forever. In reality, no system is perfectly isolated. In order to perform a measurement on a quantum system, an observer and the system have to interact. In addition, *uncontrollable* degrees of freedom of the *environment* couple to any real quantum. These degrees of freedom could be electrical noise from a resistor [99, 100], the vacuum fluctuations of the electromagnetic field acting as a quantum noise source [101, 28], coupling to other TLS's [16, 33] in the dielectrics or magnetic flux noise [102, 103, 29]. Some of these sources of noise [100, 28, 101] cause a qubit to lose energy through relaxation, while other sources [102, 29] cause the qubit quantum state to lose its phase coherence and gradually *dephase* into an incoherent statistical mixture. Together, these effects combine to cause decoherence in qubits, compromising their use for quantum computation.

In Chapter 6, I discussed the spectroscopy of my transmons. The gate-times (pulse lengths), used for qubit state preparation in those measurements were long ($\sim 10\,\mu$s). The coherent oscillations in my qubits decayed on timescales shorter than that ($\sim 1\,\mu$s) and the system reached a steady state. The density matrix for the steady state of a such a driven system corresponds to that of an incoherent statistical

mixture, as described in Chapter 3.

In this Chapter, I discuss my time-domain measurements to resolve the qubit energy relaxation and coherent oscillations. I begin by describing the measurement technique I used for measuring energy relaxation, Rabi oscillations, and Ramsey free-induction decay. I then review earlier work by Z. Kim *et al.* [75] on the correlation between relaxation and Rabi coupling. This work was important because in essence I extend this study to Transmons coupled to lumped element resonators. As part of this study, I describe the design changes I made to decouple the transmons from the dissipative environment. Finally, I conclude with a discussion of the new limits on T_1 set by dielectric loss in my devices.

7.2 Energy relaxation or T_1 measurements

I measured relaxation of the excited state of the transmon by first exciting the qubit and then monitoring the probability in the excited state as a function of time. To do this measurement, I used the Jaynes-Cummings read-out [35] (see Chapter 5) as follows. First, I sent a $5\,\mu$s long calibration read-out pulse with frequency ω_r and optimal read-out amplitude. After waiting for $\sim 80\,\mu$s to ensure that the photons in the resonator had dissipated away, I sent a qubit excitation pulse or "probe pulse", resonant with the qubit transition frequency $\tilde{\omega}_{ge}$. The probe pulse was then turned off. A delay time t after turning off the probe pulse, I sent a second read-out pulse. Since the qubit was excited during the excitation pulse, the difference of the average transmitted voltages of the two read-out pulses was proportional to the probability

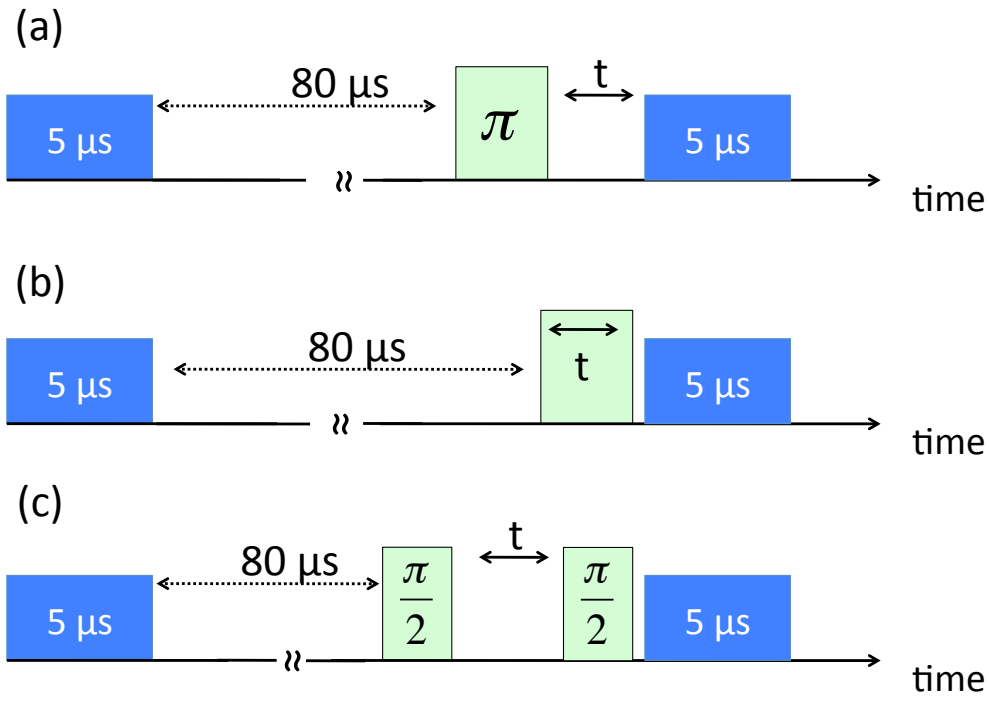

Figure 7.1: Pulse sequence for time-domain coherence measurements. The difference in the mean transmitted pulsed amplitude for the two read-out pulses (blue) is calibrated to P_e. (a) T_1 measurement. P_e vs delay t shows an exponential decay $\sim e^{-t/T_1}$. (b) P_e vs pulse-width t shows exponentially damped sinusoidal oscillations $\sim e^{-t/T'} \sin \Omega_p t$. (c) P_e vs delay t between the $\pi/2$-pulses shows exponentially damped Ramsey fringes $\sim e^{-t/T_2^*} \sin \delta t$ where $\delta = |\omega_{ge} - \omega_p|$.

in the excited state [35].

The pulse sequence for the T_1 measurement is shown in Fig. 7.1(a). This sequence is repeated about 5000 times for each delay t and then the delay time t is swept. By fitting the difference in the average transmitted voltage amplitude of the two read-out pulses to an exponential decay

$$V_{out}(t) = V_0\, e^{-t/T_1} = V_0\, e^{-\Gamma t} \tag{7.1}$$

the energy relaxation time or lifetime T_1 can be measured, where $\Gamma = 1/T_1$ is the qubit relaxation rate.

Device LEv5-7 (Figure 7.2(a)) was the first transmon that I characterized the coherence. The resonant frequency of the lumped-element resonator was around 5.46 GHz. The resonator was separated from the CPW transmission line by a 2 μm strip of ground plane. The total quality factor of the resonator was around $Q_L = 18,000$. The transmon had a single Josephson junction (see Fig. 7.2(b)) shunted by an IDC. The transmon was fabricated between the capacitor of the resonator and the ground plane (see Fig.7.2(a)). The qubit excitation frequency for this device was 8 GHz.

Figure 7.3 shows the relaxation data for device LEv5-7. I fit an exponential decay (shown in red in Fig. 7.3), to the qubit excited state probability P_e plotted vs time and found $T_1 = 270$ ns. The probe pulse used for this measurement was a π-pulse with a length of $\tau_\pi = 42$ ns, in order to initialize the qubit in the excited state. The microwave drive power at the CPW transmission line was around -110 dBm. The length of the $\pi-$pulse for this drive power was obtained from Rabi oscillations

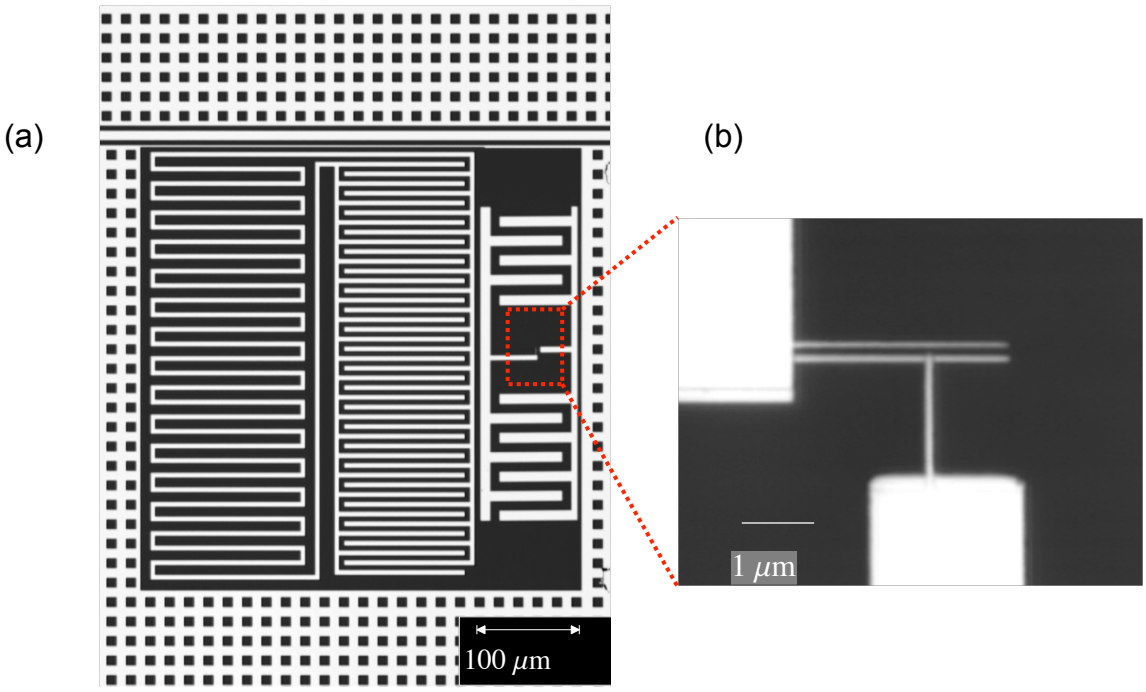

Figure 7.2: (a)Micrograph of transmon LEv5-7 coupled to resonator. The resonator and transmission line are separated by a 2 μm strip of ground plane giving an external quality factor $Q_e = 20,000$. Lumped element resonator has a resonant frequency of 5.4 GHz. (b) Detailed view of transmon LEv5-7 Josephson junction. Total area of the Josephson junction is 150 nm $\times$ 150 nm.

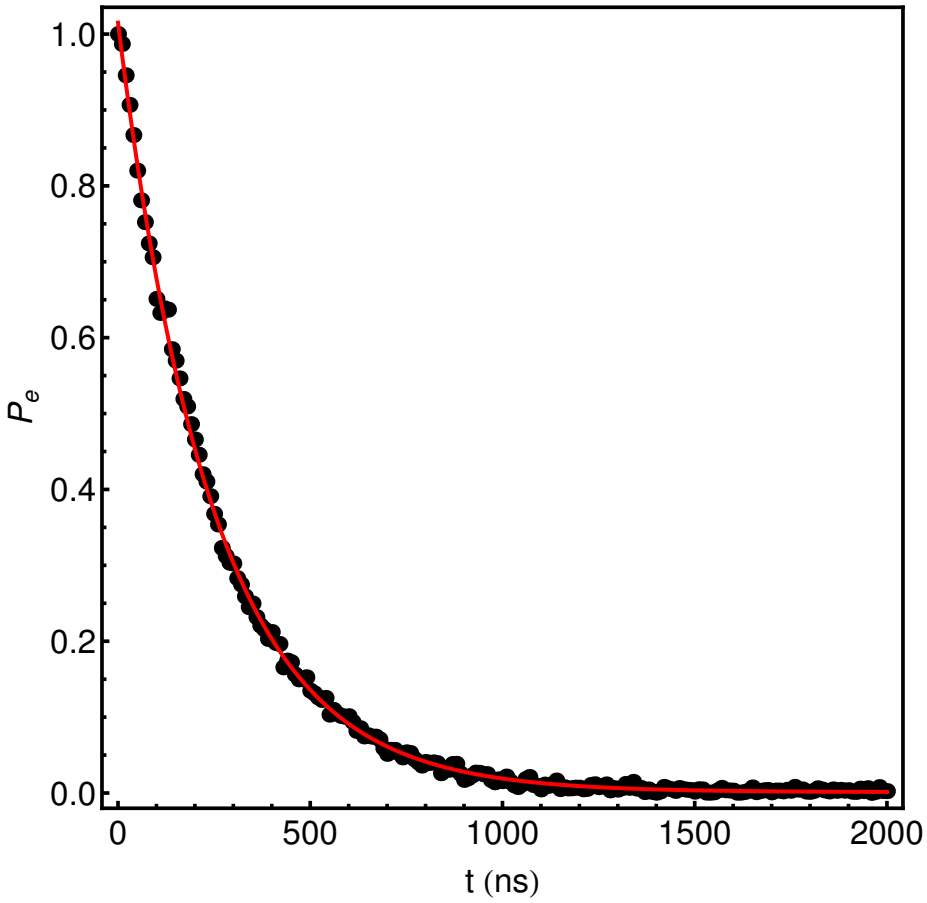

Figure 7.3: Measured excited state probability P_e vs t for device LEv5-7. Black dots are data. Red curve is the exponential decay fit giving a decay time of $T_1 = 270\,\text{ns}$.

measurements discussed later in this Chapter.

7.2.1 T_1 and noise at the qubit transition frequency

Qubit relaxation can be viewed as being due to noise at the qubit transition frequency. A detailed discussion of this subject is given in [101]. Consider a pure TLS specified by the Hamiltonian

$$H_0 = \frac{\hbar\omega_{ge}}{2}\sigma_z \tag{7.2}$$

where ω_{ge} is the qubit transition frequency. Let the noise source be treated, for the time being, as a time-dependent random signal $f(t)$. The particular details of the noise and its causes are not relevant for this analysis. The interaction of this noise with the qubit causes qubit transitions. The perturbation can be written simply as

$$V = A\, f(t)\, \sigma_x \tag{7.3}$$

where A is the strength with which the noise couples to the qubit.

Let the qubit be initially prepared in the excited state $|e\rangle$. If the coupling is weak, the time evolution for short times can be predicted using first-order time-dependent perturbation theory. Working in the interaction picture of the qubit transition, the time-dependent probability amplitude for the qubit to transition to the ground state can be written as

$$\alpha_g(t) \approx -\frac{iA}{\hbar} \int_0^t \mathrm{d}\tau\, \langle g|e^{iH_0\tau/\hbar}\sigma_x e^{-iH_0\tau/\hbar}|e\rangle f(\tau) \tag{7.4}$$

$$= -\frac{iA}{\hbar} \int_0^t \mathrm{d}\tau\, e^{-i\omega_{ge}\tau} f(\tau). \tag{7.5}$$

The probability for the transition can then be written as

$$|\alpha_g|^2 \approx \frac{A^2}{\hbar^2} \int_0^t \mathrm{d}\tau_1 \int_0^t \mathrm{d}\tau_2\, e^{i\omega_{ge}(\tau_1-\tau_2)} f^*(\tau_1) f(\tau_2). \tag{7.6}$$

Since $f(t)$ is a random signal, we can consider an ensemble average. The average ground state probability $\bar{p}_g$ is then

$$\bar{p}_g \approx \frac{A^2}{\hbar^2} \int_0^t \mathrm{d}\tau_1 \int_0^t \mathrm{d}\tau_2\, e^{i\omega_{ge}(\tau_1-\tau_2)} \langle f^*(\tau_1) f(\tau_2)\rangle. \tag{7.7}$$

. We can now impose the condition of stationarity for the noise source, which means that the correlation function $\langle f^*(\tau_1) f(\tau_2)\rangle$ is time-translation invariant, and therefore

can be written as $\langle f^*(\tau_1 - \tau_2) f(0)\rangle$. Moreover, if the noise is sufficiently broad-band, or *Markovian* [105], the auto-correlation function behaves as $\langle f^*(\tau) f(0)\rangle \sim e^{-\tau/\tau_f}\langle f^*(0) f(0)\rangle$ for a correlation time τ_f that is *very small* compared to the time scales of evolution of the Hamiltonian. We now make the transformation to the new variables $T \equiv (\tau_1 + \tau_2)/2$ and $\tau \equiv \tau_1 - \tau_2$. Under these assumptions Eq. 7.7 becomes

$$\bar{p}_g = \frac{A^2}{\hbar^2}\int_0^t \mathrm{d}T \int_{-\infty}^{\infty} \mathrm{d}\tau\, e^{i\omega_{ge}\tau}\langle f^*(\tau) f(0)\rangle \tag{7.8}$$

$$= \frac{A^2 t}{\hbar^2}\int_{-\infty}^{\infty} \mathrm{d}\tau\, e^{i\omega_{ge}\tau}\langle f^*(\tau) f(0)\rangle \tag{7.9}$$

$$= \frac{A^2 t}{\hbar^2} S_f(\omega_{ge}) \tag{7.10}$$

where I have defined the *spectral density* of the noise

$$S_f(\omega) = \int_{-\infty}^{\infty} \mathrm{d}\tau\, e^{i\omega\tau}\langle f^*(\tau) f(0)\rangle. \tag{7.11}$$

In Eq. 7.10 the linear increase of the probability with time implies that this results holds only for short time-intervals, when first order perturbation theory is valid. We can now define the decay rate Γ_- as

$$\Gamma_- = \frac{\mathrm{d}\bar{p}_g}{\mathrm{d}t} \tag{7.12}$$

$$= \frac{A^2}{\hbar^2} S_f(\omega_{ge}). \tag{7.13}$$

This expression shows that a noise at the qubit transition frequency will cause relaxation of the excited state.

One could do a similar calculation in which the qubit in initialized in the ground state. The resulting excitation rate Γ_+ is found to be

$$\Gamma_+ = \frac{A^2}{\hbar} S_f(-\omega_{ge}) \tag{7.14}$$

with the only difference being that the relevant component of the noise spectrum is at the negative frequency $-\omega_{ge}$. In other words, the qubit *samples* the noise spectral density at the transition frequency.

So far we have treated $f(t)$ as a real function and this gives $S_f(\omega_{ge}) = S_f(-\omega_{ge})$. This is the case in the classical realm, which will valid at temperatures $T \gg \hbar\omega_{ge}/k_B$. However, at low temperatures $T \ll \hbar\omega_{ge}/k_B$, the qubit is sampling *quantum* noise [105], and in general $S_f(\omega_{ge}) \neq S_f(-\omega_{ge})$.

To understand the T_1 decay of the qubit from the noise point of view, I first consider the system initially in steady state. If the noise is in thermal equilibrium at temperature T, in the steady state from Einstein's principle of detailed balance [81, 82] we have for a TLS that

$$\bar{p}_g\Gamma_+ = \bar{p}_e\Gamma_- \tag{7.15}$$

and

$$\Gamma_+ = e^{-\beta\hbar\omega_{ge}}\Gamma_- \tag{7.16}$$

and thus:

$$\bar{p}_e = \bar{p}_g e^{-\beta\hbar\omega_{ge}}. \tag{7.17}$$

At $T = 0$, this gives an excitation rate $\Gamma_+ = 0$.

The steady state density matrix of an undriven TLS coupled to a bath at temperature T is given by

$$\rho_{ss} = \bar{p}_g|g\rangle\langle g| + \bar{p}_e|e\rangle\langle e| \tag{7.18}$$

where $\bar{p}_g + \bar{p}_e = 1$. If at $t = 0$ we displace the system into a state given by

$$\rho' = (\bar{p}_g - \delta p_e)|g\rangle\langle g| + (\bar{p}_e + \delta p_e)|e\rangle\langle e| \tag{7.19}$$

we can deduce from detailed balance that the excess probability in the excited state evolves with time according to the equation

$$\frac{\mathrm{d}(\delta p_e)}{\mathrm{d}t} = -\delta p_e(\Gamma_+ + \Gamma_-) \tag{7.20}$$

giving us an exponential decay into the steady state

$$\delta p_e(t) = \delta p_e(0)\, e^{-\Gamma t} = \delta p_e(0)\, e^{-t/T_1} \tag{7.21}$$

where the decay-rate $\Gamma \equiv \Gamma_+ + \Gamma_- \equiv 1/T_1$.

If the temperature is sufficiently low, we can ignore the excitation rate and $\Gamma \approx \Gamma_-$. This approximation is quite accurate at dilution refrigerator temperatures – at 50 mK the exponential factor $e^{-\beta\hbar\omega_{ge}} \approx 10^{-4} \ll 1$ for $\omega_{ge}/2\pi \simeq 5\,\mathrm{GHz}$. Therefore, by measuring the T_1 as described earlier we measure Γ_- that is proportional to the spectral density of noise at the qubit transition frequency $S_f(\omega_{ge})$ (Eq. 7.13).

To determine the spectral density of noise fully, we need to know the strength of the qubit coupling A to the noise. Since in this generic analysis I have not specified the physical source of $f(t)$, A represents the *effective* coupling to *all* the noise sources. In the following, I discuss the coupling of a transmon to *one* of those sources of noise - voltage noise in the 50 Ω transmission line. For my transmons coupled to lumped element resonators, I found that the coupling to the 50 Ω transmission line can be a significant source of T_1 decay. This coupling strength can be determined by measuring the Rabi oscillations of the qubit, as I discuss in the next section.

7.3 Rabi oscillations

7.3.1 Theory

When a qubit is driven with a classical harmonic excitation resonant with the transition frequency, the probability to be in the excited state oscillates sinusoidally between 0 and 1.

Consider the pure TLS Hamiltonian H_0 given in Eq. 7.2. For the perturbation Hamiltonian, instead of a random noise signal, I consider a sinusoidal excitation

$$V(t) = -\hbar\Omega_p\sigma_x \cos\omega_p t \tag{7.22}$$

where the particular form of the perturbation Hamiltonian is chosen to be consistent with the notation in the rest of this thesis. The total Hamiltonian governing the evolution is $H = H_0 + V(t)$. I now consider an initial state of the system

$$|\psi_S(0)\rangle = \alpha_g^0|g\rangle + \alpha_e^0|e\rangle \tag{7.23}$$

where the S denotes explicitly that we are working in the Schrodinger picture.

It is convenient to now go into the interaction frame of the unperturbed Hamiltonian, also called the Dirac picture [67, 83]. This is achieved by the unitary transformation $U(t) = e^{iH_0t/\hbar}$. Under this transformation, the Schrodinger kets transform into the interaction kets as $|\psi_I(t)\rangle = U|\psi_S(t)\rangle$. The Hamiltonian itself gets transformed into $H_I = UVU^\dagger$. In this picture, the Schrodinger equation can be written as

$$i\hbar\frac{\mathrm{d}|\psi_I\rangle}{\mathrm{d}t} = H_I|\psi_I\rangle \tag{7.24}$$

For the particular case of a qubit driven by a harmonic excitation, Eq. 7.24 can be solved exactly. Transforming the solution back into the Schrodinger picture, we find

$$|\psi_S(t)\rangle = \left(\alpha_g^0 \cos\frac{\Omega_p t}{2} - i\alpha_e^0 \sin\frac{\Omega_p t}{2}\right)|g\rangle + \left(\alpha_e^0 \cos\frac{\Omega_p t}{2} + i\alpha_g^0 \sin\frac{\Omega_p t}{2}\right)|e\rangle \quad (7.25)$$

This is the general solution. If we begin with the qubit in the ground state, such that $\alpha_g^0 = 1$ and $\alpha_e^0 = 0$, we obtain the particular solution

$$|\psi_S(t)\rangle = \cos\frac{\Omega_p t}{2}|g\rangle + i\sin\frac{\Omega_p t}{2}|e\rangle \quad (7.26)$$

The ground and excited state probabilities are then given by

$$P_e = |\langle e|\psi_S\rangle|^2 = \frac{1-\cos\Omega_p t}{2} \quad (7.27)$$

$$P_g = |\langle g|\psi_S\rangle|^2 = \frac{1+\cos\Omega_p t}{2}. \quad (7.28)$$

From Eq. 7.27 and Eq. 7.28, one can see that the probability of the excited state oscillates with a frequency Ω_p, called the Rabi frequency. Figure 7.4(a) shows the probability P_g for the qubit to be in the ground state (black curve) and P_e to be in the excited state (blue curve) as a function of time. In the absence of decoherence, these coherent oscillations would go on without decaying. By controlling the duration of excitation, one can transfer a required fraction of probability into the excited state, or create specific superposition states. In particular, for a duration $\tau_\pi = \pi/\Omega_p$, the excited state probability reaches 1, *i.e.* there is a 100% population inversion into the excited state. A pulse of duration τ_π is called a π-pulse and I used such pulses to initialize qubits in the excited state.

7.3.2 Rabi oscillation measurement

To measure the Rabi oscillations, I used the following pulse sequence (see Fig. 7.1(b)). I first sent a 5 μs long reference pulse. After waiting 80 μs, a qubit excitation pulse of length t was then sent, resonant with the qubit frequency. About 10 ns after the qubit excitation pulse was turned off, a second read-out pulse was sent. The difference of the mean transmitted amplitudes of the two read-out pulses is proportional to the excited state probability P_e [35]. This measurement was repeated 5000 times for each pulse length t, and then t was swept. Plotting the mean transmitted voltage vs the pulse length of the qubit excitation, we see oscillations as shown in Fig. 7.4(b).

The data (black dots) in Fig. 7.4(b) is from device LEv5-7 (see Fig. 7.2). The frequency of the qubit excitation was 8 GHz and microwave power at the device was -116 dBm for this measurement. The y-axis in the figure was calibrated to the excited state probability P_e by normalizing the output voltage with the maximum amplitude of the oscillation, which I assumed was a 100% population in the excited state. The striking difference between theory (Fig. 7.4(a)) and experiment (Fig. 7.4(b)) is the exponential decay of the oscillation amplitude.

In Fig. 7.4(b), I also show the the data was fit (red curve) to an exponentially decaying sinusoidal function $y(t) = y_0 + Ae^{-t/T'} \sin \Omega_p(t - t_0)$, where T' is the Rabi decay time constant. From the fit, the Rabi frequency was determined to be $\Omega_p/2\pi = 4$ MHz. The π-pulse for this data was ~ 120 ns and the fit gave a Rabi decay time $T' = 377$ ns.

From the system master equation discussed in Chapter 3, one expects that T'

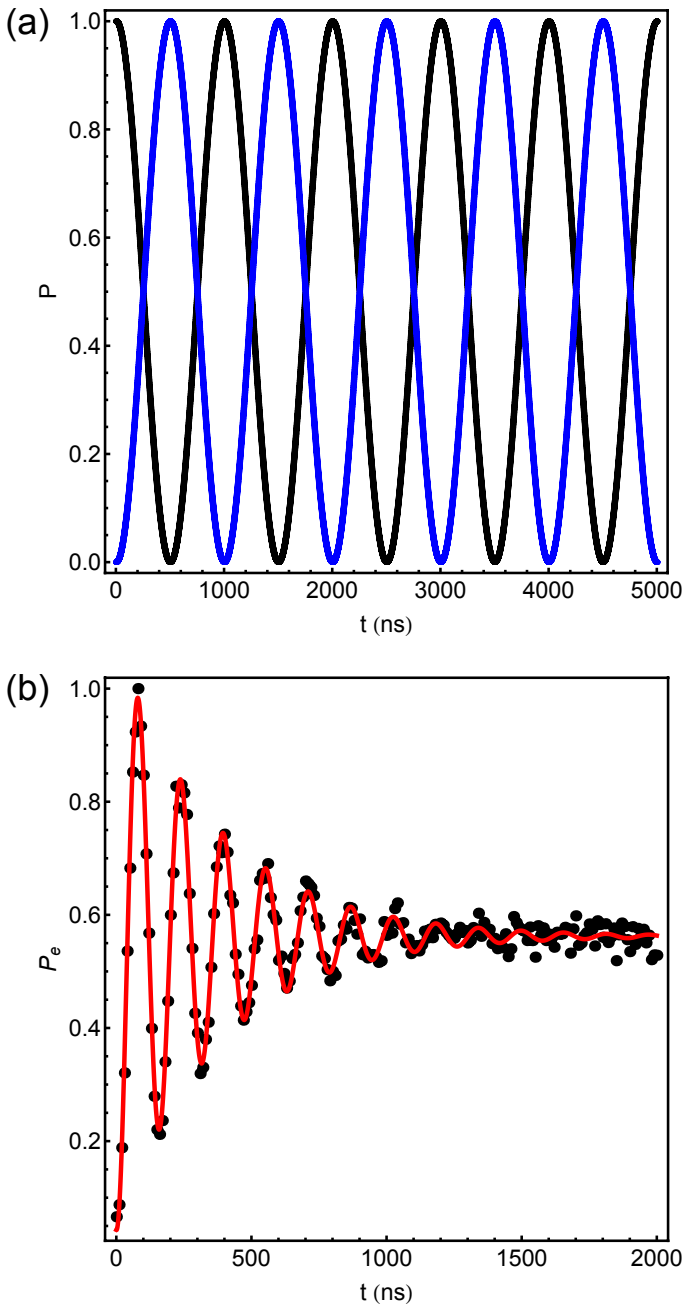

Figure 7.4: Rabi oscillations in a qubit - Theory vs Experiment. (a) P_e (Blue) and P_g (Back) calculated using Eq. 7.27 and Eq. 7.28. The oscillations do not decay in time in the absence of dissipation. (b) Measured Rabi oscillations of excited state for device LEv5-7 with a -116 dBm qubit drive power. Black dots are data and Red curve is an exponentially damped sinusoidal fit. The Rabi frequency is 4 MHz and Rabi decay time $T' = 0.37\,\mu$s from the fit.

is related to the relaxation time T_1 and the coherence time T_2 of the qubit via

$$\frac{1}{T'} = \frac{1}{2T_1} + \frac{1}{2T_2}. \tag{7.29}$$

A lower bound for the T_2 is obtained from the spectroscopic coherence time T_2^* that can be measured from the decay of Ramsey fringes, as discussed later in this Chapter. T_2^* is in general smaller than T_2 since it also includes inhomogeneous broadening [75]. Since the coherence time is fundamentally limited by the relaxation according to $T_2 \leq 2T_1$ [68], one finds that $T' \leq 4T_1/3$. For device LEv5-7, $T_1 = 270\,\text{ns}$ and the Rabi decay time of 377 ns is close to the limit of $4T_1/3 \approx 370\,\text{ns}$. The coherence of a device operating in this limit is termed as being nearly 'T_1 - limited'. In this limit, improving T_1 improves the coherence time T_2 until other factors (such as dephasing) limit it.

7.3.3 Rabi coupling to the drive

The frequency of the Rabi oscillations is expected to change linearly with the drive voltage in the limit $\Omega_p\sqrt{T_1T_2} \gg 1$ [18]. To see this explicitly in the context of cQED, I can revisit the derivation of the cQED Hamiltonian from the circuit analysis (see Chapter 2). The Hamiltonian for the qubit-resonator circuit shown in Fig. 2.9, in terms of the node-fluxes and node-charges can be written as

$$\mathcal{H} = \frac{Q_r^2}{2C_{res}} + \frac{\Phi_r^2}{2L_r} + \frac{Q_J^2}{2C_\Sigma} - E_J\cos\left(2\pi\frac{\phi_J}{\phi_0}\right) + \beta_{rJ}Q_rQ_J + \beta_rVQ_r + \beta_JVQ_J. \tag{7.30}$$

where the subscript r stands for resonator and J stands for the transmon Josephson junction. The term β_JVQ_J in this Hamiltonian corresponds to the qubit drive. The

term β_J depends only on the capacitances in the network:

$$\beta_J = \frac{C_g C_s}{C_g C_s + C_g C_r + C_b C_r + C_b C_s + C_b C_g}. \tag{7.31}$$

If the transmon is driven using a harmonic drive $V = V_0 \cos \omega_p t$ with voltage amplitude V_0 and frequency ω_p applied to the CPW transmission line, then the drive term takes the form

$$H' = \beta_J V_0 Q_J \cos \omega_p t. \tag{7.32}$$

Quantizing the transmon charge operator and making the two-level approximation for the transmon (see Chapter 2), I can write:

$$Q_J = -e \left(\frac{E_J}{2E_c} \right)^{1/4} \sigma_x. \tag{7.33}$$

The interaction Hamiltonian then reads

$$H' = -\beta_J e V_0 \left(\frac{E_J}{2E_c} \right)^{1/4} \sigma_x \cos \omega_p t. \tag{7.34}$$

This is of the form

$$H' = -\hbar \Omega_p \sigma_x \cos \omega_p t \tag{7.35}$$

where

$$\Omega_p = \frac{e}{\hbar} \beta_J \left(\frac{E_J}{2E_c} \right)^{1/4} V_0. \tag{7.36}$$

And in terms of the RMS voltage of the microwaves, we have

$$f_{Rabi} = \frac{\Omega_p}{2\pi} = \frac{e}{h} \beta_J \left(\frac{2E_J}{E_c} \right)^{1/4} V_{rms} \tag{7.37}$$

or:

$$\frac{\mathrm{d}f_{Rabi}}{\mathrm{d}V_{rms}} = \frac{e}{h} \beta_J \left(\frac{2E_J}{E_c} \right)^{1/4}. \tag{7.38}$$

Equation 7.37 explicitly shows the linear relation between Rabi frequency and the applied microwave voltage V_{rms} at the transmission line. The proportionality constant $\mathrm{d}f_{Rabi}/\mathrm{d}V_{rms}$ given in 7.38, simply termed the Rabi coupling in this thesis, gives the strength with which the transmon couples to the microwave drive.

7.3.4 Coupling to the quantum noise of the transmission line

In a real system, any channel that drives transitions in the qubit can act as a source of noise. In my devices, voltage on the CPW transmission line of the device drives qubit transitions and random fluctuations in the voltage signal constitute a noise source that can cause relaxation. From Eq. 7.13, the decay rate of a qubit due to coupling to the voltage noise on the drive channel can be expressed in terms of the Rabi coupling as

$$\Gamma_- = \left(\frac{\mathrm{d}f_{Rabi}}{\mathrm{d}V_{rms}}\right)^2 4\pi^2 S_V(\omega_{ge}) \tag{7.39}$$

where $S_V(\omega_{ge})$ is the spectral density of voltage noise on the transmission line of the device.

Since the transmission line is designed to offer an impedance $Z_0 = 50\,\Omega$ to the propagating microwaves, I assume it behaves as an ideal frequency-independent $50\,\Omega$ resistance [99, 100]. In thermal equilibrium, a resistive element has spontaneous fluctuations caused by thermal agitation of the charge carriers [99, 100, 104]. The spectral density of voltage noise at frequency ω for a pure resistance R in thermal equilibrium at a temperature given by $k_B T = 1/\beta$, is given by

$$S_V(\omega) = \frac{2R\hbar\omega}{1 - e^{-\beta\hbar\omega}}. \tag{7.40}$$

In the limit of high temperature $T \gg \hbar\omega/k_B$, this becomes the classical Johnson noise for a resistor given by $S_V(\omega) = 2Rk_BT$ for $\omega > 0$. In this limit, the noise spectrum is independent of frequency or "white noise". I note that here I am using the 'two-sided' convention for the noise spectrum, as in [105]. In the quantum limit of $\hbar\omega \gg k_BT$, the spectral density becomes linear in frequency $S_V(\omega) = 2R\hbar\omega$. At millikelvin temperatures ($T \sim 20\,\mathrm{mK}$) and for frequencies in the microwave region ($\omega/2\pi \sim 6\,\mathrm{GHz}$), it is the quantum limit of the noise that is relevant. In this limit, qubit relaxation rate can be written as

$$\Gamma_- = \frac{1}{T_1} = \left(\frac{\mathrm{d}f_{Rabi}}{\mathrm{d}V_{rms}}\right)^2 8\pi^2 R\hbar\omega. \tag{7.41}$$

7.3.5 Rabi coupling measurement

To find the Rabi coupling to the transmission line, I measured the frequency f_{Rabi} of the Rabi oscillations of the excited state probability of my qubits for different RMS microwave voltages V_{rms} applied at the transmission line. The differential coefficient $\mathrm{d}f_{Rabi}/\mathrm{d}V_{rms}$ then gave the Rabi coupling to the transmission line.

Figure 7.5(a) shows Rabi oscillations for device LEv5-7 at a microwave power of -116 dBm, and Fig. 7.5(b) shows Rabi oscillations for a microwave power of $-119\,\mathrm{dBm}$, with the power being specified on the CPW transmission line. In order to calculate the microwave power at the device from the microwave power at the source, I had to first calculate the total attenuation between the microwave source and the device. I used the photon number-splitting data shown in Chapter 6 to calibrate the line attenuation. From the number-splitting data, the total attenuation on the input

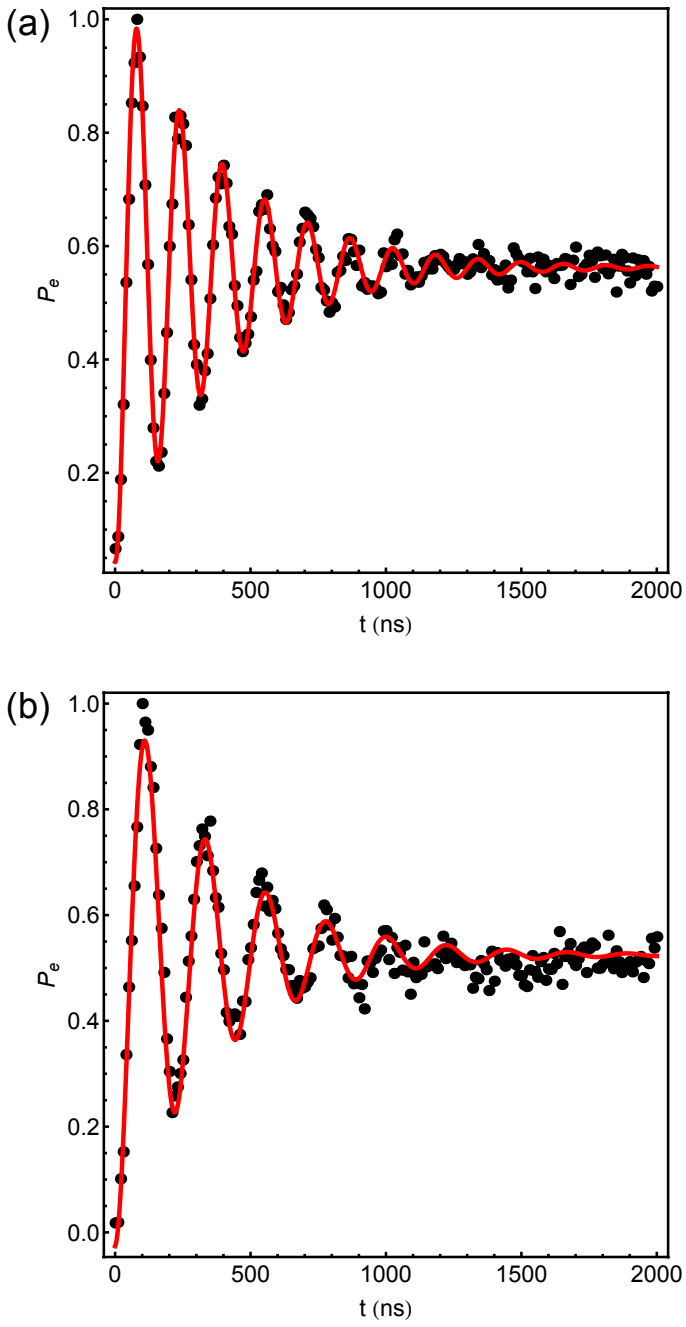

Figure 7.5: Plot of measured Rabi oscillations for device LEv5-7 for a drive power of -116 dBm and -119 dBm. Black dots are data. Red curve is exponentially damped sinusoidal fit. (a) Qubit drive power of -116 dBm. Rabi frequency $= 4$ MHz and Rabi decay time $T' = 0.37\,\mu$s from thefit. (b)Qubit drive power of -119 dBm. Rabi frequency $= 3.2$ MHz and Rabi decay time $T' = 0.37\,\mu$s from the fit.

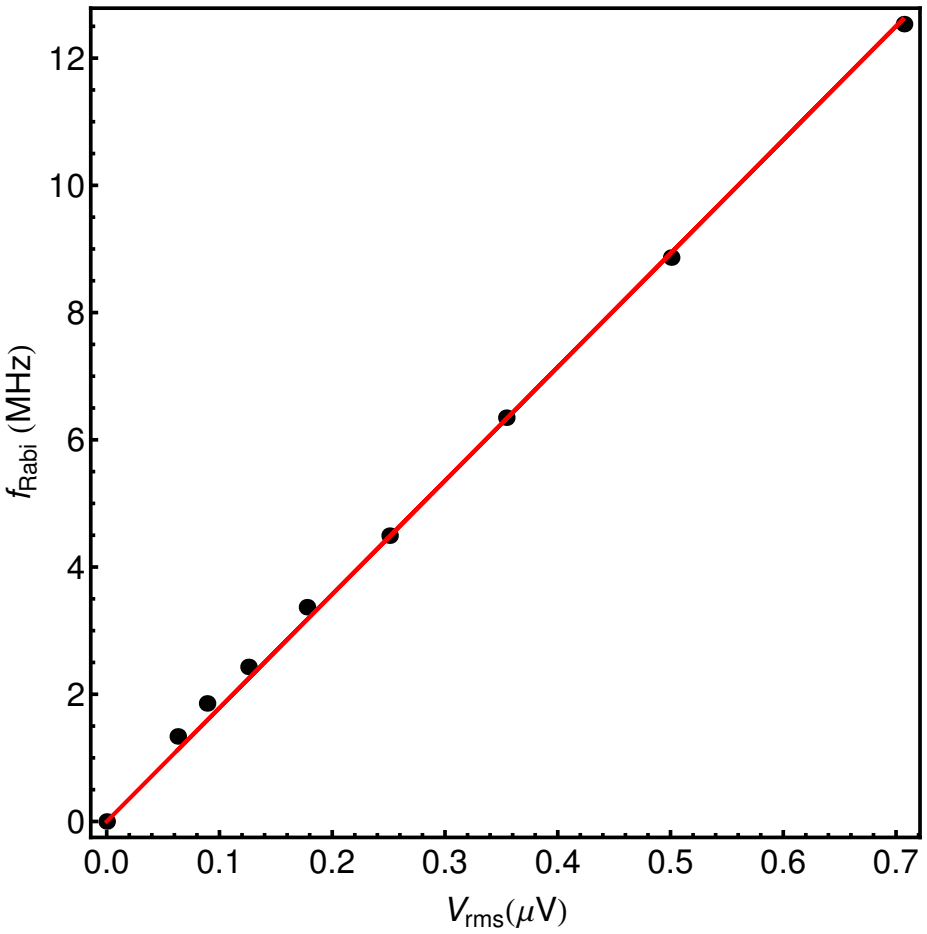

Figure 7.6: Plot of measured Rabi frequency vs applied drive voltage for device LEv5-7. Black dots are data. Red curve is straight line fit giving a Rabi coupling of 17.3 MHz/μV.

microwave line to the device was estimated to be close to 70 dB at 5 GHz.

Figure 7.6 shows the measured Rabi frequency (black dots) in MHz for device LEv5-7 plotted vs the applied microwave RMS voltage V_{rms} at the CPW transmission line. From a straight line fit (red) to the data, the Rabi coupling to the drive was measured to be $\mathrm{d}f_{Rabi}/\mathrm{d}V_{rms} = 17.3\,\mathrm{MHz}/\mu\mathrm{V}$.

I can now use Eq. 7.41 to check if the T_1 of the qubit is being limited by coupling

to the voltage noise on the CPW. The CPW transmission line is designed to have an impedance of $Z_0 = 50\,\Omega$. Since the input and output sections of the CPW both present $Z_0 = 50$ in parallel, the transmon couples to voltage noise due to an effective $R = 25\,\Omega$ (see Appendix B Fig.D.3). For a frequency $f = 8\,\mathrm{GHz}$, and $\mathrm{d}f_{Rabi}/\mathrm{d}V_{rms} = 17.3\,\mathrm{MHz}/\mu\mathrm{V}$ and $R = 25\,\Omega$, I find from 7.41 that $T_1 = 1/\Gamma_- \approx 380\,\mathrm{ns}$. Since the measured $T_1 = 270\,\mathrm{ns}$ is of the same order of magnitude as the prediction from the Rabi coupling to transmission line, I can conclude that coupling to the transmission line was playing a significant role in limiting T_1.

Later in this Chapter, I consider further the fact that strong coupling to a dissipative environment was a dominant source of relaxation in all my early transmons. I also motivate and discuss the design changes I made to decouple the transmons from the dissipative environment.

7.4 T_1 and Rabi coupling in a Cooper-pair box

In this section I briefly review our group's earlier measurements on a long-lived Cooper-pair Box (CPB) coupled to a lumped-element resonator [28] (see Fig. 7.7(a)) and discuss its relevance to my work on transmons. I note that this sample was fabricated by Zaeill Kim. In this device, a split Cooper-pair box made of Al/ AlO_x/Al was capacitively coupled to a lumped element resonator made of aluminum on a sapphire substrate, with a resonant frequency of 5.5 GHz. The dipole coupling constant between the CPB and the resonator was $g/2\pi = 5\,\mathrm{MHz}$. The resonator was coupled to a transmission line with a total quality factor of $Q_L = 22,000$ giving a photon loss-

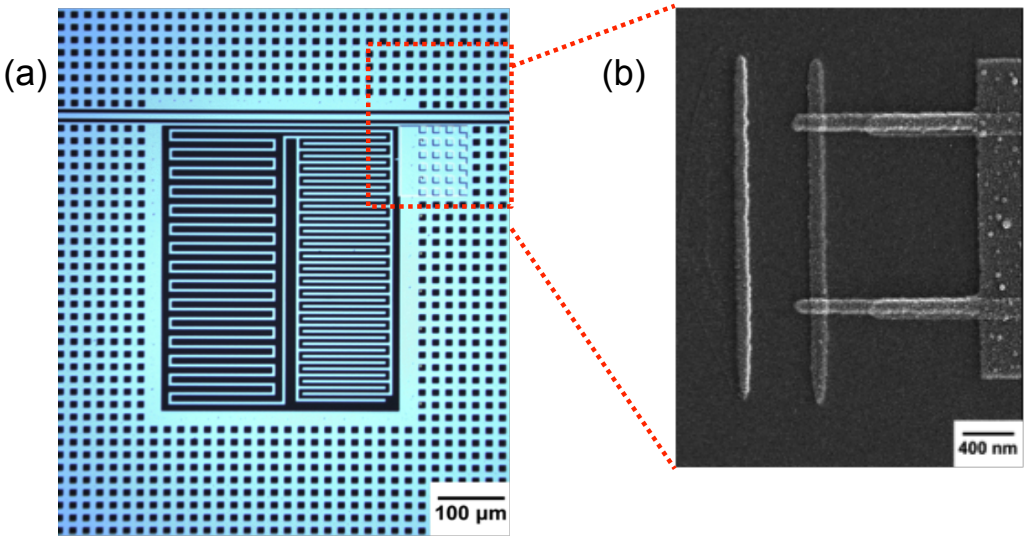

Figure 7.7: Micrograph of CPB device LEQED2 [28]. (a) False color micrograph showing resonator coupled to transmission line. (b) Detailed view of the CPB coupled to the resonator with 100 nm × 100 nm Josephson junctions.

rate of $\kappa/2\pi = 180\,\text{kHz}$. Figure 7.7(b) shows a detailed view of the 100 nm × 100 nm Josephson junctions forming a SQUID loop. By changing the magnetic flux threading the SQUID loop using an external magnet, we could tune the Josephson energy of the junctions, and thereby tune the transition frequency of the CPB. The device was measured at 20 mK in our Oxford dilution refrigerator.

We measured the T_1 of the CPB over the frequency range of of 4 GHz to 8 GHz and found a strong frequency dependence. Figure 7.8 shows a plot of T_1 (black dots) vs the qubit frequency. The qubit showed an impressively long lifetime of 200 μs at the lowest frequency of 4 GHz. This was the longest lifetime for a charge qubit, and one of the longest T_1's for any superconducting qubit up to that time. From Fig. 7.8(b) one sees that as the qubit frequency increased, the T_1 steadily dropped. Close to

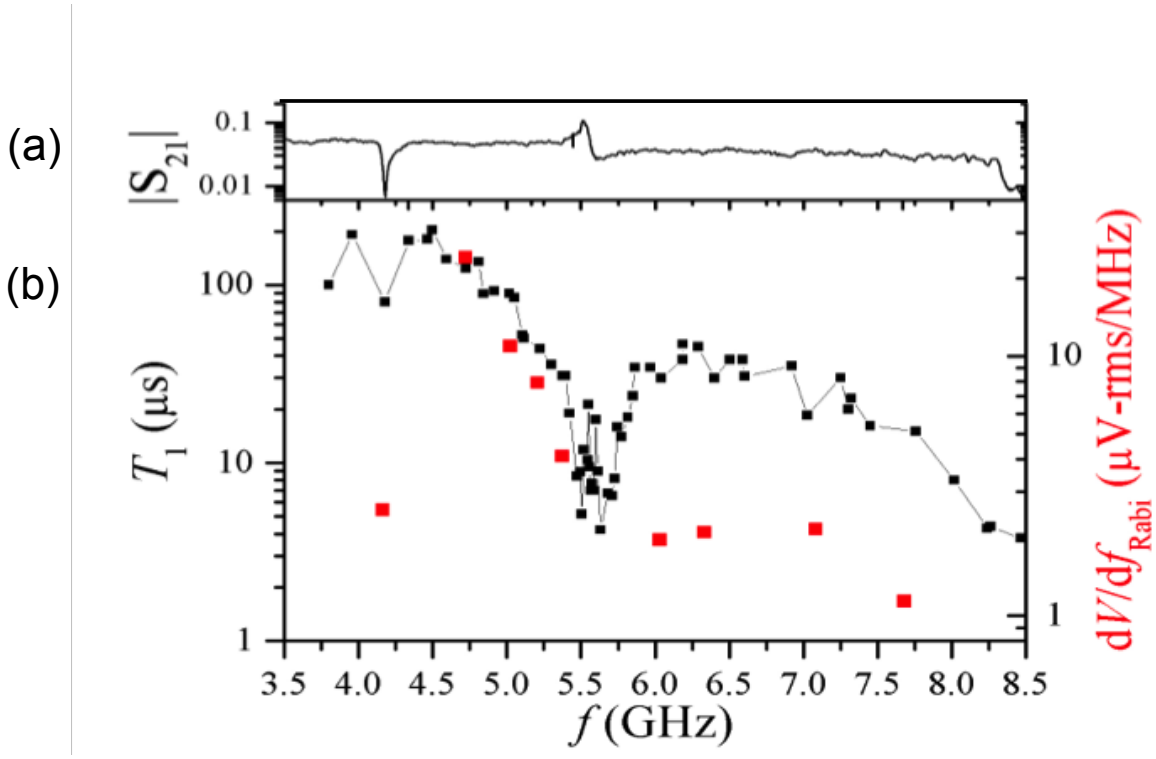

Figure 7.8: (a) S_{21} vs f and (b) Plot of measured T_1 and 'decoupling' vs f for a CPB. Black points are measured T_1. Red squares are the decoupling, which inverse of the Rabi coupling.

the resonant frequency of the resonator $\sim 5.5\,\text{GHz}$, there was enhanced spontaneous emission due to the Purcell effect [23, 24, 31], with the T_1 dropping to about $3\,\mu\text{s}$. Above the resonance, the T_1 recovered to about $10\,\mu\text{s}$ at $6\,\text{GHz}$ followed by a steady decline at higher frequencies.

The measurements also showed variations in the T_1 due to spurious modes in the electromagnetic environment, notably, the dip in the T_1 close to $4.2\,\text{GHz}$ and the peak close to $5.6\,\text{GHz}$ (see Fig. 7.8(b)) [28]. The microwave S_{21} transmission measurements show the spurious resonances (see Fig. 7.8(a)).

Another striking result was the frequency dependence of the Rabi coupling to the drive. By measuring Rabi oscillations for qubit frequencies between $4 - 8\,\mathrm{GHz}$, we measured the Rabi coupling ($\mathrm{d}f_{Rabi}/\mathrm{d}V_{rms}$) to the drive. I found that the Rabi coupling was small $\sim 0.1\,\mathrm{MHz}/\mu\mathrm{V}$ when the $T_1 \sim 200\,\mu\mathrm{s}$ was long and vice versa. The red points in Fig. 7.8(b) show the variation of the inverse of the Rabi coupling $1/(\mathrm{d}f_{Rabi}/\mathrm{d}V_{rms})$ with frequency. The more decoupled the qubit is from the transmission line, the longer the lifetime.

We also modeled the T_1 of the device as caused by coupling to a $50\,\Omega$ quantum dissipative environment, where the coupling strength was given by the Rabi coupling to the transmission line. Using this model, the T_1 was given by [28]

$$\Gamma = \frac{1}{T_1} = \left\{5 \times 10^3 + (\mathrm{d}f_{Rabi}/\mathrm{d}V_{rms})^2\, 8\pi^2 Z_0 h f\right\}\ \ \mathrm{s}^{-1} \tag{7.42}$$

including a frequency independent additive constant of $5 \times 10^3 \mathrm{s}^{-1}$. The spectral density of Nyquist noise [99, 100] for the $Z_0 = 50\,\Omega$ environment was taken in the quantum limit ($hf \gg k_B T$) to be $S_V(f) = 2Z_0 hf$. The T_1 prediction from the Rabi coupling model is shown in Fig. 7.9(b) (blue squares) and we see reasonable qualitative agreement.

The fact that T_1 could be quantitatively modeled to some extent using the Rabi coupling suggested that coupling to the transmission line was a significant source of relaxation. While the model agreed reasonably well with the data, it did not explain the frequency dependence *per se* and at the time of the publication [28], the frequency dependence of T_1 and Rabi coupling were not well understood. Later, I extended this type of study to my transmon qubits coupled to lumped-element resonators and

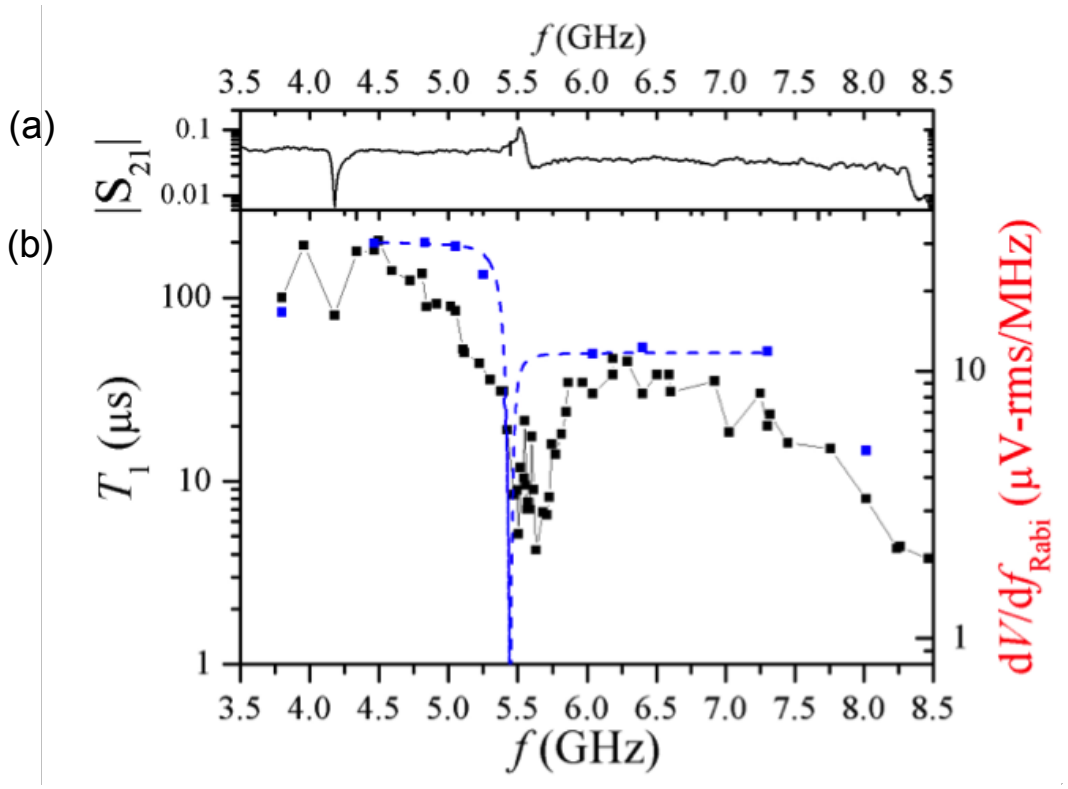

Figure 7.9: (a) S_{21} vs f. (b) Plot of measured T_1 vs$f$ for CPB. (Black dots)– data. (Blue squares)– prediction using Eq. 7.41. (Blue dashed curve)– contribution to T_1 using a background loss of $5 \times 10^3 s^{-1}$ below the resonance and $2 \times 10^4 s^{-1}$ above the resonance.

through modeling and simulations, have been able to explain some of these aspects.

7.5 Transmon measurements - LEv5 class of devices

In this section I present T_1 and Rabi coupling measurements of my early transmon devices. I refer to the style of the resonator used in this case as LEv5. The treatment is chronological, to facilitate understanding of the evolution of my transmon-resonator designs.

7.5.1 LEv5-7

I discussed T_1 and Rabi coupling measurements I made on device LEv5-7 above in Sec. 7.2 and Sec. 7.3.2. Device LEv5-7 was the first of the LEv5 line of devices. To recap, the device is shown in Fig. 7.2. The resonant frequency of the resonator was around 5.46 GHz, with a total quality factor of $Q_L = 18,000$. The resonator was separated from the transmission line by a $2\,\mu$m ground strip. The transmon had a single $100\,\text{nm} \times 100\,\text{nm}$ junction (see Fig. 7.2) shunted by an interdigital capacitor. The qubit transition frequency was $\omega_{ge}/2\pi = 8\,\text{GHz}$.

Figure 7.3 shows the energy relaxation with a measured lifetime of $T_1 = 270\,\text{ns}$. The Rabi coupling $\mathrm{d}f_{Rabi}/\mathrm{d}V_{rms} = 17.3\,\text{MHz}/\mu\text{V}$. The measured T_1 was close to $T_1 \approx 319\,\text{ns}$, which was predicted using Eq. 7.41 for from coupling to the quantum voltage noise in the $R = 25\,\Omega$ resistance of the CPW transmission line. This suggested that this device was limited by coupling to the transmission line.

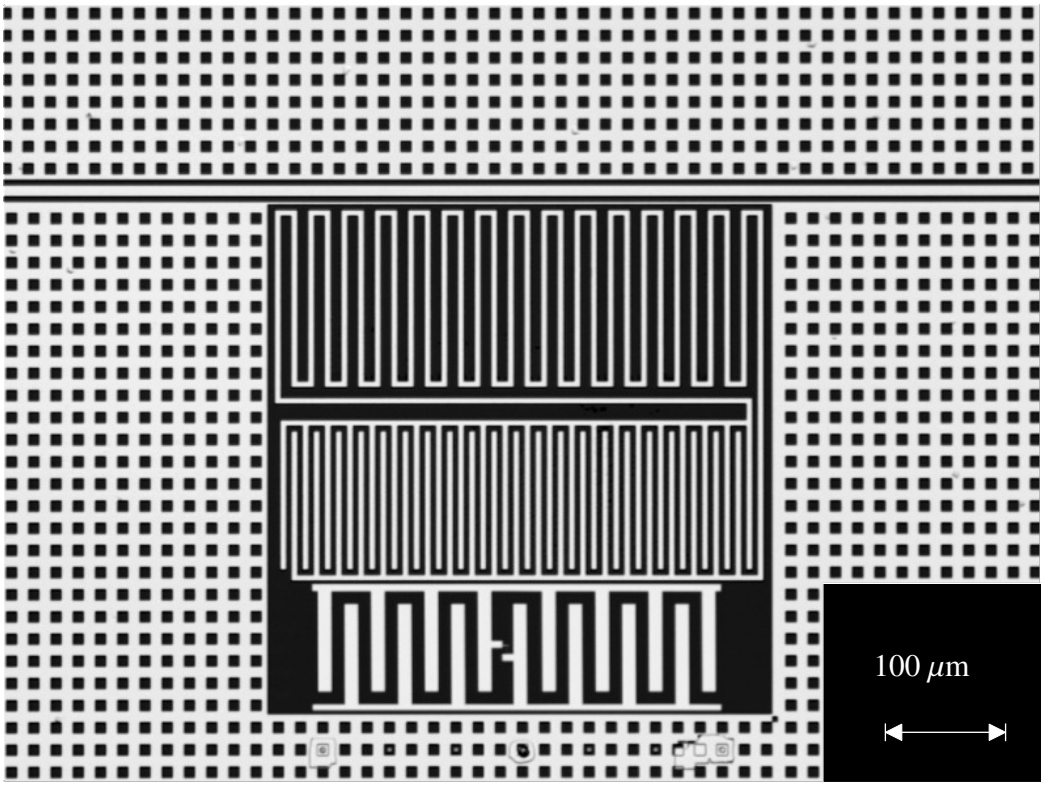

Figure 7.10: Micrograph of device LEv5-15. The resonator is rotated by 90° relative to device LEv5-7.

7.5.2 LEv5-15

To reduce the coupling to the transmission line, I increased the spatial separation between the transmon and the CPW transmission line. This was partly achieved by rotating the resonator by 90° relative to device LEv5-7. An optical micrograph of device LEv5-15 is shown in Fig. 7.10. By rotating the resonator, the transmon was placed at a distance of around 300 μm from the transmission line, compared to the 100 μm separation in the case of device LEv5-7 (see Fig. 7.2).

The ground strip separating the resonator and the transmission line was 2 μm wide, similar to that in device LEv5-7. The resonator frequency was $\omega_r/2\pi = 5.4\,\mathrm{GHz}$

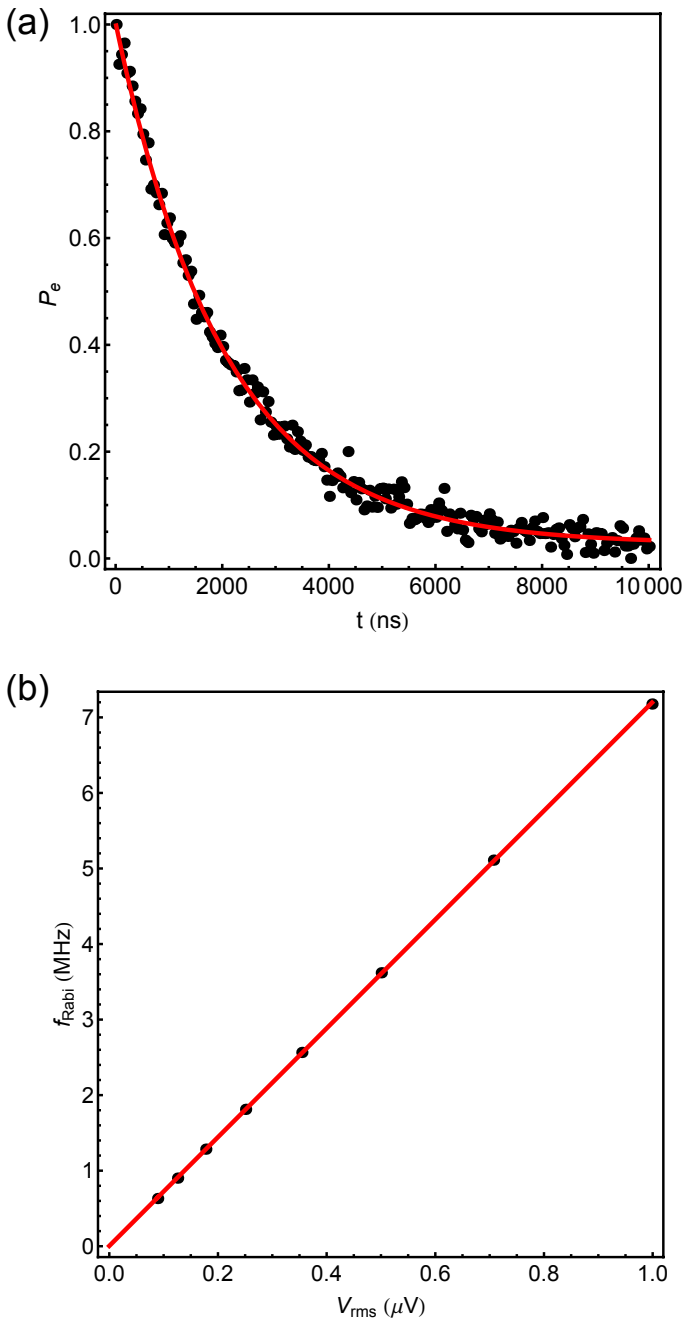

Figure 7.11: Plot of T_1 decay and Rabi coupling for device LEv5-15, with fits. (a) T_1 decay for device LEv5-15, with fit. Black points are data. Red curve is exponential decay fit giving $T_1 = 1.8\,\mu$s. (b) Measured Rabi frequency vs applied drive voltage for device LEv5-15, with fit. Black points are data. Red curve is linear fit with Rabi coupling $8\,\mathrm{MHz}/\mu\mathrm{V}$

with a total quality factor of $Q_L = 14,500$. By rotating the resonator, the longer side of the resonator now coupled to the transmission line. The stronger coupling of the resonator to the transmission line was possibly caused by this larger overlap length $\sim 400\,\mu$m, as opposed to $300\,\mu$m in device LEv5-7. The transmon in LEv5-15 had a single Josephson junction shunted by an IDC. Otherwise, the design and dimensions of the IDC and the Josephson junction were similar to that of device LEv5-7.

The transmon transition frequency of LEv5-15 was 4.18 GHz. From our earlier CPB measurements [28] shown in Fig. 7.8(b), we expected the device to have better T_1 when the qubit transition frequency was below the resonance. Figure 7.11(a) shows a measurement of T_1 for this device. From the exponential fit, I found $T_1 = 1.8\,\mu$s. This was about 7 times longer than that of LEv5-7. I also measured the Rabi coupling, shown in Fig. 7.11(b), and from the straight line fit, the coupling was determined to be $\mathrm{d}f_{Rabi}/\mathrm{d}V_{rms} = 8\,\mathrm{MHz}/\mu\mathrm{V}$. I note that this is about a factor of 2 weaker Rabi coupling than in device LEv5-7.

Using Eq. 7.41, I estimated the decay rate caused by the coupling to the $25\,\Omega$ resistance of the transmission line and find $T_1 \sim 2.8\,\mu$s for device LEv5-15. Thus the $T_1 = 1.8\,\mu$s of LEv5-15 was the same order of magnitude as $T_1 = 2.8\,\mu$s predicted from the Rabi coupling, suggesting that the device LEv5-15 was also limited by coupling to the transmission line.

7.5.3 LEv5-17

Both devices LEv5-7 and LEv5-15 showed signs of T_1 being limited by coupling the transmission line. In my next device, LEv5-17 (see Fig. 7.12), I decreased the coupling of the resonator to the CPW. This was done by increasing the width of the ground strip separating the resonator and the CPW transmission line from $2\,\mu$m to $7\,\mu$m. This resulted in a higher total quality factor of around $Q_L = 50,000$ for the resonator. The resonant frequency of the resonator for LEv5-17 was $5.4\,$GHz. The orientation of the resonator was similar to LEv5-7 (not rotated). Based on other results in our group [53], I also placed the transmon further away from the transmission line, asymmetrically in the gap between the resonator and the ground plane (see Fig. 7.12). The IDC and the single Josephson junction of the transmon in device LEv5-17 are similar to those in devices LEv5-7 and LEv5-15. The transmon transition frequency for this device came out to be $\omega_{ge}/2\pi = 3.5\,$GHz, which was smaller than intended, but acceptable.

A T_1 relaxation plot for device LEv5-17 is shown in Fig. 7.13(a). The measured lifetime was $T_1 = 4.5\,\mu$s for this device, which was about a factor of two longer than that of LEv5-15 and 15 times longer than that of LEv5-7. Figure 7.13(b) shows the straight line fit to the data, giving a Rabi coupling of $\mathrm{d}f_{Rabi}/\mathrm{d}V_{rms}$ =$3.5\,$MHz/μV, which was about half the Rabi coupling in device LEv5-15 and about 1/4 of that in device LEv5-7. The Rabi coupling for this device was the lowest I observed among the LEv5 class of devices The T_1 predicted from Eq. 7.41 for this device was $17.8\,\mu$s. Since the measured $T_1 = 4.5\,\mu$s was less than one-fourth the prediction from Rabi

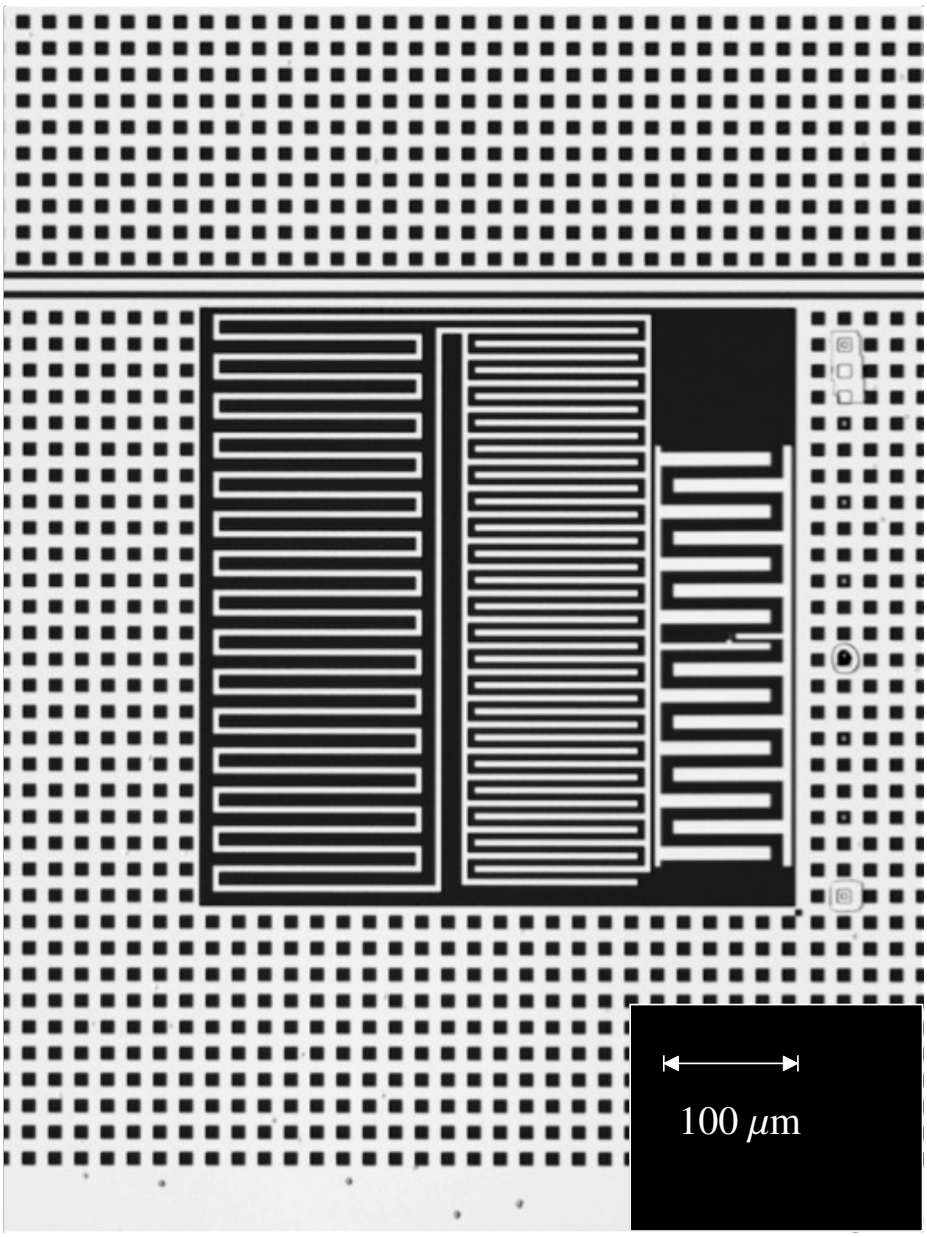

Figure 7.12: Micrograph of device LEv5-17. The width of the ground strip separating the resonator and transmission line was increased to 7 μm to decouple the resonator. The transmon was displaced by an additional 50 μm away from the transmission line to reduce direct coupling to the transmission line.

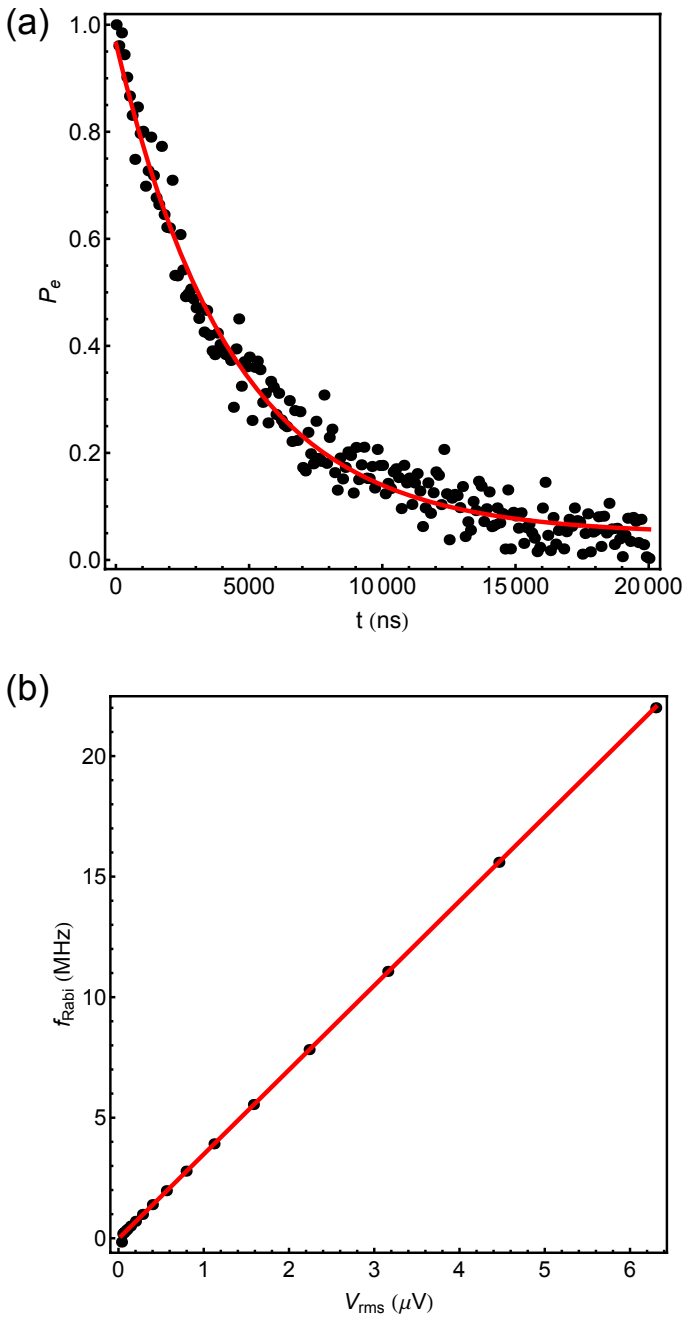

Figure 7.13: Plot of T_1 decay and Rabi coupling for device LEv5-17, with fits. (a) T_1 decay for device LEv5-17, with fit. Black points are data. Red curve is exponential decay fit giving $T_1 = 4.5\,\mu$s. (b) Measured Rabi frequency vs applied drive voltage for device LEv5-17, with fit. Black points are data. Red curve is linear fit with Rabi coupling $3.5\,\mathrm{MHz}/\mu\mathrm{V}$

coupling $T_1 = 17.8\,\mu$s, I concluded that LEv5-17 was not entirely limited by the coupling to the transmission line.

This result encouraged me to examine more closely the design, the circuit analysis, and microwave simulations, to see if I could further lower the coupling to the transmission line, and identify other sources of loss. In the next section, I discuss the circuit analysis method I used to understand the T_1 of transmons coupled to lumped element resonators. Even though this analysis is not very accurate in its modeling of the physical layout, it does provide useful insights into the design of better circuits.

7.6 Circuit analysis

7.6.1 Significance of Re(Y)

Relaxation of a quantum system is caused by coupling to environmental degrees of freedom. Since the systems I examined in this thesis are superconducting circuits, I can represent this interaction of the transmon with the environment by a simple circuit. In Fig. 7.14, C_b represents the shunt capacitance across the Josephson junction of the transmon and $Y(\omega)$ is the effective frequency-dependent admittance due to the environment. In circuit terminology, the time-constant T_1 for a charge on the plate of the capacitor C_b to discharge through the admittance $Y(\omega)$ is given by

$$T_1(\omega) = \frac{C_b}{\mathrm{Re}[Y(\omega)]}. \tag{7.43}$$

If we know the real part of the admittance across the capacitor as a function of frequency, we can compute the time-constant as a function of frequency.

In fact Eq. 7.43 can be used to compute the decay time T_1 of a transmon coupled to a frequency-dependent environment. At first glance this does not seem possible, as Eq. 7.43 was found from a purely classical argument. The reason this simple relation still applies in the case of a transmon is due to the fundamentally quantum origins of electrical resistance, along with the fact that a transmon is quasi-harmonic or weakly anharmonic. There exists a general class of fluctuation-dissipation relations which give the relation between fundamentally quantum mechanical phenomena such as the zero point motion, or vacuum fluctuations of voltage in conductors, and a purely classical, phenomenological dissipative parameter such as the electrical resistance. The most famous among such relations is Eq. 7.40, which relates the spectral density of quantum fluctuations to a classical parameter such as the resistance Z_0 [99, 100]. The pure-resistance is a particular case of a general relation given by Johnson and Nyquist

$$S_V(\omega) = \frac{2\mathrm{Re}(Z)\hbar\omega}{1 - e^{-\beta\hbar\omega}} \tag{7.44}$$

where $\mathrm{Re}(Z) = \mathrm{Re}(Y)/|Y|^2$ represents the real part of the frequency-dependent impedance.

The extension of the Nyquist relation to the frequency-dependent case has implications for the frequency dependence of the Rabi coupling that was seen in the CPB measurements by Z. Kim *et al.* [28] (see Fig. 7.8), which was not initially appreciated. Because a general cQED circuit is composed mainly of reactive elements, *i.e.* capacitances and inductances, the electromagnetic environment around the qubit is frequency-dependent. Even though an ideal impedance-matched transmission line

behaves as a purely resistive element over a wide frequency band in the microwave region, the rest of the circuit *renormalizes* the *bare* coupling strength and imparts a frequency dependence to it. It is the renormalized coupling strength that we measure in the experiment via $\mathrm{d}f_{Rabi}/\mathrm{d}V_{rms}$.

Given this intuitive understanding of the significance of the impedance and admittance of the overall circuit for the relaxation of a transmon, in the rest of the discussion, I emphasize understanding and designing $\mathrm{Re}(Y)$.

7.6.2 Circuit model for T_1

The circuit in Fig. 7.15 represents the cQED architecture of a transmon-resonator system coupled to a $50\,\Omega$ transmission line. The transmon has a single Josephson junction shunted by a capacitance C_b. The resonator is a simple LC oscillator with capacitance C_r and inductance L_r. The resistive losses in the resonator are represented by R. The input and output transmission lines are represented by inductances L_t and capacitances C_t, and each is connected to a $50\,\Omega$ terminating resistor. The direct resonator-transmission line coupling is modeled by the capacitance C_s and the transmon-resonator coupling is modeled by the capacitance C_g.

When the transmission line is designed such that the characteristic impedance $Z_t = (L_t/C_t)^{1/2}$ is matched to $Z_0 = 50\,\Omega$, we can simplify the circuit to the one in Fig. 7.16. A detailed step-wise simplification of the circuit is given in Appendix D. From this reduced circuit the admittance across the capacitance C_b due to the rest of the circuit can be calculated as follows.

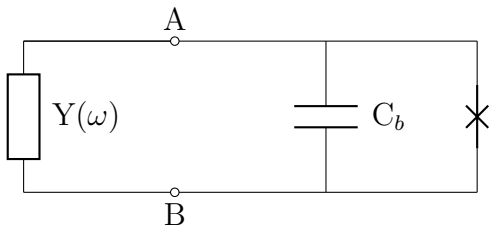

Figure 7.14: Schematic of a transmon qubit coupled to a frequency-dependent environmental admittance $\mathrm{Y}(\omega)$

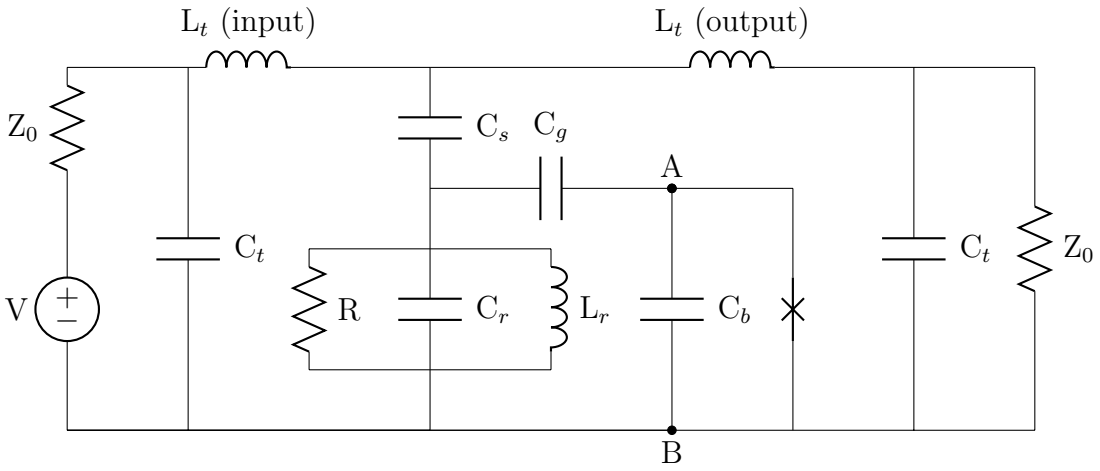

Figure 7.15: Full circuit schematic for transmon-resonator cQED architecture including the input and output transmission line inductances L_t and capacitances C_t. The transmission line is terminated in a resistance $Z_0 = 50\,\Omega$.

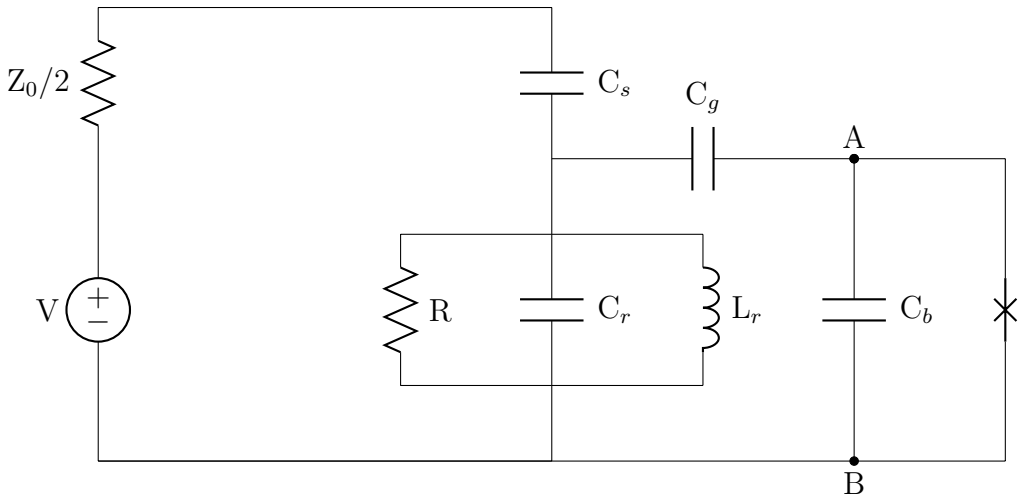

Figure 7.16: Reduced external circuit for transmon-resonator system.

$$Z_{res} = \frac{j\omega L_r R}{R(1-\frac{\omega^2}{\omega_0^2}) + j\omega L_r} \tag{7.45}$$

$$Z(\omega) = \frac{1}{j\omega C_g} + \frac{Z_{res}(Z_0/2 + 1/(j\omega C_s))}{Z_{res} + Z_0/2 + 1/(j\omega C_s)}. \tag{7.46}$$

Knowing the equivalent impedance $Z(\omega)$ across the transmon, the real part of the admittance $Y(\omega)$ can be determined as

$$Y(\omega) = \frac{1}{Z(\omega)} \tag{7.47}$$

$$\frac{1}{\mathrm{Re}(Y)} = \frac{|Z|^2}{\mathrm{Re}(Z)}. \tag{7.48}$$

The real part of the admittance can be written explicitly, after quite some

algebra, as

$$\frac{1}{Re(Y)} = \frac{\left(\frac{1}{R} + \frac{\omega^2 Z_0 C_s^2}{2(1+\omega^2 Z_0^2 C_s^2/4)}\right)^2 + \left(\omega C_g - \frac{\omega C_s}{1+\omega^2 C_s^2 Z_0^2/4} - \frac{1-\omega^2/\omega_0^2}{\omega L_r}\right)^2}{\omega^2 C_g^2 \left(\frac{1}{R} + \frac{\omega^2 Z_0 C_s^2/2}{1+\omega^2 Z_0^2 C_s^2/4}\right)} \tag{7.49}$$

For my device, this can be greatly simplified as shown in greater detail in Appendix D, to the more elegant form

$$\frac{1}{Re(Y)} \simeq \left\{ \frac{Z_0 C_s^2}{2C_g^2} + \frac{2}{Z_0 \omega^2 C_g^2} \left[\frac{C_r}{C_s} \left(1 - \frac{\omega_0^2}{\omega^2}\right) + \frac{C_g}{C_s} \right]^2 \right\}. \tag{7.50}$$

where $\omega_0 = 1/\sqrt{L_r C_r}$ is the resonant frequency of the resonator. The first term has no frequency-dependence and is negligibly small for typical values of the circuit parameters. From Eq. 7.43, we can now write the frequency dependent T_1 of the transmon as

$$T_1 = \frac{C_b}{Re(Y)} = C_b \left\{ \frac{Z_0 C_s^2}{2C_g^2} + \frac{2}{Z_0 \omega^2 C_g^2} \left[\frac{C_r}{C_s} \left(1 - \frac{\omega_0^2}{\omega^2}\right) + \frac{C_g}{C_s} \right]^2 \right\}. \tag{7.51}$$

For frequencies $\omega \ll \omega_0$, the T_1 predicted from Eq. 7.51 increases as $1/\omega^4$. For frequencies $\omega \gg \omega_0$, the second term in Eq. 7.51 falls off as $1/\omega^2$. Only in the very high frequency limit, that we are not interested in, will the first term become relevant. Also, I note that the resistive element R, representing the dielectric losses in the resonator, has been ignored for the moment in deriving Eq. 7.51.

In Fig. 7.17, the blue curve shows a Log-plot of T_1 vs f calculated using Eq. 7.51 for $C_r = 400\,\text{fF}$, $L_r = 2\,\text{nH}$, $\omega_0/2\pi = 5.5\,\text{GHz}$, $C_g = 30\,\text{fF}$, $C_s = 6\,\text{fF}$, $C_b = 48\,\text{fF}$

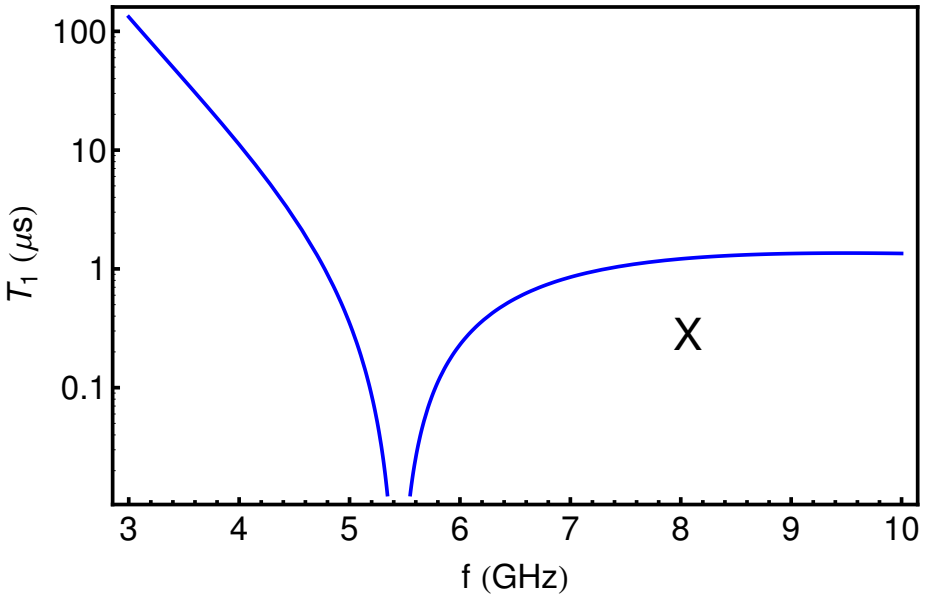

Figure 7.17: Plot of T_1 vs f from circuit analysis for device LEv5-7. Blue curve shows T_1 prediction from Eq. 7.51 for circuit parameters corresponding to those of device LEv5-7. Black 'X' represents the measured $T_1 = 0.27\,\mu$s. Predicted $T_1 = 0.9\,\mu$s at 8GHz, is a factor 3 higher, but of the same order of magnitude.

and $Z_0 = 50\,\Omega$. From the circuit Hamiltonian analysis given in Chapter 2, these parameters give $E_c/h = 254\,\text{MHz}$, $g/2\pi = 90\,\text{MHz}$, $Q_L = 18,000$ for the device. These values are close to the actual parameters for LEv5-7 (see Table 6.3).

At the transition frequency for LEv5-7 at $\omega_{ge}/2\pi = 8\,\text{GHz}$, the circuit model predicts a lifetime of about 900 ns, which is three times larger than, but of the same order of magnitude as the measured $T_1 = 270\,\text{ns}$. At frequencies below the resonant frequency of the resonator, the simulated T_1 values reach as high as $100\,\mu$s at 3 GHz. While a simple circuit model cannot exactly simulate the complexity of the experiment, the model provides intuition about the designs. I also note that the frequency dependence of the T_1 of the CPB [28] in Fig. 7.8 is qualitatively reminiscent of the

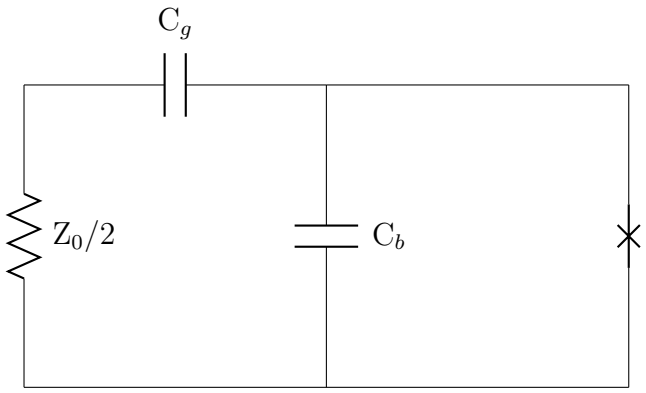

Figure 7.18: Schematic of a transmon qubit coupled directly to the 50 Ω transmission line through a capacitance C_g.

frequency dependence shown in Fig. 7.19 and suggests that the complex electromagnetic environment played a role in renormalizing the bare parameters and gave a strong frequency dependence.

7.6.3 Note on the Purcell effect

Another remarkable feature of the circuit model is that it predicts a dip in the T_1 in the region close to the resonator frequency $\omega_0/2\pi = 5.5\,\mathrm{GHz}$ (see Fig. 7.17). Close to the resonator frequency, there is enhanced relaxation of the qubit. This behavior was predicted by Purcell in 1946 [23, 24, 19]. For a resonator of quality factor Q, the density of states on resonance increases approximately by a factor of Q, enhancing the decay rate by the same factor. Further, Kleppner *et al.* [25, 27, 26] and Haroche *et al.* [106] showed that away from resonance, the resonator offers protection or inhibits relaxation of the qubit.

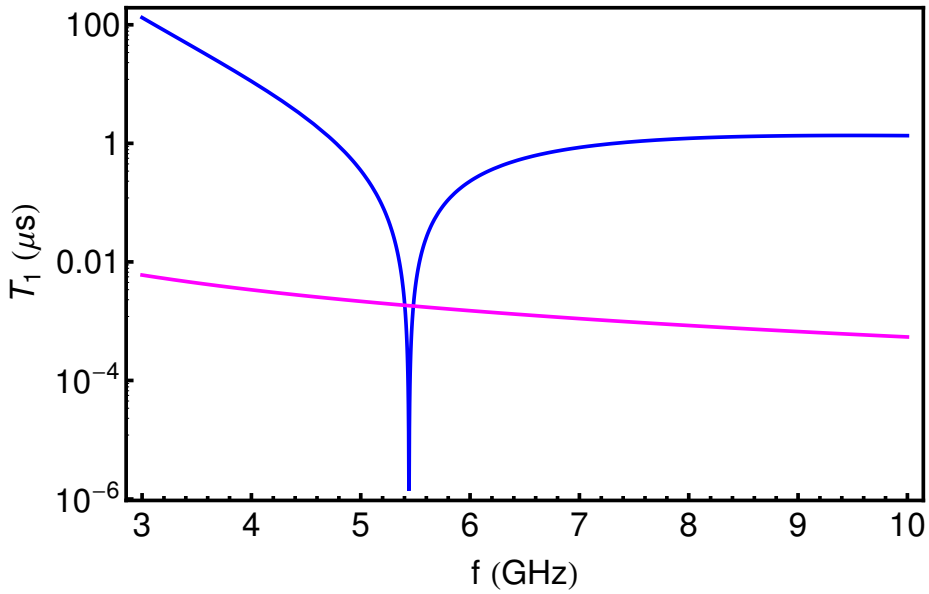

Figure 7.19: Plot of T_1 vs f from circuit analysis with and without resonator. Blue curve shows T_1 calculated using Eq. 7.51 with resonator present. Magenta curve shows T_1^d from Eq. 7.52 with no resonator. The resonator offers Purcell protection to the qubit away from the resonance, while enhancing relaxation on resonance.

To verify this, I consider the simple circuit in Fig. 7.18, in which the transmon is directly coupled to the $Z_0/2 = 25\,\Omega$ dissipative environment through a capacitance C_g. The decay time T_1^d for this direct coupling model can be computed from

$$T_1^d = \frac{C_b(1+\omega^2 C_g^2 Z_0^2/4)}{\omega^2 C_g^2 Z_0/2}. \tag{7.52}$$

The magenta curve in Fig. 7.19 shows a plot of T_1^d vs frequency for $C_g = 30\,\text{fF}$ and $Z_0 = 50\,\Omega$. Comparing the magenta (no resonator) and the blue curve (with resonator) in Fig. 7.19, one sees that on resonance there is a factor of 10^4 enhancement of relaxation in the presence of the resonator, which is approximately a factor of $Q_L = 18,000$ for the parameters of the blue curve. Away from the resonance, the

blue curve is several orders of magnitude higher than the magenta curve, showing clearly that the resonator inhibits spontaneous emission away from the resonance. This behavior is one reason why cQED architectures are popular.

The fact that a simple analytical circuit model captures the Purcell effect should not be surprising in the wake of the fluctuation-dissipation relation. It can be shown [104] that the real part of the admittance $\mathrm{Re}(Y)$ is related to the energy density of states $\rho(E)$ according to

$$\mathrm{Re}[Y(\omega)] = \pi\omega\left\{1 - e^{-\beta\hbar\omega}\right\} \times \int_0^\infty |\langle E + \hbar\omega|P|E\rangle|^2 \rho(E + \hbar\omega)\rho(E) f(E) dE \quad (7.53)$$

where P is the dipole-moment operator causing transitions between levels of energy E and $E + \hbar\omega$. From this equation, we can see that the real part of the admittance is large when the density of states is large. For a resonator, the density of states is large at the resonant frequency. This can also be understood to mean that the quality factor Q enhances the electromagnetic vacuum fluctuations by a factor Q. Because the resonator does not support off-resonant modes, the density of states drops drastically away from resonance, making $\mathrm{Re}(Y)$ small away from the resonance.

The asymmetry in the spontaneous emission above and below the resonator frequency in Fig. 7.19 merits some discussion. Houck *et al.* found in their system [31] that an asymmetry was caused by strong coupling to the higher modes of the CPW half-wavelength resonator. However, in my experiments, I used a lumped element resonator, which is a single mode oscillator up to at least 30 GHz. This suggests that the origin of the asymmetry in my case is not from coupling to higher modes, but due to the capacitive impedance that decreases with frequency as $1/\omega$. This is not just

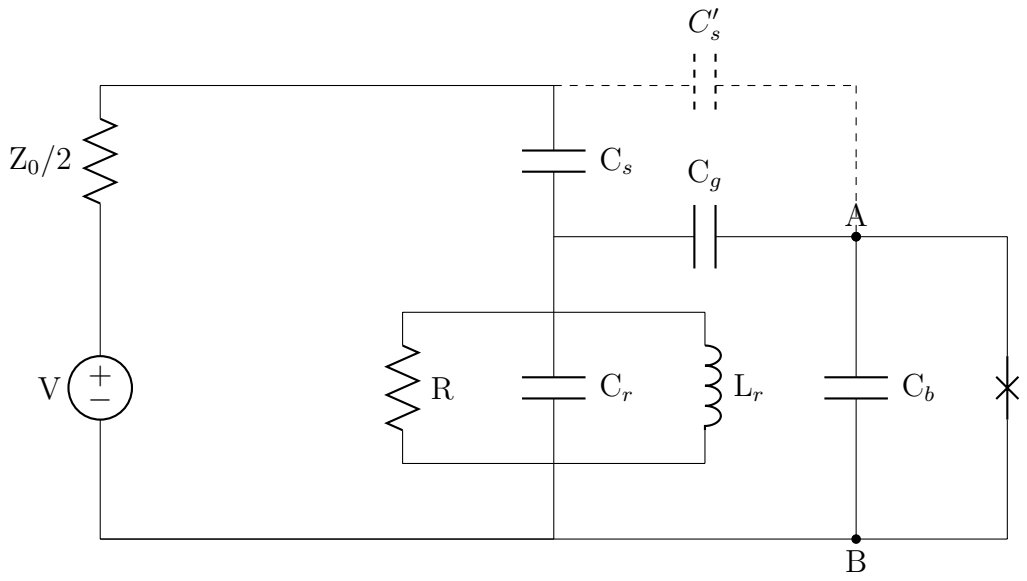

Figure 7.20: Reduced external circuit model for transmon-resonator system with a direct capacitance C_s' between transmon and 50 Ω input and output lines.

because the present circuit models all the couplings as primarily capacitive. A full microwave simulation of the device geometry, as will be shown in the next section, shows a similar asymmetry, suggesting that the capacitive component of the circuit was dominant.

7.6.4 Direct capacitance between the transmon and transmission line.

Before I conclude this section, I want to draw attention to an approximation that was made in drawing Fig. 7.15 and Fig. 7.16. In principle, a direct capacitance C_s' between the transmon and the transmission line, denoted by the dashed line in Fig. 7.20 was neglected in deriving Eq. 7.51. If this stray capacitance caused the dominant source of loss, then ignoring the rest of the circuit, the T_1^d from Eq. 7.52 can

be used to make an estimate of the magnitude of the capacitance. For the parameters of device LEv5-7 ($C_b = 48\,\mathrm{fF}$, $\omega_{ge}/2\pi = 8\,\mathrm{GHz}$) and for a measured $T_1 \approx 270\,\mathrm{ns}$ one finds $C_s' \sim 1.7\,\mathrm{fF}$.

To see if this capacitance was reasonable, I used FastCap to estimate the direct capacitance between the transmon IDC and the transmission line for device LEv5-7. I found from the capacitance matrix (see Chapter 4 Eq. 4.10) that $C_s' \sim 0.4\,\mathrm{fF}$ for device LEv5-7 which was a factor 4 smaller than $C_s' \sim 1.7\,\mathrm{fF}$ estimated above, using Eq. 7.52. For my other devices, ignoring this direct capacitance should not have had any effect since the C_s' values from FastCap were in the range of $\sim 10\,\mathrm{aF}$, placing the bound on $T_1^d \sim 600\,\mu\mathrm{s}$. Therefore, including this capacitance would not significantly improve the numerical agreement of the prediction from the circuit model and would make the T_1 expression unwieldy. For this reason, the direct capacitance was not included in the model. It should be emphasized, however, that FastCap is a low-frequency model, and therefore it may not perfectly capture the effective capacitance at microwave frequencies.

7.7 LEv6 class of devices

7.7.1 Design criteria

To better understand how the various device parameters influence the Rabi coupling and T_1, I analyzed the cQED circuit shown in Fig. 7.16 in the Hamiltonian approach, as described in detail in Chapter 2. Using this method, for a given choice of capacitances and inductances in the circuit, I computed the parameters of the

Hamiltonian. For the circuit in Fig. 7.16, the Hamiltonian is

$$\mathcal{H} = \frac{Q_r^2}{2C_{res}} + \frac{\Phi_r^2}{2L_r} + \frac{Q_J^2}{2C_\Sigma} - E_J \cos\left(2\pi\frac{\phi_J}{\phi_0}\right) + \beta_{rJ} Q_r Q_J + \beta_r V Q_r + \beta_J V Q_J \quad (7.54)$$

where

$$C_{res} = C_r + C_s + \frac{C_b C_g}{C_b + C_g} \quad (7.55)$$

$$C_\Sigma = C_b + \frac{C_g(C_s + C_r)}{C_g + C_s + C_r} \quad (7.56)$$

$$\beta_r = \frac{C_s(C_b + C_g)}{C_b(C_g + C_r + C_s) + C_g(C_r + C_s)} \quad (7.57)$$

$$\beta_J = \frac{C_g C_s}{C_b(C_g + C_r + C_s) + C_g(C_r + C_s)} \quad (7.58)$$

$$\beta_{rJ} = \frac{C_g}{C_b(C_g + C_r + C_s) + C_g(C_r + C_s)}. \quad (7.59)$$

Quantizing 7.54, as shown in Chapter 2, I obtained:

$$H = \hbar\omega_r\left(a^\dagger a + \frac{1}{2}\right) + \hbar\omega_J\left(b^\dagger b + \frac{1}{2}\right) - \frac{E_c}{12}\left(6\,(b^\dagger b)^2 + 6\,b^\dagger b + 3\right)$$
$$- \hbar\Omega_c(a + a^\dagger)\cos(\omega t) - \hbar\Omega_p(b + b^\dagger)\cos(\omega t) + \hbar g(a + a^\dagger)(b + b^\dagger) \quad (7.60)$$

where $\omega_r = 1/\sqrt{C_{res}L_r}$ is the frequency of the resonator, $E_c = e^2/2C_\Sigma$ is the charging energy of the transmon, g is the coupling between the transmon and the resonator and Ω_p is the Rabi frequency of the qubit drive.

I showed in the previous section that devices of class LEv5 had short lifetimes ($T_1 \sim 1\,\mu$s) caused by a relatively strong coupling ($\mathrm{d}f_{Rabi}/\mathrm{d}V_{rms} \sim 10\,\mathrm{MHz}/\mu\mathrm{V}$) to the transmission line. The best performing device of the lot, LEv5-17 with $T_1 \sim 4\,\mu$s and a weaker Rabi coupling ($3.5\,\mathrm{MHz}/\mu\mathrm{V}$) had a weaker coupling of the resonator ($Q \sim 50,000$). From circuit analysis and FastCap, I found that the direct capacitance coupling the transmon to the transmission line should have had a negligible effect

on the T_1 of my devices. These two facts suggested that the relevant parameters governing the Rabi coupling in the circuit model were mainly the resonator-transmon coupling g and the resonator coupling to the transmission line. The coupling of the resonator to the CPW also sets the external quality factor Q_e of the resonator, and is determined by the capacitance C_s in the reduced circuit model in Fig. 7.16.

The Rabi coupling of the transmon can be expressed according to Eq. 7.38 as:

$$\frac{\mathrm{d}f_{Rabi}}{\mathrm{d}V_{rms}} = \frac{\Omega_p}{2\pi V_{rms}} = \frac{e}{h}\beta_J \left(\frac{2E_J}{E_c}\right)^{1/4}. \tag{7.61}$$

Similarly, the coupling g can be expressed as

$$g = \frac{e}{4}\beta_{rJ}\sqrt{\frac{1}{\pi\hbar Z_r}}\left(\frac{8E_J}{E_c}\right)^{1/4}. \tag{7.62}$$

In the limit $C_r \gg \{C_b, C_g, C_s\}$, we can write $\beta_{rJ} \approx C_g/(C_r C_\Sigma)$ and $\beta_J \approx C_s C_g/(C_r C_\Sigma)$. Using these relations, I can write the Rabi coupling as

$$\frac{\mathrm{d}f_{Rabi}}{\mathrm{d}V_{rms}} = \frac{C_s}{C_r}\frac{g}{\omega_r}\sqrt{\frac{8}{\hbar Z_r}}. \tag{7.63}$$

Equation 7.63 serves as a useful guide for choosing the design parameters to lower the Rabi coupling. I arrived at the following design principles:

1. Reducing the factor C_s/C_r makes the resonator weakly coupled and lowers the Rabi coupling.

2. Reducing the transmon-resonator coupling g also lowers the Rabi coupling.

3. Increasing the resonator frequency ω_r lowers the Rabi coupling.

4. Increasing the resonator impedance Z_r lowers the Rabi coupling.

It is important to note that the Rabi coupling predicted by Eq. 7.38 using the parameters of the Hamiltonian is the *bare* Rabi coupling and not the measured Rabi coupling. In other words, the Rabi coupling predicted from Eq. 7.38 does not have any dependence on the qubit frequency, whereas the measured Rabi coupling varies strongly with qubit frequency (see Fig. 7.8(b)). However, if the bare Rabi coupling is small, I expect the measured Rabi coupling is more likely to be small.

7.7.2 Circuit analysis - comparison of LEv6 and LEv5 designs

Corresponding to the above design principles, I chose a set of parameters for a new design with $C_s = 2.5\,\text{fF}$, $C_g = 10\,\text{fF}$, $C_r = 440\,\text{fF}$, $L_r = 1.1\,\text{nH}$, $C_b = 48\,\text{fF}$, which gave $E_c/h = 330\,\text{MHz}$, $\omega_0/2\pi = 7.2\,\text{GHz}$, $Q_L = 69,000$ and $g/2\pi = 40\,\text{MHz}$. I called this new design LEv6.

The black curve in Fig. 7.21 shows the predicted T_1 vs f from Eq. 7.51 for this set of parameters. The blue curve in Fig. 7.21 is the T_1 prediction using Eq. 7.51 for parameters corresponding to those of device LEv5-7. The T_1 prediction from circuit analysis for the new parameters clearly indicates an improved T_1 due to reduced Rabi coupling over the entire range of frequencies, except at the resonance of the resonator due to the Purcell effect [23, 24].

7.7.3 Microwave Office simulations with no dielectric loss

I designed a new resonator-transmon layout in Microwave Office (MWO) before I proceeded to fabrication. Figure 7.22 shows an image of the actual device LEv6-1

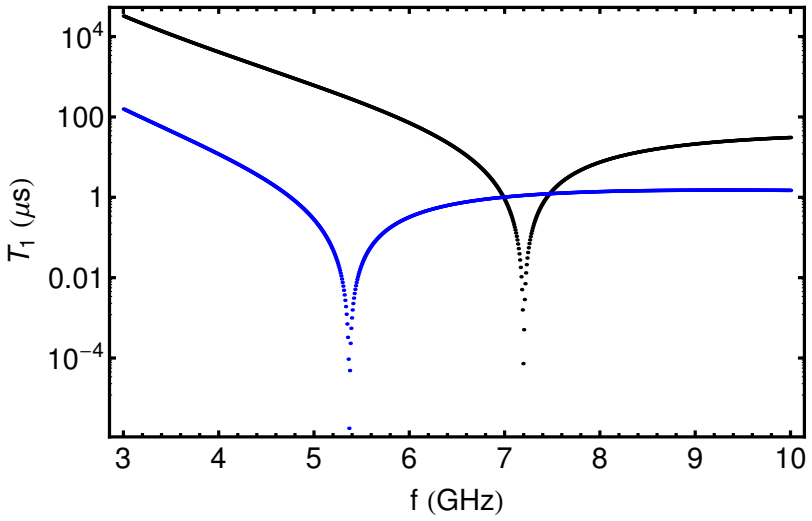

Figure 7.21: Plot of T_1 vs f calculated from circuit analysis for designs LEv5 and LEv6 using Eq. 7.51. Blue points are for circuit parameters corresponding to device LEv5-7. Black points are for circuit parameters corresponding to device LEv6-7.

after fabrication. The design changes I made to achieve the target parameters were as follows:

1. To raise the resonator frequency, I reduced the inductance of the resonator by a factor of 2. This pushed the resonator frequency up from 5.5 GHz to 7.2 GHz, but lowered the resonator impedance by a factor $\sqrt{2}$. Since $\mathrm{d}f_{Rabi}/\mathrm{d}V_{rms} \propto 1/(\omega_r\sqrt{Z_r})$, I expected this design change to lower the Rabi coupling slightly, by a factor of $2^{1/4}$.

2. I rotated the orientation of the capacitor, making the fingers longer by a factor of 2, and halved their number to keep the capacitance constant. The width and separation between the fingers was unchanged at 5 μm each. The smaller number of fingers meant that I could open up a gap between the fingers to place

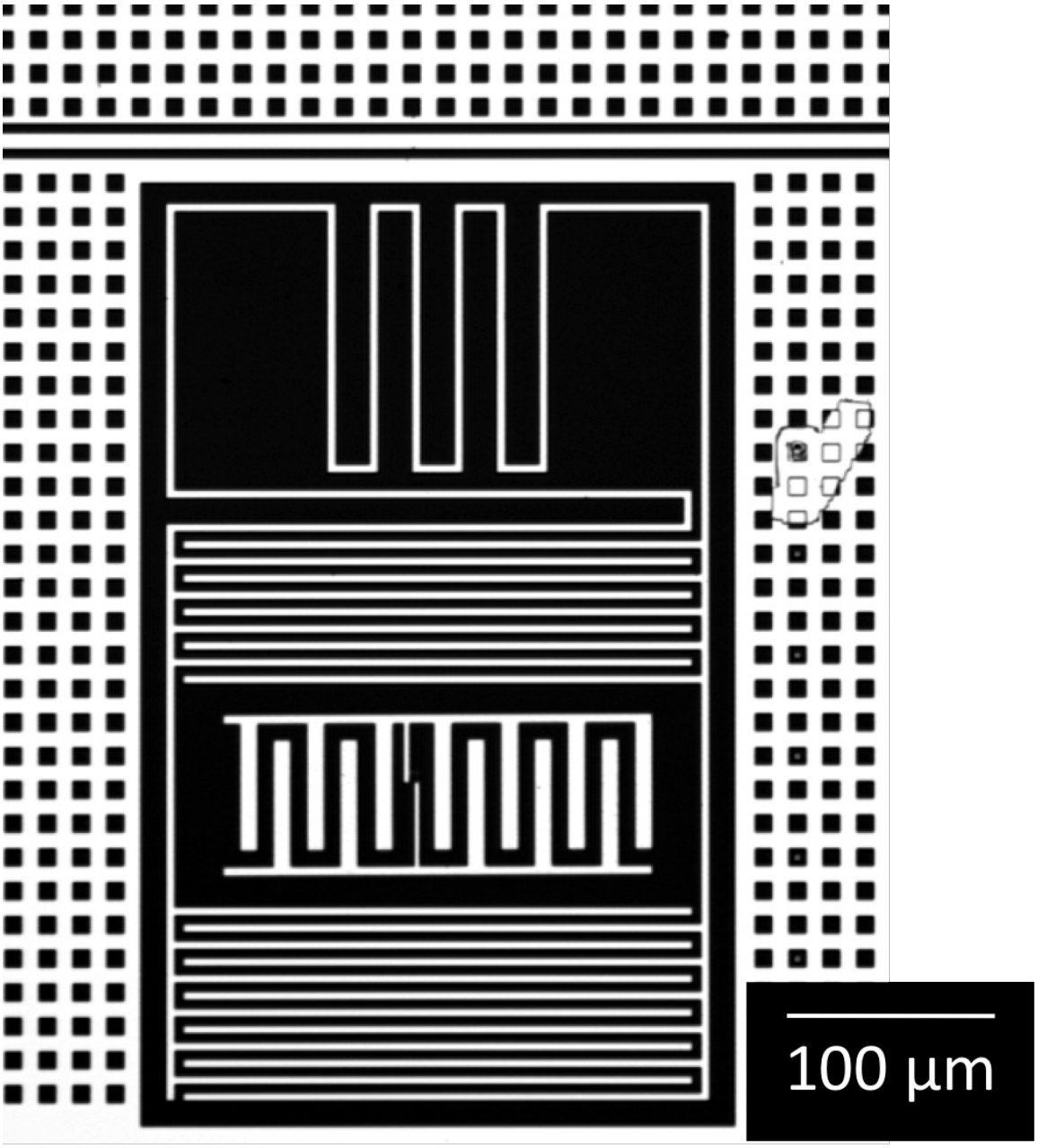

Figure 7.22: Micrograph of device LEv6-1. The ground strip between the transmission line and resonator is 15 μm wide, giving $Q_e = 70,000$.

the transmon *inside* the capacitor, as opposed to between the resonator and the ground plane in LEv5 (see Fig. 7.2). In this configuration, the device would mimic an 'atom-in-a-cavity' system more closely. Rotating the orientation also served the purpose of spatially separating the transmon from the transmission line, making it less susceptible to direct coupling.

3. In order to decouple the resonator and achieve a quality factor of $Q_L = 70,000$, I widened the ground strip separating the resonator and the transmission line from $7\,\mu$m in device LEv5-17 to $15\,\mu$m in the new design.

4. To lower the coupling g to about 30 MHz between the transmon and the resonator, I increased the separation between the plates of the transmon IDC and the resonator capacitance. In design LEv5, the separation between the transmon IDC and the resonator capacitance was $\sim 2\,\mu$m. In devices LEv6-1 and LEv6-7, I made the separation $\sim 15\,\mu$m as shown in Fig. 7.22. To compare, the g for device LEv5-7 was 80 MHz. In addition to lowering g, a wider separation would further reduce the fill factor of surface dielectrics [38, 37].

To simulate the T_1 of the transmon in MWO, I placed an internal port in the place of the Josephson junction, as described in Chapter 4. Since I was interested in the limits on the T_1 from coupling to the environment, I made the $\tan\delta$ of the bulk dielectric (sapphire) zero. I then used the layout as a 'subcircuit' within a circuit schematic, as shown in Fig. 7.23. The real part of the admittance $\mathrm{Re}(Y_{33})$ of the port 3 in Fig.7.23 was then computed and taking $C_b = 50\,$fF, I found $T_1 = C_b/\mathrm{Re}(Y_{33})$.

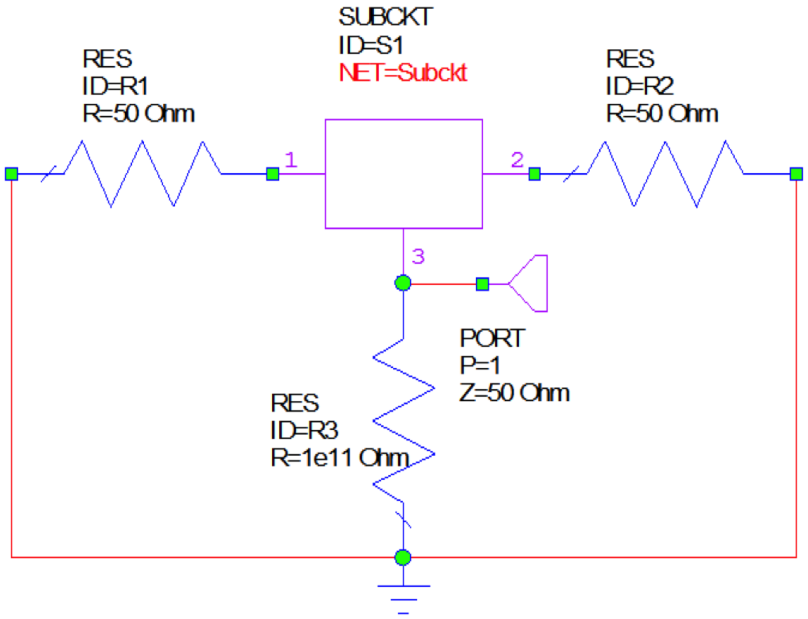

Figure 7.23: Circuit schematic in MWO to compute the real part of admittance across the transmon Josephson junction. Port 3 denotes the transmon Josephson junction.

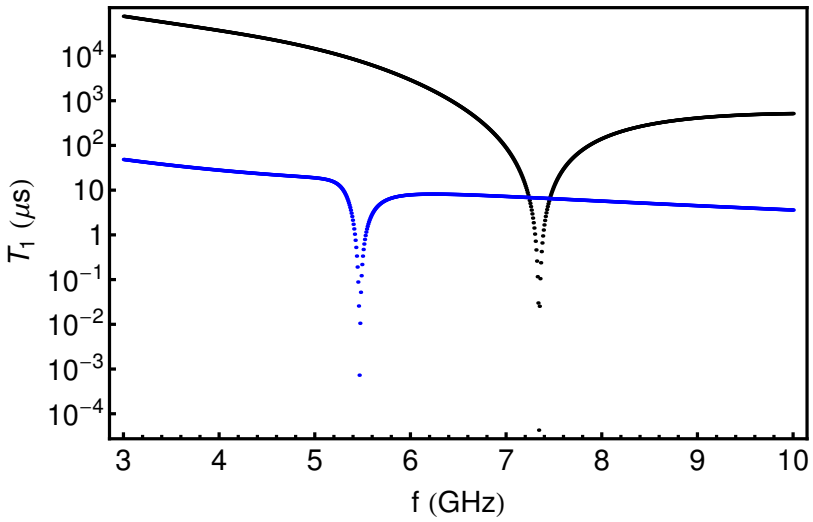

Figure 7.24: Plot of T_1 vs f from Microwave Office simulation of devices LEv5-7 and LEv6-7. Re(Y) was computed using Microwave Office. Black points are for simulation of device LEv6-7 and Blue points are for simulation of device LEv5-7.

Figure 7.24 shows the T_1 predictions from MWO simulation of $\mathrm{Re}(Y_{33})$. Clearly the simulations of device LEv6-1 show longer T_1 predictions than the LEv5 design. The particular design of LEv5 shown here corresponds to that of device LEv5-7. The MWO T_1 vs f plots in Fig. 7.24 are very similar to those from the circuit analysis shown in Fig. 7.21. The main difference is in the less steep frequency dependence of the MWO simulations. This is possibly due to a mixed inductive and capacitive coupling for the resonator, whereas in the circuit analysis I considered a purely capacitive model for the coupling.

7.8 T_1 and Rabi coupling measurements – LEv6 devices

7.8.1 Transmons LEv6-1 and LEv6-7

I fabricated and measured two nominally identical devices, LEv6-1 and LEv6-7, based on the new design. Both the devices had single junction transmons, with junction and IDC designs similar to those in LEv5. Figure 7.22 shows a micrograph of device LEv6-1. As designed, both devices had a resonator frequency around 7.2 GHz. LEv6-1 had a measured external quality factor of Q_e =70,000 and LEv6-7 had Q_e =56,000, close to the designed value of $Q_e = 70,000$. The resonator-transmon coupling g in both devices was close to 40 MHz, as designed. The transmon frequency for device LEv6-1 was 5.4 GHz. Device LEv6-7 had a transition frequency of 6.26 GHz. This discrepancy was likely due to variations in the oxidation of the junctions.

LEv6-1 showed a T_1 ranging between 4 μs and 6 μs. The measured Rabi coupling for this device was 0.2 MHz/μV. Device LEv6-7 had $T_1 = 4\,\mu$s. The Rabi coupling

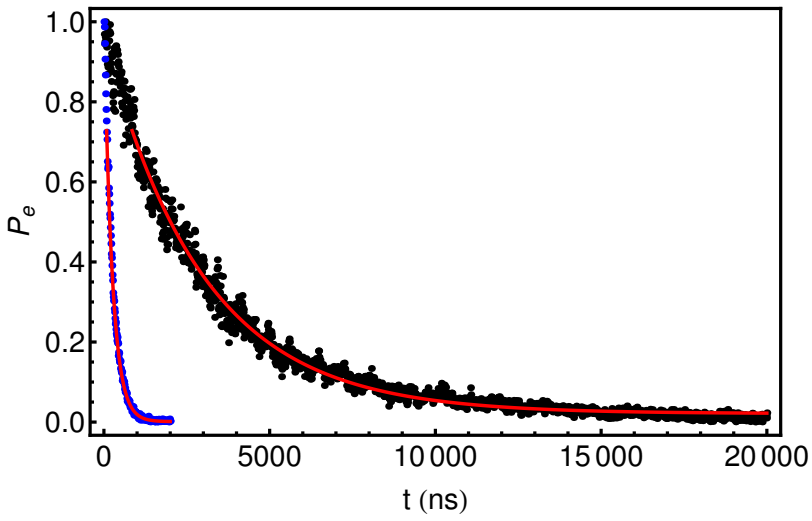

Figure 7.25: Plot of T_1 decay for device LEv5-7 and LEv6-7 with fits. Blue dots are data for device LEv5-7 with $T_1 = 0.277\,\mu$s from fit (Red curve). Black dots are data for device LEv6-7 with $T_1 = 4\,\mu$s from fit (red curve).

for this device was $0.8\,\mathrm{MHz}/\mu\mathrm{V}$. Figure 7.25 shows examples of T_1 measurements on LEv6-7 and LEv5-7.

Although the T_1 values have improved going from LEv5-7 to LEv6, the increase was much less than expected based on the decrease in Rabi coupling (see Eq. 7.41). A comparison of the measured Rabi coupling for the early device LEv5-7 and LEv6-7 is given in Fig. 7.26. The Rabi coupling of device LEv6-7 (black dots) was $0.8\,\mathrm{MHz}/\mu\mathrm{V}$. This is nearly a factor 20 lower than in LEv5-7. From Eq. 7.41, the bound on the T_1 due to coupling to the CPW for device LEv6-7 is around $120\,\mu$s. Since the measured $T_1 = 4\,\mu$s is much less than this limit, we can conclude that device LEv6-7 is not limited by the Rabi coupling to the transmission line. Similarly for device LEv6-1, which has a bound of $T_1 = 2\,\mathrm{ms}$ from the Rabi coupling ($0.2\,\mathrm{MHz}/\mu\mathrm{V}$), based on Eq. 7.41. This strongly suggested the presence of an additional mechanism causing qubit

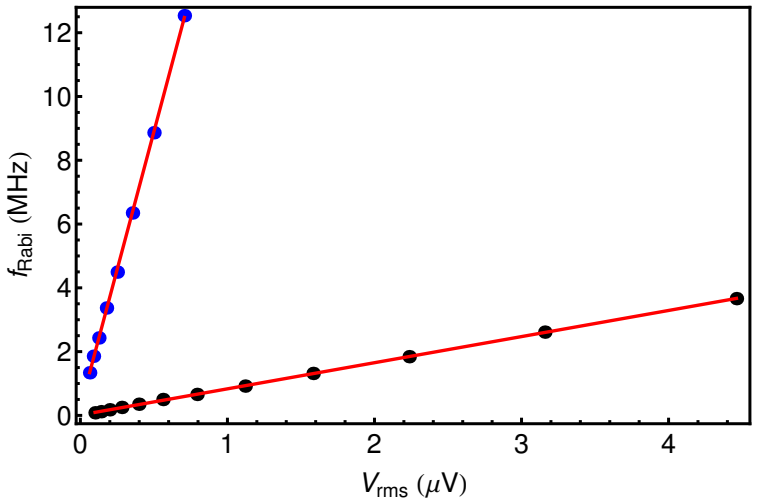

Figure 7.26: Plot of measured Rabi frequency vs applied voltage for device LEv5-7 and LEv6-7 with fits. Blue dots are data for device LEv5-7 with Rabi coupling from fit (Red curve) $\mathrm{d}f_{Rabi}/\mathrm{d}V_{rms} = 17.3\,\mathrm{MHz}/\mu\mathrm{V}$. Black dots are data for device LEv6-7 with Rabi coupling from fit (Red curve) $\mathrm{d}f_{Rabi}/\mathrm{d}V_{rms} = 0.8\,\mathrm{MHz}/\mu\mathrm{V}$

relaxation in devices LEv6-1 and LEv6-7.

7.8.2 Transmons LEv6-2 and LEv6-3

I also fabricated and measured transmons that had a third type of design. In this instance I made a departure from the IDC design of the transmon. This design change was prompted by the observation that there could be other loss mechanisms, in addition to coupling to the transmission line, limiting the T_1 of the transmons in the class LEv6. A prominent candidate was dielectric loss. The fact that the resonators in all my devices had intrinsic quality factors of 200,000 or less in all the devices (see Table 6.2) was consistent with this cause. Recently, groups at Yale [40] and IBM [41] have shown that an interdigital design is prone to dielectric losses because of the

relatively high fill-factor or participation-ratio of the surface oxide. This prompted me to fabricate the design shown in Fig.7.27, where the IDC of the transmon was replaced by "two pads" similar to 3D transmons [40, 41, 66].

Prior to fabrication, I used MWO to simulate the fill-factor of the surface oxide in the total loss. For the simulation, I placed a 2 nm thick lossy dielectric layer between the sapphire substrate and the superconducting layer. In order to better isolate the participation of the surface oxide in the loss, I set the loss-tangent of the sapphire substrate to zero, and varied the loss-tangent ($\tan\delta$) of the 2 nm thick surface dielectric. For each value of $\tan\delta$, I simulated the $\mathrm{Re}(Y)$ for the transmon at a single frequency $\omega/2\pi = 4\,\mathrm{GHz}$. Using $T_1 = C_b/\mathrm{Re}(Y)$, I then computed T_1 from the simulated $\mathrm{Re}(Y)$ at this frequency for $C_b = 50\,\mathrm{fF}$. The quantity $1/(\omega T_1)$ is then expected to vary linearly with $\tan\delta$ [32, 40], with the slope proportional to the fill-factor for the surface oxide. I used this simulation to compare the fill-factor of the surface oxide for a transmon with an IDC (see Fig. 7.22) vs a transmon with a two-pad design (see Fig. 7.27).

Figure 7.28 shows a plot of $1/(\omega T_1)$ vs $\tan\delta$ of a 2 nm thick surface dielectric for both an IDC (black points) and the "two-pad" design (blue points). From the linear fits (red curves), I found that the fill-factor (0.004) for the two-pad design was nearly 3 times smaller than that of an IDC (0.011).

I made two nominally identical devices with this design, LEv6-2 and LEv6-3. The major difference between these two devices and my other transmons was the design of the transmon shunt capacitance. In particular, I moved away from the IDC design used in all my earlier devices. Instead, I fabricated two pads roughly 140 μm

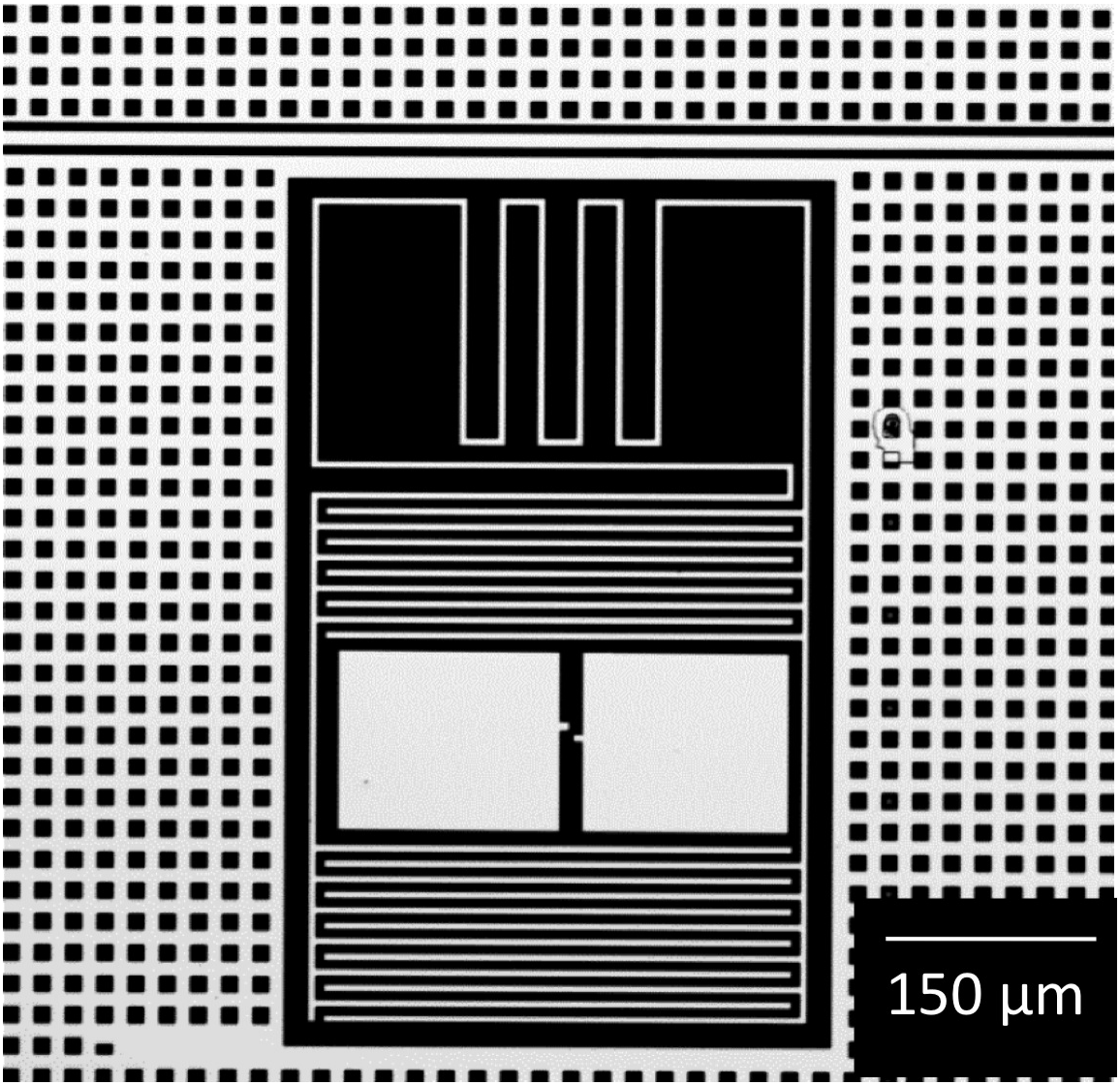

Figure 7.27: Micrograph of device LEv6-2. The transmon shunt capacitance is provided by the two large pads.

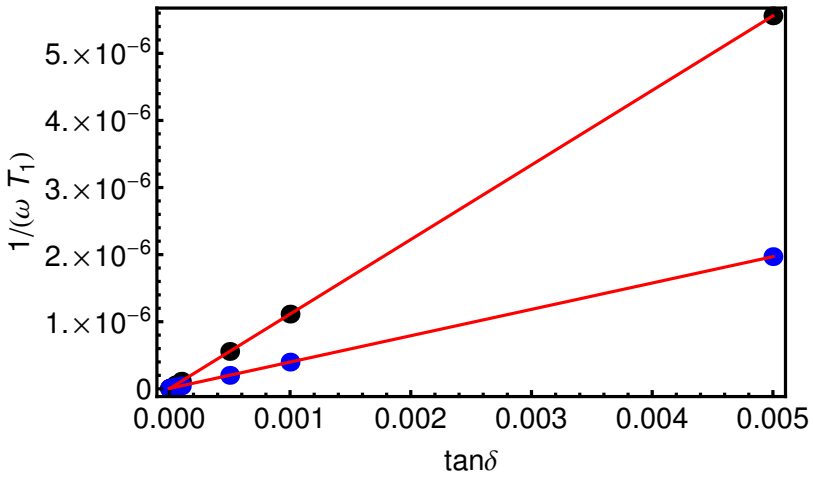

Figure 7.28: Plot of simulated $1/(\omega T_1)$ vs $\tan\delta$ for the 2 nm thick surface dielectric for both an IDC (black points) and the "two-pad" design (blue points) from MWO. From the linear fits (red curves), the fill-factor for two-pad design is 0.004, and that of the IDC is 0.011.

$\times$ 140 μm wide.

These devices had nominally identical parameters. The resonator parameters were the same as in devices LEv6-1 and LEv6-7, with a resonator frequency of 7.19 GHz and an external quality factor of $Q_e = 70,000$, as designed. The intrinsic quality factors for the resonators of both devices were around 180, 000. The charging energy of the transmons came out to be $E_c/h \approx 580$ MHz, a factor of 2 higher than my previous transmons, while the design value was close to $E_c/h = 450$ MHz. The transition frequency of the devices came out to be 9.9 GHz. This was higher than expected, probably due to a combination of factors – the charging energy E_c was higher than designed, and E_J was too large, possibly due to variations in oxidation. The transmon-resonator coupling $g/2\pi = 120$ MHz also turned out higher than expected.

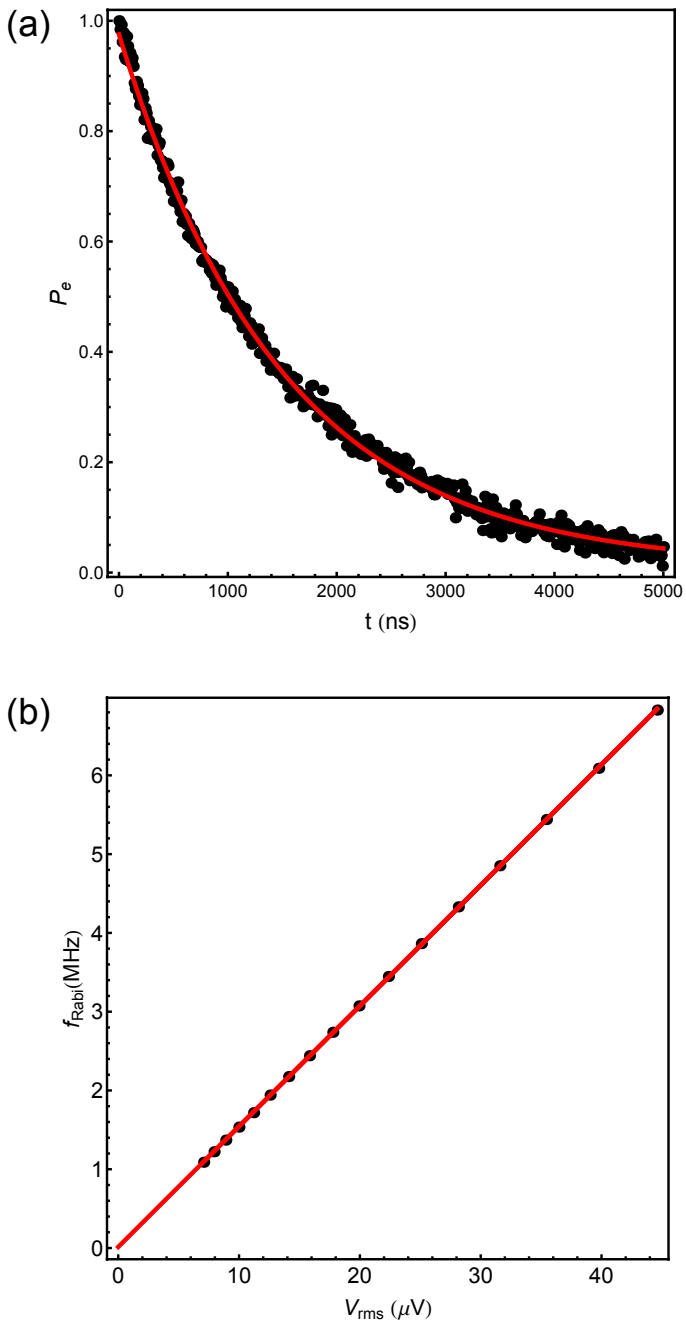

Figure 7.29: Plot of T_1 decay and Rabi coupling for device LEv6-2, with fits. (a) T_1 decay (black points) for device LEv6-2 with fit to exponential decay (red curve) giving $T_1 = 1.2\,\mu$s. (b) Measured Rabi frequency (black points) vs applied drive voltage for device LEv6-2 with linear fit (Red curve) giving a Rabi coupling of $0.15\,\mathrm{MHz}/\mu\mathrm{V}$

This could have been caused by an asymmetrical placement of the transmon within the gap between the resonator capacitor plates. This brought one of the pads closer to one of the plates by $5\,\mu$m. Whether this explains the large g is unclear and needs to be examined further.

Device LEv6-2 had a measured $T_1 = 1.2\,\mu$s as shown in Fig. 7.29(a). The measured Rabi coupling for this device was $\mathrm{d}f_{Rabi}/\mathrm{d}V_{rms} = 0.15\,\mathrm{MHz}/\mu\mathrm{V}$ from the fit in Fig.7.29(b). Device LEv6-3 had a similar T_1 of $0.8\,\mu$s. The Rabi coupling for this device was $0.23\,\mathrm{MHz}/\mu\mathrm{V}$. Needless to say, in both cases T_1 was much shorter than anticipated. Also, there was no evidence from the data for devices LEv6-2 and LEv6-3 to support the simulated decrease in the fill-factor of the surface oxide compared to the other transmons (see Fig. 7.28).

In summary, the Rabi couplings measurements for devices in the class LEv6 show that they were not limited by strong coupling to the transmission line. The Rabi coupling values for transmons in both classes LEv5 and LEv6 are shown in Fig. 7.30. The Rabi coupling values for design LEv6 were an order of magnitude smaller $\sim 0.2\,\mathrm{MHz}/\mu\mathrm{V}$ compared to those of LEv5 $\sim 10\,\mathrm{MHz}/\mu\mathrm{V}$. Despite this, the T_1 measurements did not show a commensurate improvement. A summary of my T_1 and Rabi coupling measurements for all my devices is given in Table 7.3.

The intrinsic quality factor of the resonators points to dielectric loss as a possible cause of energy loss in my transmons. For comparison the RC time constants of the resonators are shown in Table 7.3, given by $\tau_R = Q_i/\omega_r$. For all my resonators, this time constant was around $5\,\mu$s. For transmons that were not dominantly limited by Rabi coupling – LEv5-17 and all devices in LEv6 – τ_R is of the same order of

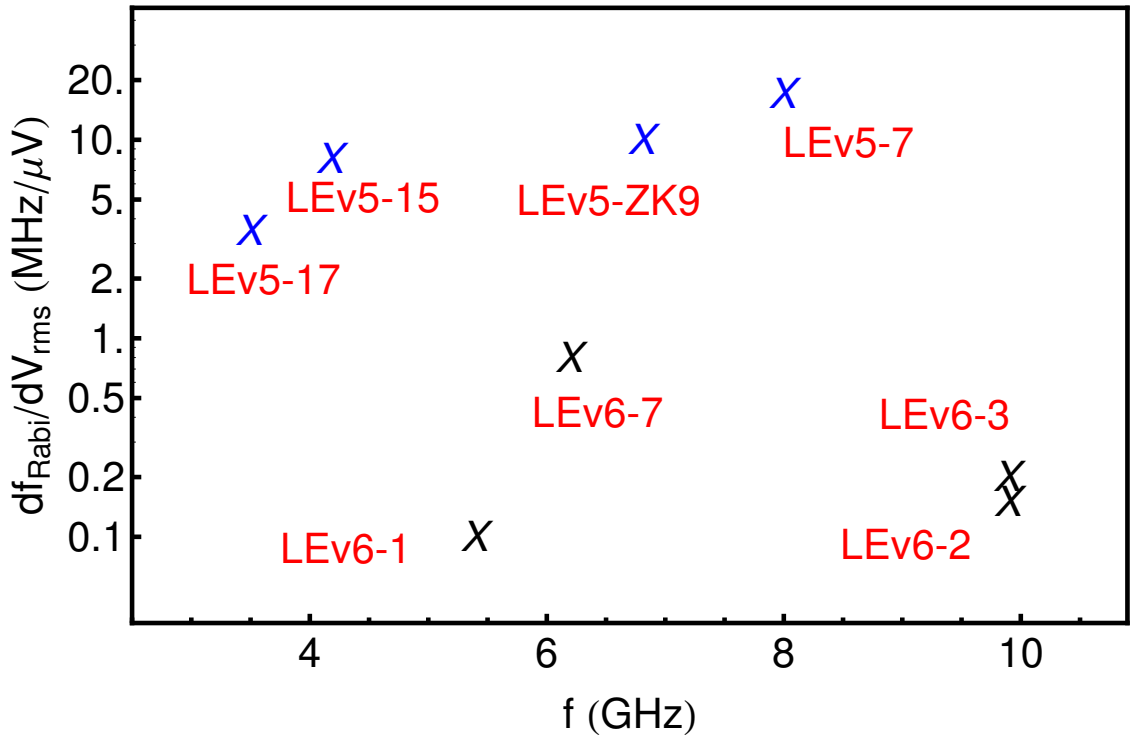

Figure 7.30: Plot of measured Rabi coupling for all transmons. Blue is for LEv5 devices and Black is for LEv6 devices. The LEv6 devices have Rabi coupling nearly an order of magnitude smaller than that of LEv5.

magnitude as the measured T_1 (see Table 7.3). This suggests that dielectric loss is a possible source of noise limiting T_1 of my recent transmon devices.

7.9 Dielectric losses

As discussed above, the lifetimes of transmons in the class LEv6 were found to be limited by a loss that was not due to coupling to the transmission line. Unfortunately, the Microwave Office simulations shown in Fig. 7.24 had no dielectric loss. In other words, the $\tan\delta$ was set to zero for the simulations in Fig. 7.24. In Fig. 7.31 the black curve shows the T_1 prediction from MWO simulations for no loss in the substrate. The gray curve shows the T_1 prediction in the presence of a bulk dielectric loss tangent $\tan\delta = 5.5 \times 10^{-6}$. This value was chosen to match the intrinsic quality factors of the resonators $Q_i = 1/\tan\delta \sim 180,000$. The gray curve agrees closely with the measured T_1 values of transmons of class LEv6, shown in Fig.7.31 with the blue 'x' marks.

I extended this simulation to both LEv5 and LEv6 designs. Figure 7.32 shows T_1 predictions for design LEv5 (blue curve) and for design LEv6 (black curve) with a bulk loss tangent of $\tan\delta \sim 5.5 \times 10^{-6}$. The points marked by the blue 'x' s represent the measured T_1 values of devices in the class LEv5. The black 'x' correspond to the measured T_1 values for devices in class LEv6. From the plot, one sees that the simulations come close to the measured values. This suggests that dielectric loss is consistent with the relaxation I see in my transmon devices.

The actual location of the dielectric loss needs to be further investigated, and I have not conducted a systematic study of that aspect as part of my dissertation.

Table 7.1: Table of measured T_1 and Rabi coupling and a few other parameters for LEv5 and LEv6 transmons. The blanks denote that those measurements were not done. T_1^{coup} is the lifetime predicted using Eq. 7.41.

Device Name	$\omega_{ge}/2\pi$ (GHz)	T_1 (μs)	$\mathrm{d}f_{Rabi}/\mathrm{d}V_{rms}$ (MHz/μV)	T_1^{coup} (μs)	Q_i	Q_i/ω_r (μs)
LEv5-56	6.5	≤ 1.6	-	-	199,644	5.8
LEv5-7	8.001	0.277	17.3	0.33	180,000	5.3
LEv5-ZK9	4.982	1.6	-	-	180,000	5.3
LEv5-ZK9	6.81	0.9	9.0	1.2	180,000	5.3
LEv5-15	4.18	1.8	8.0	2.8	80,000	2.4
LEv5-17	3.5	4.5	3.5	17.5	200,000	5.9
LEv6-1	5.4	5$\pm$1	0.2	2000	200,000	4.5
LEv6-7	6.26	3.5$\pm$0.5	0.8	120	213,000	4.8
LEv6-2	9.995	1.2	0.15	3000	187,000	4
LEv6-3	9.989	0.9	0.23	2000	181,000	3.9

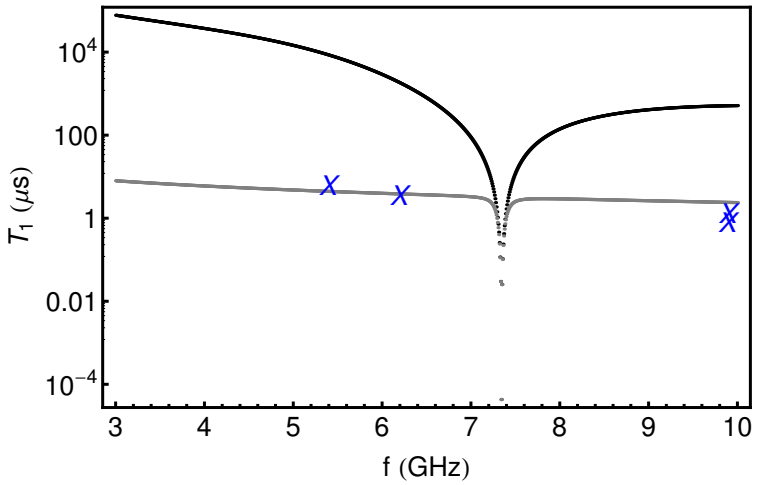

Figure 7.31: Plot of T_1 vs f simulated using MWO with no dielectric loss for device LEv6-1. Black curve is for no loss in dielectric, $\tan\delta = 0$. Gray curve is for $\tan\delta = 5.5 \times 10^{-6}$ corresponding to a resonator intrinsic quality factor of 180,000. Blue 'x's represent measured T_1 for LEv6 transmons.

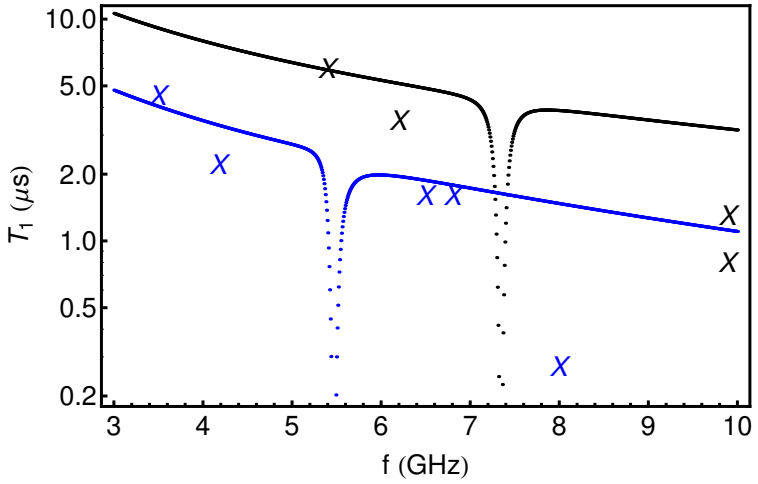

Figure 7.32: Plot of T_1 vs f simulated using MWO with a bulk $\tan\delta = 5.5 \times 10^{-6}$. Blue curve is simulated T_1 for parameters corresponding to device LEv5-7. Blue 'x's are measured T_1's for LEv5 devices. Black curve is simulated T_1 for parameters corresponding to device LEv6-1. Black 'x's are measured T_1's for LEv6 devices.

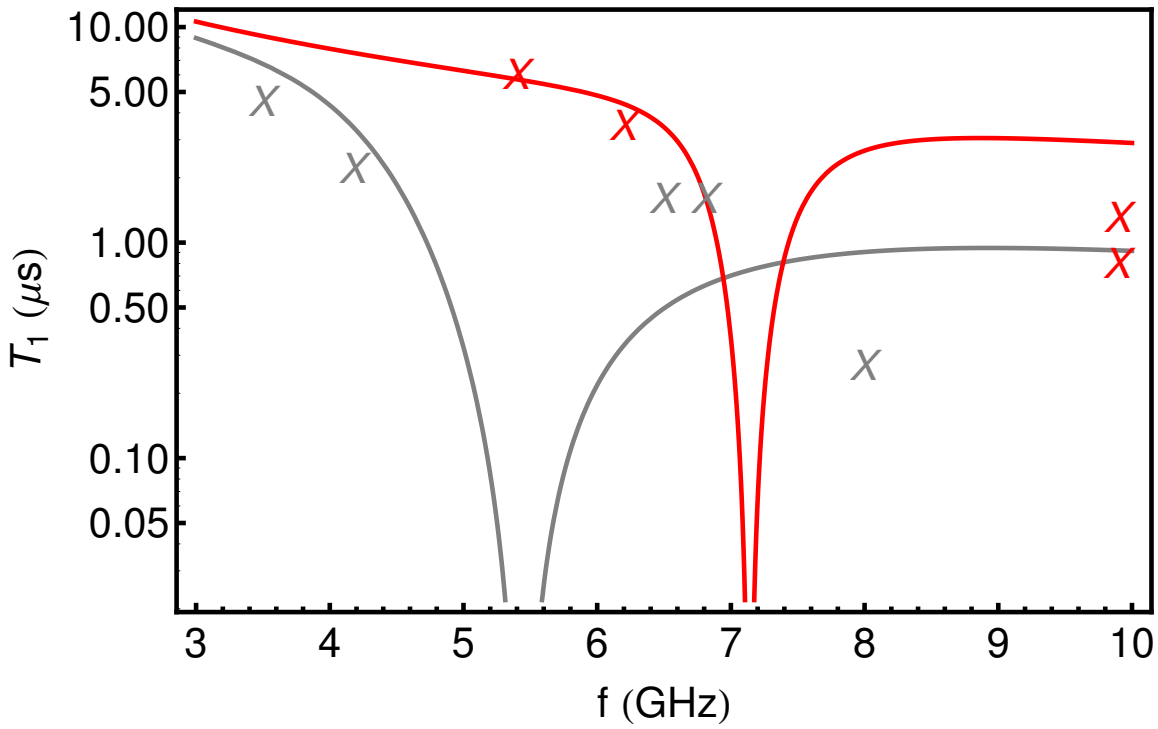

Figure 7.33: Plot of T_1 vs f calculated using circuit analysis Eq. 7.64 for $\tan\delta \simeq 5.5 \times 10 - 6$. Gray curve is T_1 prediction for parameters corresponding to device LEv5-7. Gray 'x's are measured T_1's for LEv5 devices. Gray curve is T_1 prediction for parameters corresponding to device LEv6-1. Red 'x's are measured T_1's for LEv6 devices.

However, SEM imaging of some of my devices has revealed residual contaminants remaining on the surface after fabrication. Such residue close to the Josephson junction (see Fig. 4.18) may cause qubit relaxation. A thorough investigation of each step of the fabrication process needs to be carried out to resolve this problem. I also note that no additional surface preparation was done to the sapphire substrate in my devices, and such preparation has been used by other groups [88] to achieve better quality factors for their resonators.

I also used the analytical model from circuit analysis with an additional background loss to simulate the dielectric loss. The model cannot account for distributed dielectric loss in a straight forward manner, so I used a parallel loss mechanism instead. The T_1 prediction from the Eq. 7.51 was combined with a dielectric loss according to

$$T_1^{eff} = \left\{ \frac{1}{T_1} + \omega \tan\delta \right\}^{-1} \tag{7.64}$$

Figure 7.33 shows the T_1 prediction from Eq. 7.64 for a background loss tangent value of $\tan\delta = 5.5 \times 10^{-6}$, similar to the MWO case. The red curve in Fig. 7.33 shows the T_1^{eff} for devices of class LEv6. The gray curve shows the T_1^{eff} prediction for devices of class LEv5. The points marked by gray 'x' correspond to measured T_1 values of the transmons in class LEv5. The points marked by red 'x' correspond to the measured T_1 for transmons in class LEv6. Although the agreement is not spectacular, the model is qualitatively and quantitatively in agreement with the data.

7.10 Ramsey measurement

In this section I briefly present my Ramsey free-induction decay measurements on some of the transmons (LEv5-7 and LEv6-3). My thesis was mainly about the lifetime and Rabi coupling measurements that were discussed in detail earlier in this Chapter. While T_1 measures the timescale on which the excited state of the qubit decays to the ground state, Ramsey fringes measure the timescale T_2^*, which is related to the coherence time T_2 during which the qubit loses coherence, when prepared in a superposition state. In the absence of inhomogeneous broadening of the qubit

lineshape, $T_2^* = T_2$, which is the coherence time. In general, $T_2^* \leq T_2$. Therefore, measuring T_2^* places a lower bound on the coherence time.

The T_2 time is related to the T_1 time and the pure dephasing time T_φ [51] by

$$\frac{1}{T_2} = \frac{1}{2T_1} + \frac{1}{T_\varphi}. \tag{7.65}$$

From this relation, in the limit of very long T_φ, we find that T_2 is limited by $2T_1$. Since $T_2^* \leq T_2$, we can also write

$$T_2^* \leq 2T_1. \tag{7.66}$$

While discussing Rabi oscillations, I mentioned that the duration of the qubit excitation pulse determines the state in which the qubit is initialized. In the case of the T_1 measurements, in order to initialize the qubit in the excited state, I used a $\pi-$pulse. In the Ramsey experiment, in order to prepare the superposition state $(|g\rangle + |e\rangle)/\sqrt{2}$, I used a $\pi/2$-pulse. The length $\tau_{\pi/2}$ of the $\pi/2$-pulse is determined from the Rabi oscillations, and corresponds to $\Omega_p \tau_{\pi/2} = \pi/2$, which is half the length of the π-pulse.

The pulse sequence of the Ramsey measurement is shown in Fig. 7.1(c). I first sent a $5\,\mu$s long read-out pulse. After waiting $\sim 80\,\mu$s to allow photons in the resonator to decay, I sent a pair of $\pi/2$-pulses at a detuned frequency of $\omega_g e \pm \delta$, with a given gap t between the pulses. About 10 ns after the second $\pi/2$-pulse was turned off, a second read-out pulse was sent. The difference in the mean transmitted voltage between the two read-out pulses is proportional to the probability of the excited state P_e. This measurement was repeated about 5000 times for each delay t and then t was swept. When the drive was exactly on resonance with the qubit transition or

when $\delta = 0$, $P_e \propto e^{-t/T_2^*}$. When the detuning is non-zero, $P_e \propto e^{-t/T_2^*} \sin \delta t$. The fact that Ramsey fringes oscillate at the frequency given by the detuning of the drive from the qubit transition can be used to measure the qubit transition frequency quite accurately.

In Fig. 7.34 black dots show the measured P_e vs the delay t between the $\pi/2$-pulses for device LEv5-7. Note that in the detuned Ramsey case, the qubit excited state probability does not reach 1. So, the y-axis in Fig. 7.34 is not the excited state probability P_e, but only proportional to it. I chose the proportionality constant to be unity for convenience. The power of the qubit drive at the transmission line for this measurement was $-116\,\mathrm{dBm}$, with $\tau_{\pi/2} = 45\,\mathrm{ns}$. By fitting the data to the function $e^{-t/T_2^*} sin(\delta)$ the fit (shown in red in Fig. 7.34), the frequency of the Ramsey fringes was $\delta/2\pi = 2.22$ MHz, and $T_2^* = 530\,\mathrm{ns}$. Since, $T_1 = 277\,\mathrm{ns}$ for this device, from Eq. 7.66, I concluded that this device was nearly T_1 limited. From Eq. 7.65, I can now place an upper bound on the $T_\varphi \leq 12\,\mu\mathrm{s}$ on dephasing in this device.

7.10.1 Ramsey fringes and dressed dephasing

While some of my devices (LEv5-7 and LEv6-2) showed nearly T_1-limited behavior, the other devices had T_2^* limited by pure dephasing T_φ. In such cases, I found that the measured T_2^* was not close to $2T_1$. Figure 7.35(a) shows the measured Ramsey fringes (black points) for device LEv6-3 (see Fig. 7.27). The T_2^* for this device from the fit (shown as red curve in Fig. 7.35(a)) was found to be $1.3\,\mu\mathrm{s}$. The T_1 relaxation data for this device is shown in Fig. 7.35(b). From the exponential decay fit (red

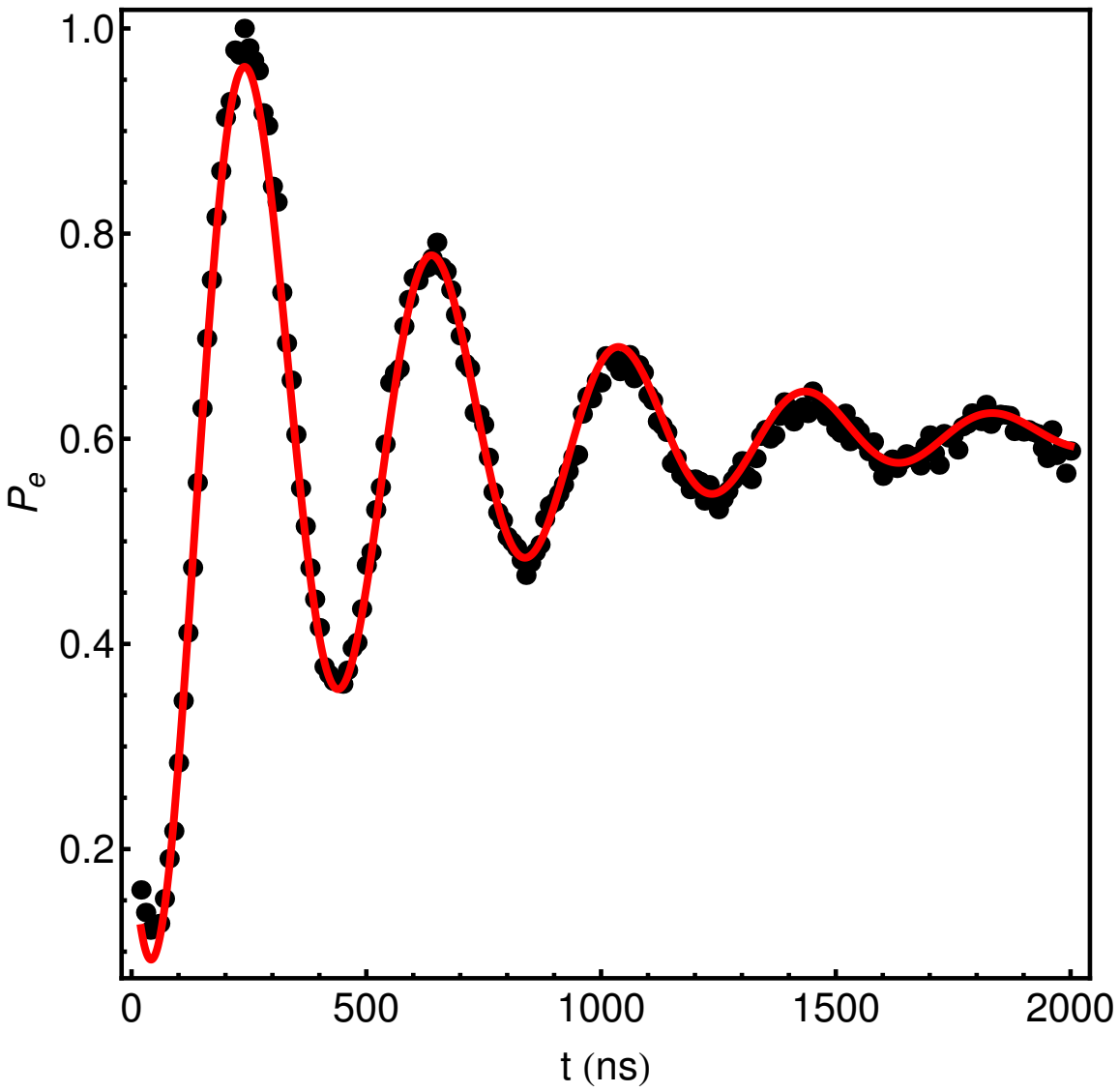

Figure 7.34: Ramsey free-induction decay for device LEv5-7. Black dots are the measured probability of excited state P_e and red curve is fit with $T_2^* = 530\,\text{ns}$. $T_2^* \approx 2T_1 = 554\,\text{ns}$, suggesting nearly T_1 limited behavior.

curve) to the data (black points) in Fig. 7.35(b), I find a $T_1 = 0.89\,\mu$s for this device. Since $T_2^* = 1.3\,\mu$s was not close to $2T_1 = 1.780\,\mu$s, I concluded that this device was not nearly T_1-limited. From Eq. 7.65, the bound on the pure dephasing time for this device was $T_\varphi \leq 4.8\,\mu$s.

From the Ramsey fringes measurement alone the cause of the pure dephasing in LEv6-3 could not be established. However, transmon spectroscopy (see Fig. 7.35(c)) in addition to the Ramsey fringes measurement suggested that a thermal population of photons in the resonator may be causing the dephasing of the qubit in LEv6-3. Figure 7.35(c) shows a spectrum of the qubit close to the $|g\rangle \rightarrow |e\rangle$ transition frequency with no coherent drive on the resonator. The prominent peak at 9.887 GHz in Fig. 7.35(c) is the qubit transition frequency corresponding to $n = 0$ photons present in the resonator. I also noticed a weak $n = 1$ photon number-peak at 9.885 GHz (marked by the red dashed circle in Fig. 7.35(c)). Since the resonator was not coherently driven in this case, the $n = 1$ photon number-peak was caused by thermal excitations. From a number-weighted average of the peak-heights using Eq. 6.12, I estimated the average number of thermal photons in the resonator $n_{th} \approx 0.05$. For a resonant frequency of 7.2 GHz, this corresponds to an effective resonator temperature of 122 mK. For comparison, the mixing chamber of the dilution refrigerator is close to 20 mK.

Following Boissonneault *et al.* [108], one can estimate the dephasing caused by this thermal population of photons in the resonator, according to the "dressed dephasing model". According to this model [108], for a mean photon number $\bar{n}$ in the resonator with a photon loss-rate κ, a qubit that is coupled to the resonator has

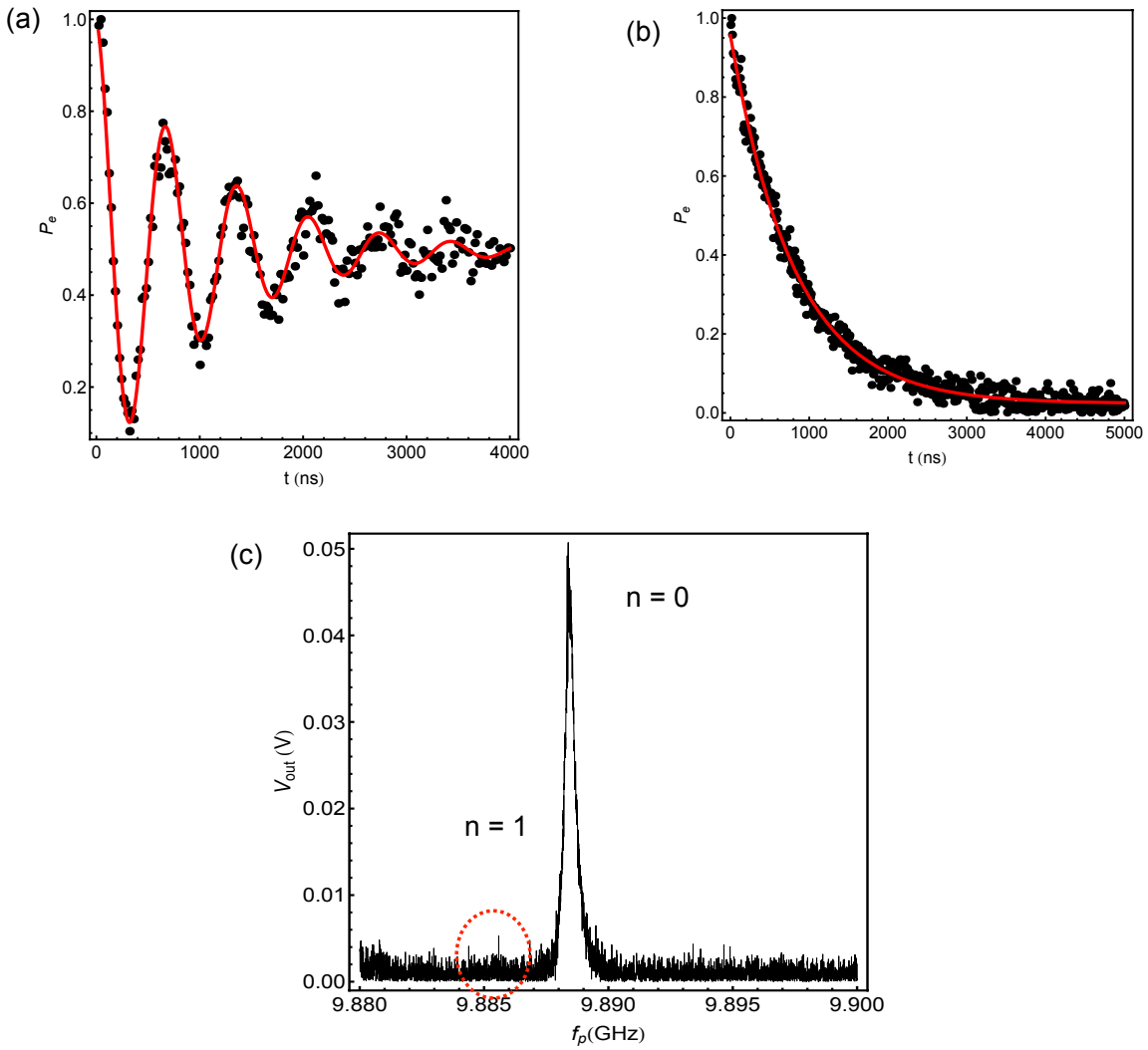

Figure 7.35: Plots of measured Ramsey fringes, T_1 decay and transmon spectroscopy for device LEv6-3. (a) Black points are measured Ramsey fringes with fit (red curve) giving $T_2^* = 1.3\,\mu$s. (b) Black dots show T_1 relaxation data with fit (red curve) with a $T_1 = 0.89\,\mu$s. T_2^* is much less than $2T_1$, suggesting that the device is not nearly T_1-limited. (c) Transmon spectrum close to the $|g\rangle \rightarrow |e\rangle$ transition showing a prominent $n = 0$ photon qubit transition peak, and a weak $n = 1$ thermal photon-peak.

a dephasing time given by

$$T_{\varphi}^{dd} = \frac{1}{2\bar{n}\kappa(\tan^{-1}(2\chi/\kappa))^2} \tag{7.67}$$

where 2χ is the ac Stark shift of the qubit frequency per photon in the resonator. This model is strictly valid only in the weak dispersive limit ($\chi < \kappa$), whereas my transmon devices were operated in the strong dispersive limit ($\chi > \kappa$). However, applying this model may still give an insight into the cause of dephasing in my devices.

For device LEv6-3, using Eq. 7.67, for $2\chi/2\pi = 2\,\mathrm{MHz}$, $\kappa/2\pi = 0.11\,\mathrm{MHz}$, for $\bar{n} = 0.06$, I find $T_{\varphi} = 5.55\,\mu\mathrm{s}$. This estimate $T_{\varphi}^{dd} \approx 5.55\,\mu\mathrm{s}$ made using the dressed dephasing model is in good agreement with the $T_{\varphi} = 4.8\,\mu\mathrm{s}$ estimated from the Ramsey fringes measurement. This suggests that thermal population of photons in the resonator may be a possible source of dephasing in some of my transmon devices. The actual cause of heating in the resonator is unclear at the moment and needs to be examined further. Improper thermal contact of the device with the mixing chamber of the refrigerator, heating of microwave attenuators and other components close to the device, heating of the device due to microwave power, stray infrared radiation leaking into the refrigerator from the environment *etc.* are possible factors causing heating, and thereby dephasing the qubit. Table 7.2 gives a comparison between the dephasing time T_{φ} estimated from the Ramsey fringes measurement vs T_{φ}^{dd} estimated from Eq. 7.67. In almost all the cases, the dressed dephasing model seems to predict dephasing time close to that estimated from Ramsey fringes measurement, suggesting that a residual thermal population of the resonator could be causing dephasing of my qubits.

Table 7.2: Table of dephasing time T_φ determined from Ramsey measurement vs that calculated from the dressed dephasing model Eq. 7.67. n_{th} is determined from transmon spectroscopy close to the fundamental transition frequency.

Device Name	T_1 (μs)	T_2^* (μs)	T_φ (μs)	n_{th}	T_φ^{dd} (μs)	Charge dispersion ϵ_1 (MHz)
LEv5-ZK9	0.9	1.0	2.25	0.1	2.24	-0.011
LEv5-15	1.8	2.7	3.98	0.105	2.62	-0.027
LEv5-17	5.0 ± 1.0	2.4	3.44	< 0.08	> 3.25	-1.9925
LEv6-7	3.5 ± 0.5	2.5±0.5	3.84	0.1	5.4	-0.02
LEv6-2	1.2	2.2	26.4	< 0.04	> 6.4	-0.415
LEv6-3	0.89	1.3	4.8	0.05	5.55	-0.415

Table 7.3: Table of measured coherence parameters for LEv5 and LEv6 transmons. The blanks denote that those particular data were not available.

Device Name	$\omega_{ge}/2\pi$ (GHz)	T_1 (μs)	T_2^* (μs)	T_φ (μs)
LEv5-56	6.5	≤ 1.6	-	-
LEv5-7	8.001	0.277	0.55	14.1
LEv5-ZK9	4.982	1.6	-	-
LEv5-ZK9	6.81	0.9	1.0	2.25
LEv5-15	4.18	1.8	2.7	3.98
LEv5-17	3.5	4.5	2.4	3.44
LEv6-1	5.4	5±1.0	-	-
LEv6-7	6.26	3.5±0.5	2.5±0.5	3.84
LEv6-2	9.995	1.2	2.2	26.4
LEv6-3	9.989	0.89	1.3	4.8

7.11 Conclusion

In this Chapter I described my time domain measurements of devices (mainly LEv5-7,LEv5-15, LEv5-17, LEv6-1, LEv6-7, LEv6-2 and LEv6-3) each of which had a transmon coupled to a lumped-element resonator. A summary of the coherence parameters I measured for my transmon devices is given in Table 7.3. I gave a detailed description of my T_1 measurements, Rabi coupling measurements, and Ramsey measurements (LEv5-7 and LEv6-3). From the measurements of the early transmon devices (LEv5), I concluded that their T_1 times were possibly limited by coupling to the transmission line. By studying the approximate equivalent circuit in a circuit Hamiltonian approach as well as from the point of view of an admittance calculation, I arrived at ways to lower the Rabi coupling. To achieve this, I lowered the resonator coupling to the transmission line by widening the ground strip separating them from $2\,\mu$m to $15\,\mu$m. This increased the loaded quality factor of the resonator from 15,000 to 70,000. I also lowered the coupling g between the resonator and the transmon from 80 MHz to 30 MHz to achieve the same. I designed devices with the new set of parameters and my experimental measurements confirmed that the Rabi coupling was an order of magnitude lower, placing bounds on T_1 due to coupling to the CPW transmission line in the range of $T_1 \sim 200\,\mu$s. However the new devices in class LEv6 also showed relatively short lifetimes. Microwave simulations and circuit analysis both indicate that this could be caused by surface dielectric loss. The intrinsic quality factors of the resonators, $Q_i \sim 200,000$, were consistent with this mechanism and implying that a $T_1 \approx 5\,\mu$s should be expected for these designs.

Chapter 8

Conclusions

8.1 Devices

In this dissertation I described the design, fabrication and measurement at millikelvin-temperatures of Al/AlO_x/Al Josephson junction-based transmon qubits coupled to superconducting thin film lumped-element microwave resonators made of aluminum on sapphire. Some of my devices (LEv5-56, LEv5-7, LEv5-ZK9, LEv5-15, LEv5-17) had resonators with resonant frequency around 5.4 GHz with a total quality factor Q_L between 15,000 (LEv5-7) and $50,000$ (LEv5-17). The other devices (LEv6-1, LEv6-2, LEv6-3, LEv6-7) had a resonator frequency around 7.2 GHz, with a quality factor $Q_L \approx 70,000$. See Table 6.2, Table 6.3 and Table 7.3 for a summary of the key properties of these devices.

The transmon junctions had a total area of approximately 150 nm × 150 nm. The charging energy of the transmons E_c, arising mostly from the large interdigital shunt capacitance, ranged from 200 MHz to 400 MHz for devices LEv5-56, LEv5-7, LEv5-15, LEv5-ZK9, LEv5-17, LEv6-1 and LEv6-7. For devices LEv6-2 and LEv6-3, the charging energy of the transmon was $E_c/h \approx 600$ MHz.

8.2 Summary of Spectroscopic measurements

I presented a detailed spectroscopic characterization of some of my transmon devices, mainly LEv5-56, LEv5-ZK9, LEv6-1 and LEv6-7 in Chapter 6. The most interesting results from my spectroscopic measurements were two unexpected effects observed in device LEv5-ZK9:

1. A nonlinear variation of the average photon occupancy in the resonator as the coherent drive power was increased, caused by the Jaynes-Cummings nonlinearity.

2. The first clear experimental observation of the Autler-Townes effect involving the dressed states of the Jaynes-Cummings Hamiltonian.

8.2.1 Jaynes-Cummings Nonlinearity

Operating in the strong dispersive limit ($\chi = g^2/\Delta >> \Gamma, \kappa$) with $g/2\pi = 70$ MHz and at $\Delta = -500\,\mathrm{MHz}$ in device LEv5-ZK9, I was able to resolve distinct photon number peaks due to the AC stark shift caused by each photon stored in the resonator. Unlike previous measurements of photon number-splitting [44], I used a pulsed Jaynes-Cummings read-out [35] for spectroscopy, while coherently populating the resonator with a weak coupler tone. This gave me a better SNR, making data acquisition considerably faster. When a coherent coupler tone was applied to the resonator, I observed discrete photon number peaks in the qubit spectrum by sweeping the 'probe' spectroscopy tone. From a weighted average of the relative peak heights, I was able to calculate the average number of photons stored in the resonator. I was also able to

calibrate the attenuation of the input microwave line between the microwave source and the transmission line from the average number of photons in the resonator.

The average photon occupancy $\bar{n}$ in the resonator was found to vary nonlinearly with the applied power P_{rf}. In Chapter 6, I described my study of this nonlinearity through steady state numerical solution of the full system master equation. The parameters input into the master equation were measured through independent spectroscopic and time domain measurements leaving no free parameters in the simulation. The Jaynes-Cummings Hamiltonian used for the master equation simulation included terms up to the fourth order Kerr-type nonlinearities. In the low power limit, the master equation solution agreed almost exactly with data. I found good qualitative agreement with data in the large power limit. For better quantitative agreement at higher powers, perturbative corrections, of order higher than four, need to be taken into account in calculating the eigenvalues of the Hamiltonian.

I also studied the nonlinear variation of $\bar{n}$ with P_{rf} using a steady-state solution of the semi-classical driven damped oscillator equation. The nonlinearity in this equation was found to be caused by the change in the resonance frequency with increasing power of the drive tone, which in turn was computed through an exact diagonalization of the Jaynes-Cummings Hamiltonian. I solved the nonlinear equation self-consistently for $\bar{n}$ and found very good agreement with the experimental data.

8.2.2 Autler-Townes effect in a dressed Jaynes-Cummings system

In Chapter 6, I also described my observation of a weak $n = 1$ photon peak that appeared in the qubit spectroscopy even in the absence of a coherent coupler tone driving the resonator. From the relative weights of the $n = 0$ and $n = 1$ photon peaks, I determined an average thermal population $n_{th} = 0.1$ of 5.47 GHz of microwave photons stored in the resonator. This corresponded to an effective temperature of 120 mK, presumably caused by stray radiation or improper thermalization of the device or an attenuator situated close to the device. In the presence of a strong coupler field and a weak probe field, I observed an Autler-Townes splitting of this thermal $n = 1$ photon peak. The size of the splitting increased linearly with the amplitude of the coupler tone. I explained this effect using an Autler-Townes mechanism involving a 'lambda' system formed by the $|\widetilde{g,1}\rangle$, $|\widetilde{e,0}\rangle$, $|\widetilde{e,1}\rangle$ levels of the dressed Jaynes-Cummings system. I also did numerical simulations of the steady state system-bath master equation with two qubit levels and up to ten resonator levels and found good agreement with the data.

While the Autler-Townes effect has previously been observed in superconducting qubits [46, 66], this was the first experimental observation of this effect involving both the photon number states in the resonator and the states of the transmon. A detailed account of this work was presented in [53].

8.3 Summary of T_1 and Rabi coupling measurements

In Chapter 7, I presented T_1 and Rabi oscillation measurements of transmons coupled to lumped-element resonators. The key result of these measurements was the realization that my early transmons (LEv5-7, LEv5-ZK9, LEv5-15) were strongly coupled to the $50\,\Omega$ dissipative environment of the input/output coplanar waveguide transmission line of the device. This strong coupling caused enhanced spontaneous emission and resulted in short lifetimes $T_1 \sim 1\mu$s for these transmons. This coupling strength was characterized by the quantity df_{Rabi}/dV, which I called the Rabi coupling in this thesis.

In Chapter 7, I also presented my study of the transmon-resonator system through circuit analytical methods, as well as through microwave simulations of the device geometries in Microwave Office. The goal of these simulations was to develop designs with reduced Rabi coupling, and thereby improve the lifetime. From the circuit analysis, I found that the Rabi coupling could be decreased by increasing the resonator frequency, decreasing the resonator coupling to the transmission line κ, and lowering the transmon-resonator coupling strength g.

Based on this analysis, I developed a new design that I termed LEv6. In going from design LEv5 to LEv6, I made the following changes. (i) I increased the resonator frequency to 7 GHz. (ii) I lowered the coupling between the resonator and the transmission line to $\kappa/2\pi = 120\,$kHz. (iii) I also lowered the transmon-resonator coupling to $g/2\pi \sim 30\,$MHz. Measurements of the LEv6 transmons showed that the Rabi coupling was reduced by a factor of nearly 20 relative to that of devices LEv5.

Based on Rabi coupling, the predicted $T_1 \sim 0.5\,\mathrm{ms}$ was very long, at about $2\,\mathrm{GHz}$ away from the resonance.

However, to my surprise, the relaxation times of the LEv6 devices were not significantly higher than those of LEv5. Moreover, the measured T_1's for the LEv6 devices were much shorter than what would be expected from the lower Rabi coupling to the CPW. This meant that the LEv6 design was not limited by strong coupling to the $50\,\Omega$ transmission line. Instead the short lifetimes also indicated the presence of another strong channel for relaxation.

One likely candidate was surface and interface dielectric loss [32]. This conjecture was supported by the internal quality factors measured for my resonators ($Q_i \sim 150,000$). Microwave Office simulations with a dielectric loss $\tan\delta = 1/Q_i$ in the substrate showed good agreement with the measured T_1 values, supporting the conjecture that dielectric loss is the dominant mechanism. However, if the loss were in the bulk of the substrate, it would lead to 3D transmons having similarly short lifetimes, which was not the case [40, 41]. This makes surface dielectric loss the more plausible mechanism.

8.4 Future work

Based on my results, it would be interesting in the future to examine a few areas to try to improve the lifetimes of transmons coupled to lumped-element resonators.

While it was encouraging that the LEv6 design was not limited by Rabi coupling to the transmission line, they must have been limited by some other source of

dissipation. Microwave Office and circuit analytic simulations suggested that surface dielectric loss may have been the cause. To reduce dielectric loss, other groups [37, 38] have reduced the fill factor of the surface oxide layers by increasing the physical dimensions of their interdigital capacitor components. My Al resonators have shown poor intrinsic quality factors of $Q_i \sim 200,000$. This is quite typical for conventionally deposited resonators, but would imply that a transmon with comparable size would be limited to a $T_1 \approx Q_i/\omega \simeq 6\,\mu$s. This is close to what I observed for my transmon T_1s. Therefore I recommend substantially widening the gap between the fingers of the interdigital capacitor of the resonator, and increasing their width, to reduce the fill -factor of the surface oxide. This change was found to improve the lifetimes of transmon devices with interdigital shunt capacitors by other groups [37, 38].

Another interesting question is to simulate surface oxide loss in 3D-transmons to see if this is consistent with my 2D results. Such a 2D to 3D comparison might yield insight into how to improve both the 2D and 3D transmons.

One method I employed to lower the Rabi coupling involved lowering the coupling of the resonator to the transmission line. However, this also makes the read-out slower, which is not desirable. To have a fast read-out, one method that could be employed is to use a tunable coupling for the resonator [107].

Finally I note that some of my devices showed two-level fluctuations in their properties (ω_{ge}, T_1, Rabi oscillations *etc.*) on the time-scale of minutes to hours. Eliminating such fluctuations remains a key challenge.

Appendix A

Appendix-A

A.1 From Kirchhoff's circuit laws to the circuit Hamiltonian - a general recipe

In this section, I shall delineate the general recipe for arriving at the Hamiltonian of a non-dissipative circuit. This has been discussed in various references such as [71, 68].

1. A network consisting of two-terminal passive and active elements can be divided into *branches* and *nodes*, with each branch consisting of one or more elements in series and each node having two or more concurrent branches. Ideal voltage sources are replaced by capacitors and current sources by inductors initially. If the original circuit can be simplified using equivalent combinations of elements, start with the simplified version of the circuit.

2. We can assign a *branch* voltage v_b and current i_b for each branch. The *orientation* for the branch is based on the sign convention shown in Fig. A.1, where a voltage drop is along the direction of current in the branch. Note that since voltages and currents add and subtract algebraically, it is important to be consistent in the use of the sign-convention. From the definition of the branch voltage and current, we can define branch flux and charge according to

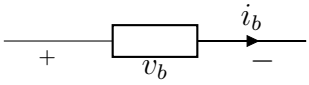

Figure A.1: A branch of an electrical circuit showing the current and voltage sign-convention

$$\Phi_b(t) = \int_{-\infty}^{t} v_b(\tau)\mathrm{d}\tau \tag{A.1}$$

$$Q_b(t) = \int_{-\infty}^{t} i_b(\tau)\mathrm{d}\tau \tag{A.2}$$

We also know that the branch voltages and currents must satisfy the constraints imposed by Kirchhoff's current and voltage laws – that the algebraic sum of the branch voltages around a loop should be zero, and the algebraic sum of the currents arriving at a node must be zero. Written in terms of the branch fluxes and charges, the integral form of Kirchhoff's circuit laws reads

$$\sum_{\text{all } b \text{ around loop } l} \Phi_b = \tilde{\Phi}_l = constant \tag{A.3}$$

$$\sum_{\text{all } b \text{ meeting at node } n} Q_n = \tilde{Q}_n = constant \tag{A.4}$$

Therefore the branch variables are not independent variables. This precludes their direct use in a Hamiltonian formulation. This brings us to the requirement of *node* variables. At this point, it is also useful to note that while the branch voltages and currents are independent of the topology of the circuit, node variables depend on the choice of a reference point, much like the freedom in choice of gauge in electrodynamics.

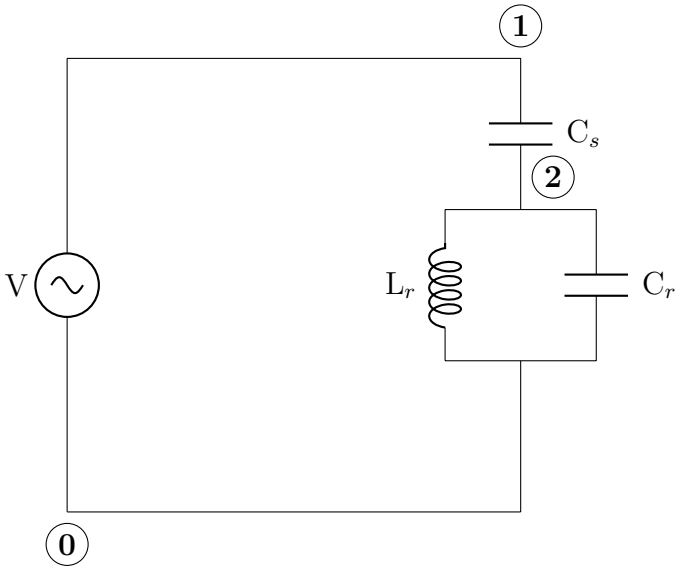

Figure A.2: Driven LC resonator circuit

3. The first step in defining node variables is to choose a node as the reference or *ground* node. In Fig. A.2 we choose the node 0 as the ground node.

4. Then we define a *spanning tree* (T) for the given network. For the circuit in Fig. A.2, a choice of spanning tree is shown in red in Fig. A.3a. A spanning tree is a subnetwork that includes all the nodes and has a unique path that connects every node to the ground node. The requirement of the unique path also implies that there are no *loops* in a spanning tree. Choosing a spanning tree (T) for a circuit divides the circuit into two sets of branches - those belonging to T and those belonging to the complement C. By definition, adding any branch belonging to C to T forms a loop.

5. Given the branch voltages for all the branches in the circuit according to the

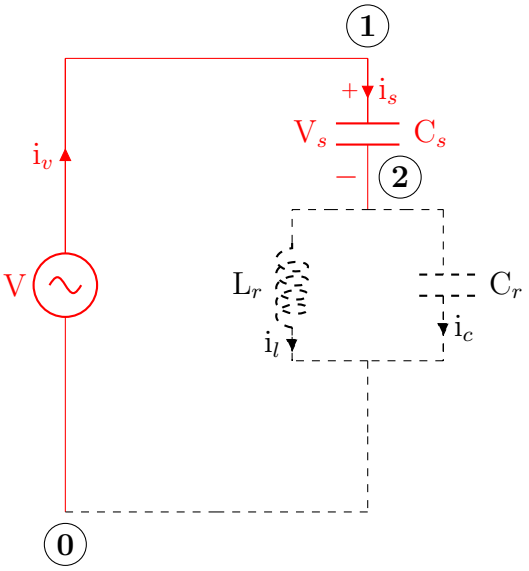

(a)

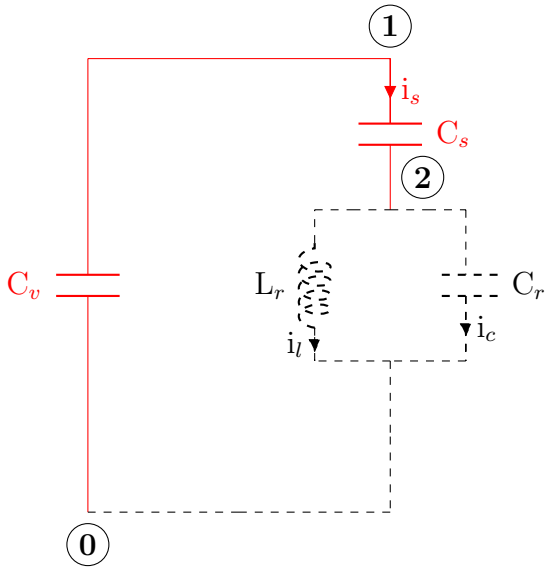

(b)

Figure A.3: (a) Spanning tree of the driven LC resonator circuit. (b) Spanning tree with battery replaced by capacitor C_v

sign convention mentioned earlier, and the fact that the ground node is assigned a zero voltage, we can now iteratively define the node-voltages for every node in the spanning tree. By noting that the branch voltage is the algebraic difference of the constituent node voltages, we arrive at the definition for the voltage of node i

$$V_i = \sum_{b \in \mathbf{T}} S_{ib} v_b \tag{A.5}$$

where the summation is over all the branches that lie along the path from the ground node to the node i. S_{ib} encodes the sign-convention according to

$$S_{ib} = \begin{cases} +1 & \text{if } b \text{ is traversed along increasing voltage} \\ 0 & \text{if } b \notin \mathbf{T} \\ -1 & \text{if } b \text{ is traversed along decreasing voltage} \end{cases} \tag{A.6}$$

6. Having defined the node voltages, we can now define the *node-fluxes* as

$$\phi_i = \int_{-\infty}^{t} V_i(\tau) \mathrm{d}\tau \tag{A.7}$$

$$= \sum_{b \in \mathbf{T}} S_{ib} \int_{-\infty}^{t} v_b(\tau)\, \mathrm{d}\tau \tag{A.8}$$

$$= \sum_{b \in \mathbf{T}} S_{ib} \Phi_b \tag{A.9}$$

where the summation is over all the branches that lie along the path from the ground node to the node i. An important subtlety is worth noting in this context. If the circuit has loops, and a static external flux ($\tilde{\Phi}_{l(b)}$) is threading the loop l formed by adding the branch $b \in \mathbf{C}$, this must be included while calculating the branch fluxes.

$$\Phi_{b\in\mathbf{T}} = \phi_i - \phi_j \tag{A.10}$$

$$\Phi_{b\in\mathbf{C}} = \phi_i - \phi_j + \tilde{\Phi}_{l(b)}. \tag{A.11}$$

where i and j form the end nodes for the branch b. Note that since there are no loops in a spanning tree, and since the node-fluxes have been defined for the spanning tree, they form a set of independent variables by design.

7. To arrive at the equations of motion for the given circuit, for each node i apply Kirchhoff's current equations. In other words, the algebraic sum of the currents along all the branches emanating from that node should equal zero. Note that we have to include *all* branches, those belonging to both T and C. We have to include any external static fluxes that might be threading the loops formed when including branches in C. Specifically for circuits comprising only capacitive and inductive elements, for every node i we can write

$$\sum_{j\neq i} \left\{ C_{ij}(\dot{V}_i - \dot{V}_j) + \frac{(\phi_i - \phi_j)}{L_{ij}} \right\} = 0 \tag{A.12}$$

or, equivalently

$$\sum_{j\neq i} \left\{ C_{ij}(\ddot{\phi}_i - \ddot{\phi}_j) + \frac{(\phi_i - \phi_j)}{L_{ij}} \right\} = 0 \tag{A.13}$$

where C_{ij} and L_{ij} are the capacitance (if any) and inductance (if any) connecting node i to node j.

8. We then construct a Lagrangian, $\mathcal{L}[\phi_i, \dot{\phi}_i]$, such that the resultant Euler-Lagrange equations given by

$$\frac{d}{dt}\left(\frac{\partial \mathcal{L}}{\partial \dot{\phi}_i}\right) = \frac{\partial \mathcal{L}}{\partial \phi_i} \tag{A.14}$$

are equivalent to the above node-current equations. The node-fluxes ϕ_i are chosen as the *generalized coordinates* and the node-voltages, $V_i = \dot{\phi}_i$, play the role of the *generalized velocities*. In many cases, for a capacitive-inductive network, the Lagrangian can be easily written in the form

$$\mathcal{L} = \sum_{\substack{i,j \\ i \neq j}} \left\{ \frac{C_{ij}\left(\dot{\phi}_i - \dot{\phi}_j\right)^2}{4} - \frac{(\phi_i - \phi_j)^2}{4L_{ij}} \right\} \tag{A.15}$$

where the factor 4 in the denominator takes care of the double-counting due to swapping the indices i and j while summing up the terms. We again note that any static fluxes threading loops should be included in the lagrangian.It can be verified easily that the Euler-Lagrange equations applied to this lagrangian give rise to the correct Kirchhoff's current equations.

9. Having defined the Hamiltonian, we can now define the canonical momenta, or in this context the *node-charges*, according to

$$Q_i \equiv \frac{\partial \mathcal{L}}{\partial \dot{\phi}_i}. \tag{A.16}$$

10. We then make a Legendre transformation to get the Hamiltonian

$$\mathcal{H}(\phi, Q) = \sum_i Q_i \dot{\phi}_i - \mathcal{L} \tag{A.17}$$

and the canonical Hamilton's equations of motion are given by

$$\dot{\phi}_i = \frac{\partial \mathcal{H}}{\partial Q_i} \equiv \{\phi, \mathcal{H}\}_{PB} \tag{A.18}$$

$$\dot{Q}_i = -\frac{\partial \mathcal{H}}{\partial \phi_i} \equiv \{Q_i, \mathcal{H}\}_{PB} \tag{A.19}$$

where the right hand side is the Poisson bracket representation of the equations. The canonical variables satisfy the canonical conditions

$$\{\phi_i, Q_j\}_{PB} = \delta_{ij} \tag{A.20}$$

where δ_{ij} is the Kronecker delta.

11. Now, we are ready to quantize the circuit. We replace the classical variables ϕ_i and Q_i with quantum operators $\hat{\phi}_i$ and $\hat{Q}_i$ respectively apply Dirac's correspondence principle and impose the commutation relations

$$\left[\hat{\phi}_i, \hat{Q}_j\right] = i\hbar\delta_{ij}. \tag{A.21}$$

The Hamiltonian can then be written in terms of the operators after employing techniques like symmetrization etc. This method is illustrated in detail in the following section with the example of a driven oscillator.

Appendix B

Appendix-B

B.1 Dispersive transformation of the driven Jaynes-Cummings Hamiltonian

In this section I am going to consider the driven Jaynes-Cummings Hamiltonian

$$H = \hbar\omega_r \left(a^\dagger a + \frac{1}{2}\right) + \frac{\hbar\omega_{ge}}{2}\sigma_z + \hbar g_{ge}(a\sigma^+ + a^\dagger\sigma^-) - \frac{\hbar\Omega_r}{2}(ae^{i\omega_c t} + a^\dagger e^{-i\omega_c t}) - \frac{\hbar\Omega_p}{2}(\sigma^- e^{i\omega_p t} + \sigma^+ e^{-i\omega_p t}) \tag{B.1}$$

$$H = H_{JC} + H_d \tag{B.2}$$

where H_{JC} is the undriven part of the Hamiltonian and H_d contains the driving terms. That is

$$H_{JC} = \hbar\omega_r \left(a^\dagger a + \frac{1}{2}\right) + \frac{\hbar\omega_{ge}}{2}\sigma_z + \hbar g_{ge}(a\sigma^+ + a^\dagger\sigma^-) \tag{B.3}$$

$$H_d = -\frac{\hbar\Omega_r}{2}(ae^{i\omega_c t} + a^\dagger e^{-i\omega_c t}) - \frac{\hbar\Omega_p}{2}(\sigma^- e^{i\omega_p t} + \sigma^+ e^{-i\omega_p t}. \tag{B.4}$$

In the following section I make a unitary transformation of H in Eq. B.1 using

$$\mathcal{T} = \exp\left\{\frac{g_{ge}(a\sigma^+ - a^\dagger\sigma^-)}{\Delta}\right\}. \tag{B.5}$$

B.1.1 Dispersive transformation of the undriven Jaynes-Cummings Hamiltonian

I consider first the undriven part of the Hamiltonian given by Eq. B.1. To compute $\mathcal{T}H_{JC}\mathcal{T}^\dagger$, I make use of the Baker-Campbell-Hausdorff formula [83].

$$e^Y X e^{-Y} = X + [Y,X] + \frac{1}{2!}[Y,[Y,X]] + \frac{1}{3!}[Y,[Y,[Y,X]]] + \ldots \tag{B.6}$$

For convenience, let us define $\Lambda \equiv \lambda(a\sigma^+ - a^\dagger\sigma^-)$ and $\lambda = g_{ge}/\Delta$.

$$\mathcal{T} = e^\Lambda. \tag{B.7}$$

In the dispersive limit $g_{ge}/\Delta \ll 1$, we can ignore terms higher than second order in $\lambda = g_{ge}/\Delta$. To second order in λ the relevant commutators that need to be computed are

$$[\Lambda, a^\dagger a] = \lambda\{a\sigma^+ + a^\dagger\sigma^-\} \tag{B.8}$$

$$[\Lambda,[\Lambda, a^\dagger a]] = \lambda^2\{2(a^\dagger a)\sigma_z + \sigma_z + 1\} \tag{B.9}$$

$$[\Lambda, \sigma_z] = \lambda\{-2(a\sigma^+ + a^\dagger\sigma^-)\} \tag{B.10}$$

$$[\Lambda,[\Lambda,\sigma_z]] = \lambda^2\{-4(a^\dagger a)\sigma_z - 2\sigma_z - 2\} \tag{B.11}$$

$$[\Lambda, a\sigma^+ + a^\dagger\sigma^-] = \lambda\{2(a^\dagger a)\sigma_z + \sigma_z + 1\} \tag{B.12}$$

$$\begin{aligned}[\Lambda,[\Lambda, a\sigma^+ + a^\dagger\sigma^-]] = \lambda^2\{&2(a\sigma^+ + a^\dagger\sigma^-)\sigma_z \\ &- 4(a^\dagger a)(a\sigma^+ + a^\dagger\sigma^-) - 2(a\sigma^+ + a^\dagger\sigma^-)\}.\end{aligned} \tag{B.13}$$

Using these commutators, I evaluate the transformations of the terms in H_{JC}

and find

$$e^{\Lambda}(\hbar\omega_r a^\dagger a)e^{-\Lambda} = \hbar\omega_r\{a^\dagger a + \lambda(a\sigma^+ + a^\dagger\sigma^-) + \frac{\lambda^2}{2}(2(a^\dagger a)\sigma_z + \sigma_z + 1)\} \tag{B.14}$$

$$e^{\Lambda}\frac{\hbar\omega_{ge}\sigma_z}{2}e^{-\Lambda} = \hbar\omega_{ge}\{\frac{\sigma_z}{2} - \lambda(a\sigma^+ + a^\dagger\sigma^-) - \lambda^2\{(a^\dagger a)\sigma_z + \frac{\sigma_z}{2} + \frac{1}{2}\}\} \tag{B.15}$$

For the coupling term, I do a perturbation expansion to first order in λ, since the prefactor of g_{ge} multiplying that term provides an extra factor of λ , to get

$$e^{\Lambda}\hbar g_{ge}(a\sigma^+ + a^\dagger\sigma^-)e^{-\Lambda} = \hbar g_{ge}\{a\sigma^+ + a^\dagger\sigma^- + \lambda(2(a^\dagger a)\sigma_z + \sigma_z + 1)\} \tag{B.16}$$

$$= \hbar\Delta\lambda\{a\sigma^+ + a^\dagger\sigma^- + \lambda(2(a^\dagger a)\sigma_z + \sigma_z + 1)\}. \tag{B.17}$$

Adding all the above terms, the transformed Hamiltonian to second order in λ becomes

$$\mathcal{T}H_{JC}\mathcal{T}^\dagger \approx H_{JC}^{(2)} = \hbar\omega_r(a^\dagger a) + \frac{\hbar\tilde{\omega}_{ge}\sigma_z}{2} + \hbar\chi(a^\dagger a)\sigma_z \tag{B.18}$$

where $\chi = g_{ge}^2/\Delta$ is the dispersive shift of the resonator frequency, and $\tilde{\omega}_{ge} = \omega_{ge} + \chi$ is the Lamb-shifted qubit frequency.

B.1.2 Transformation of the driving terms

To see the effect of this transformation on the driving terms, I have to evaluate terms of the form $\mathcal{T}X\mathcal{T}^\dagger$ where $X = \{a, a^\dagger, \sigma^+, \sigma^-\}$. Using the Baker-Campbell-Hausdorff formula, the relevant terms in the expansion look like

$$\mathcal{T}X\mathcal{T}^\dagger = e^{\Lambda}Xe^{-\Lambda} = X + [\Lambda, X] + \frac{1}{2!}[\Lambda, [\Lambda, X]] + \ldots \tag{B.19}$$

The relevant commutators up to second order in λ are

$$[\Lambda, a] = \lambda\sigma^- \tag{B.20}$$

$$[\Lambda, [\Lambda, a]] = \lambda^2 a\sigma_z \tag{B.21}$$

$$[\Lambda, \sigma^+] = \lambda a^\dagger \sigma_z \tag{B.22}$$

$$[\Lambda, [\Lambda, \sigma^+]] = \lambda^2\{\sigma_z\sigma^+ - 2(a^\dagger a)\sigma^+ - 2\sigma^+ - 2(a^\dagger)^2\sigma^-\} \tag{B.23}$$

$$[\Lambda, [\Lambda, \sigma^-]] = \lambda^2\{\sigma_z\sigma^- - 2(a^\dagger a)\sigma^- - 2a^2\sigma^-\}. \tag{B.24}$$

We can now write the transformed driving terms to second order in λ as:

$$e^\Lambda(ae^{i\omega_c t} + a^\dagger e^{-i\omega_c t})e^{-\Lambda} = (1 + \frac{\lambda^2}{2}\sigma_z)\{ae^{i\omega_c t} + a^\dagger e^{-i\omega_c t}\} + \lambda(\sigma^- e^{i\omega_c t} + \sigma^+ e^{i\omega_c t}) \tag{B.25}$$

$$\begin{aligned} e^\Lambda(\sigma^- e^{i\omega_p t} + \sigma^+ e^{-i\omega_p t})e^{-\Lambda} = &(1 + \frac{\lambda^2}{2}(\sigma_z - 2a^\dagger a))\{\sigma^- e^{i\omega_p t} + \sigma^+ e^{-i\omega_p t}\} \\ &+ \lambda\sigma_z(ae^{i\omega_p t} + a^\dagger e^{-i\omega_p t}) - \lambda^2\{(a^\dagger)^2\sigma^- + \sigma^+\}e^{-i\omega_p t} \\ &- \lambda^2 a^2\sigma^+ e^{i\omega_p t}. \end{aligned} \tag{B.26}$$

In the limit of weak driving $\{\omega_r, \omega_{ge}\} \gg \Omega_c, \Omega_p$, when the qubit and resonator frequencies are far detuned and for $\omega_c \approx \omega_r$ and $\omega_p \approx \omega_{ge}$, terms such as $ae^{i\omega_p t}, a^\dagger e^{-i\omega_p t} and \sigma^\pm e^{\mp i\omega_c t}$, where the qubit drive is driving the resonator and *vice-versa* can be neglected in the RWA. After the RWA, we are left with

$$e^\Lambda(ae^{i\omega_c t} + a^\dagger e^{-i\omega_c t})e^{-\Lambda} = (1 + \frac{\lambda^2}{2}\sigma_z)\{ae^{i\omega_c t} + a^\dagger e^{-i\omega_c t}\} \tag{B.27}$$

$$e^\Lambda(\sigma^- e^{i\omega_p t} + \sigma^+ e^{-i\omega_p t})e^{-\Lambda} = (1 + \frac{\lambda^2}{2}(\sigma_z - 2a^\dagger a))\{\sigma^- e^{i\omega_p t} + \sigma^+ e^{-i\omega_p t}\}. \tag{B.28}$$

When $\lambda \ll 1$ we can neglect the second order terms too. In other words, to a very good approximation,

$$\mathcal{T}(H_d)\mathcal{T}^\dagger \approx H_d \tag{B.29}$$

The full Jaynes-Cummings Hamiltonian can now be written in the dispersive approximation to second order in $\lambda = g_{ge}/\Delta$ as

$$\tilde{H}^{(2)} = \tilde{H}^{(2)}_{JC} + H_d \tag{B.30}$$

$$= \hbar\omega_r a^\dagger a + \frac{\hbar\tilde{\omega}_{ge}\sigma_z}{2} + \hbar\chi(a^\dagger a)\sigma_z - \frac{\hbar\Omega_r}{2}(ae^{i\omega_c t} + a^\dagger e^{-i\omega_c t}) - \frac{\hbar\Omega_p}{2}(\sigma^- e^{i\omega_p t} + \sigma^+ e^{-i\omega_p t}). \tag{B.31}$$

B.1.3 Transforming into the rotating frame of the drive fields

In this section I make a unitary transformation of the driven Jaynes-Cummings Hamiltonian to remove the time dependence of the driving terms. Having a time-independent Hamiltonian is convenient in studying the steady-state dynamics of the system numerically. To go into the interaction picture of the drive fields, I use the unitary transformation given by

$$U = e^{i\omega_c(a^\dagger a)t + i\frac{\omega_p\sigma_z}{2}t} \tag{B.32}$$

The transformed Hamiltonian can then be written using

$$H_I = UHU^\dagger + i\hbar\dot{U}U^\dagger. \tag{B.33}$$

To evaluate the first term, I note that

$$UaU^\dagger = ae^{-i\omega_c t} \tag{B.34}$$

$$U\sigma^- U^\dagger = \sigma^- e^{-i\omega_p t} \tag{B.35}$$

The second term can be evaluated directly as

$$i\hbar\dot{U}U^{\dagger} = i\hbar\left(i\omega_c(a^{\dagger}a) + i\frac{\omega_p\sigma_z}{2}\right)UU^{\dagger} \tag{B.36}$$

$$= -\hbar\left(\omega_c(a^{\dagger}a) + \frac{\omega_p\sigma_z}{2}\right). \tag{B.37}$$

Using these results, the interaction picture Hamiltonian can be written as

$$H_I = \hbar\omega_r(a^{\dagger}a) + \frac{\hbar\tilde{\omega}_{ge}}{2} + \hbar\chi(a^{\dagger}a)\sigma_z - \frac{\hbar\Omega_c}{2}(a + a^{\dagger}) - \frac{\hbar\Omega_p}{2}(\sigma^- + \sigma^+)$$
$$-\hbar\left(\omega_c(a^{\dagger}a) + \frac{\omega_p\sigma_z}{2}\right) \tag{B.38}$$

$$= \hbar\tilde{\Delta}_c a^{\dagger}a + \frac{\hbar\tilde{\Delta}_p\sigma_z}{2} + \hbar\chi(a^{\dagger}a)\sigma_z - \frac{\hbar\Omega_c}{2}(a + a^{\dagger}) - \frac{\hbar\Omega_p}{2}(\sigma^- + \sigma^+) \tag{B.39}$$

where $\tilde{\Delta}_c \equiv \omega_r - \omega_c$ is the detuning of the coupler tone from the resonator frequency and $\tilde{\Delta}_p \equiv \tilde{\omega}_{ge} - \omega_p$ is the detuning of the probe tone from the qubit frequency. The Hamiltonian given by Eq. B.39 is independent of time.

Appendix C

Appendix C

C.1 Classical driven damped harmonic oscillator

Here I review the classical driven damped harmonic oscillator. However, unlike the standard classical treatment, I take an approach that is the classical analogue of Dirac's quantization recipe using the ladder operators.

To begin, the general equation of motion for a driven, dissipative, simple harmonic oscillator would be

$$m\ddot{x} + m\kappa\dot{x} + m\omega_0^2 x = F(t) \tag{C.1}$$

where m is the mass, κ is the damping coefficient, and $F(t)$ is the time-dependent force. Noting that the momentum $p = m\dot{x}$ classically, we get a set of first order equations in position x and momentum p

$$\dot{p} = -m\omega_0^2 x - \kappa p + F(t) \tag{C.2}$$

$$\dot{x} = \frac{p}{m}. \tag{C.3}$$

I now define a complex quantity α and its complex conjugate α^* as

$$\alpha = \sqrt{\frac{m\omega_0}{2\hbar}}\left(x + i\frac{p}{m\omega_0}\right) \tag{C.4}$$

$$\alpha^* = \sqrt{\frac{m\omega_0}{2\hbar}}\left(x - i\frac{p}{m\omega_0}\right) \tag{C.5}$$

where $\hbar$ is just a number and has no relation to the Planck's constant in this context. In terms of α the equation of motion will be

$$\dot{\alpha} = -i\omega_0\alpha - \frac{\kappa}{2}\alpha + \frac{\kappa}{2}\alpha^* + \frac{iF(t)}{\sqrt{2\hbar m\omega_0}} \tag{C.6}$$

$$\dot{\alpha}^* = i\omega_0\alpha^* - \frac{\kappa}{2}\alpha^* + \frac{\kappa}{2}\alpha - \frac{iF(t)}{\sqrt{2\hbar m\omega_0}}. \tag{C.7}$$

So far I have not specified the exact time-dependence of the force. Since we can always write a real force as a sum of sinusoidal terms, for simplicity, I will assume

$$F(t) = \sqrt{2\hbar m\omega_0}\ \ 2f_0\cos(\omega_d t). \tag{C.8}$$

This gives an equation of motion

$$\dot{\alpha} = -i\omega_0\alpha - \frac{\kappa}{2}\alpha + \frac{\kappa}{2}\alpha^* + i\ 2f_0\cos(\omega_d t) \tag{C.9}$$

where I have chosen the coefficient for algebraic convenience.

I now make a change of variable from α to β, where

$$\alpha(t) = \beta(t)e^{-i\omega_d t}. \tag{C.10}$$

Under this change, the equation of motion becomes

$$\dot{\beta} = -i(\omega_0 - \omega_d)\beta - \frac{\kappa}{2}\beta + \frac{\kappa}{2}\alpha^* e^{i2\omega_d t} + if_0(1 + e^{i2\omega_d t}). \tag{C.11}$$

If $\omega_d \approx \omega_0$ for driving close to resonance, the first term in the above equation is small and the variation in β is typically slow in time. On that time scale, the fast counter-rotating terms with frequency $2\omega_d$ average to nearly zero, so they can be neglected. This is the classical origin of the rotating wave approximation (RWA) discussed in 3.2.1. Under this approximation, the equation of motion becomes

$$\dot{\beta} = -i(\omega_0 - \omega_d)\beta - \frac{\kappa}{2}\beta + if_0 \tag{C.12}$$

which, upon transforming back to α becomes

$$\dot{\alpha} = -i\omega_0\alpha - \frac{\kappa}{2}\alpha + if_0e^{-i\omega_d t}. \tag{C.13}$$

We are primarily interested in the steady-state solution of C.13. In the steady state, we have $\dot{\alpha_{ss}} = 0$. Therefore

$$\alpha_{ss} = \frac{f_0e^{-i\omega_d t}}{\omega_0 - \omega_d - \frac{i}{2}\kappa} \tag{C.14}$$

C.1.1 Energy of the oscillator

The energy of the oscillator is given by

$$E = \frac{p^2}{2m} + \frac{1}{2}m\omega_0^2x^2. \tag{C.15}$$

In terms of the variable α, this can be written as

$$E = \hbar\omega_0|\alpha|^2. \tag{C.16}$$

The energy of the oscillator in steady state is thus:

$$E_{ss} = \hbar\omega_0|\alpha|^2 \tag{C.17}$$

$$E_{ss} = \frac{\hbar\omega_0 f_0^2}{(\omega_0 - \omega_d)^2 + \left(\frac{\kappa}{2}\right)^2}. \tag{C.18}$$

Away from steady state, the rate of increase of the energy of the oscillator has to be balanced by the power input and the power dissipated, *i.e.*

$$\frac{\mathrm{d}E}{\mathrm{d}t} = P_{abs} - P_{diss} \tag{C.19}$$

$$= \hbar\omega_0\frac{\mathrm{d}|\alpha|^2}{\mathrm{d}t} \tag{C.20}$$

$$= \hbar\omega_0(\dot{\alpha}\alpha^* + \alpha\dot{\alpha}^*). \tag{C.21}$$

Using the equations of motion for α and α^*, I get

$$\frac{\mathrm{d}E}{\mathrm{d}t} = \hbar\omega_0 \left\{ i\left(\alpha^* f_0 e^{-i\omega_d t} - \alpha f_0 e^{i\omega_d t}\right) - \kappa|\alpha|^2 \right\} \tag{C.22}$$

$$= \underbrace{2\hbar\omega_0 \,\mathrm{Im}\left(\alpha f_0 e^{i\omega_d t}\right)}_{P_{abs}} \quad - \quad \underbrace{\hbar\omega_0\kappa|\alpha|^2)}_{P_{diss}}. \tag{C.23}$$

We identify the first term with the power absorbed or input and the second term with the power dissipated. In steady state, when the energy of the oscillator is constant in time, we have

$$P_{abs}^{ss} = P_{diss}^{ss} = \quad \hbar\omega_0\kappa|\alpha_{ss}|^2 \tag{C.24}$$

$$= \frac{\hbar\omega_0\kappa f_0^2}{(\omega_0 - \omega_d)^2 + \left(\frac{\kappa}{2}\right)^2} \tag{C.25}$$

$$= \kappa E_{ss}. \tag{C.26}$$

When the driving force is on resonance with the oscillator frequency, using $\omega_d = \omega_0$ in Eq.C.25 I find

$$P_{abs}^{ss} = \frac{\hbar\omega_0 f_0^2}{\kappa/4}. \tag{C.27}$$

Rearranging this equation, I get

$$f_0 = \sqrt{\frac{P_{abs}^{ss}\kappa}{4\hbar\omega_0}} \tag{C.28}$$

and finally defining $Q = \omega_0/\kappa$, I get

$$f_0 = \sqrt{\frac{P_{abs}^{ss}}{4\hbar Q}}. \tag{C.29}$$

C.2 Thermal photon distribution

Consider a single mode oscillator of frequency ω_0. The Hamiltonian, ignoring the zero-point energy is given by

$$H = \hbar\omega_0 a^\dagger a \tag{C.30}$$

When the oscillator is in thermal equilibrium with a bath at temperature T, the probability that the n^{th} energy level is occupied can be found from the Gibbs distribution law and is given by

$$w_n^{th} = \frac{e^{-\beta n\hbar\omega_0}}{Z} \tag{C.31}$$

where Z is the normalization constant chosen to give

$$\sum_{n=0}^{\infty} w_n^{th} = 1. \tag{C.32}$$

This gives us

$$Z = \sum_{n=0}^{\infty} e^{-\beta n\hbar\omega_0} \tag{C.33}$$

$$= \frac{1}{1 - e^{-\beta\hbar\omega_0}} \tag{C.34}$$

and

$$w_n^{th} = e^{-\beta n\hbar\omega_0}(1 - e^{-\beta\hbar\omega_0}). \tag{C.35}$$

The average number of photons in equilibrium can be determined by

$$\bar{n} = \sum_{n=0}^{\infty} n w_n^{th} \tag{C.36}$$

$$= \sum_{n=0}^{\infty} \left\{ n e^{-\beta n\hbar\omega_0} - n e^{-\beta(n+1)\hbar\omega_0} \right\}. \tag{C.37}$$

We make the substitution $e^{-\beta\hbar\omega_0} = x$ to simplify the above expression

$$= \sum_{n=0}^{\infty} \left\{ nx^n - nx^{n+1} \right\} \tag{C.38}$$

$$= (x - x^2) \sum_{n=0}^{\infty} nx^{n-1} \tag{C.39}$$

$$= (x - x^2) \frac{\partial}{\partial x} \sum_{n=0}^{\infty} x^n \tag{C.40}$$

$$= (x - x^2) \frac{\partial}{\partial x} \left(\frac{1}{1-x} \right) \tag{C.41}$$

$$= \frac{x}{1-x}. \tag{C.42}$$

Substituting back for x, we have for the average number of photons in equilibrium

$$\bar{n} = \frac{1}{e^{\beta\hbar\omega_0} - 1}. \tag{C.43}$$

In terms of $\bar{n}$, the thermal photon distribution Eq. C.31 can then be written as

$$w_n^{th} = \frac{\bar{n}^n}{(\bar{n}+1)^{n+1}}. \tag{C.44}$$

C.3 Coherent states of a harmonic oscillator

C.3.1 Photon distribution in a coherent state

A coherent state [77] of a harmonic oscillator is an eigenstate of the annihilation operator a. Let $|\alpha\rangle$ be eigenket of this operator with eigenvalue $|\alpha\rangle$

$$a|\alpha\rangle = \alpha|\alpha\rangle. \tag{C.45}$$

A general ket of the oscillator can be written as a superposition of the energy eigenkets $|n\rangle$

$$|\alpha\rangle = \sum_{n=0}^{\infty} c_n |n\rangle. \tag{C.46}$$

Substituting this into the two sides of the eigenvalue equation, we have

$$a|\alpha\rangle = \sum_{n=0}^{\infty} c_{n+1}\sqrt{n+1}\,|n\rangle \tag{C.47}$$

$$\alpha|\alpha\rangle = \alpha \sum_{n=0}^{\infty} c_n |n\rangle \tag{C.48}$$

Equating the two we find a recursion relation for the coefficients c_n

$$c_{n+1}\sqrt{n+1} = \alpha c_n. \tag{C.49}$$

Solving the set of equations, we obtain the general coefficient c_n in terms of the coefficient c_0 as

$$c_n = \frac{\alpha^n c_0}{\sqrt{n!}}. \tag{C.50}$$

Further imposing the requirement that the state $|\alpha\rangle$ is normalized, we get

$$\langle\alpha|\alpha\rangle = \sum_{n=0}^{\infty} |c_n|^2 = 1 \tag{C.51}$$

$$= \sum_{n=0}^{\infty} \frac{|\alpha|^{2n}|c_0|^2}{n!} = 1 \tag{C.52}$$

$$= |c_0|^2 e^{|\alpha|^2} = 1 \tag{C.53}$$

giving us $|c_0|$ and thereby $|c_n|$

$$|c_0|^2 = e^{-|\alpha|^2} \tag{C.54}$$

$$|c_n|^2 = \frac{|\alpha|^{2n} e^{-|\alpha|^2}}{n!}. \tag{C.55}$$

Choosing the phase of alpha to be 1, we also have the coherent state $|\alpha\rangle$ given by

$$|\alpha\rangle = e^{-|\alpha|^2/2} \sum_{n=0}^{\infty} \frac{\alpha^n}{\sqrt{n!}} |n\rangle. \tag{C.56}$$

The average number of photons in the coherent state can be given by

$$\bar{n} = \langle\alpha|a^\dagger a|\alpha\rangle = |\alpha|^2 \tag{C.57}$$

In terms of $\bar{n}$ we have

$$|c_n|^2 = \frac{\bar{n}^n e^{-\bar{n}}}{n!} \tag{C.58}$$

$|c_n|^2$ is the probability of having n photons in the oscillator. This gives us the Poisson distribution of photons in a coherent state.

$$w_n^{coh} = \frac{\bar{n}^n e^{-\bar{n}}}{n!}. \tag{C.59}$$

C.3.2 The displacement operator

Consider the unitary operator

$$D(\alpha) = e^{\alpha a^\dagger - \alpha^* a}. \tag{C.60}$$

From the Baker-Campbell-Hausdorff formula, we can show that

$$D(\alpha) = e^{|\alpha|^2/2} e^{-\alpha^* a} e^{\alpha a^\dagger}. \tag{C.61}$$

From this, it is seen that the coherent state $|\alpha\rangle$ can be generated by transforming the vacuum $|0\rangle$ with the operator $D(\alpha)$

$$|\alpha\rangle = D(\alpha)|0\rangle = e^{-|\alpha|^2/2} \sum_{n=0}^{\infty} \frac{\alpha^n}{\sqrt{n!}} |n\rangle. \tag{C.62}$$

The operator $D(\alpha)$ is called the 'displacement' operator because of the transformation properties of the bosonic operators $a, a^\dagger$ under $D(\alpha)$

$$D^\dagger(\alpha) a D(\alpha) = a + \alpha \tag{C.63}$$

$$D^\dagger(\alpha) a^\dagger D(\alpha) = a^\dagger + \alpha^*. \tag{C.64}$$

Appendix D

Appendix D

D.1 T_1 for a cQED architecture using circuit analysis.

The diagram in Fig. D.1 represents a capacitive model for the transmon-resonator system coupled *capacitively* to a transmission line. It is important to note here that a complete model have to include a mutual inductive coupling of the resonator to the transmission line. For ease of analysis, I begin with this capacitive model. I then simplify this circuit by making a series of approximations, which I delineate below.

As a first step, the *external* circuit comprising the transmission line, represented by the capacitance C_t and inductance L_t and the external impedance Z_0 can be simplified, using a simple argument of symmetry, to the circuit in Fig. D.2. The only assumption made at this point is that the voltage source V is an *ideal* voltage source that has no internal resistance.

If I further invoke the assumption that the transmission line impedance, given by $Z_t = \sqrt{L_t/C_t}$, is well matched with the $Z_0 = 50\,\Omega$ of the input and output – an assumption that is valid for the coplanar waveguide transmission line in my devices – I can further reduce the circuit to that shown in Fig. D.3. This can be proven by the following simple calculation. For either half of the *external* circuit comprising the transmission line (L_t,C_t) and the dissipative environment Z_0 in Fig. D.1, I can write

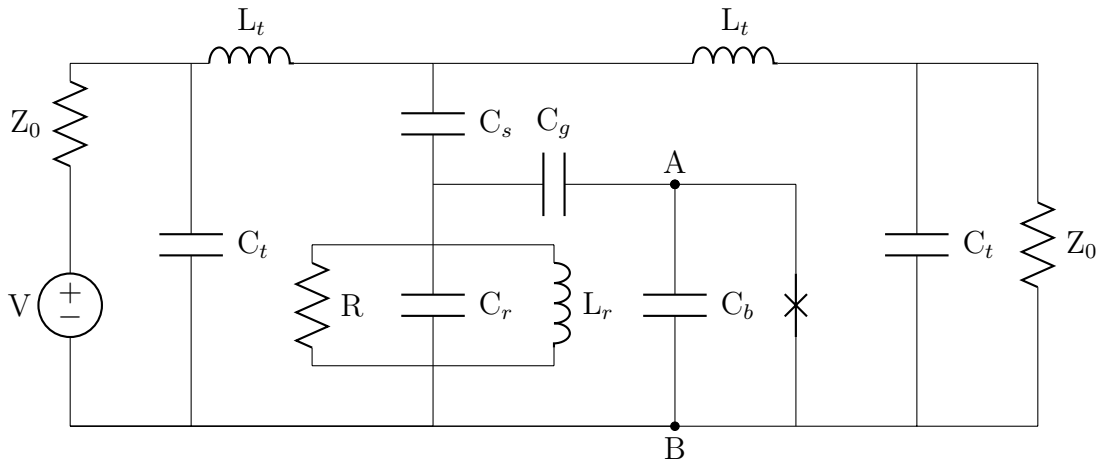

Figure D.1: Full circuit schematic for transmon-resonator cQED architecture

.

$$Z_t = \sqrt{\frac{L_t}{C_t}} = Z_0 = 50\Omega \tag{D.1}$$

$$\omega_t = \frac{1}{\sqrt{L_t C_t}} \gg \omega. \tag{D.2}$$

From these definitions, I can write the inductance and capacitance of the transmission line as,

$$L_t = Z_t/\omega_t \tag{D.3}$$

$$C_t = 1/\omega_t Z_t \tag{D.4}$$

and also

$$Z_{ext} = j\omega(L_t) + \frac{Z_0/(j\omega C_t)}{Z_0 + 1/(j\omega C_t)} \tag{D.5}$$

$$= j\omega(L_t) + \frac{Z_0}{j\omega C_t Z_0 + 1} \tag{D.6}$$

$$= j\frac{\omega}{\omega_t}Z_t + \frac{Z_0}{j\frac{\omega}{\omega_t}\frac{Z_0}{Z_t} + 1}. \tag{D.7}$$

Since $Z_t = Z_0$,

$$Z_{ext} = j\frac{\omega}{\omega_t}Z_0 + \frac{Z_0}{j\frac{\omega}{\omega_t} + 1} \tag{D.8}$$

$$\approx j\frac{\omega}{\omega_t}Z_0 + Z_0(1 - j\frac{\omega}{\omega_t}) \tag{D.9}$$

$$\approx Z_0. \tag{D.10}$$

Thus, from the above calculation we can replace the combination of transmission line and the external environmental impedance of Z_0 by a single resistor Z_0. This leads to a simplification of the circuit in figure D.1, to the one shown in Fig. D.3.

D.1.1 Exact expression for $1/\mathrm{Re}(Y)$

The analysis beyond this point starts with the circuit shown in Fig. D.3, with the goal of computing the equivalent admittance across the transmon, or equivalently, looking into the terminals A and B marked in the circuit diagram D.3

$$Z_{res} = \frac{j\omega L_r R}{R\left(1 - \frac{\omega^2}{\omega_0^2}\right) + j\omega L_r} \tag{D.11}$$

$$Z(\omega) = \frac{1}{j\omega C_g} + \frac{Z_{res}(Z_0/2 + 1/(j\omega C_s))}{Z_{res} + Z_0/2 + 1/(j\omega C_s)}. \tag{D.12}$$

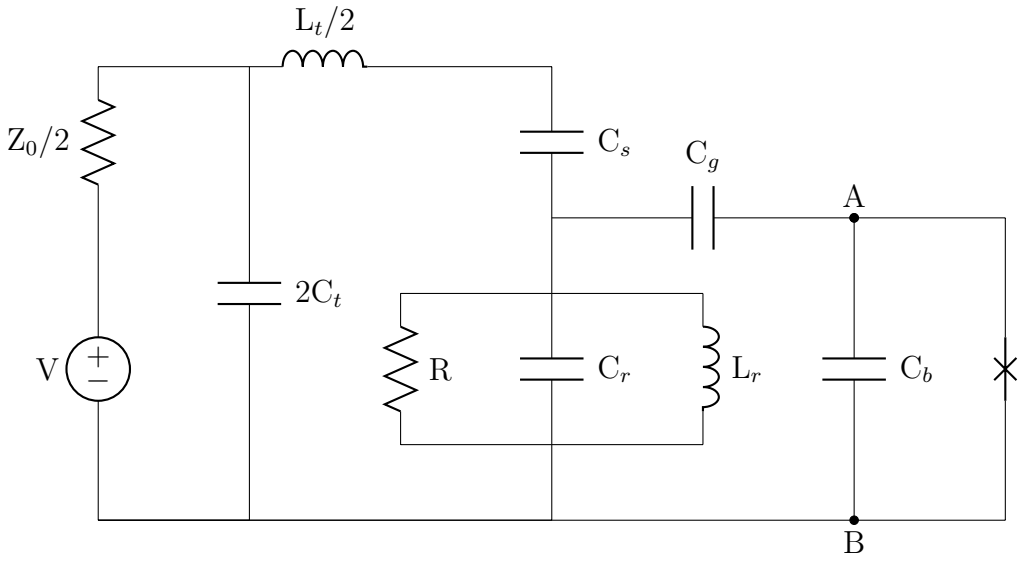

Figure D.2: Partly simplified external circuit schematic for transmon-resonator cQED architecture. The input and output transmission lines can be replaced by the effective external circuit shown here.

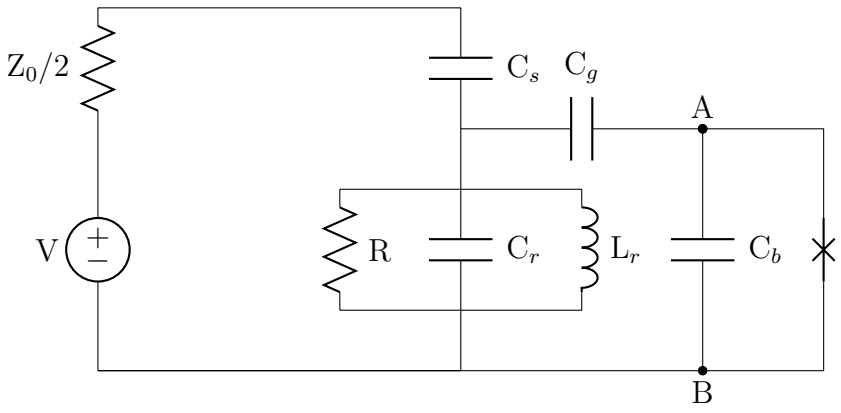

Figure D.3: Reduced external circuit for an impedance-matched transmission line of a transmon-resonator cQED architecture

Knowing the equivalent impedance across the transmon, the admittance $Y(\omega)$ is:

$$Y(\omega) = \frac{1}{Z(\omega)} \tag{D.13}$$

$$= \frac{1}{Re(Z) + jIm(Z)} \tag{D.14}$$

$$= \frac{Re(Z) - jIm(Z)}{Re(Z)^2 + Im(Z)^2} \tag{D.15}$$

or

$$Re(Y) = \frac{Re(Z)^2 + Im(Z)^2}{Re(Z)} \tag{D.16}$$

$$\frac{1}{Re(Y)} = Re(Z) + \frac{Im(Z)^2}{Re(Z)}. \tag{D.17}$$

Using

$$Z(\omega) = \frac{1}{j\omega C_g} + \frac{Z_{res}(Z_0/2 + 1/(j\omega C_s))}{Z_{res} + Z_0/2 + 1/(j\omega C_s)}, \tag{D.18}$$

the exact expression for the real part of the admittance $Y(\omega)$ can be written as

$$\frac{1}{Re(Y)} = \frac{\left(\frac{1}{R} + \frac{\omega^2 Z_0 C_s^2}{2(1+\omega^2 Z_0^2 C_s^2/4)}\right)^2 + \left(\omega C_g - \frac{\omega C_s}{1+\omega^2 C_s^2 Z_0^2/4} - \frac{1-\omega^2/\omega_0^2}{\omega L_r}\right)^2}{\omega^2 C_g^2 \left(\frac{1}{R} + \frac{\omega^2 Z_0 C_s^2/2}{1+\omega^2 Z_0^2 C_s^2/4}\right)}. \tag{D.19}$$

When $\omega^2 Z_0^2 C_s^2 \ll 1$, we can rewrite this as:

$$\frac{1}{Re(Y)} = \frac{\left(\frac{1}{R} + \omega^2 Z_0 C_s^2/2\right)^2 + \left(\omega C_g - \omega C_s - \frac{1-\omega^2/\omega_0^2}{\omega L_r}\right)^2}{\omega^2 C_g^2 \left(\frac{1}{R} + \omega^2 Z_0 C_s^2/2\right)}. \tag{D.20}$$

When I further ignore R, which is the case when R is very large, I get $Re(Y)$ given by

$$\frac{1}{Re(Y)} \approx \left\{ \frac{Z_0 C_s^2}{2C_g^2} + \frac{2}{Z_0 \omega^2 C_g^2} \left[\frac{C_r}{C_s} \left(1 - \frac{\omega_0^2}{\omega^2}\right) + \frac{C_g}{C_s} \right]^2 \right\}. \tag{D.21}$$

Note that the first term has no frequency-dependence. It turns out that for typical values of the circuit parameters, this term is negligible. In the next section, we ignore that term to get a simple-looking relation between the lifetime of the qubit and the coupling strength of the qubit to the dissipative environment.

The T_1 of the transmon can be written as

$$T_1 = \frac{C_b}{Re(Y)} \tag{D.22}$$

where C_b is the shunt-capacitance.

Appendix E

Appendix E

Here I present the Mathematica routine I developed to calculate the parameters of the transmon-resonator cQED Hamiltonian starting from the full capacitance network (see Fig. 4.7). The capacitance matrix for the conductors in the device architecture (see Fig. 4.6) was calculated using FastCap. In the FastCap simulation, the two ground planes on either side of the CPW were treated as two conductors (see Fig. 4.6). In the calculation below, I reduced the number of conductors to 5, by treating the two ground-planes as the same node, as in the actual experiment.

```
Clear["Global`*"]
(*Values of Capacitances from FastCap in femto farad – LEv5–ZK9*)

(*The labels t – transmission line, r– resonator, g–ground plane,
q1 – IDC plate 1 , q1 – IDC plate2*)
Ctg = 97 + 80;
Ctr = 14.61;
Ctq1 = 2.689;
Ctq2 = 1.148;
Crg = 30 + 140;
Crq1 = 27.4;
Crq2 = 7;
Cq1g = 4 + 13;
Cq1q2 = 48.71;
Cq2g = 3 + 31;
Cr = 278;
Lr = 2.26;
h = 6.627 × 10^-34;
echarge = 1.6 × 10^-19;

(* Circuit diagram including the capacitances between
all five conductors listed above *)
```

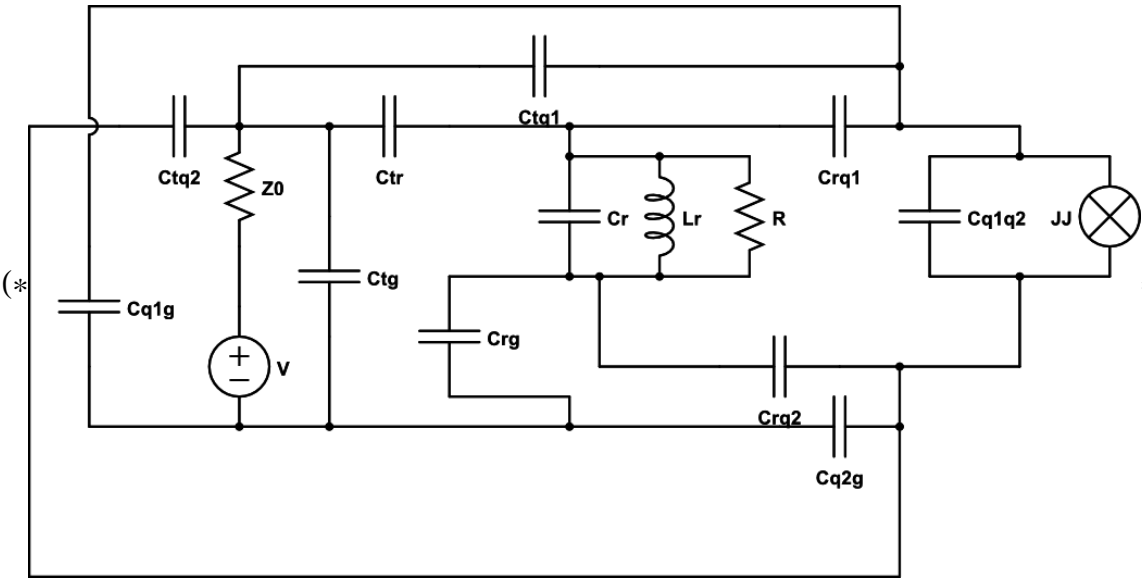


```
(*
)
```

```
(*Lagrangian for the above circuit with the voltage
source replaced by capacitance Cv*)
lagrangian = 1/2*Cv* Vt^2 + 1/2* Ctg Vt^2 + 1/2* Ctr*(Vt - Vr)^2
+ 1/2*Ctq1*(Vt - Vq1)^2 + 1/2 Ctq2 (Vt - Vq2)^2 + 1/2 Crg Vr^2
+ 1/2* Crq1 (Vr - Vq1)^2 + 1/2* Crq2 (V1 - Vq2)^2 + 1/2 Crg (V1)^2
+ 1/2* Cq1g (Vq1)^2 + 1/2* Cq1q2 (Vq1 - Vq2)^2 + 1/2* Cq2g (Vq2)^2
+ 1/2*Cr* (Vr - V1)^2;

(* Euler-Lagrange equations for the circuit *)
eqt = ∂Vt(lagrangian) // FullSimplify;
eqr = ∂Vr(lagrangian) // FullSimplify;
eqq1 = ∂Vq1(lagrangian) // FullSimplify;
eqq2 = ∂Vq2(lagrangian) // FullSimplify;
eq1 = ∂V1(lagrangian) // FullSimplify;

sol = Solve[eqt == Qt && eqr == Qr && eqq1 == Qq1
      && eqq2 == Qq2 && eq1 == Q1, {Vt, Vr, Vq1, Vq2, V1}];

(* Legendre transform to derive the Hamiltonian from the Lagrangian. *)
hamiltonian = Apart[Vt *eqt + Vr eqr + Vq1 *eqq1
      + Vq2* eqq2 + V1*eq1 - lagrangian /. sol ];

Kt = Coefficient[hamiltonian, Qt^2] // Together;
Kr = Coefficient[hamiltonian, Qr^2] // Together;
Kq1 = Coefficient[hamiltonian, Qq1^2] // Together;
Kq2 = Coefficient[hamiltonian, Qq2^2] // Together;
```

```
K1 = Coefficient[hamiltonian, Q1^2] // Together;
(*c5= Together[Coefficient[hamiltonian,Q5^2]]*)
Ktr = Coefficient[hamiltonian, Qt Qr] // Together;
Ktq1 = Coefficient[hamiltonian, Qt Qq1] // Together;
Ktq2 = Coefficient[hamiltonian, Qt Qq2] // Together;
Kt1 = Coefficient[hamiltonian, Qt Q1] // Together;
(*c15= Together[Coefficient[hamiltonian,Q1 Q5]]*)
Krq1 = Coefficient[hamiltonian, Qr Qq1] // Together;
Krq2 = Coefficient[hamiltonian, Qr Qq2] // Together;
Kr1 = Coefficient[hamiltonian, Qr Q1] // Together;
(*c25 = Together[Coefficient[hamiltonian,Q2 Q5]]*)
Kq1q2 = Coefficient[hamiltonian, Qq1 Qq2] // Together;
Kq11 = Coefficient[hamiltonian, Qq1 Q1] // Together;
Kq21 = Coefficient[hamiltonian, Qq2 Q1] // Together;


(* Replacing the large capacitance Cv back with the voltage source V. *)
transham = Limit[Kr, Cv → Infinity] * Qr^2 +
    Limit[K1, Cv → Infinity] * Q1^2 + Limit[Kq2, Cv → Infinity] * Qq2^2
+Limit[Kq1, Cv → Infinity] * Qq1^2 + Limit[Krq1, Cv → Infinity] * Qr * Qq1
+Limit[Krq2, Cv → Infinity] * Qr * Qq2 + Limit[Kr1, Cv → Infinity] * Qr * Q1
+Limit[Kq1q2, Cv → Infinity] * Qq1 * Qq2 +
  Limit[Kq11, Cv → Infinity] * Qq1 * Q1
+Limit[Kq21, Cv → Infinity] * Q1 * Qq2 +
  Limit[Ktr * Cv, Cv → Infinity] * V Qr
+Limit[Kt1 * Cv, Cv → Infinity] * V * Q1 +
  Limit[Ktq2 * Cv, Cv → Infinity] * V * Qq2
+ Limit[Ktq1 * Cv, Cv → Infinity] * V * Qq1 + 1 / (2 L) (Φr)^2 +
    1 / (2 Lj) (Φ1 − Φ2)^2;


(* Define new variables rsum = Qr/2 + Q1/2, rdiff = Qr/2 − Q1/2
, qsum = Qq1/2 + Qq2/2, qdiff = Qq1/2−Qq2/2 *)

solveq = Solve[Qq1 / 2 + Qq2 / 2 == qsum && Qq1 / 2 − Qq2 / 2 == qdiff
        && Qr / 2 + Q1 / 2 == rsum && Qr / 2 − Q1 / 2 == rdiff,
      {Qq1, Qq2, Qr, Q1}];

hamvarchangetoq = transham /. solveq // Expand;
```

```
Cres = 1 / (2 (Coefficient[hamvarchangetoq, rdiff^2]));(*femtofarad*)
fres = 1 / (2 π 10^9 Sqrt[Cres * 10^-15 * Lr * 10^-9]) ;(*GHz*)
crqdiffeff = Coefficient[hamvarchangetoq, rdiff qdiff] ;(*femtofarad*)
Cqdiffeff = 1 / (2 (Coefficient[hamvarchangetoq, qdiff^2])) ;(*femtofarad*)
βtreff = Coefficient[hamvarchangetoq, rdiff V];(*voltage ratio*)
βtqdiffeff = Coefficient[hamvarchangetoq, qdiff V];(*voltage ratio*)
Ecqdiff = echarge^2 / (2 Cqdiffeff 10^-15) / h * 10^-6;(*femtofarad*) (*MHz*)
gqdiff = echarge * Sqrt[h * fres * 10^9 / (2 Cres * 10^-15)]
* (crqdiffeff * Cres * 10^-15 * 10^15) 10^-6 / h ;(*femtofarad*) (*MHz*)
Rabifrequency = 2 * echarge * V * (βtqdiffeff) / h ;(*Hertz*)
rabicoupling = Rabifrequency / V (10^-6 / 10^6) ;
(*MHz/μV*)

(* Output of parameters calculated using the circuit Hamiltonian approach used above *)
Row[{" Capacitance of the resonator (C_res) = ", Cres, " fF"}]
Row[{" Resonance frequency of the resonator (f_res) = ", fres, " GHz"}]
Row[{" Transmon capacitance (C_Σ) = ", Cqdiffeff, " fF"}]
Row[{" Transmon charging energy (E_c/h) = ", Ecqdiff, " MHz"}]
Row[{" Transmon−resonator coupling (g / 2π) = ", gqdiff, " MHz"}]
Row[{" Rabi coupling (df_Rabi/dV_rms) = ", rabicoupling, " MHz/ μV"}]
```

Capacitance of the resonator (C_{res}) = {{372.695}} fF

Resonance frequency of the resonator (f_{res}) = {{5.48389}} GHz

Transmon capacitance (C_{Σ}) = {{70.5527}} fF

Transmon charging energy (E_c/h) = {{273.766}} MHz

Transmon−resonator coupling ($g / 2\pi$) = {{60.1796}} MHz

Rabi coupling (df_{Rabi}/dV_{rms}) = {{8.30404}} MHz/ μV

Appendix F

Appendix F

I numerically simulated the system master equation (Eq. 6.11) in steady state to study photon number-splitting and Autler-Townes effects in device LEv5-ZK9. Here I present the Mathematica routine that I used for the simulation. This code was originally developed by Lev Bishop and is described in detail in his thesis [68]. I note that this routine requires the "qmatrix" and "Developer" packages. The parameters of the simulation are listed in Sec. 6.4.2.2. The number-split spectrum simulated using this code is shown in red in Fig. 6.12.

```
(*This code solves the master equation in the
steady state to simulate the number−split
spectrum of the transmon. Parameters
correspond to those of device LEv5−ZK9*)
Clear["Global`*"];
(* Directory with data *)
SetDirectory[NotebookDirectory[]];
(*Packages necessary for this program*)
Needs["qmatrix`"];
Needs["Developer`"];
```

```
\n package qmatrix, version 2.2.1\n \n  (C) Timo Felbinger (timo@felbinger.net),
    \n1999, 2000, 2001\n \n  last modified:  20010430.210546utc
    by: timof@amadeus\n \n  \nThis package is free software and you
    are welcome to\n \n  redistribute \nit; type qmatrix`license for the
    details.\n \n  \nType qmatrix`help to get help on this package.\n
```

```
(*Setting up the Hilbert space
q − transmon − 5 levels
c − cavity/resonator − 15 levels*)
setSystem[sys = {q, c}];
setModeType[q, {bosonic, 5}];
setModeType[c, {bosonic, 15}];
d = dimension@sys;
orderm = {ket[c], ket[q], bra[c], bra[q]};
orderv = {ket[c], ket[q]};
iid = identityMatrix[sys];
tomatrix[m_?properMatrixQ] :=
    Developer`ToPackedArray@flatten[reorderMatrix[m ** iid, orderm]][[1]];
tovector[v_?properMatrixQ] :=
    Developer`ToPackedArray@flatten[reorderMatrix[v, orderv]][[1]];
{oa, oad, oia} = matrix[op[#, c]] & /@ {a, ad, id};
{ob, obd, oib} = matrix[op[#, q]] & /@ {a, ad, id};
```

(*Hamiltonian for the system
In units of h=1
dc = detuning of the resonator drive
dq = detuning of the qubit drive
xq = Rabi freq. of qubit drive.
xc = Rabi freq. of resonator drive.
chi2 = 2χ, ck2 = 2ζ, sk2 = 2ζ', sq = E_c *)

```
Hq = dc oad ** oa  + dq  obd ** ob + chi2 oad ** oa ** obd ** ob − xc / 2 (oa + oad)
− xq / 2 (ob + obd) + ck2 oad ** oa ** (oad ** oa)  ** (obd ** ob)
− sq obd ** ob ** (obd ** ob − oib) / 2 + sk2 oad ** oa ** (oad ** oa);
```

(*Creating the matrices representing
the operators in qmatrix*)

```
H = tomatrix[Hq];
H // MatrixForm;
am = tomatrix[oa];
adm = tomatrix[oad];
adam = tomatrix[oad ** oa];
bm = tomatrix[ob];
bdm = tomatrix[obd];
bdbm = tomatrix[obd ** ob];
```

(*Density matrix ρ *)

```
ρ = Table[Symbol["ρ" <> ToString[i] <> "x" <> ToString[j]], {i, d}, {j, d}];
ρs = Flatten[ρ];
```

(*Lindblad form of super−operators *)

```
𝒟[A_, r_] := A.r.A⁺ − (A⁺.A.r + r.A⁺.A) / 2;
L = − i (H.ρ − ρ.H) + κ 𝒟[am, ρ] + γ 𝒟[bm, ρ] + κp 𝒟[adm, ρ] + γp 𝒟[bdm, ρ]
+ 1 / 2 γphi 𝒟[bdbm, ρ];
```

```
(*Constraints on ρ *)
{off, mat} =
    CoefficientArrays[{Tr@ρ - 1}~Join~Rest@Flatten[L], Flatten[ρ]];

(*Sparse matrix operations*)
pv = {dc, dq, xc, xq, κ, κp, γ, γp, chi2, sk2, sq , ck2, γphi};
nzv = mat["NonzeroValues"];
nzp = mat["NonzeroPositions"];
dims = Dimensions@mat;
nzvv =
    Developer`ToPackedArray[#, Complex] & /@
      Normal /@ CoefficientArrays[nzv, pv];

(*Numerical simulation. In units of h=1. All
frequencies are in MHz. In these units, T1 = 1/(2π γ) *)


(*This section of the code aims to plot a linecut
  at the splitting and fit it to a double lorentzian*)
xmin = -100;
xmax = 10;
deltax = 0.1;
nx = (xmax - xmin)/deltax + 1;
nrange = Range[xmin/starkshift, xmax/starkshift, deltax/starkshift];
xrange = Range[xmin, xmax, deltax];
Length[xrange]

Block[{xc = 1.1, xq = 0.3, dc = 0, κ = 0.3, κp = 0.03, γ = 0.1, γp = 0.01,
    chi2 = -9.3, sk2 = -0.046, sq = -270, ck2 = 0.17, γphi = 0.05},
  spectrum = Table[Block[{dq = x},
          sol = LinearSolve[SparseArray[nzp → nzvv[[1]]
                  + nzvv[[2]].pv, dims], -off];
          Abs@Tr[Partition[sol, d].bdbm]], {x, xmin, xmax, deltax}];]
```

Bibliography

[1] R. P. Feynman, "Simulating physics with computers", *Int. J. Theor. Phys.* **21**, 467 (1982).

[2] D. P. DiVincenzo, "Quantum Computation", *Science* **270**, 255 (1995).

[3] Y. Nakamura, Y. A. Pashkin, J. S.Tsai, "Coherent control of macroscopic quantum states in a single-Cooper-pair box", *Nature* **398**, 786 (1999).

[4] J. M. Martinis, M. Devoret, J. Clarke, "Energy-Level Quantization in the Zero-Voltage State of a Current-Biased Josephson Junction", *Phys. Rev. Lett.* **55**, 1543 (1985).

[5] A. O. Caldeira, A. J. Leggett, "Influence of Dissipation on Quantum Tunneling in Macroscopic Systems", *Phys. Rev. Lett.* **46**, 1981.

[6] A. O. Caldeira, A. J. Leggett, "Quantum tunnelling in a dissipative system", *Ann. Phys.* **149**, 374 (1983).

[7] G. J. Dolan, "Offset masks for lift-off photoprocessing", *App. Phys. Lett.* **31**, 337 (1977).

[8] T. A. Fulton, G. J. Dolan, "Observation of single-electron charging effects in small tunnel junctions", *Phys. Rev. Lett.* **59**, 109 (1987).

[9] D. Vion, A. Aassime, A. Cottet, P. Joyez, "Manipulating the quantum state of an electrical circuit", *Science* **296**, 886 (2002).

[10] I. Chiorescu, Y. Nakamura, C. J. P. M. Harmans, J. E. Mooij, "Coherent quantum dynamics of a superconducting flux qubit", *Science* **299**, 1869 (2003).

[11] R.C. Ramos, M.a. Gubrud, A.J. Berkley, J.R. Anderson, C.J. Lobb, F.C. Wellstood, "Design for effective thermalization of junctions for quantum coherence", *IEEE Trans. Appiled Supercond.* **11**, 998 (2001).

[12] S. Han, Y. Yu, X. Chu, S. I. Chu, Z. Wang, "Time-resolved measurement of dissipation-induced decoherence in a Josephson junction", *Science* **293**, 1457 (2001).

[13] F. Strauch, P. Johnson, A. Dragt, C. Lobb, J. Anderson, and F. Wellstood, "Quantum Logic Gates for Coupled Superconducting Phase Qubits", *Phys. Rev. Lett.* **91**, 167005 (2003).

[14] R. J. Schoelkopf, "The Radio-Frequency Single-Electron Transistor (RF-SET): A Fast and Ultrasensitive Electrometer", *Science* **280**, 1238 (1998).

[15] I. Siddiqi, R. Vijay, F. Pierre, C. M. Wilson, M. Metcalfe, C. Rigetti, L. Frunzio, and M. H. Devoret, "RF-driven Josephson bifurcation amplifier for quantum measurement", *Phys. Rev. Lett.* **93**, 207002 (2004)

[16] Z. Kim, V. Zaretskey, Y. Yoon, J. Schneiderman, M. Shaw, P. Echternach, F. Wellstood, B. S. Palmer, "Anomalous avoided level crossings in a Cooper-pair box spectrum". *Phys. Rev. B* **78**, 144506 (2008).

[17] A. Wallraff, D. I. Schuster, A. Blais, L. Frunzio, R-S Huang, J. Majer, S. Kumar, S. M. Girvin, R. J. Schoelkopf, "Strong coupling of a single photon to a superconducting qubit using circuit quantum electrodynamics", *Nature* **431**, 162 (2004).

[18] A. Blais, R. -S. Huang, A. Wallraff, S. M. Girvin, R. J. Schoelkopf, "Cavity quantum electrodynamics for superconducting electrical circuits: An architecture for quantum computation", *Phys. Rev. A* **69**, 062320 (2004).

[19] P. Goy, J. M. Raimond, M. Gross, S. Haroche, "Observation of Cavity-Enhanced Single-Atom Spontaneous Emission", *Phys. Rev. Lett.* **50**, 1903 (1983).

[20] J. M. Raimond, M. Brune, S. Haroche, "Manipulating quantum entanglement with atoms photons in a cavity", *Rev. Mod. Phys.* **73**, 565 (2001).

[21] M. Brune, S. Haroche, V. Lefevre, "Quantum Nondemolition Measurement of Small Photon Numbers by Rydberg-Atom Phase-Sensitive Detection", *Phys. Rev. Lett.* **65**, 976 (1990).

[22] O. Astafiev, Y. A. Pashkin, Y. Nakamura, T. Yamamoto, J. S. Tsai, "Quantum noise in the Josephson charge qubit", *Phys. Rev. Lett.* **93**, 267007 (2004).

[23] E. M. Purcell, H. Torrey, R. V. Pound, "Resonance Absorption by Nuclear Magnetic Moments in a Solid", *Phys. Rev.* **69**, 37 (1946).

[24] E. M. Purcell, "Proceedings of the American Physical Society", *Phys. Rev.* **69**, 674 (1946).

[25] D. Kleppner, "Inhibited Spontaneous Emission", *Phys. Rev. Lett.* **47**, 233 (1981).

[26] A. G. Vaidyanathan, W. P. Spencer, D. Kleppner. "Inhibited Absorption of Blackbody Radiation", *Phys. Rev. Lett.* **47**, 1592 (1981).

[27] R. Hulet, E. Hilfer, D. Kleppner, "Inhibited Spontaneous Emission by a Rydberg Atom", *Phys. Rev. Lett.* **55**, 2137 (1985).

[28] Z. Kim, B. Suri, V. Zaretskey, S. Novikov, K. D Osborn, A. Mizel, F. C Wellstood, B. S Palmer, "Decoupling a Cooper-Pair Box to Enhance the Lifetime to 0.2 ms", *Phys. Rev. Lett.* **106**, 120501 (2011).

[29] V. Zaretskey, B. Suri, S. Novikov, F. C. Wellstood, B. S. Palmer, "Spectroscopy of a Cooper-pair box coupled to a two-level system via charge critical current", *Phys. Rev. B* **87**, 174522 (2013).

[30] J. Koch, T. M Yu, J. Gambetta, A. A. Houck, D. I. Schuster, J. Majer, A. Blais, M. H. Devoret, S. M. Girvin, R. J. Schoelkopf, "Charge-insensitive qubit design derived from the Cooper pair box", *Phys. Rev. A* **76**, 042319 (2007).

[31] A. A. Houck, J. A. Schreier, B. R. Johnson, J. M. Chow, J. Koch, J. M. Gambetta, D. I. Schuster, L. Frunzio, M. H. Devoret, S. M. Girvin, R. J, Schoelkopf, "Controlling the spontaneous emission of a superconducting transmon qubit", *Phys. Rev. Lett.* **101**, 4 (2008).

[32] J. Gao, M. Daal, P. Day, B. Mazin, H. LeDuc, A. Vayonakis, S. Kumar, B. Sadoulet, J. Zmuidzinas, "Experimental evidence for a surface distribution of two-level systems in superconducting lithographed microwave resonators", *App. Phys. Lett.* **92**, 152505 (2008).

[33] A. D. O'Connell, M. Ansmann, R. C. Bialczak, M. Hofheinz, N. Katz, E. Lucero, C. McKenney, M. Neeley, H. Wang, E. M. Weig, A. N. Cleland, J. M. Martinis. "Microwave dielectric loss at single photon energies millikelvin temperatures", *Appl. Phys. Lett.* **92**, 112903 (2008).

[34] A. D. Córcoles, J. M Chow, J. M. Gambetta, C. Rigetti, J. R. Rozen, G. A. Keefe, M. B. Rothwell, M. B. Ketchen, M. Steffen, "Protecting superconducting qubits from radiation", *App. Phys. Lett.* **99**, 181906 (2011).

[35] M. D. Reed, L. DiCarlo, B. R. Johnson, L. Sun, D. I. Schuster, L. Frunzio, R. J. Schoelkopf, "High-Fidelity Readout in Circuit Quantum Electrodynamics Using the Jaynes-Cummings Nonlinearity", *Phys. Rev. Lett.*, **105**, 173601 (2010).

[36] J. M. Gambetta, A. A. Houck, A. Blais, "Superconducting Qubit with Purcell Protection Tunable Coupling", *Phys. Rev. Lett.* **106**, 030502 (2011).

[37] J. M Chow, J. M. Gambetta, A. D. Córcoles, S. T. Merkel, J. A. Smolin, C. Rigetti, S. Poletto, G. A. Keefe, M. B. Rothwell, J. R. Rozen, M. B. Ketchen, M. Steffen, "Universal Quantum Gate Set Approaching Fault-Tolerant Thresholds with Superconducting Qubits", *Phys. Rev. Lett.* **109**, 060501 (2012).

[38] J. B. Chang, M. R. Vissers, A. D. Córcoles, M. Sandberg, J. Gao, D. W. Abraham, J. M. Chow, J. M. Gambetta, M. B. Rothwell, G. A. Keefe, M. Steffen, D. P. Pappas, "Improved superconducting qubit coherence using titanium nitride", *App. Phys. Lett.* **103**, 012602 (2013).

[39] R. Barends, J. Kelly, A. Megrant, D. Sank, E. Jeffrey, Y. Chen, Y. Yin, B. Chiaro, J. Mutus, C. Neill, P. O'Malley, P. Roushan, J. Wenner, T. C. White, A. N. Cleland, J. M. Martinis, P. O'Malley, "Coherent Josephson Qubit Suitable for Scalable Quantum Integrated Circuits", *Phys. Rev. Lett.* **111**, 080502 (2013).

[40] H. Paik, D. I. Schuster, L. S. Bishop, G. Kirchmair, G. Catelani, A. P. Sears, B. R. Johnson, M. J. Reagor, L. Frunzio, L. I. Glazman, S. M. Girvin, M. H. Devoret, R. J. Schoelkopf, "Observation of High Coherence in Josephson Junction Qubits Measured in a Three-Dimensional Circuit QED Architecture", *Phys. Rev. Lett.* **107**, 240501 (2011).

[41] C. Rigetti, J. M. Gambetta, S. Poletto, B. L. T. Plourde, J. M. Chow, A. D. Córcoles, J. A. Smolin, S. T. Merkel, J. R. Rozen, G. A. Keefe, M. B. Rothwell, M. B. Ketchen, M. Steffen, "Superconducting qubit in a waveguide cavity with a coherence time approaching 0.1 ms", *Phys. Rev. B* **86**, 100506(R) (2012).

[42] C. J Hood, T. W. Lynn, A. C. Doherty, A. S. Parkins, H. J. Kimble, "The Atom-Cavity Microscope: Single Atoms Bound in Orbit by Single Photons", *Science*, **287**, 1447 (2000).

[43] A. Fragner, M. Göppl, J. M. Fink, M. Baur, R. Bianchetti, P. J. Leek, A. Blais, A. Wallraff, "Resolving vacuum fluctuations in an electrical circuit by measuring the lamb shift", *Science* **322**, 1357 (2008).

[44] D. I. Schuster, A. A. Houck, J. A. Schreier, A. Wallraff, J. M. Gambetta, A. Blais, L. Frunzio, J. Majer, B. Johnson, M. H. Devoret, S. M. Girvin, R. J. Schoelkopf, "Resolving photon number states in a superconducting circuit", *Nature* **445**, 515 (2007).

[45] J. Gambetta, A. Blais, D. I. Schuster, A. Wallraff, L. Frunzio, J. Majer, M. H. Devoret, S. M. Girvin, R. J. Schoelkopf, "Qubit-photon interactions in a cavity: Measurement-induced dephasing number splitting", *Phys. Rev. A* **74**, 042318 (2006).

[46] M. Baur, S. Filipp, R. Bianchetti, J. Fink, M. Göppl, L. Steffen, P. Leek, A. Blais, A. Wallraff, "Measurement of Autler-Townes Mollow Transitions in a Strongly Driven Superconducting Qubit", *Phys. Rev. Lett.* **102**, 243602 (2009).

[47] Lev. S. Bishop, J. M. Chow, J. Koch, A. A. Houck, M. H. Devoret, E. Thuneberg, S. M. Girvin, R. J. Schoelkopf, "Nonlinear response of the vacuum Rabi resonance", *Nat. Phys.* **5**, 105 (2008).

[48] J. M. Fink, M. Göppl, M. Baur, R. Bianchetti, P. J. Leek, A. Blais, A. Wallraff, "Climbing the Jaynes-Cummings ladder observing its nonlinearity in a cavity QED system", *Nature* **454**, 315 (2008).

[49] J. Q. You, F. Nori. "Atomic physics quantum optics using superconducting circuits", *Nature* **474**, 589 (2011).

[50] E. T. Jaynes, F. W. Cummings, "Comparison of quantum semiclassical radiation theories with application to the beam maser", *Proc. IEEE* **51**, 89 (1963).

[51] Lev S. Bishop, E. Ginossar, S. M. Girvin, "Response of the Strongly Driven Jaynes-Cummings Oscillator", *Phys. Rev. Lett.* **105**, 100505 (2010).

[52] M. Boissonneault, J. M. Gambetta, A. Blais. "Improved Superconducting Qubit Readout by Qubit-Induced Nonlinearities", *Phys. Rev. Lett.* **105**, 100504 (2010).

[53] B. Suri, Z. K. Keane, R. Ruskov, Lev S. Bishop, C. Tahan, S. Novikov, J. E. Robinson, F. C. Wellstood, B. S. Palmer, "Observation of Autler–Townes effect in a dispersively dressed Jaynes–Cummings system", *New J. Phys.* **15**, 125007 (2013).

[54] M. Hatridge, R. Vijay, D. H. Slichter, J. Clarke, I. Siddiqi, "Dispersive magnetometry with a quantum limited SQUID parametric amplifier" *Phys. Rev. B* **83**, 134501 (2011).

[55] R. Vijay, D. H. Slichter, I. Siddiqi, "Observation of quantum jumps in a superconducting artificial atom", *Phys. Rev. Lett.* **106**, 110502 (2011).

[56] R. Vijay, C. Macklin, D. H. Slichter, S. J. Weber, K. W. Murch, R. Naik, A. N. Korotkov, I. Siddiqi, "Stabilizing Rabi oscillations in a superconducting qubit using quantum feedback", *Nature* **490**, 77 (2012).

[57] K. W. Murch, S. J. Weber, C. Macklin, I. Siddiqi, "Observing single quantum trajectories of a superconducting quantum bit", *Nature* **502**, 211 (2013).

[58] S. J. Weber, A. Chantasri, J. Dressel, A. N. Jordan, K. W. Murch, I. Siddiqi, "Mapping the optimal route between two quantum states", *Nature* **511**, 570 (2014).

[59] A. A. Houck, D. I. Schuster, J. M. Gambetta, J. A. Schreier, B. R. Johnson, J. M. Chow, L. Frunzio, J. Majer, M. H. Devoret, S. M. Girvin, R. J. Schoelkopf. "Generating single microwave photons in a circuit", *Nature* **449**, 328 (2007).

[60] I. -C. Hoi, T. Palomaki, J. Lindkvist, G. Johansson, P. Delsing, C. M. Wilson, "Generation of Nonclassical Microwave States Using an Artificial Atom in 1D Open Space", *Phys. Rev. Lett.* **108**, 263601 (2012).

[61] I. -C. Hoi, A. F. Kockum, L. Tornberg, "Probing the quantum vacuum with an artificial atom in front of a mirror", *arXiv:1410.8840v1* (2014).

[62] I. -C. Hoi, C. M. Wilson, G. Johansson, T. Palomaki, B. Peropadre, P. Delsing, "Demonstration of a Single-Photon Router in the Microwave Regime", *Phys. Rev. Lett.* **107**, 073601 (2011).

[63] M. V. Gustafsson, T. Aref, A. F. Kockum, M. K. Ekström, G. Johansson, P. Delsing, "Propagating phonons coupled to an artificial atom", *Science* 346, 207 (2014).

[64] S. H. Autler C. H. Townes, "Stark Effect in Rapidly Varying Fields", *Phys. Rev.* **100**, 703 (1955).

[65] M. Sillanpää, J. Li, K. Cicak, F. Altomare, J. Park, R. Simmonds, G. Paraoanu, P. Hakonen, "Autler-Townes Effect in a Superconducting Three-Level System", *Phys. Rev. Lett.* **103**, 193601 (2009).

[66] S. Novikov, J. E. Robinson, Z. K. Keane, B. Suri, F. C. Wellstood, B. S. Palmer, "Autler-Townes splitting in a three-dimensional transmon superconducting qubit", *Phys. Rev. B*, **88**, 060503(R) (2013).

[67] P. A. M. Dirac, "Principles of quantum mechanics". *International Series of Monographs on Physics*, 4th Ed. (revised), Oxford, Clarendon press, 1932.

[68] Lev S. Bishop, "Circuit Quantum Electrodynamics". PhD thesis, Yale University (2010).

[69] C. Guerlin, J. Bernu, S. Deléglise, C. Sayrin, S. Gleyzes, S. Kuhr, M. Brune, J. Raimond, and S. Haroche, "Progressive field-state collapse quantum nondemolition photon counting", *Nature* **448**, 889 (2007).

[70] H. Goldstein, "Classical mechanics". *3rd Ed. Addison Wesey* (1962).

[71] M. H. Devoret, J. M. Martinis, "Implementing qubits with superconducting integrated circuits", *Quantum Inf. Process.* **3**, 163 (2004).

[72] B. D. Josephson, "Possible new effects in superconductive tunnelling", *Phys. Lett.* **1**, 251 (1962).

[73] J. Clarke, F. K. Wilhelm, "Superconducting quantum bits", *Nature* **453**, 1031 (2008).

[74] M. Tinkham, "Introduction to Superconductivity", 2nd Ed. Dover Publications (2004).

[75] Z. Kim, "Dissipative dispersive measurements of a Cooper pair box", PhD Thesis, University of Maryland (2010).

[76] A. Cottet, "Implementation of a quantum bit in a superconducting circuit", PhD Thesis, L'Universite Paris VI (2002).

[77] R. J. Glauber, "Coherent Incoherent States of the Radiation Field", *Phys. Rev.* **131**, 2766 (1963).

[78] F. Bloch, A. Siegert, "Magnetic Resonance for Nonrotating fields", *Phys. Rev.* **526** , 522 (1940).

[79] P. Carbonaro, G. Compagno, F. Persico, "Canonical dressing of atoms by intense radiation fields", *Phys. Lett. A* **73**, 97 (1979).

[80] M. I. Dykman, M. A. Krivoglaz, "Profiles of no-phonon lines of impurity centers interacting with local or quasilocal vibrations", *Fiz. Tverd. Tela* **29**, 368 (1987).

[81] A. Einstein, "On The Quantum Theory Of Radiation", *Z. Phys* (1917).

[82] P. W. Bridgman, "Note on the principle of detailed balancing", *Phys. Rev.* **392**, 1926 (1928).

[83] R. Shankar, "Principles of Quantum Mechanics", 2nd Ed. Springer (1994).

[84] G. D Alley, "Interdigital Capacitors Their Application to Lumped-Element Microwave Integrated Circuits", *IEEE Trans. Microw. Theory Tech.* **18**, 1028 (1970).

[85] M. S. Khalil, M. J.. a. Stoutimore, F. C. Wellstood, K. D. Osborn, "An analysis method for asymmetric resonator transmission applied to superconducting devices", *J. Appl. Phys.* **111**, 054510 (2012).

[86] M. Boissonneault, J. M. Gambetta, A. Blais, "Dispersive regime of circuit QED: Photon-dependent qubit dephasing relaxation rates", *Phys. Rev. A*, **79**, 013819 (2009).

[87] J. Wenner, Y. Yin, E. Lucero, R. Barends, Y. Chen, B. Chiaro, J. Kelly, M. Lenander, M. Mariantoni, A. Megrant, C. Neill, P. J. J. O'Malley, D. Sank, A. Vainsencher, H. Wang, T. C. White, A. N. Cleland, J. M. Martinis, "Excitation of Superconducting Qubits from Hot Nonequilibrium Quasiparticles" *Phys. Rev. Lett.* **110**, 150502 (2013).

[88] A. Megrant, C. Neill, R. Barends, B. Chiaro, Yu Chen, L. Fiegl, J. Kelly, E. Lucero, M. Mariantoni, P. J. J. O'Malley, D. Sank, A. Vainsencher, J. Wenner, T. C. White, Y. Yin, J. Zhao, C. J. Palmstrøm, J. M. Martinis, A. N. Cleland, "Planar superconducting resonators with internal quality factors above one million", *Appl. Phys. Lett.* **100**, 113510 (2012).

[89] J. Li, G. S Paraoanu, K. Cicak, F. Altomare, J. I Park, R. W Simmonds, M. Sillanpää, P. J. Hakonen. "Dynamical Autler-Townes control of a phase qubit", *Sci. Rep.* **2**, 645 (2012).

[90] I. -C. Hoi, C. M. Wilson, G. Johansson, J. Lindkvist, B. Peropadre, T. Palomaki, P. Delsing, "Microwave quantum optics with an artificial atom in one-dimensional open space", *New J. Phys.* **15**, 025011 (2013).

[91] K. J. Boller, A. Imamolu, S. E. Harris, "Observation of electromagnetically induced transparency", *Phys. Rev. Lett.* **66**, 2593 (1991).

[92] P. M. Anisimov, J. P. Dowling, B. C. Sanders, "Objectively Discerning Autler-Townes Splitting from Electromagnetically Induced Transparency", *Phys. Rev. Lett.* **107**, 163604 (2011).

[93] H. Ian, Y. Liu, F. Nori, "Tunable electromagnetically induced transparency absorption with dressed superconducting qubits", *Phys. Rev. A* **81**, 063823 (2010).

[94] A. Wallraff, D. I. Schuster, A. Blais, J. M. Gambetta, J. Schreier, L. Frunzio, M. H. Devoret, S. M. Girvin, R. J. Schoelkopf, "Sideband Transitions Two-Tone Spectroscopy of a Superconducting Qubit Strongly Coupled to an On-Chip Cavity", *Phys. Rev. Lett.* **99**, 50501 (2007).

[95] L. V Hau, S. E Harris, Zachary Dutton, Cyrus. H Behroozi, "Light speed reduction to 17 metres per second in an ultracold atomic gas", *Nature*, 397(February):594–598, 1999.

[96] K. Murali, Z. Dutton, W. Oliver, D. Crankshaw, T. Orlando, "Probing Decoherence with Electromagnetically Induced Transparency in Superconductive Quantum Circuits", *Phys. Rev. Lett.*, 93(8):087003, August 2004.

[97] A. A. Abdumalikov, O. Astafiev, A. M. Zagoskin, Y. A. Pashkin, Y. Nakamura, J. S. Tsai, "Electromagnetically Induced Transparency on a Single Artificial Atom", *Phys. Rev. Lett*, **104**:193601 (2010).

[98] J. Joo, J. Bourassa, A. Blais, B. C. Sanders, "Electromagnetically Induced Transparency with Amplification in Superconducting Circuits", *Phys. Rev. Lett.* **105**, 073601 (2010).

[99] J. B. Johnson, "Thermal Agitation of Electricity in Conductors", *Nature* **119**, 2984 (1927).

[100] H. Nyquist, "Thermal agitation of electric charge in conductors", *Phys. Rev.* **32**, 110 (1928).

[101] R.J. Schoelkopf, A. A. Clerk, "Qubits as spectrometers of quantum noise", *Quantum noise Mesoscopic Phys.*, NATO Science Series, Ed. by Yuli Nazarov, Pages 175–203 (2003).

[102] F. C. Wellstood, C. Urbina, J. Clarke, "Low-frequency noise in dc superconducting quantum interference devices below 1 K", *Appl. Phys. Lett.* **50**, 772 (1987).

[103] J. Bylander, S. Gustavsson, F. Yan, F. Yoshihara, K. Harrabi, G. Fitch, D. G. Cory, Y. Nakamura, J. S. Tsai, W. D. Oliver, "Noise spectroscopy through dynamical decoupling with a superconducting flux qubit", *Nat. Phys.* **7**, 565 (2011).

[104] H. Callen, T. Welton, "Irreversibility Generalized Noise", *Phys. Rev.* **83**, 34 (1951).

[105] R.J. Schoelkopf, A. A. Clerk, "Qubits as spectrometers of quantum noise", *Quantum noise Mesoscopic Phys.*, NATO Science Series, Ed. by Yuli Nazarov, Pages 175–203 (2003).

[106] W. Jhe, A. Anderson, E. A. Hinds, D. Meschede, "Suppression of Spontaneous Decay at Optical Frequencies: Test of Vacuum-Field Anisotropy in Confined Space", *Phys. Rev. Lett.* **58**, 666 (1987).

[107] M. Pierre, I. Svensson, S. R. Satyamoorthy, G. Johansson, P. Delsing, "Storage and on-demand release of microwaves using superconducting resonators with tunable coupling", *Appl. Phys. Lett.* **104**, 232604 (2014).

[108] M. Boissonneault, J. M. Gambetta, A. Blais, "Dispersive regime of circuit QED: Photon-dependent qubit dephasing and relaxation rates ", *Phys. Rev. A.* **79**, 013819 (2009).

[109] "The Maxwell Capacitance Matrix - White Paper", *FastFieldSolvers, Revision01* WP110301 (2011).

[110] J. Hackley, D. Ali, J. DiPasquale, J. D. Demaree and C. J. K. Richardson, "Graphitic carbon growth on Si(111) using solid source molecular beam epitaxy", *Appl. Phys. Lett.* **95**, 133114 (2009).

[111] S.Novikov *et al.*, (to be published).